Photon performance studies with Radiative Z decays, and the search for the Higgs boson in the H $\rightarrow \gamma\gamma$ and H $\rightarrow$ Zγ channels with the ATLAS detector of the LHC

Rangel-Smith Camila

THÈSE DE DOCTORAT

présentée par

Camila Rangel Smith

Pour obtenir le grade de

DOCTEUR EN SCIENCES
DE L'UNIVERSITÉ PARIS DIDEROT

Spécialité :

Particules, Noyaux, Cosmologie (ED 517)

Étude des performances de photons avec les désintégrations radiatives du Z, et recherche du boson de Higgs dans les modes $H \to \gamma\gamma$ et $H \to Z\gamma$ auprès du détecteur ATLAS au LHC

Soutenue le 27 Septembre 2013 devant le jury composé de:

Claude	Charlot	Rapporteur
Abdelhak	Djouadi	Examinateur
Fabrice	Hubaut	Rapporteur
José	Ocariz	Directeur de thèse
Vanina	Ruhlmann-Kleider	Présidente
Kerstin	Tackmann	Examinatrice

PHILOSOPHIÆ DOCTOR THESIS

presented by

Camila Rangel Smith

Submitted in fulfilment of the requirements for the degree of

DOCTOR OF SCIENCES
OF THE UNIVERSITÉ PARIS DIDEROT

Speciality:

Particles, Nuclei, Cosmology (ED 517)

Photon performance studies with Radiative Z decays, and the search for the Higgs boson in the $H \to \gamma\gamma$ and $H \to Z\gamma$ channels with the ATLAS detector of the LHC

Defended on September 27$^{\text{th}}$ 2013 in front of the committee:

Claude	Charlot	Referee
Abdelhak	Djouadi	Examiner
Fabrice	Hubaut	Referee
José	Ocariz	Supervisor
Vanina	Ruhlmann-Kleider	President
Kerstin	Tackmann	Examiner

A mis abuelos Norman y Nora.
A mi hermanito Tomás

Résumé

Dans cette thèse, mes contributions personnelles à l'expérience ATLAS sont présentées. Elles consistent en des études de performance et des analyses physiques concernant les photons, dans le cadre de la recherche du boson de Higgs.

La première partie de cette thèse contient des analyses de performance sur le détecteur. Une étude de performance du système de haute tension du calorimètre électromagnétique (EMCAL) est présentée. Plus précisement, l'effet du aux résistances d'électrodes du EMCAL sur la mesure de l'énergie est investigué, et mesuré négligeable dans la plupart des cas. Par la suite, des études de performance de la reconstruction des photons sont présentées, l'étalonnage standard du EMCAL est validé à l'aide de photons provenant de désintégrations radiatives du boson Z.

La deuxième partie de ce document concerne deux analyses de physique, portant sur la recherche du boson de Higgs dans les canaux de désintégration $\gamma\gamma$ et $Z\gamma$. Ma contribution principale à ces analyses fut le développement d'un modèle analytique de résolution du signal, construit pour répondre à la nécessité d'une interpolation de la fonction de densité de probabilité de la masse invariante du signal.

Les résultats présentés sur la recherche du boson de Higgs dans le canal en di-photon proviennent de $4,8$ fb^{-1} de données enregistrées à une énergie du centre de masse de $\sqrt{s} = 7$ TeV et de $5,9$ fb^{-1} à $\sqrt{s} = 8$ TeV. Un excès d'événements est observé dans la distribution de masse invariante des paires de photons, aux alentours de 126,5 GeV, avec une significance locale de 4,5 déviations standard. La combinaison de ce résultat avec ceux obtenus dans les recherches du boson de Higgs dans les canaux $H \to ZZ$ et $H \to WW$ démontre l'existence d'une nouvelle particule a une masse de $126,0 \pm 0,4(\text{stat.}) \pm 0,4(syst.)$ GeV. Ce résultat est compatible avec le boson scalaire du modèle standard de la physique de particules.

La recherche du boson de Higgs dans le canal $Z\gamma$, est effectuée à l'aide de $4,8$ fb^{-1} de données enregistrées à $\sqrt{s} = 7$ TeV et de $20,7$ fb^{-1} à $\sqrt{s} = 8$ TeV. Aucune deviation significative du bruit de fonds prédict par le modèle standard est observée. Les limites supérieures à 95% de niveau de confiance sur le produit de la section efficace avec le rapport d'embranchement sont à 18,2 (observé) et à 13,6 (attendu) fois le modèle standard pour une masse de 125 GeV.

Abstract

In this thesis my personal contributions to the ATLAS experiment are presented, consisting of detector oriented studies and physics analyses concerning photons in the context of the search for the Higgs boson.

The first part of this thesis contains detector performance analyses on the electromagnetic calorimeter (EMCAL) high-voltage system. The effect of the resistors in the electrodes of the EMCAL on the energy measurement is investigated and found to be small in most of the cases. Furthermore, photon reconstruction performance studies are presented, where a data-driven validation to the standard calibration is performed by extracting the photon energy scales from a sample of Z radiative decays.

The second part of this document concerns the physics analyses, such as the searches for the Higgs Boson in the $\gamma\gamma$ and $Z\gamma$ decay channels. My main contribution to these analysis consists of an analytical resolution model for the signal, built to satisfy the need for an interpolation of the invariant mass probability density function to perform the search.

The di-photon decay channel results uses 4.8 fb^{-1} of data recorded at a centre-of-mass energy of $\sqrt{s} = 7$ TeV and 20.7 fb^{-1} at $\sqrt{s} = 8$ TeV. An excess of events is observed around a mass of 126.5 GeV with a local significance of 4.5 standard deviations. These results, combined with those obtained in the in the $H \to ZZ$ and $H \to WW$ channel confirm the discovery of a new boson with a mass of $126.0 \pm 0.4(\text{stat}) \pm 0.4(sys)$ GeV, consistent with the long searched-for Higgs boson.

In the $H \to Z\gamma$ channel, the search is performed using 4.8 fb^{-1} at f $\sqrt{s} = 7$ TeV and 20.7 fb^{-1} at $\sqrt{s} = 8$ TeV. No significant deviations from the SM background expectations are observed and upper limits on the cross sections times branching ratio are set. For a mass of 125 GeV, the expected and observed limits are 13.5 and 18.2 times the SM, respectively.

Acknowledgements

I would like to thank Reynald Pain and Giovanni Calderini for hosting me at the LPNHE and the ATLAS group during these last years. I am specially grateful with Fabrice Hubaut and Claude Charlot for accepting to be the referees of this document, and to Vanina Ruhlmann, Kerstin Tackmann and Abdelhak Djouadi for accepting to be part of the jury.

I would like to thank to Fundación Gran Mariscal de Ayacucho for its financial support during my three years of PhD studies. I'm very thankful to the Venezuelan state for this great experience of doing my PhD in France. Many thanks to Luis Nunez and Alejandra Melfo for their support and the "catapulta" into doing graduated studies in Europe and at CERN.

I want to express a special acknowledgement to my supervisor José Ocariz for leading me into the world of particle physics from an internship to three years of a doctoral thesis. Thank you for everything you thought me, the patience, the many many hours of discussion, for helping me to see the big picture and for your contagious enthusiasm for physics, which was always very motivating.

Thanks to the past and present members of the LPNHE-Higgs group: Bertrand, Lydia, Irena, Sandrine, Marine, the Giovannis, Yuji, Sandro for the active discussion and good fit-back during the group meetings. I also want to thank the PhD students, Heberth, Olivier, Liwen, Kun and Li for the discussions about technicalities, physics and the much needed team work. I need to thank Didier Lacour and Philippe Schwemling for all the help during my qualification task on the high voltage system.

The analyses presented in this thesis would not have been possible without the support and team work of the ATLAS Egamma Calibration and HSG1 groups. I'm very thankful to Louis Fayard, Kerstin Tackmann, Maarten Boonekamp and Stathes Paganis for the very useful discussions about several aspects of my work.

I want to thank the thesards (and also some post-docs) of LPNHE for the many lunches, coffees, beers, parties and letters in french (yes, Guillaume and Marine) during these three years. Thank you all for your friendship!

To my Latin-American friends: Homero, Rebeca, Reina, Anais, Daniela, Barbara, Heberth, Joany, Henso, Jesus, Katherine, Roger, Jacobo, Cachorro. Thank you for being my family here in Europe. Homero, my eternal "coloc", I'm grateful for all

the moments shared in and outside our flat and all the very long talks about work, life, etc. I will never forget our adventures in Paris. To the girls of Quedada, for being reliable friends, thanks to you I never felt alone. Rebeca, thanks for all the encouragement talks, especially in the final part of the writing of this thesis where I needed them the most. Anais, thank you for your company this years in Paris and all the talking, cooking, and dancing. Reina, thanks for offering me your friendship since the very beginning of my stay in France, the every day phone/skype talks and the traveling together. There are not enough words to express my gratitude to all of you, you have enriched enormously my years as a PhD student.

To Harvey, thanks for all the love and support you gave me during the last year of my thesis, which was definitely the hardest. Thank you for making me happy, for your patience with my anxieties and insecurities. You were my rock and I don't know how I would have done it without you.

Finally I want to thank my family. Tanto la chilena como la venezolana, les agradezco inmensamente todo su soporte a la distancia. Gracias papá por apoyarme en todos los medios posibles, creer en mi y estar siempre desde el otro lado del teléfono diciendo "Mi reina, usted puede". Gracias mamá por inculcarme desde chiquita la curiosidad y el amor a la ciencia, recuerdo tener menos de 10 años, leer juntas "La historia del tiempo" y conversar sobre el gato de Schrodinger. Mami esta tesis no existiría si no fuera por ti! Sé muy bien que ese amor a la ciencia se origina en la casa Smith Pinto, por lo que esta tesis está dedicada a mis queridos abuelos, Nora y Norman y también a mi hermanito Tomás: eres mi antítesis perfecta, y me llena de gran orgullo ser tu hermana!!! Gracias a todos, los quiero!

Contents

List of Figures

List of Tables

Introduction

The Standard Model (SM) of particle physics, provides a nearly complete view of the elementary composition of matter and the electromagnetic, weak and strong forces, which are the three dominant interactions at subatomic level. Built over the last half of the 20th century, the SM has successfully explained most experimental results and precisely predicted a wide variety of phenomena.

One important piece of the SM is the mechanism responsible for the electroweak symmetry breaking (EWSB) which provides masses to the vector bosons $W^{\pm}$ and Z and the fermions. This mechanism predicts the existence of a particle, the so-called Higgs boson. For many years, experiments from colliders such as LEP and Tevatron searched for the Higgs boson without finding any direct strong evidence to confirm the theory. This scenario changed after the first run of the Large Hadron Collider (LHC).

The LHC is the largest and most powerful particle accelerator ever built. Its operations started up in the year 2010, when the first proton-proton collisions with a centre-of-mass energy of $\sqrt{s} = 7$ TeV and instantaneous luminosities up to $10^{32}\text{cm}^{-2}\text{s}^{-1}$ were recorded, setting the beginning of a new era in high energy physics experiments. The LHC ran for three years, initially at $\sqrt{s} = 7$ TeV in 2010-2011 and at $\sqrt{s} = 8$ TeV in 2012 and delivered proton-proton (and also heavy ions) collisions to four main experiments. The ATLAS detector is one of the two general purpose experiments, with an extensive physics program including the search for the SM Higgs boson and the search for new physics. By the end of the first run of the LHC, the elusive Higgs boson was finally observed, and some of its properties measured.

This thesis presents both detector oriented studies and physics analyses concerning photons. The first part of the document contains detector and performance analyses, where a study on the high-voltage system of the electromagnetic calorimeter

(EMCAL) is performed. Furthermore, photon performance studies are presented, where the standard calibration of the EMCAL is validated using radiative Z decays. Concerning physics analyses, the results of the searches for the Higgs Boson in the $\gamma\gamma$ and $Z\gamma$ decay channels in ATLAS are presented, using 4.8 fb^{-1} of data recorded at $\sqrt{s} = 7$ TeV and 5.9/20.7 fb^{-1} at $\sqrt{s} = 8$ TeV in the $\gamma\gamma$ and $Z\gamma$ channels, respectively. The main motivation of studying simultaneously these channels is that in the SM, both decays are mediated via top and W loops. These two channels are therefore sensitive to new physics, as any deviation of these decays rates with respect to the SM may occur via contributions from new heavy charged particles.

Outline

In Chapter 1, a brief introduction on the theoretical framework of the SM and Higgs phenomenology is presented. Chapter 2 describes the LHC complex at CERN and the ATLAS detector. In Chapter 3, a detailed description of the EMCAL, including studies performed in the high-voltage system are exposed. Chapter 4 describes the standard reconstruction, identification and calibration of photons in ATLAS. A data-driven method to validate the standard EMCAL in-situ calibration using Z radiative decays is presented in Chapter 5. Chapter 6 describes the search for the SM Higgs boson decaying into a photon pair, the content of this chapter includes preliminary MonteCarlo-based signal studies and the analysis which lead to the observation a Higgs boson-like particle with a mass of about 126.5 GeV. Finally, in Chapter 7, the first ATLAS result in the search for the SM Higgs boson in the $Z\gamma$ decay channel is presented.

Personal Contributions

Research in experimental high energy physics relies heavily on collaboration. Therefore, the work presented in this thesis is the result of contributions made by many people working on different areas. Leading personal contributions of various analyses presented in this thesis, divided by chapter, are presented below.

Chapter 3: High-Voltage studies. A study on the effect of resistors in the electrodes of the EMCAL on the high-voltage system and on the energy measurement is presented. This study is documented in [1].

Chapter 5: Photon energy scales. A data-driven validation to the standard calibration is performed extracting the photon energy scales from a sample of Z radiative decays. The analysis is performed using both 7 and 8 TeV data. The results presented in this thesis at 7 TeV are obtained in collaboration with the ATLAS Tokyo group. The complete 8 TeV results correspond to personal contributions. The 7 TeV results can be found in [2], and documentation for the results at 8 TeV is in the final stages of editing.

Chapter 6: Signal studies for the $H \to \gamma\gamma$ channel. A number of studies were performed to investigate the photon performance in the MC and to improve the signal model used in the final statistical analysis. An analytical signal resolution model is built to satisfy the need for an interpolation of the signal invariant mass probability density function for the search. The global signal resolution model is used in the discovery analysis, and plays an important role in the mass measurement in this channel. This contribution appears in [3].

Chapter 7: Search for the SM Higgs boson in the $H \to Z\gamma$ channel. Personal contributions at several levels of the analysis are presented, which includes the choice of the discriminanting variable for the search, optimisations of the photon selection, background parametrization studies and the signal modelling for the final result. These contributions are documented in [4, 5].

Chapter 1

The Standard Model of Particle Physics and the Higgs boson

Contents

According to the current understanding, the building blocks of matter and their interactions through fundamental forces are described by the Standard Model of particle physics (SM). This model is an accumulation of knowledge describing the strong, weak and electromagnetic interactions and has been rigorously tested and found to agree exceptionally well with results of numerous experiments.

In the SM, all interactions are mediated by exchange of particles (force carriers). Matter is described in terms of fermions (particles that follow the Fermi-Dirac statistics) and forces in terms of bosons (following the Bose-Einstein statistics). In the SM, the fundamental particles are: *three families of leptons and quarks, force carriers and the Higgs boson.* All these particles and their charge, mass and spin properties are shown in Figure 1.1.

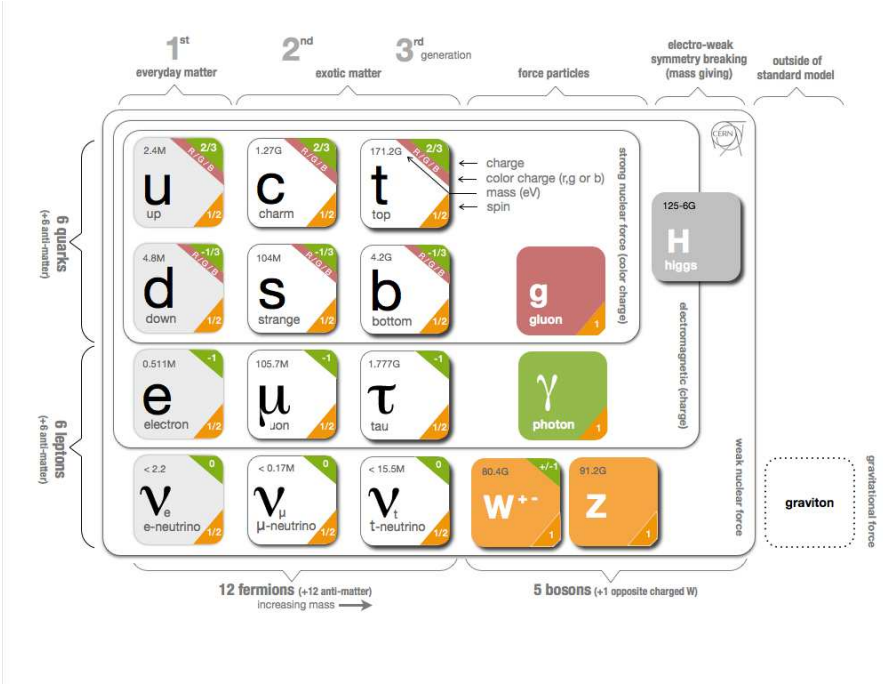

FIGURE 1.1: The Standard Model of elementary particles, with some of the particles properties: mass, charge, colour and spin. The quarks, leptons, bosons are presented. The particles that interact through strong nuclear, electromagnetic and weak force are shown. The graviton mediator of the gravitational force is also shown, even though is not part of the Standard Model [6].

The bosons are the mediators of the fundamental forces of physics: strong, electromagnetic, and weak. Each fundamental force has its associated boson:

- The electromagnetic interaction is mediated by the photon (γ), a massless particle with no electrical charge.
- The strong interaction which holds quarks together to form protons, neutrons or other particles, is mediated by the gluons (g). The gluons are massless, electrically neutral and carry *colour charge* (so-called red, blue or green). The strong force also acts binding protons and neutrons together to form atoms.
- The weak interaction, responsible for some nuclear decays such as β decay, is mediated by the massive $W^{\pm}$ and Z bosons.
- Gravitational interaction is the weakest of all the fundamental forces (under the Planck scale 10^{19} GeV) and is not included in the SM.

The quarks and leptons (fermions) are classified into three generations of identical structure except for the particle masses. Within the charged leptons, the electron (e) is the lightest particle, followed by the muon (μ) and the tau (τ). Whilst the electron is stable, the muon and the tau are unstable and decay spontaneously. These three leptons are sensitive to weak and electromagnetic interactions, they carry integer electrical charge and are paired with a neutral lepton of the same *flavour* called neutrino (ν_e, ν_μ and ν_τ). The quarks carry fractional electric charges of $+2/3e$ or $-1/3e$ and have a colour charge, which is relevant for their strong interaction (they are also sensitive to weak and electromagnetic interaction), which binds them together inside of colourless particles called hadrons or baryons.

The SM is a quantum field theory built from the principle that physics should be invariant under local symmetry transformations (gauge symmetry), providing a framework to describe the electromagnetic, weak and strong interactions based on a combination of local gauge symmetry groups: $SU(2)_L \otimes U(1)_Y \otimes SU(3)_C$. The conserved quantities in each transformation are, weak isospin (I), weak hyper-charge (Y) and colour (C), respectively.

The Electroweak theory (EW) proposed by Glashow, Salam and Weinberg in the 1960s [7–9], describes the electromagnetic and weak iterations between quarks and leptons. It is based on the gauge symmetry group $\mathrm{SU}(2)_L \otimes \mathrm{U}(1)_Y$ and postulates four massless mediating bosons, for which three bosons belong to the non-abelian group SU(2), and the fourth, is an isoscalar ($I = 0$), belonging to the abelian U(1) group of weak hypercharge.

In addition to the matter and interaction particles described above, a scalar SU(2) doublet is introduced in the SM, to generate a spontaneous breaking of the EW symmetry (EWSB). Through this EWSB mechanism, three of the gauge bosons acquire masses; the remaining neutral scalar field is called the Higgs field. The mass of this Higgs boson is the only unknown parameter of this theory.

The Quantum Chromodynamic theory (QCD) is based on the gauge symmetry group $SU(3)_C$, describes the strong interaction between the coloured quarks. The gauge bosons (gluons) which mediate the interaction, carry a colour and an anti-colour and belong to an octet of the $SU(3)_C$ group.

In this chapter, the theoretical context and the existing experimental results for the Higgs searches are presented. In Section 1.1, gauge invariance in Quantum Electrodynamics is discussed to introduce the concept of local symmetries. It is followed by basic concepts of QCD in Section 1.2. The electroweak theory and the Higgs mechanism are developed in Section 1.3, and the constraints (theoretical and experimental) on the Higgs boson mass are described in 1.4. The Higgs production and decays modes are presented in 1.5; the $H \to \gamma\gamma$ and $H \to Z\gamma$ decay modes, which are the subject for this thesis, are discussed in 1.6. Finally, in Section 1.7, some theoretical models beyond the SM which could affect the $\gamma\gamma$ and/or $Z\gamma$ decay rates are described.

1.1 Gauge symmetries in Quantum Electrodynamics

Quantum Electrodynamics (QED) is a quantum field theory based on a *local gauge symmetry*. The QED symmetry group is the abelian U(1), so that a gauge transformation is defined by applying an arbitrary phase to the state function of the system (U(1) transformation), in the following way:

$$\psi(x) \to e^{ie\phi(x)}\psi(x), \tag{1.1}$$

where ψ is a Dirac spinor. The transformation is local due to the ϕ phase dependency on a space time coordinate. The free Lagrangian that describes a Dirac fermion with spin 1/2 and mass m is the following:

$$\mathcal{L}_{Dirac} = \bar{\psi}(i\gamma_\mu \partial^\mu - m)\psi, \tag{1.2}$$

where γ_μ are the Dirac matrices. The Lagrangian would be invariant under a U(1) transformation in Equation 1.1, only if the ϕ phase is an arbitrary real constant. Considering that this is not the case, and the U(1) transformation is local, the Lagrangian in Equation 1.2 does not remain invariant under the transformation, as shown by:

$$\partial_\mu \psi \rightarrow e^{ie\phi(x)}(\partial_\mu + ie\partial_\mu)\psi. \tag{1.3}$$

In order to restore the gauge invariance under the local U(1) transformation, a new vector field A_μ is introduced, which transforms as the following:

$$A_\mu(x) \rightarrow A'_\mu(x) = A_\mu(x) + \frac{1}{e}\partial_\mu \phi, \tag{1.4}$$

A covariant derivative is defined as

$$D_\mu = \partial_\mu - ieA_\mu, \tag{1.5}$$

that transforms in a similar way as the field itself:

$$D_\mu \psi \rightarrow D'_\mu \psi = e^{ie\phi} D_\mu \psi. \tag{1.6}$$

The Lagrangian for a vector field A^μ, associated with a spin 1 particle, is

$$\mathcal{L} = -\frac{1}{4}F^{\mu\nu}F_{\mu\nu} + \frac{1}{2}m_A^2 A^\mu A_\mu \tag{1.7}$$

where, $F^{\mu\nu} = \partial^\mu A^\mu - \partial^\nu A^\nu$, is the kinetic term of the field. The fist term of the Lagrangian is invariant under local U(1), whereas the second term is not. This forces the vector field to be massless (m_A=0), to keep the local gauge invariance.

After the introduction of the vector field, the resulting new Lagrangian is the one for Quantum Electrodynamics:

$$\mathcal{L}_{QED} = \bar{\psi}(i\gamma_\mu \partial^\mu - m)\psi + e\bar{\psi}\gamma^\mu \psi A_\mu - \frac{1}{4}F^{\mu\nu}F_{\mu\nu}, \tag{1.8}$$

The vector field A_μ represents the photon field, the Lagrangian describes the interactions between Dirac (fermions) fields and the photon field.

1.2 Basics of Quantum Chromodynamics

The strong interaction is based on the symmetry group $SU(3)_C$, that describes the quark colours (three colours and their associated anti colours). The gauge fields $G^a_{\mu\nu}$ correspond to the 8 generators T_a with the possible combination of colour (anti colour), which are identified as gluons. The gluon gauge fields have self-couplings, that allow for self interactions.

The QCD Lagrangian is described as:

$$\mathcal{L}_{QCD} = \sum \bar{\psi}_{q,j}(i\gamma^\mu(D_\mu)_{j,k} - m_q\delta_{jk})\psi_{q,k} - \frac{1}{4}G^a_{\mu\nu}G^{a\mu\nu}, \tag{1.9}$$

where $\psi_{q,j}$ is the quark field for flavour q carrying a colour j. The covariant derivative D_μ and the gluon field strength tensor $G^a_{\mu\nu}$ are defined as:

$$D_\mu = \partial_\mu + ig_sT^aA^a_\mu, \tag{1.10}$$

$$G^a_{\mu\nu} = \partial_\mu A^a_\nu - \partial_\nu A^a_\mu - g_S f^{abc}A^b_\mu A^c_\nu, \tag{1.11}$$

where A^a_ν are the gluon fields with index a, a=1,...8. The generators of the SU(3) group are the Gell-Mann matrices T_a, which satisfy the algebra $[T^a, T^b] = if^{abc}T^c$, where f^{abc} are the group structure constants. Finally, $g_s = \sqrt{(}4\pi\alpha_S)$ with α_s is the strong coupling constant.

QCD has peculiar properties: quarks and gluons behave as quasi-free particles at high energies or short distances, while at low energy or large distances, quarks are confined into hadrons. These properties are called asymptotic freedom and confinement, respectively.

1.3 Electroweak theory and the Higgs mechanism

1.3.1 Electroweak theory

The electroweak theory is based on the gauge symmetry group $\mathrm{SU}(2)_L \otimes \mathrm{U}(1)_Y$. As stated before, in the $\mathrm{SU}(2)_L$ group, the conserved quantity is the weak isospin (I) and the weak hypercharge (Y) in the $\mathrm{U}(1)_Y$ groups. These conserved quantities are connected to the no conserved electric charge (Q) by:

$$Q = I_3 + Y/2, \tag{1.12}$$

where I_3 is the third component of the weak isospin.

The EW theory is constructed under the same principle of gauge invariance as described for the QED theory in Section 1.1. There is one gauge field associated to the $U(1)_Y$ symmetry, B_μ and three W^i_μ fields associated to $\mathrm{SU}(2)_L$. Whilst the W^i_μ field only couples to the left-handed components of the fermion fields, the B_μ gauge field couples to both left- and right-handed components (ψ_L and ψ_R).

To ensure the invariance of the EW Lagrangian, the covariant derivates $D_{\mu L}$ and $D_{\mu R}$ are introduced. These are defined in the following way:

$$D_{\mu L}\psi_L = (\partial_\mu + ig\frac{\sigma_i}{2}W^i_\mu + ig'\frac{Y_L}{2}B_\mu)\psi_L \tag{1.13}$$

$$D_{\mu R}\psi_R = (\partial_\mu + ig'\frac{Y_R}{2}B_\mu)\psi_R \tag{1.14}$$

where g and g' are the coupling constants of $SU(2)_L$ and $U(1)_Y$ respectively, σ_i are the Pauli matrices, and Y_L and Y_R are the weak hypercharge for the left- and right-handed components of the fermion fields.

Finally ,the gauge invariant Lagrangian of the EW theory is:

$$\mathcal{L}_{EW} = i\bar{\psi}_L\gamma^\mu D_{\mu L}\psi_L + i\bar{\psi}_R\gamma^\mu D_{\mu R}\psi_R - \frac{1}{4}W^i_{\mu\nu}W^{\mu\nu}_i - \frac{1}{4}B^i_{\mu\nu}B^{\mu\nu}_i, \tag{1.15}$$

where the fist two terms describe the kinetic terms for the interaction between fermion and gauge fields and the last two terms are the gauge field terms, with:

$$W^i_{\mu\nu} = \partial_\mu W^i_\nu - \partial_\nu W^i_\mu - g\epsilon^{ijk} W^j_\mu W^k_\nu, \tag{1.16}$$

$$B^i_{\mu\nu} = \partial_\mu B^i_\nu - \partial_\nu B^i_\mu, \tag{1.17}$$

whew ε^{ijk} are the $SU(2)_L$ structure constants. The weak gauge bosons γ, Z and $W^\pm$ are linear combinations of the four gauge fields:

$$A_\mu = B_\mu \cos\theta_W + W^3_\mu \sin\theta_W, \tag{1.18}$$

$$Z_\mu = -B_\mu \sin\theta_W + W^3_\mu \cos\theta_W, \tag{1.19}$$

$$W^\pm_\mu = \frac{W^1_\mu \mp W^2_\mu}{\sqrt{2}}, \tag{1.20}$$

with θ_W (Weinberg's angle or weak mixing angle) defined as:

$$\cos\theta_W = \frac{g'}{\sqrt{g^2 + g'^2}}, \tag{1.21}$$

$$\sin\theta_W = \frac{g}{\sqrt{g^2 + g'^2}}. \tag{1.22}$$

Under the same principle presented in Section 1.1, the EW Lagrangian in Equation 1.15 describes fermions and gauge bosons as massless, given that inserting a mass term in the Lagrangian would break gauge invariance. Nevertheless, the $W^\pm$ and Z^0 bosons that mediate the weak interaction are massive, with a mass of approximately 80 to 90 GeV. To address this problem of explaining the masses of the $W^\pm$ and Z bosons, Higgs, Brout and Englert proposed in 1964 the mechanism of spontaneous breaking of the symmetry or the Higgs mechanism [10–13].

1.3.2 The Higgs Mechanism

In the Higgs mechanism, a doublet of complex scalar fields is introduced:

$$\Phi_H = \frac{1}{\sqrt{2}}\begin{pmatrix}\Phi^+ \\ \Phi^0\end{pmatrix} = \frac{1}{\sqrt{2}}\begin{pmatrix}\phi_1 + i\phi_2 \\ \phi_3 + i\phi_4\end{pmatrix}, \tag{1.23}$$

where Φ^+ and Φ^0 are a charged and a neutral field respectively. The scalar field Φ_H is incorporated in the EW Lagrangian as:

$$\mathcal{L}_{\mathcal{H}} = (D^{\mu}\Phi_H)^{\dagger}(D_{\mu}\Phi_H) - V(\Phi_H). \tag{1.24}$$

The covariant derivative has the form:

$$D_{\mu}\Phi_H = (\partial_{\mu} + ig\frac{\sigma_i}{2}W_{\mu}^{i} + ig'\frac{Y_{\Phi_H}}{2}B_{\mu})\Phi_H, \tag{1.25}$$

and $V(\Phi_H)$ is a potential term defined as:

$$V(\Phi_H) = -\mu^2\Phi_H^{\dagger}\Phi_H + \lambda(\Phi_H^{\dagger}\Phi_H)^2. \tag{1.26}$$

Figure 1.2 shows the form of this potential for $\mu^2 < 0$ and $\lambda > 0$. The negative sign in μ^2 forces Φ_H to take a non-vanishing vacuum expectation value. The ground state of the Higgs field is given by the minimum of the potential. One state is chosen as the reference for the local gauge transformation, it is commonly selected as the following:

$$\Phi_{min} = \frac{1}{\sqrt{2}}\begin{pmatrix}0\\v\end{pmatrix}, \quad (\phi_1 = \phi_2 = \phi_4 = 0, \phi_3 = v), \tag{1.27}$$

where $v = \sqrt{\mu^2/\lambda}$ is called the *vacuum expectation value* of Higgs field. The choice of one particular direction of the space means that the system symmetry breaks spontaneously.

1.3.3 The SM Higgs boson

The Higgs field can be parametrized with four real fields θ_a(with a= 1,2,3) and $H(x)$, is the following

$$\Phi_H = \frac{1}{\sqrt{2}}e^{i\sigma^a\theta_a(x)}\begin{pmatrix}0\\v + H(x)\end{pmatrix}. \tag{1.28}$$

The θ_i fields are called Goldstone (or Nambu-Goldstone) bosons, and are absorbed in an unitary gauge transformation of the W_i^{μ} fields. It is said that the three θ_i fields have been *eaten* by the gauge fields, to form the longitudinal components of the $W^{\pm}$ and Z weak gauge bosons. In this way, the $W^{\pm}$ and Z bosons have become massive.

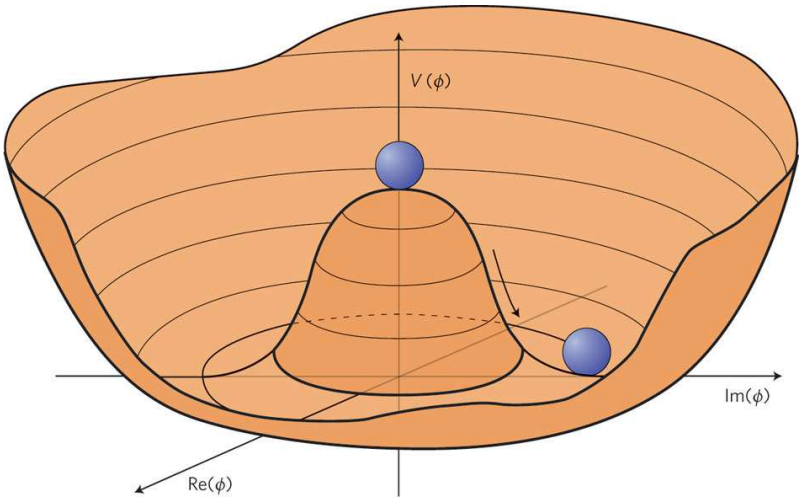

FIGURE 1.2: Higgs potential $V(\Phi_H)$ in the plane $\mathfrak{Re}(\Phi_H) - \mathfrak{Im}(\Phi_H)$

Inserting Equations 1.19, 1.20 and 1.28 into the Lagrangian in Equation 1.24, the following result is found:

$$\mathcal{L}_{\mathcal{H}} = \frac{1}{2}\partial^{\mu}H\partial_{\mu}H + \left(\frac{gv}{2}\right)^{2}\frac{(W_{\mu}^{+}W^{+\mu} + W_{\mu}^{-}W^{-\mu})}{2} + \left(\frac{gv}{2\cos\theta_W}\right)^{2}\frac{Z^{\mu}Z_{\mu}}{2} - V(\Phi_H). \tag{1.29}$$

The mass terms from the Z and $W^{\pm}$ bosons are provided by the broken symmetry and the photon remains massless. The Z and $W^{\pm}$ are related via the weak-mixing angle (and thus the coupling constants g and g') as follows:

$$m_W = \cos\theta_W m_Z = gv/2. \tag{1.30}$$

Developing the potential term $V(\Phi_H)$ using Equation 1.28, the Higgs mass is obtained:

$$m_H = \sqrt{-2\mu^2} = \sqrt{2\lambda v^2}, \tag{1.31}$$

where the vacuum expectation value is $v = \sqrt{2}G_F{}^{-1/2} = 246$ GeV (this result comes from the relation of the Fermi coupling constant $\frac{G_f}{\sqrt{2}} = \frac{g^2}{8M_W^2}$ and). Given that λ is a free parameter, the Higgs mass is a free parameter in the theory.

The fermion masses can be introduced through the Higgs field in the Yukawa interactions. The interaction of the fermions with the Higgs field has a coupling (λ_f)

proportional to their mass and to the value of the vacuum ground state:

$$m_f = \frac{\lambda_f v}{\sqrt{2}}, \tag{1.32}$$

leaving the couplings of the Higgs to other particles well defined, once the fermion mass is measured.

1.4 Constraints in the SM Higgs mass

As stated above, the Higgs mass is a free parameter in the SM. Nevertheless, some theoretical constraints on its can be derived from assumptions on the energy range where the SM is valid (before perturbation theory breaks down). There are also experimental constraints that come from direct searches performed at LEP, Tevatron and the LHC[1], and from experimental measurements of other SM parameters correlated with the Higgs mass.

1.4.1 Theoretical Constraints

Perturbative Constraints

Since interactions of the longitudinal components of the massive gauge bosons grow with their momenta, cross sections of processes involving W or Z bosons would lead to cross-sections that increase with the energy and that would violate unitarity at some stage. An example is the elastic WW scattering, for which diagrams are shown in Figure 1.3. Including only the diagrams (a), (b) and (c) in the perturbative approximation makes the scattering amplitude increase with the centre-of-mass energy, resulting at energies above 1.2 TeV in a violation of unitarity[2]. The Higgs mechanism introduces the diagrams (d) and (e). For a certain Higgs mass, it balances the contributions that increase with the scattering energy. Considering that the WW can be coupled with the other channels such as ZZ, HH, ZH, W^+H and

[1]The experimental constraints presented in this chapter are state of the art at the beginning of this thesis (end of 2010), which correspond mainly to LEP and Tevatron results. LHC results will be discussed towards the end of this document.

[2]This means that New Physics beyond the SM should manifest itself at energies in the TeV range to restore unitary in the scattering amplitudes of longitudinal gauge bosons.

htp]

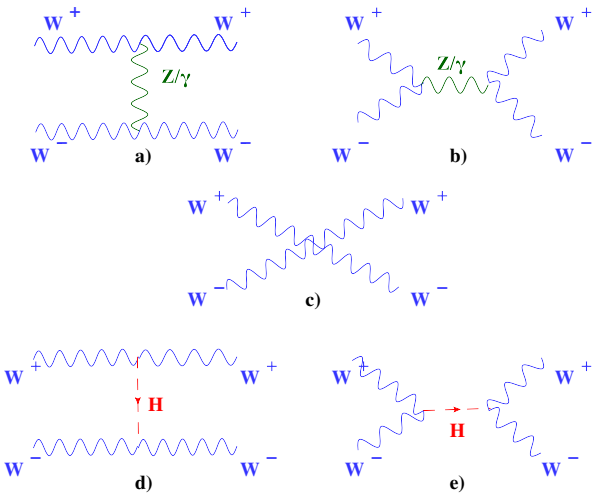

FIGURE 1.3: The complete gauge invariant set of Feynman diagrams for $W^+W^- \to W^+W^-$ scattering.

W^+Z, the unitarity constrains the Higgs mass to an upper limit of:

$$M_H \lesssim 710 \text{ GeV} \tag{1.33}$$

Thus, in the SM, if the Higgs boson mass exceeds $\mathcal{O}(700 \text{ GeV})$, unitary would be violated unless new phenomena appear to restore it[3].

Triviality and stability bounds

The couplings and masses that appear in the SM Lagrangian depend on the considered energy. The Higgs quartic coupling monotonically increases with the energy scale $|Q|$. This leads to constraints on this coupling and therefore, on the Higgs mass.

Triviality bound

The Feynman diagrams for the tree level and the one loop corrections to the Higgs boson self coupling are shown in Figure 1.4. The variation of the Higgs quartic

[3]This calculation has been performed a tree level. Considering that the Higgs boson self-coupling becomes strong for high masses, the theory could stop being perturbative, invalidating this result. To obtain this constrain, it has to be assumed that the SM remains perturbative and that higher order corrections are not large [14].

coupling (λ) with the energy scale $|Q|$ is described by the Renormalisation Group Equation (RGE).

$$\frac{d}{dQ^2}\lambda(Q^2) = \frac{3}{4\pi^2}\lambda^2(Q^2) + \text{higher orders.} \tag{1.34}$$

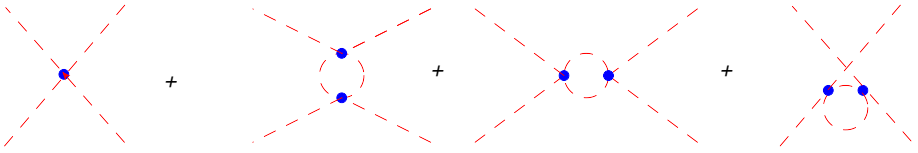

FIGURE 1.4: Typical Feynman diagrams for the tree-level and one-loop Higgs self coupling.

The solution to this equation, choosing as a reference energy point the electroweak symmetry breaking scale $Q_0 = v$, is the following (at one-loop):

$$\lambda(Q^2) = \lambda(v^2)\left[1 - \frac{3}{4\pi^2}\lambda(v^2) log\frac{Q^2}{v^2}\right]^{-1}. \tag{1.35}$$

which shows that the quartic coupling increases logarithmically with Q^2. In the case where the energy is much smaller than the electroweak breaking scale ($Q^2 \ll v^2$), the coupling becomes extremely small and eventually vanishes. In this scenario it is said that the theory is trivial, i.e there is no interaction since the coupling is zero. In the opposite limit when the energy is much higher than the weak scale ($Q^2 \gg v^2$), the quartic coupling grows, eventually becoming infinite, in the so-called Landau pole:

$$\Lambda_C = ve^{4\pi^2/3\lambda} = ve^{4\pi^2 v^2/M_H^2}. \tag{1.36}$$

From this limit, the energy scale where the SM is valid can be extracted, i.e the energy cut-off, Λ_C below which the self-coupling λ remains finite. For large Λ_c, the Higgs mass should be small to avoid the Landau pole, whereas a small Λ_c would imply a large Higgs mass. If the cut-off is set to the Higgs mass ($\Lambda_c = M_H$), the Higgs mass has to be smaller than 700 GeV, to have a finite quartic coupling.

Similar to the perturbative constraints from the WW scattering, when λ or M_H are too large, perturbation theory can no longer be used and this constraint is not valid.

However, from simulation of gauge theories on a lattice, where non-perturbative effects are taken into account, the mass limit is found to be:

$$M_H < 640 \text{ GeV}, \tag{1.37}$$

which is in good agreement with the result obtained using perturbation theory [14].

Stability bound

In the preceding discussion, only the contribution from the Higgs boson itself is included in the calculation of the quartic coupling λ. By including the additional contributions from fermions and gauge bosons (Figure 1.5), the quartic coupling λ can not be too small, because it would lead to a unstable vacuum, where the scalar potential $V(Q^2) < V(v)$, has no minimum. A requirements on λ puts a strong constraint on the Higgs boson mass, which depends on the value of the cut-off Λ_c.

FIGURE 1.5: Diagrams for the one-loop contributions of fermions and gauge bosons to λ.

Figure 1.6 shows the stability (lower band) and triviality (upper band) constraints, which provide an allowed range of M_H as a function of the scale of new physics Λ_C. As observed in the Figure, if the scale Λ_C is at the TeV scale, the Higgs boson mass is allowed in the range

$$50 \text{ GeV} \lesssim M_H \lesssim 800 \text{ GeV}, \tag{1.38}$$

while, requiring the SM to be valid up to the Grand Unification scale, $\Lambda_{GUT} \sim 10^{16}$ GeV, the Higgs boson mass would be in the range of

$$130 \text{ GeV} \lesssim M_H \lesssim 180 \text{ GeV}. \tag{1.39}$$

Fine-tuning constraint

The fine-tuning problem arises from the radiative corrections to the Higgs boson mass, shown in Figure 1.7, which involve fermions, massive gauge bosons and Higgs

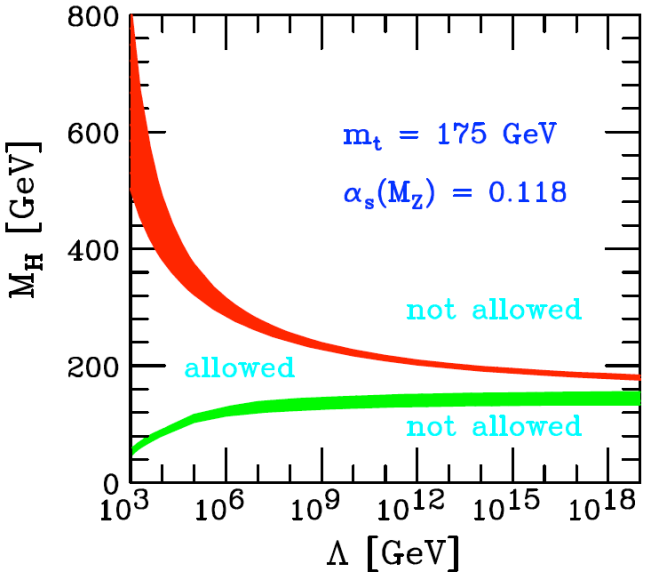

FIGURE 1.6: The triviality (upper) bound and the vacuum stability (lower) bound on the Higgs boson mass as a function of the New Physics or cut-off scale for a top quark mass $m_t = 175 \pm 6$ GeV and $\alpha_s(MZ) = 0.118 \pm 0.002$; the allowed region lies between the bands and the coloured/shaded bands illustrate the impact of various uncertainties [15].

boson loops. Cutting off the loop integral momenta at a scale Λ, and keeping only the dominant contribution in this scale, the following relation is found

$$\Delta M_H^2 = \frac{\Lambda^2}{8\pi^2 v^2}[M_H^2 + 2M_W^2 + M_Z^2 - 4m_t^2], \tag{1.40}$$

where only the contribution of the top quark for the fermion loops is retained. Equation 1.40 is an unusual situation in the SM as there are quadratic divergences instead of the logarithm ones observed in the previous sections. In the case of a very large cut-off Λ, such as 10^{16} GeV (Grand Unification scale), there has to be a very fine arrangement of the 16 digits between the bare Higgs mass and the electroweak corrections to have a physical M_H in the range of the electroweak symmetry breaking scale, M_H from 100 GeV to 1 TeV as required for SM consistency. For low values of the scale Λ (less than 1 TeV), there is no fine-tuning problem for any reasonable Higgs boson mass value. More information can be found in [14].

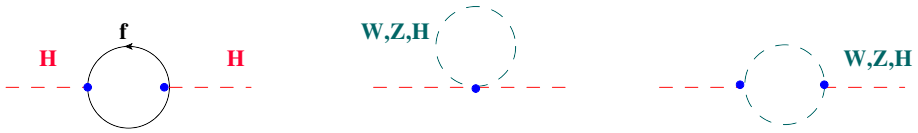

FIGURE 1.7: Feynman diagrams for the one-loop corrections to the SM Higgs boson mass.

1.4.2 Experimental constraints before the LHC

Direct Higgs searches

Previous to the start of the LHC, the quest for the Higgs boson had been performed by the experiments of two big accelerators. The Large Electron-Positron collider (LEP), ran from 1989 to 2000 with a varying centre-of-mass energy of 91-210 GeV, and excluded the existence of the SM Higgs boson with a mass below 114.4 GeV at 95% of confidence level [16]. In electron-positron collisions in LEP, the Higgs boson was expected to be produced via the Higgs-strahlung process (see Section 1.5.1), where the Higgs boson is radiated by a vector boson. In Figure 1.8, the final results from LEP are shown.

The Tevatron accelerated and collided protons and antiprotons at a centre-of-mass energy of 1.96 TeV, and set exclusions on the SM Higgs boson mass. In Figure 1.9, the results published by Tevatron by summer 2011 with 8 fb^{-1} of collected data are shown [17].

Indirect experimental contrains

The SM Higgs boson contributes to the radiative corrections to the EW observables, for instance as shown in Figure 1.10, through the gauge bosons self energies. Constraints on the Higgs mass can be derived from precision measurements to these EW observables. The measured EW parameters are for instance the W and Z boson mass, the electroweak mixing angle, the top mass and the Fermi coupling constant. Most of these measurements have been performed at LEP and Tevatron. Nevertheless, these constraints are weak since the dependence with the Higgs mass is logarithmic.

The constraints on the Higgs mass are extracted from global fits to the EW parameters. These fits have been performed by different groups, as the LEP Electroweak

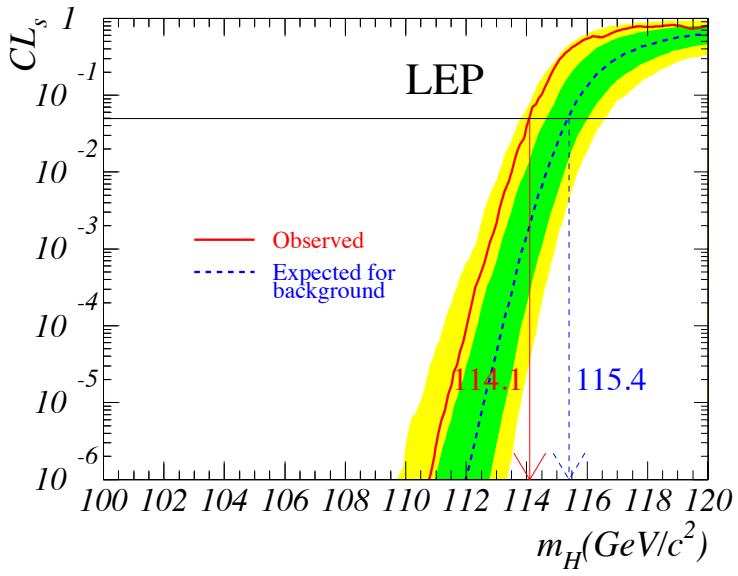

FIGURE 1.8: The CL_s ratio as a function of the Higgs boson mass. The observed exclusion limit is shown in solid line while the expectation is showed in dashed line. The bands show the 68% and 95% probability bands. The line $CL_s = 0.05$ defines de 95% C.L. [16].

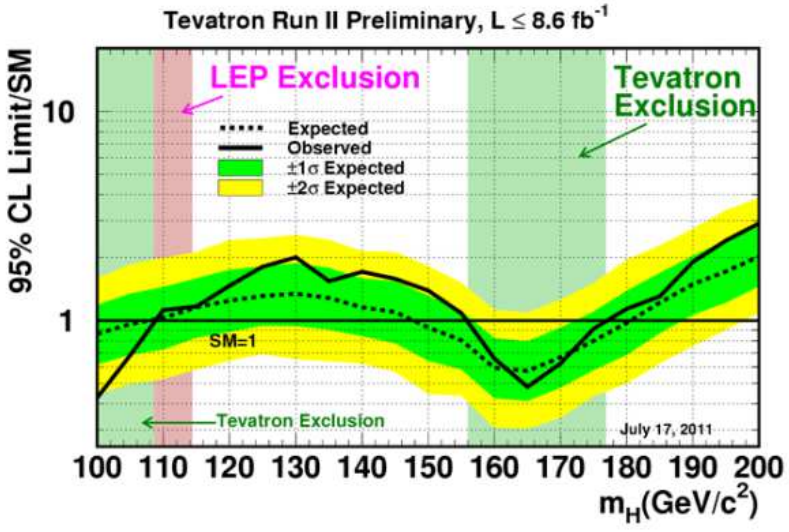

FIGURE 1.9: 95% confidence level upper limits on a SM-like Higgs boson production cross-section, normalised to the SM predicted cross-section, as a function of the boson mass hypothesis m_H, obtained by the Tevatron experiments [17] for the summer of 2011.

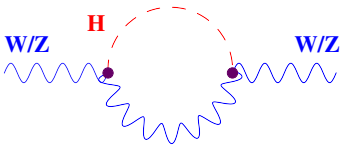

FIGURE 1.10: Higgs boson contribution to the EW gauge bosons self energy (correction logarithmically dependent of the Higgs mass).

Working Group [18] and the GFitter group [19]. Figure 1.11 shows the $\Delta\chi^2$ curve derived from the precision electroweak measurements, performed at LEP, as a function of the Higgs-boson mass. According to the minimum of the curve the preferred value for the Higgs mass is:

$$m_H = 94^{+29}_{-24} \text{ GeV}. \tag{1.41}$$

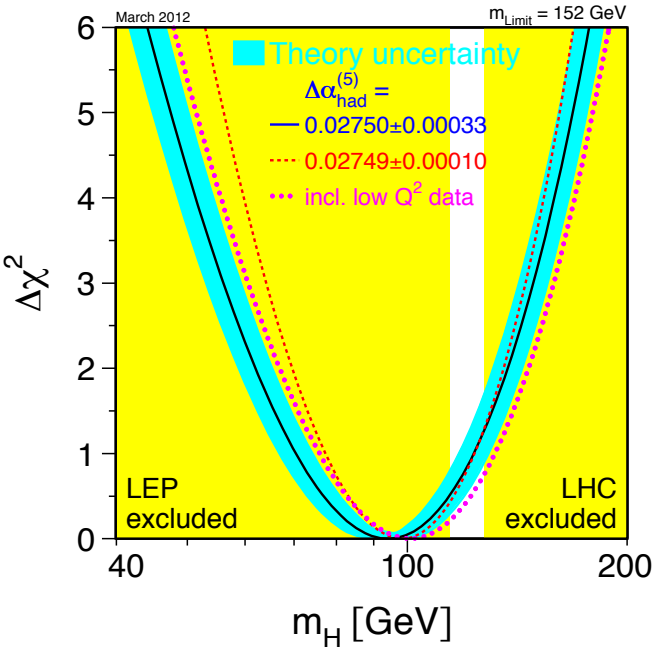

FIGURE 1.11: $\Delta\chi^2$ vs. m_H curve. The line is the result from the fit to the electroweak parameters; the band represents an estimate of the theoretical error. The yellow band show the exclusion limit from the direct searches from LEP and Tevatron [18].

While this is not a proof of the existence of the SM Higgs boson, it provides a guideline on what mass range to look for it. The result of the fit implies that m_H is lower than about 152 GeV (one-sided 95 percent confidence level upper limit). In Figure 1.12, using results available by summer 2010, of the direct searches for the

Higgs boson at LEP and Tevatron, the global fit is performed by the GFitter group. These results give the following constraint on the Higgs boson mass:

$$m_H = 120.6^{+17.9}_{-5.2} \text{ GeV}. \tag{1.42}$$

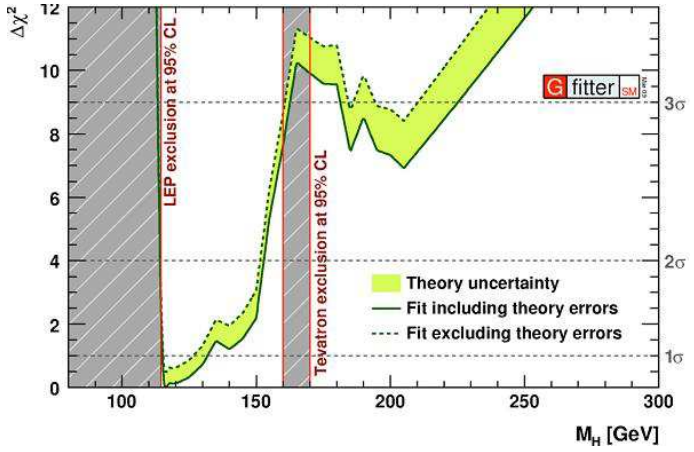

FIGURE 1.12: $\Delta\chi^2$ as a function of m_H obtained by the gFitter group by summer 2010 (before the start of LHC operations). The solid (dashed) lines corresponds to the results when including (ignoring) the theoretical errors [19].

1.5 The SM Higgs boson at the LHC

1.5.1 The Higgs production

In the SM the Higgs boson couples preferentially to heavy particles, such as the Z and W bosons, and the top quark. Thus, there are mainly four production models for the SM in proton collisions. In Figure 1.13, the Feynman diagrams of the productions modes are presented.

- The dominant is gluon-gluon fusion (ggF), where the Higgs boson couples indirectly to gluons via a triangular loop of quarks dominated by the top.
- The Vector-boson fusion (VBF), in which the Higgs boson is produced by the fusion of two weak vector bosons radiated from quarks. The two final quarks fragment into two forward jets, and no QCD activity is expected between the two jets where the Higgs decay products are, leaving a special signature in the detector that can be used to suppress the QCD background.

- The associated production with vector bosons is called Higgsstrahlung (WH or ZH). It is an interesting mode to study the couplings to the vector bosons.
- The Higgs production in association with top pairs (ttH) is the smallest mode contributing in the LHC Higgs production. Nevertheless, is an important process to measure the Yukawa coupling between the Higgs and the top quark.

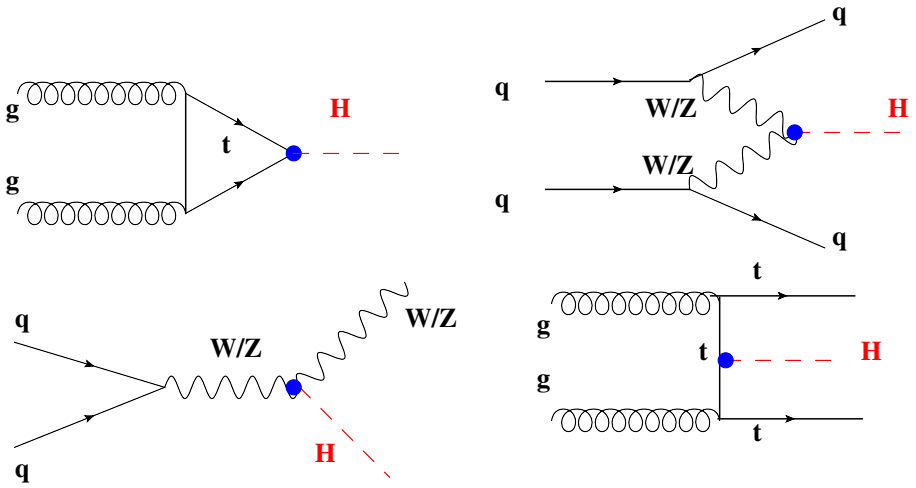

FIGURE 1.13: The main SM Higgs boson production modes in hadron collisions. The gluon-gluon fusion (top left), the Vector boson Fusion (top right), Higgsstrahlung (bottom left) and the production in association with top pairs (bottom right).

Figure 1.14, shows the Higgs cross-sections for the different production modes at 7 and 8 TeV of centre of mass energy. For the dominant production mode ggF, the signal cross-sections are computed at up to next-to-next-to-leading order (NNLO) in QCD, and next-to leading order electroweak (EW) corrections are applied. These calculations are detailed in [20–23] and [24–27]. For the VBF process, full QCD and EW corrections are applied up to NLO, together with approximate NNLO QCD corrections [28–31]. The cross-sections for the WH and ZH processes are calculated with QCD corrections up to NNLO and EW corrections up to NLO [32–34]. Finally for the ttH process, the cross-sections are calculated up to NLO QCD [35–39].

1.5.2 The Higgs decay modes

In Figure 1.15, the Higgs branching fractions as a function of m_H are shown. The branching fraction decay their uncertainties are calculated with HDECAY [41]. The main mass regions explored by the LHC are summarised in the following:

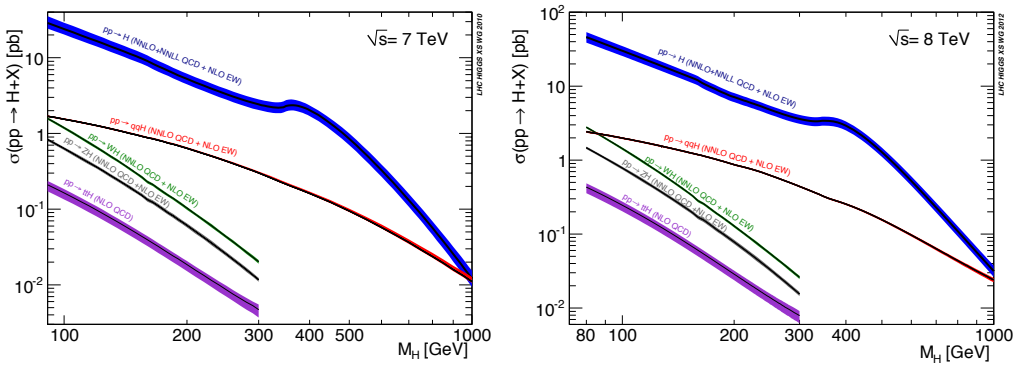

FIGURE 1.14: Cross-section of the Higgs production modes at LHC at 7 TeV (left) and 8 TeV (right), as a function of its mass [40].

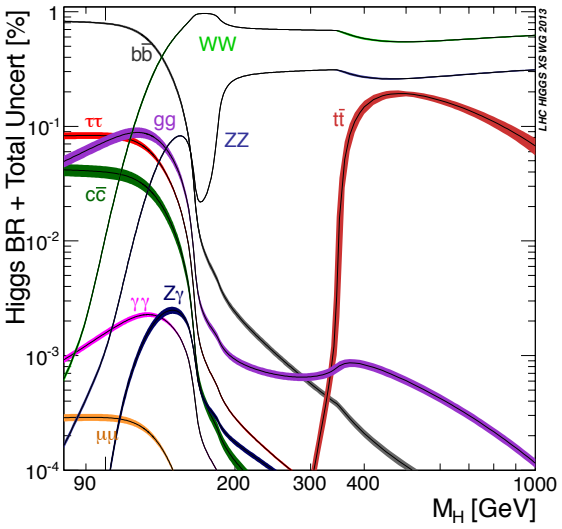

FIGURE 1.15: Standard Model Higgs boson decay branching ratios as a function of the Higgs boson mass hypothesis [40].

Low mass range:

- In the low mass range (100 GeV$\leq m_H \leq$130 GeV), the Higgs boson mainly decays into the quark pair $b\bar{b}$ (branching fraction in the order to 70% at $m_H =$ 120 GeV), due to the Higgs coupling to fermions being proportional to their mass. Nevertheless, in the LHC this particular channel has a low sensitivity due to the large QCD background from the proton collisions.
- The $H \rightarrow \tau\tau$ channel has a branching ratio of about 8%, and has a large background due to the $Z \rightarrow \tau\tau$ decay process.
- The $\gamma\gamma$ and $Z\gamma$ decay channels have a contribution of about 10^{-3}. They are discussed in further detail in the next section.

Intermediate mass range:

- The WW and ZZ channels dominate the intermediate mass range (130 GeV $\leq m_H \leq$200 GeV). The most promising channel is the WW, with a branching fraction of close to 100% in this range. The ZZ decay channel is an important channel in both low and medium mass range, since the presence of four electrons or muons in one events is a very unique signature in ambient dominated by QCD background.

High mass range:

- At $m_H > 2m_{top}$, the top pair decay appear and increases rapidly due to its very strong coupling to the Higgs. The WW and ZZ channels still dominates in this range.

1.6 The $H \to \gamma\gamma$ and $H \to Z\gamma$ channels

As discussed in the previous section, both theoretical and experimental constraints favour a SM Higgs boson with a low mass. The channel where the Higgs decays into two photons is one of the most promising for the Higgs searches in this range, due to a clean signature and a narrow width that provides a sufficient discrimination against backgrounds.

The Higgs boson decays into two photons via loops of W bosons, and fermions dominated by the top quark (as the coupling of the Higgs to fermions is proportional to the mass of the fermions, the contribution of the light fermions in the loop is negligible, compared to the top quark). The branching ratio of this decay is of about 0.2% at $m_H = 125$ GeV.

Similarly to the diphoton channel, the $H \to Z\gamma$ decay is also mediated via top and W loops as shown in Figure 1.16, the branching fraction at 125 GeV is about 0.15%, but in order to have a clean final state signature, the Z boson is required to decay leptonically (electrons or muons), the low branching fraction for the $Z \to \ell\ell$ makes the total expected Higgs events to be of about 5% the expected events in $H \to \gamma\gamma$.

In the case of the $H \to \gamma\gamma$ and $H \to Z\gamma$ channels, the common fact of decaying via loop processes mediated by the same particles, make them both sensitive to new

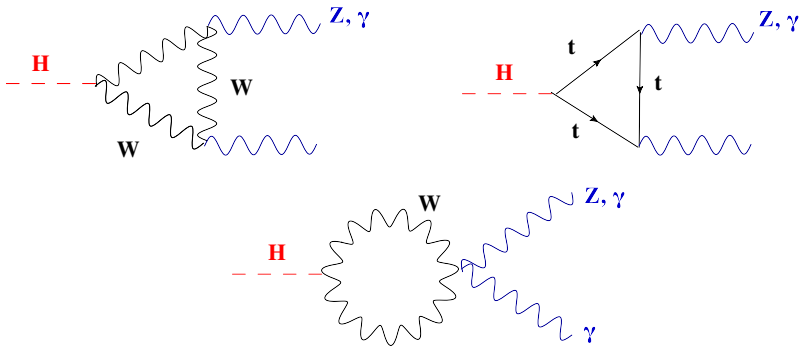

FIGURE 1.16: Leading Feynman diagrams for the $H \to \gamma\gamma$ and $H \to Z\gamma$ decays in the Standard Model.

physics, as any new charged particle coupling to the Higgs could contribute to the loops and change their relative decay rate magnitudes. Thus, the measurement (or limits) of the decay rate of the SM Higgs boson in the $Z\gamma$ channel and its comparison to $H \to \gamma\gamma$ rate, could provide hints of physics beyond the SM.

1.7 Beyond the SM

At present, the SM successfully provides the best description of phenomena observed by the experiments. The combined results of the global SM fit to precision electroweak data, severely constrains the SM Higgs mass to the low mass range, less than 150 GeV, giving clear hints to the experimentalists of which energy range should be explored. However, the SM has its natural flaws and unsolved problems. Among them are

- The SM does not describe the gravitational force, which becomes very important at high energies.
- The arbitrary number of (three) generations of quarks and leptons with such different mass scales, and the origin of the neutrinos masses are not explained by the SM.
- The SM does not provide and explanation for dark matter and dark energy, nor for CP violation responsible for the matter-antimatter observed asymmetry in the universe.

Even if the SM has proven to effectively describe the phenomena at the electroweak scale, it is an incomplete theory. The general belief is that the SM is an effective theory, a low energy limit of a more fundamental theory which would provide the unification of all four interactions in nature. The so-called "Beyond the SM" theories (BSM) try to extend the SM in order to provide answers to some of the unresolved puzzles. One of the main goals of the LHC is to search for new physics predicted by many BSM theories.

Concerning the $H \to \gamma\gamma$ and $H \to Z\gamma$ channels, there are some examples of common BSM theories which affect the decay rates and are a subject of interest in this thesis. In this section, a brief overview of some of these theories is presented.

1.7.1 Fourth Generation Model of Quarks and Leptons

Three families of charged and neutral fermions have been observed in the SM. In a fourth generation model, the production cross section of the Higgs boson in the ggF process is significantly increased due to additional quark loops. In a similar way, the partial decay width of the decay channels $H \to \gamma\gamma$ and $H \to Z\gamma$ is modified. In Figure 1.17, the branching fractions of Higgs decays in two fourth generation models where the 4th lepton and quarks masses are about 400 GeV. More information about this particular models is found in [42, 43].

The fourth generation interferes destructively with the W boson loop, resulting in a net decrease of the partial decay width into $\gamma\gamma$, and a slight increase of the $Z\gamma$ branching fraction. A large multiplicity of extra generations would increase the $\gamma\gamma$ channel total rate by an order of magnitude and systematic decrease on the $Z\gamma$ rate, as can be seen in Figure 1.18, for a Higgs boson with mass $m_H = 115$ GeV. More information can be found in [44, 45].

1.7.2 Models with Higgs extensions

In general, models with an extended Higgs sector often contain charged Higgs bosons that, among other phenomena, can contribute to the $H \to \gamma\gamma$ and $H \to Z\gamma$ decays through the loop effect. There are many possibilities for the extended Higgs sector, the two Higgs doublet models (2HDM) [46], Higgs triplet models [47–50] and the

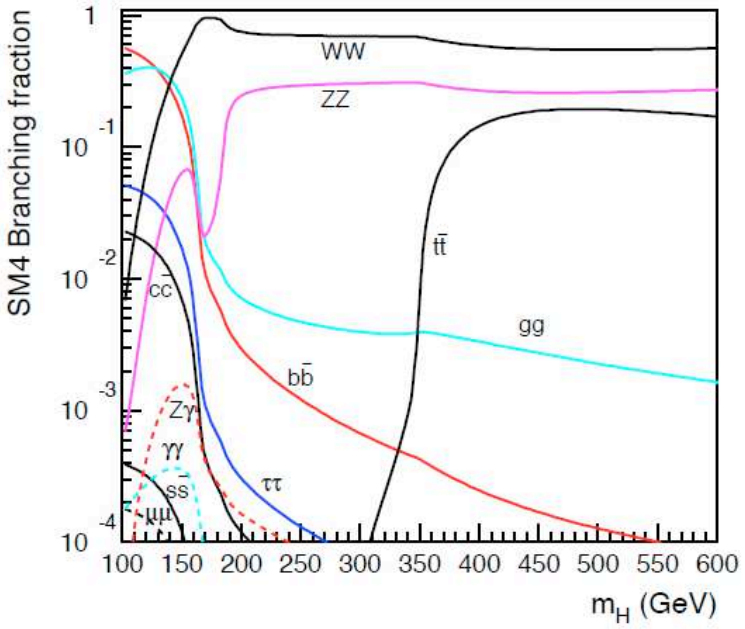

FIGURE 1.17: Branching fractions of Higgs decays in a fourth generation model with $m_{d4} = m_{l4} = 400$ GeV (right) [42].

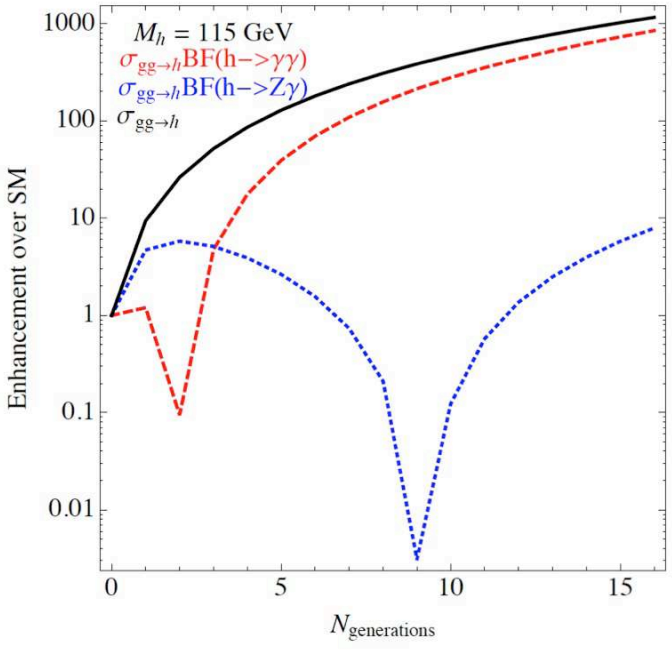

FIGURE 1.18: Enhancement in the event rate of a 115 GeV Higgs boson versus the number of extra generations [44].

minimal supersymmetric model [51]. The effects of some of these extended Higgs sector models on the decay rates of the two modes are studied in [52].

1.7.3 Fermiophobic Higgs boson

In certain models such as 2HDM or Higgs triplet models, the Higgs field couplings to some or all fermion generations can be substantially suppressed. In the fermiophobic model it is proposed that the mechanism that generates the fermion masses is independent of the Higgs mechanism; the Higgs boson is then referred to as fermiophobic. The fermiophobic Higgs decay into photons does not couples to fermions and only proceeds via W loops (Figure 1.16). Since the main SM decays ($b\bar{b}$ and $\tau\tau$) are forbidden at tree-level, the branching fraction for a low mass fermiophobic Higgs boson to decay into two photons is enhanced by an order of magnitude with respect to the SM. The resulting rate (cross-section times branching ratio) for a fermiophobic Higgs boson production decay to photons is larger than that of the SM for Higgs boson masses below 120 GeV (by a factor of about 4 for $m_H = 110$ GeV) [53]. In the $H \to Z\gamma$ the rate is predicted lower (at m_H=120 GeV) than in the SM by a few tens of percent[54]. The rates and their comparison to the SM are shown in Figure 1.19.

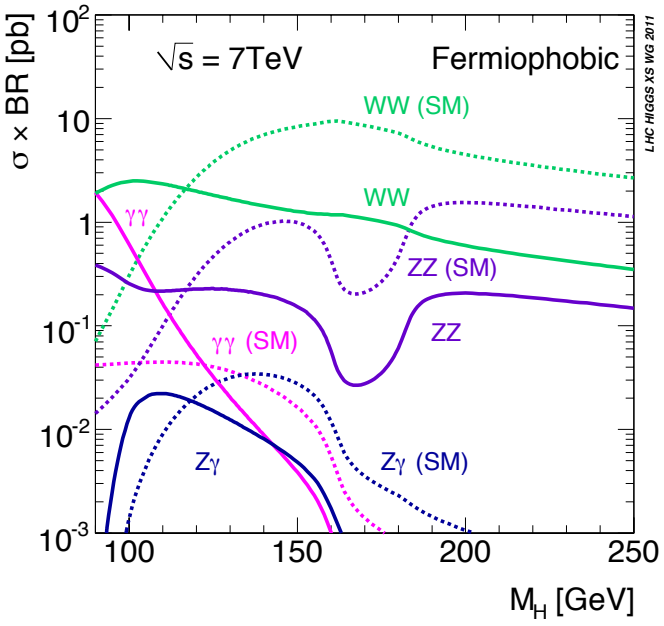

FIGURE 1.19: Higgs boson decay branching ratio times the production cross section at 7TeV in the fermiophobic Higgs model [40].

The previous models are just a small sample of the theories that predicts a deviation of the $\gamma\gamma$ and $Z\gamma$ rates from the ones in SM. In effect, a large number of the BSM theories predict new charged particles or changes in the Higgs coupling to fermions or bosons that could be indirectly tested by measuring the $H \to \gamma\gamma$ and $H \to Z\gamma$ branching fractions and their relative quotient. This fact, added to the good potential of discovery of the Higgs boson in the diphoton channel are the main motivation for the topic chosen in this thesis.

1.8 Results from the first run of the LHC Run

The first run of the LHC has brought major advances in particle physics, including the discovery of a new particle announced on 4 July 2012 [3] and confirmed as a Higgs boson particle in March 2013 [55], after the complete dataset was analysed by the ATLAS and CMS Collaborations. The analysis presented by ATLAS for the discovery, and the compatibility of the new found particle with the SM Higgs boson is presented in this thesis in Chapter 6.

The data collected during the LHC Run I is also used to test and set limits of several BSM theories, as the ones described in Section 1.7. Models such as a SM4 Higgs boson in the context of a fourth generation of fermions with masses of up to 600 GeV or a Fermiophobic Higgs boson, have been largely ruled out by the current observations [56], and limits on heavier or charged Higgs bosons predicted by models with Higgs extensions are set [57, 58]. The implications of the Higgs discovery and the results of the searches of physics beyond the SM will be discussed in Chapter 7.9.

Chapter 2

The ATLAS experiment

Contents

2.1 The LHC

The Large Hadron Collider (LHC) [59] is the largest and most powerful particle accelerator in the world. It involves a two-ring-superconducting hadron accelerator and collider installed in the 25.7 km tunnel where the CERN LEP accelerator once worked. It is located in the French-Swiss border near Geneva, and was first approved as a project in 1994 by the CERN Council, where the accelerator was conceived as a two-stage machine starting with a centre-of-mass energy of 10 TeV, to be upgraded later to 14 TeV. The LHC is mainly a proton-proton collider designed to produce

collisions at a very high rate (during some weeks per year, heavy ions beams are accelerated and collided instead). It contains four main experiments:

- Two general purpose particle detectors ATLAS [60] (A Toroidal LHC Apparatus) and CMS [61] (Compact Muon Solenoid), designed to work at high collision rates searching for the Higgs boson, perform precision measurements for the Standard Model and search for physics beyond the Standard Model (referred sometimes as new physics).
- A low rate experiment: LHCb [62] (LHC beauty) designed mostly for B physics.
- A dedicated heavy ion experiment ALICE [63] (A Large Ion Collider Experiment) for lead-lead collisions that aims to study the quark gluon plasma.

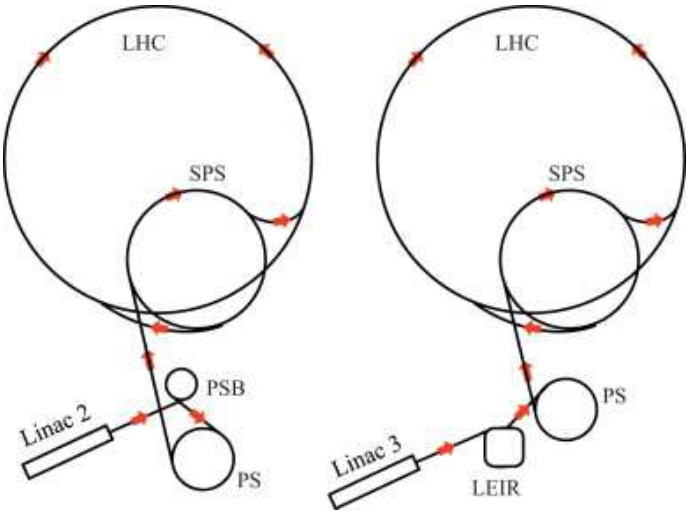

FIGURE 2.1: Schematic of the accelerator system for both protons (left) and heavy ions (right).

2.1.1 Running conditions and performance

Figure 2.1 shows the schema of the LHC injection chain for protons and heavy ions. The protons are created from hydrogen atoms ionised by an electric field. Given that the LHC cannot maintain stable beams bellow 450 GeV, the protons are accelerated in four steps before entering in the machine: first the linear accelerator LINAC 2 raises proton energy up to 50 MeV, then the Proton Synchrotron Booster (PSB) increases the energy to 1 GeV, the Proton Synchrotron (PS) to 26 GeV and finally

the Super Proton Synchrotron (SPS) to 450 GeV. In the PS, the bunch structure for the LHC is prepared: protons are arranged into bunches of about 1.15×10^{11} protons with a designed bunch spacing of 25 ns.

The SPS injects two beams into the LHC, in clockwise and counter-clockwise directions. Each beam consists of a bunch train of 2808 bunches, where the total number of protons in each beam is of the order 3×10^{14}. In design conditions the LHC would accelerate the protons to energies up to 14 TeV (a process that takes around 25 minutes). These bunches circulate in separate vacuum tubes in opposite directions. Surrounding the tubes are 1232 superconductive dipole magnets, that bend the beams until they reach their nominal energy. The dipoles lie in a single cryostat cooled down by superfluid Helium to a temperature of 1.9 K. The magnets are made of NbTi and a current of 12 kA allows for magnetic fields up to 8.4 T. Additionally, the LHC is equipped with quadrupole magnets for focusing, as well as higher multipole magnets for corrections.

Once beams are accelerated to the expected energy, stable beams are declared on the LHC and the experiments can start collecting data. The beam intensity decreases with time, with an expected beam lifetime of approximately 15 hours at the design conditions. When the intensity of the beams is too low, they are directed out of the accelerator to a solid block of graphite where they are absorbed. The dipole magnets are then ramped down to 0.54 T and they are kept in this state for some 20 to 40 minutes. For a new cycle (a beam fill), the beam injection is repeated before the magnets are ramped up again to 8.4 T [64]. The quoted nominal design values, are not identical to the performance achieved during 2010-2012 run. Table 2.1 shows the nominal and real parameters of the LHC proton-proton collisions for the data-taking periods.

Parameter	2010	2011	2012	Nominal
$\sqrt{s}$ [TeV]	7	7	8	14
N_b	1.15×10^{11}			
n_b	368	1380	1380	2808
Δt [ns]	150	50	50	25

TABLE 2.1: Parameters of the LHC proton-proton collisions for the data-taking periods: 2010, 2011 and 2012, and the design values. The quoted parameters are: the center-of-mass energy $\sqrt{s}$, the number of protons per bunch N_b, the number of bunches per beam n_b and the bunch-to-bunch time spacing Δt. Each value corresponds to the best performance achieved during the year [65, 66].

The number of events per second in the LHC collisions is given by:

$$N_{\text{event}} = \mathcal{L}\sigma_{\text{event}}, \tag{2.1}$$

where σ_{event} is the cross-section of the event under study and $\mathcal{L}$ the machine instantaneous luminosity. This luminosity depends only on beam parameters such as the number of particles per bunch, the number of bunches per beam, the revolution frequency, and the transverse beam emittance[1].

The LHC instantaneous luminosity is not constant over one data-taking period. The luminosity decays due to the degradation of the beam intensities and emittance. During nominal LHC operation one of the main causes of this degradation is the beam loss from collisions. The initial decay time of the bunch intensity due to this effect is defined as:

$$\tau = \frac{N_{\text{tot},0}}{\mathcal{L}\sigma_{\text{tot}}\kappa}, \tag{2.2}$$

where $N_{\text{tot},0}$ is the initial beam intensity, $\mathcal{L}$ the initial instantaneous luminosity, σ_{tot} the total cross section ($\sigma_{tot} = 10^{25}$ cm^{-2} at 14 TeV), and κ is the number of interaction points in the collision. Assuming an initial peak luminosity of $\mathcal{L} = 10^{34} cm^{-2} s^{-1}$ and two high luminosity experiments, Eq. 2.2 leads to a decay time of 44.85 h. From the expression above the decay of beam intensity and luminosity as a function of the time is:

$$N_{\text{tot}}(t) = \frac{N_{\text{tot},0}}{1 + t/\tau}, \tag{2.3}$$

$$L(t) = \frac{L_0}{(1 + t/\tau)^2}, \tag{2.4}$$

then, the time to reach 1/e of the initial luminosity is given by:

$$t_{1/\text{e}} = (\sqrt{e} - 1)\tau, \tag{2.5}$$

leading to a decay time of $\tau_{1/e} = 29h$. Other contributions as Touschek scattering [67] particle losses due to a slow emittance blow-up, and synchrotron radiation also decrease the beam life time. Considering all these contributions, the above decay time gives a net estimate of the luminosity lifetime of $\tau_L = 14.9h$.

[1]Emittance is a property of a charged particle beam in a particle accelerator. It is a measure for the average spread of particle coordinates in position-and-momentum phase space. Emittance has units of length, but is usually referred to as"length × angle". It can be measured in all three spatial dimensions. The dimension parallel to the motion of the particle is called the longitudinal emittance. The other two dimensions are referred to as the transverse emittances.

Integrating the luminosity over one run yields,

$$L_{\text{int}} = L_0 \tau_L \left[1 - e^{-T_{run}/\tau_L}\right], \tag{2.6}$$

where T_{run} is the total duration of the luminosity run. The overall collider efficiency depends on the ratio of the length of the run to the average turnaround time (the time it takes to do all the filling, cycling, ramping, accelerating and further aborting process described at the beginning of the section, it has a theoretical minimum of 1.15 hours and a real average of 7 hours). If the LHC can be operated for 200 days a year with the previously obtained τ_L of 15 hours, the optimum run time is 12 hours. This leads to a maximum total integrated luminosity per year of 80 fb^{-1} to 120 fb^{-1} (depending on the average turnaround time of the machine from the theoretical minimum 1.5 to the real average of 7 hours) in design conditions [59].

In high-luminosity colliders, there is a non-negligible probability that one single bunch crossing may produce several separate events, so-called pile-up events. There are two kinds of pile-up events: "in-time pile-up" when the extra collisions come from the same bunch-crossing, and "out-of-time pile-up" that refers to events from successive bunch-crossings.

The experimental observable used as estimator of the "in-time pile-up" is the number of reconstructed vertices N_{PV}. To include the "out-of-time pile-up" in the picture $\langle\mu\rangle$ is used. This refers to the average number of collisions per bunch-crossing at the time of the recorded event, and is given by:

$$\langle\mu\rangle = \frac{L \times \sigma_{\text{inel}}}{N_{\text{bunch}} \times f_{\text{LHC}}}, \tag{2.7}$$

where L is the average instantaneous luminosity over a large time period Δt ($\Delta t_{pile-up} \gg$ 600ns), σ_{inel} is the total inelastic cross section, N_{bunch} is the number of colliding bunches in the LHC and f_{LHC} is the revolution frequency. Figure 2.2 shows an example of the high pile-up environment in 2012, with an event on which 25 vertices are reconstructed, including a candidate Z boson decaying in the di-muon channel.

2.1.2 LHC Run I and perspectives

The first beams in the LHC occurred on September 10^{th}, 2008. Unfortunately a major accident happened a few days later due to a failure in the superconducting

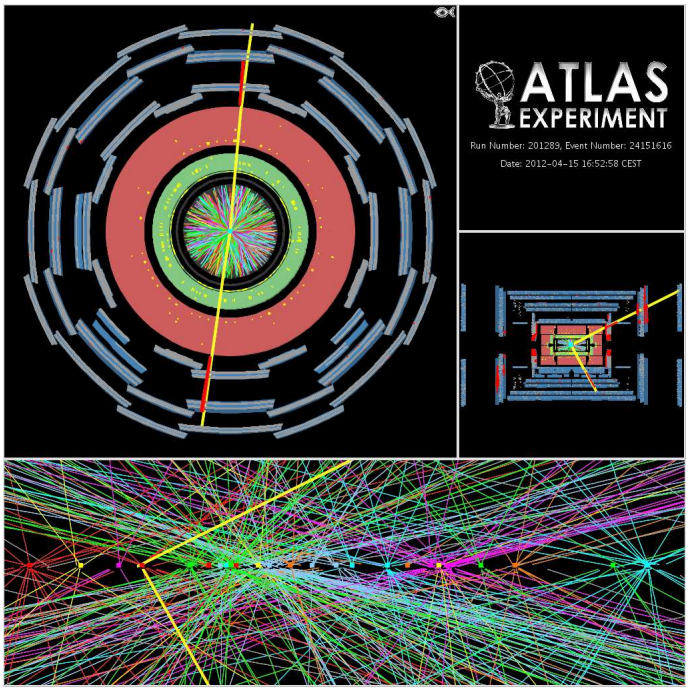

FIGURE 2.2: A Z boson event candidate decaying into a pair of muons in an environment with 25 reconstructed vertices. This event was recorded on April 15th 2012 and demonstrates the high pile-up environment in 2012 running.

connection between two magnets. This led to one year of major repairs and the development of a new quench protection system. On November 2009, first proton-proton collisions were recorded at a centre of mass energy of 900 GeV. Within less than a week, the LHC became the most powerful collider in the world, reaching collisions with 2.36 TeV at the centre of mass energy. On March 30^{th}, 2010 the first collisions at 7 TeV occurred, and an integrated luminosity of approximately 40 pb^{-1} was recorded during the whole year (from March to beginning of november, see Figure 2.3) and a peak instantaneous luminosity of $2\text{x}10^{32}\text{cm}^{-2}\text{s}^{-1}$. On May 2011, the instantaneous luminosity exceeded $10^{33}\text{cm}^{-2}\text{s}^{-1}$ (Figure 2.4), setting a new record for hadron colliders. Until summer of 2011, the average number of proton-proton collisions per bunch-crossing was between 3 and 8, with a global average of $\langle\mu\rangle = 6$ during this period. In the second semester of 2011, $\langle\mu\rangle$ increased to reach values between 5 and 17, with an average of 12. The total 2011 integrated luminosity delivered to ATLAS was 5.2 fb^{-1} (Figure 2.3). For 2012, the centre of mass energy in the collisions increased up to 8 TeV, achieving a maximum instantaneous luminosity of $7 \times 10^{33}\text{cm}^{-2}\text{s}^{-1}$. During 2012, the pile-up conditions were significantly harsher, with a global average of $\langle\mu\rangle$ at approximately 20.7 and extreme values up to 40 as

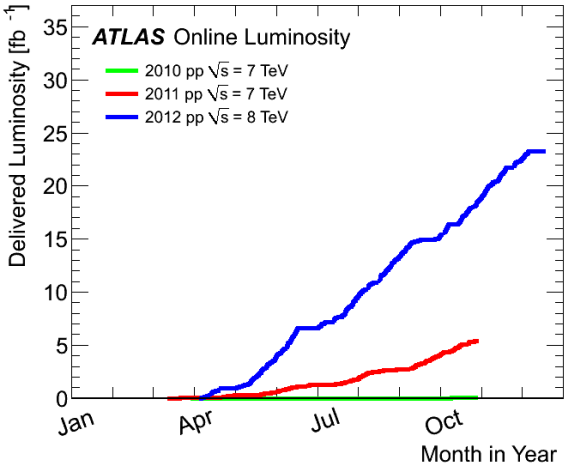

FIGURE 2.3: Cumulative luminosity versus day delivered to ATLAS during stable beams and for p-p collisions. This is shown for 2010 (green), 2011 (red) and 2012 (blue) running. The online luminosity is shown [68].

shown in Figure 2.5. The total integrated luminosity delivered to ATLAS in proton-proton collisions was 20.8 fb^{-1}. The analyses presented in this thesis will use the complete 2011 and 2012 data samples.

On February 2013, after a heavy ion run the LHC Run I was concluded. A technical stop is in process until the end of 2014 for machine and experiments development. In 2015 the LHC will resume again, getting closer to the nominal centre of mass energy (13 TeV to 14 TeV) and the nominal luminosity ($10^{34} cm^{-2} s^{-1}$) and will run for three more years. A second and shorter technical stop will occur in 2018 for injector upgrade, and LHC will resume again for three more years (2019-2021) at a luminosity about twice the nominal one. A final two-year stop is programmed from 2022 to 2023 (but is not yet approved) for major upgrades of the experiments and the CERN accelerator system in order to integrate about 3000 fb^{-1} per experiment in 2030.

2.2 The ATLAS Detector

ATLAS is a general purpose detector built to measure the particles generated in the collisions produced by the LHC (protons and heavy ions). It is specially designed to respond to the high interaction rates, radiation doses and energies in which the LHC works. The detector was installed in the underground cavern from 2003 to 2008 after many years of R&D, optimisation and construction.

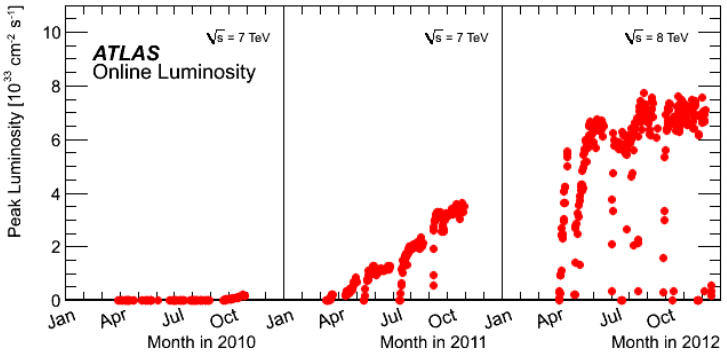

FIGURE 2.4: The peak instantaneous luminosity delivered to ATLAS per day versus time during the p-p runs of 2010, 2011 and 2012. The online luminosity measurement is used for this plot [69].

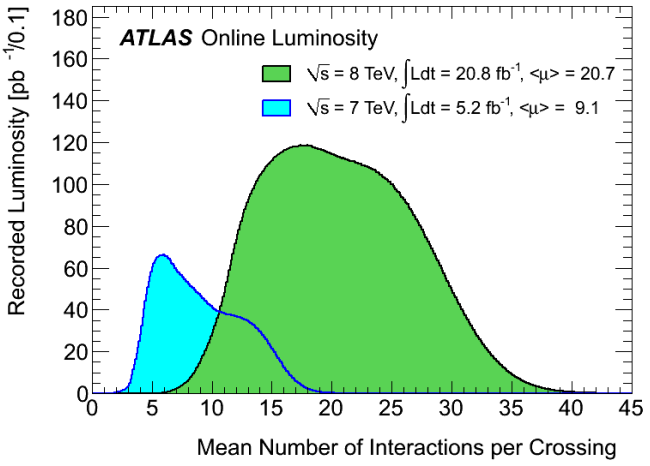

FIGURE 2.5: The luminosity-weighted distribution of the mean number of interactions per bunch-crossing for the 2011 and 2012 data. This shows the full 2011 run and 2012 data taken between April 4th and November 26th. The integrated luminosities and the mean $\langle\mu\rangle$ values are given in the figure [70].

The ATLAS detector is designed to perform high precision measurements of the Electroweak interactions, QCD tests, flavour physics and the search for the SM Higgs boson as well as new physics. The sub-systems were optimised using these physics analyses as a benchmark to establish its performances. The physics goals can be turned into a list of general requirements for the LHC detectors:

- In order to respond to the high collision rates and radiations, fast radiation-proof electronics and sensors are required.
- High detector granularity is needed to deal with the particle fluxes and reduce the contamination of overlapping events.

- The inner tracker should have a very good charged-particle momentum resolution and reconstruction efficiency.
- An electromagnetic calorimeter with a very good energy resolution and efficiency for photon and electron identification.
- The hadronic calorimeter should have a full-coverage for accurate jet and missing transverse energy measurements.
- A good muon momentum resolution and identification with a large acceptance. The detector should be able to determine unambiguously the charge of the muons with high transverse momentum.
- Some physics process require a highly efficient triggering on low transverse momentum objects with good background rejection.

The requirements stated above are successfully fulfilled by ATLAS. The detector is nominally forward-backward symmetric with respect to the interaction point (IP), and is built of several sub-detectors configured in concentric layers in the central (Barrel) and forward regions (End-Caps) (Figure 2.6). The inner detector (ID) is a tracking detector immersed in a 2 T solenoidal field where pattern recognition, momentum, vertex measurements and identification of charged particles such as electrons and muons are performed. The next layer is the calorimeter system, which is divided in a liquid argon electromagnetic (EM) component that measures the energies with an excellent performance in energy and position resolution, and a scintillator-tile component where hadrons for which the energy is not completely absorbed in the EM calorimeter, deposit their remaining energy. The calorimeter is surrounded by the muon spectrometer, where an excellent muon momentum resolution is achieved with three layers of tracking chambers. The muon spectrometer defines the overall dimension of the ATLAS detector. All these sub-systems are described in better detail in this chapter.

2.2.1 The ATLAS Coordinate System

The origin of the coordinate system is set at the nominal interaction point. The z-axis goes in the beam direction with the positive values of z pointing the counter-clockwise beam, the region with positive values is called the A side of the detector while the negative is defined as the C side. The x-y plane is transverse to the

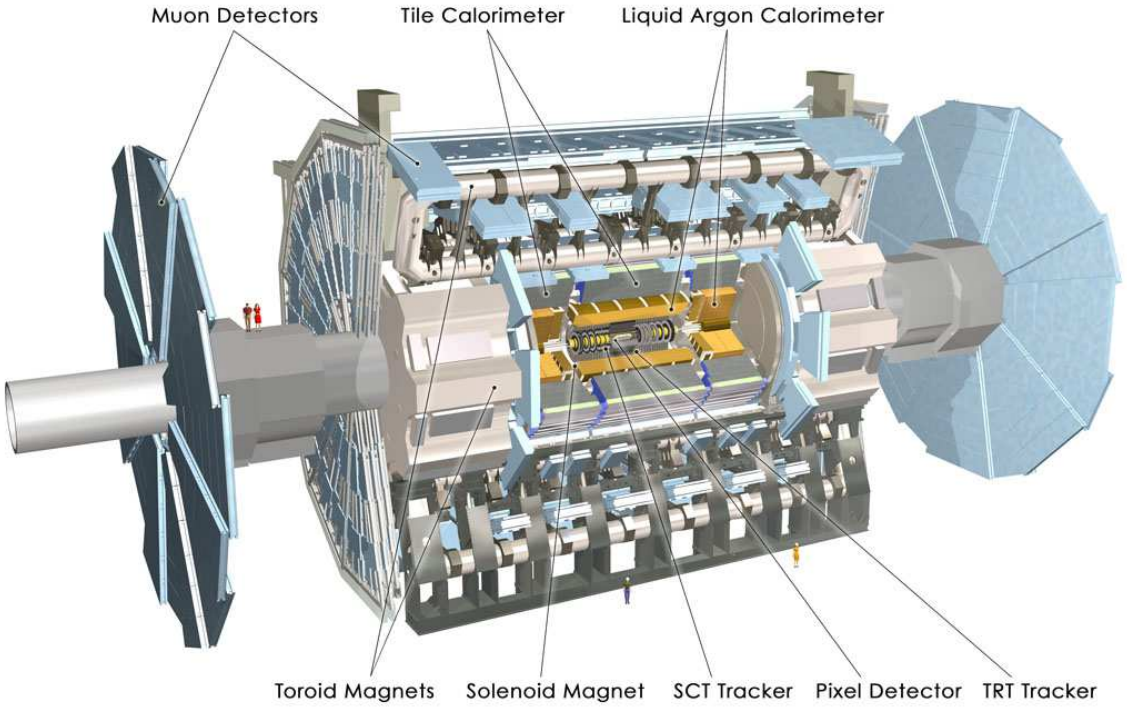

FIGURE 2.6: A detailed computer-generated image of the ATLAS detector and its subsystems [60].

beam direction (z-axis). The polar angle θ is the angle from the beam axis, and the azimuthal angle ϕ is measured around it. The transverse momentum p_{T}, the transverse energy E_{T} and the missing transverse energy $E_{\mathrm{T}}^{\mathrm{miss}}$ are defined in the x-y plane. The pseudo-rapidity is defined as:

$$\eta = -\ln\left(\tan\left(\theta/2\right)\right), \tag{2.8}$$

for massive objects such as jets, the rapidity is used:

$$y = \frac{1}{2} ln[(E + p_{\mathrm{z}})/(E - p_{\mathrm{z}})]. \tag{2.9}$$

The distance in the pseudo-rapidity-azimuthal angle space is defined as:

$$\Delta R = \sqrt{(\Delta\eta^2 + \Delta\phi^2)}. \tag{2.10}$$

The usual units of transverse energy or momentum such as p_{T}, E_{T} and $E_{\mathrm{T}}^{\mathrm{miss}}$ are GeV.

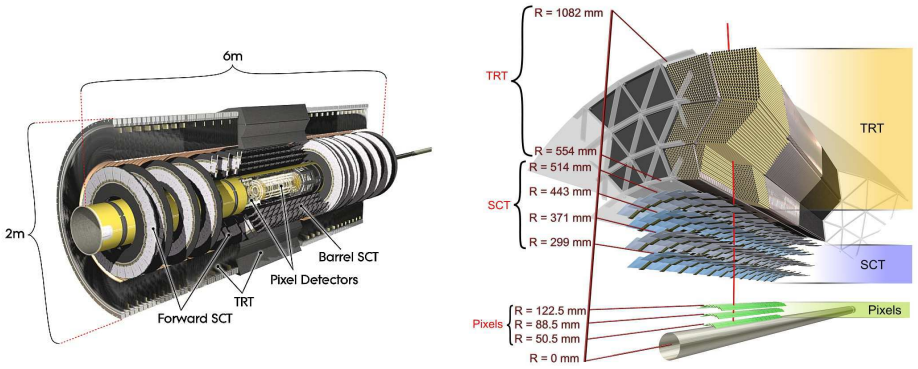

FIGURE 2.7: Left: Cut-away view of the ATLAS inner detector. Right: The different sub-detectors of the inner detector [60].

2.2.2 Inner Detector

The ATLAS inner detector (ID) was designed to provide excellent pattern recognition, momentum resolution and primary and secondary vertex measurements with high granularity to the large number of charged tracks created by the particles that emerge from the collision point within a pseudo-rapidity range of $|\eta| < 2.5$. This performance is achieved through a configuration of three complementary sub-detectors (Figure 2.7): Pixel, Silicon Microstrip Trackers (SCT) and the Transition Radiation Tracker (TRT).

The ID is contained within a cylindrical envelope of length 3512 mm and a radius 1150 mm and is immersed in a 2 T magnetic field created by the central solenoid, which extends in a length and diameter of 5.3 and 2.5 mm respectively.

The precision tracking sub-detectors (pixel and SCT) cover an acceptance of $|\eta|$ <2.5. In the barrel they are arranged in concentric regions around the beam, and have a radial configuration in the end-caps (disks perpendicular to the beam axis). The silicon pixel detector region has the highest granularity, arranged in such a way that typically three pixel layers are crossed by each track. All pixels are identical with a minimum pixel size R - $\phi \times z$ of 50 x 400 μm^2 (where R - ϕ is a lateral plane with R as the radial distance from the detector geometrical centre and ϕ the azimuthal angle). The pixel detector has approximately 80.4 million read-out channels.

Outside of the pixel regions, a track crosses eight SCT strip layers. In the barrel small angle stereo strips (40 mrad) are used to measure the coordinates with one set of strips parallel to the beam axis measuring R - ϕ. They consist of sets of two lines of sensors with a distance of 80 μm between sets. For the end-cap, one

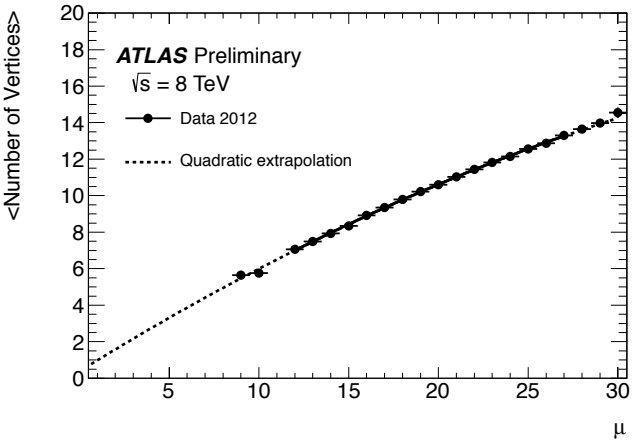

FIGURE 2.8: Average number of reconstructed primary vertices as a function of average number of pp interactions per bunch-crossing measured for the data of 2012. A second order polynomial fit is performed in the upper range of μ. For the lower values of μ, the result of mathematical extrapolation is shown [71].

set of strips runs radially and other set of stereo strips at an angle of 40 mrad, separated by a distance of 80 μm. The total number of read-out channels in the SCT is approximately 6.3 million.

The TRT is the outer sub-detector, consists of straws with a 4 mm diameter, in which a typical track has about 36 hits. It covers the region in $|\eta|$ <2.0 providing R - ϕ information with a precision of 130 μm per straw. In the barrel the straws are parallel to the beam axis and 144 cm long. In the end-caps, 37 cm long straws are radially configured in wheels. The TRT has approximately 351,000 read-out channels.

The combination of the three independent but complementary sub-detectors provides a very high precision in both R - ϕ and z coordinates, allowing an excellent vertex measurement. Figure 2.8 shows the average number of reconstructed primary vertices as a function of the average number of pp interactions per bunch-crossing for the 2012 data.

A good momentum measurement is performed due to the large number of hits in the TRT straws. With data collected at 7 TeV, the resolution was measured using muons reconstructed in the ID from $Z \rightarrow \mu\mu$ (see Figure 2.9).

The tracking system described above provides measurements in a range matched to the precision measurements of the electromagnetic calorimeter.

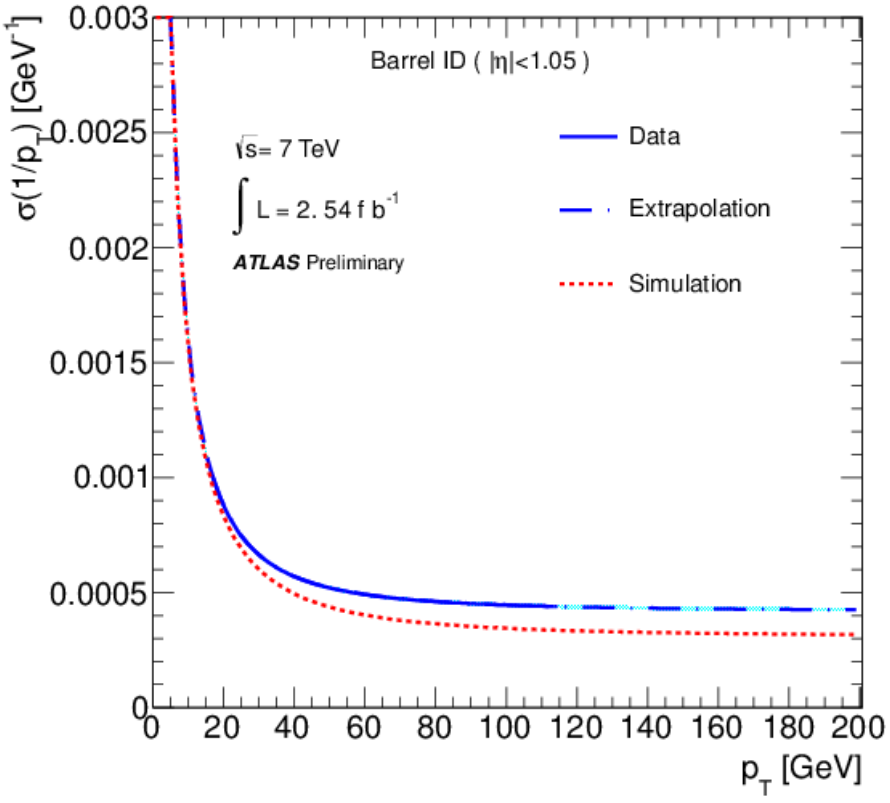

FIGURE 2.9: Resolution curve extracted from ID parameters in collision data and simulation as a function of the muon p_T, for the barrel region. The solid blue line shows determinations based on data, the dashed blue line shows the extrapolation to p_T range not accessible in this analysis and the dashed red line shows the determinations from simulation. The measurement is performed using 2.54 fb^{-1} of 7 TeV data [72].

2.2.3 Calorimeters

The ATLAS calorimeter system consists of a number of sampling detectors with full ϕ-symmetry covering the $|\eta| < 4.9$ range with different approaches depending on the physics requirements of each η region. Electrons and photons are reconstructed in the electromagnetic calorimeter (EMCAL) where its high granularity allows precise measurements. The EMCAL is complemented by the hadronic calorimeters for jet reconstruction and E_{T}^{miss} measurements.

The calorimeters closest to the beam-line, and next to the inner detector are housed in three cryostats, one barrel and two end-caps. The barrel cryostat contains the electromagnetic calorimeter (EMB), each of the end-caps contains one electromagnetic (EMEC), and one hadronic calorimeter (HEC) surrounding the EMEC and

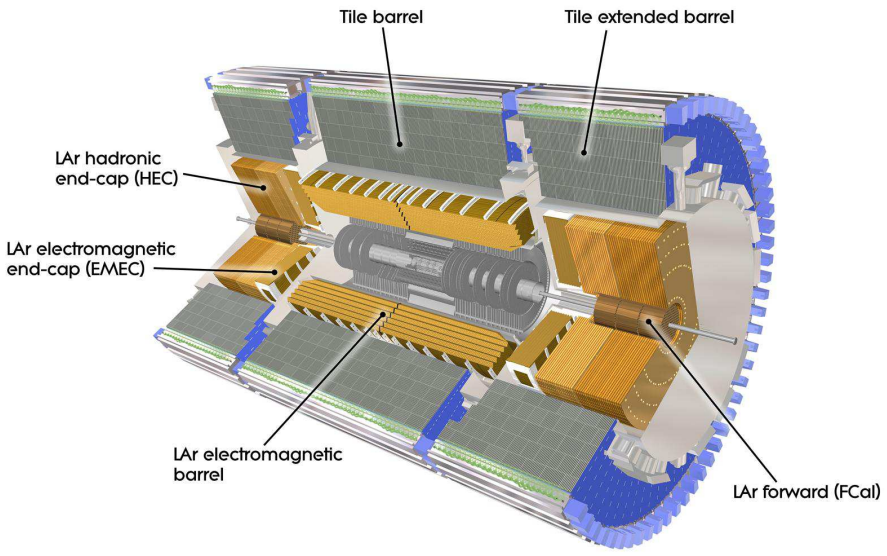

FIGURE 2.10: Left: Cut-away view of the ATLAS calorimeter system [60].

a Forward Calorimeter (FCal) covering the region closest to the beam. The active medium of these calorimeters is the Liquid Argon (LAr), chosen by its intrinsic linear behaviour, its stability of response over time and its intrinsic radiation hardness. The outer hadronic calorimeters consist of scintillator tiles located in one central barrel part and two extended barrels (see Figure 2.10).

The calorimeters provide good containment for the electromagnetic and hadronic showers and limits the punch-through into the muon system, for this the depth of the system was carefully chosen: for the EMB the thickness is $>$ 22 radiation lengths (X_0) and $> 24X_0$ in the EMEC. This gives 9.7 interaction lengths (λ) of active calorimeter in the barrel and 10 λ in the end-caps, and a total thickness (including the outer support) of 11 λ at η=0, this is enough to reduce the punch-trough below the irreducible level in muons. More details about the calorimeter geometry is found in Section 3.2.

2.2.3.1 LAr electromagnetic calorimeter

The EM barrel consists of two identical half-barrels, separated by a small gap (4mm at z=0) covering the $|\eta|$ <1.475 region. The two end-caps components cover the 1.375< $|\eta|$ <3.2 region , and are divided in to coaxial wheels: an inner wheel (1.375< $|\eta|$ <2.5) and an outer wheel (2.5< $|\eta|$ <3.2). These are lead-liquid argon detectors

with accordion shape lead absorbers and kapton electrodes. The accordion geometry provides complete ϕ symmetry without azimuthal cracks.

The physics precision measurements are performed in the $|\eta|$ <2.5 region, here the EM calorimeter is divided in three sections of depth, and for the end-cap inner wheel, the calorimeter is segmented in two sections, with a coarser lateral granularity.

A pre-sampler detector, with an active LAr layer of 1.1 cm in the barrel and 0.5 cm in the end-caps, is used to correct for the energy lost by electrons and photons upstream of the calorimeter and is located in the $|\eta|$ <1.8 region.

From test beam results, the expected energy resolution of the EM calorimeter is the following [73]:

$$\frac{\sigma_{\mathrm{E}}}{E} = \frac{10\%}{\sqrt{E}} \oplus 0.7\%. \tag{2.11}$$

The last term in Equation 2.11 of 0.7%, referred to as "constant term" corresponds to the design value. Measurements from the observed width of the $Z \to e^+e^-$ peak give as a result the effective constant terms shown in 2.2

SubSystem	$\|eta\|$-range	effective constant term (c_{data})
EMB	$\|\eta\| < 1.37$	$1.2\% \pm 0.1\%(stat)^{+0.5\%}_{-0.6\%}(syst)$
EMEC (OW)	$1.52 < \|\eta\| < 2.47$	$1.8\% \pm 0.4\%(stat) \pm 0.4\%(syst)$
EMEC (IW)	$2.5 < \|\eta\| < 3.2$	$3.3\% \pm 0.2\%(stat) \pm 1.1\%(syst)$
FCal	$3.2 < \|\eta\| < 4.9$	$2.5\% \pm 0.4\%(stat)^{+1.0\%}_{-1.5\%}(syst)$

TABLE 2.2: Effective constant term measurements from data (from the observed width of the $Z \to e^+e^-$ peak), for different subsystems of the EMCAL: Barrel, End-Cap (Inner Wheal and Outer Wheal), and the forward calorimeter [74, 75].

As the EMC is crucial to the photon analyses presented in this thesis, a more detailed description of this detector and its performance will be developed in a dedicated chapter (Chapter 3).

2.2.3.2 Hadronic calorimeters

Hadrons deposit some of their energy on the EM calorimeters but are not completely absorbed, the hadronic calorimeter contains the showers of high-energy hadrons. It has two components, the barrel hadronic calorimeter (Tile Calorimeter) and the hadronic end-cap calorimeter.

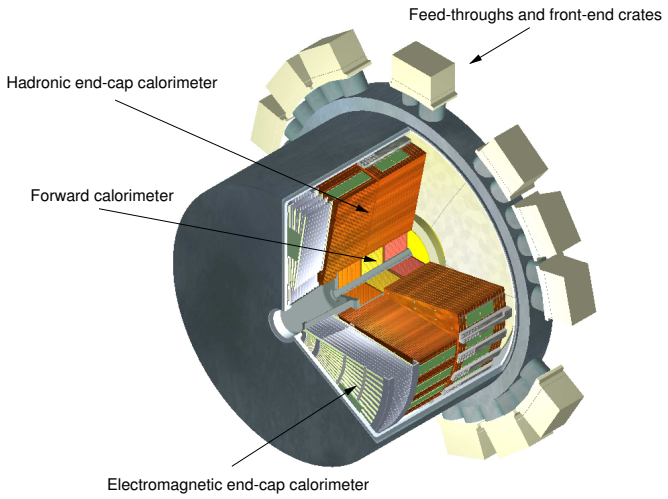

FIGURE 2.11: Cut-away view of an end-cap cryostat showing the positions of the three end-cap calorimeters. The outer radius of the cylindrical cryostat vessel is 2.25m and the length of the cryostat is 3.17m [60].

Tile Calorimeter

The Tile calorimeter is a sampling calorimeter using steel as the absorber and scintillating tiles as the active material. It is located outside of the EM calorimeter. It has a central barrel covering the $|\eta|$ <1.0 region with 5.8 m in length, and two extended barrels, with 2.6 m in length covering the 0.8< $|\eta|$ <1.7 range. Each extended barrel has an inner radius of 2.28 m and outer radius of 4.25 m, with 7.4 λ of radial depth. They are divided azimuthally in 64 modules of approximately 0.1 $|\Delta\phi|$ size.

LAr Hadronic End-Cap Calorimeters

The HEC calorimeter is a copper/liquid-argon sampling calorimeter, covering the 1.5< $|\eta|$ <3.2 range. It is placed directly behind the EMEC calorimeter and shares the same LAr cryostats together with the FCal calorimeters (see Figure 2.11). It consists of two wheels, a front wheel (HEC1) and a posterior wheel (HEC2). Each wheel is divided into two segments, with a total of four layers in each end-cap. The wheels are cylindrical with an outer radius of 2030 mm and are built with 25 mm (HEC1) and 50 mm (HEC2) parallel copper plates, which are interleaved with 8.5 mm LAr gaps.

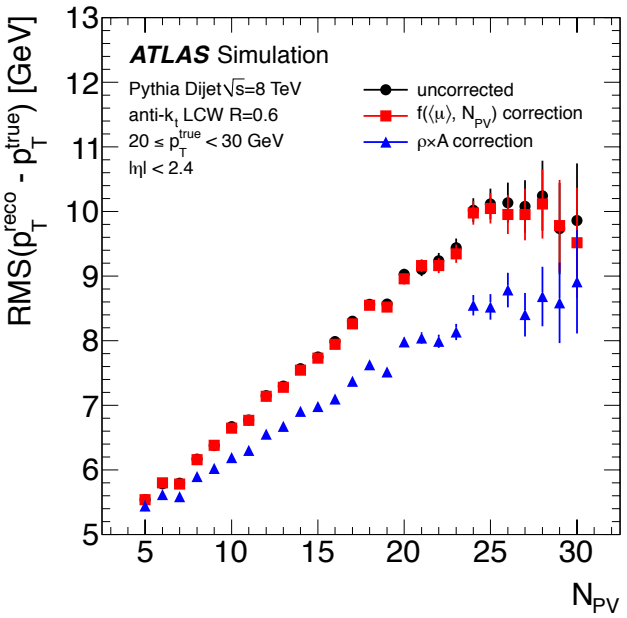

FIGURE 2.12: RMS width of the distribution of $p_T^{reco} p_T^{true}$ for jets matched to truth jets ($20 < p_T^{true} < 30$ GeV), before and after two pile-up subtraction methods. The RMS is presented as a function of the number of primary vertices (NPV) for $|\eta|$ <2.4.

LAr Forward Calorimeter

The Forward calorimeters are located in the same cryostat as the EMEC and HEC calorimeters covering over 3.1< $|\eta|$ <4.9. As the FCal are located at high η, with a distance of approximately 4.7 m from the interaction point, they are exposed to high particle fluxes. To reduce the neutron albedo in the inner detector cavity, the front of the FCal is displaced by about 1.2 m with respect to the EM calorimeter front face. The FCal design calls for a high density with limited depth (about 10 λ deep).

The FCal has three modules for each end-cap, one made of copper that measures the electromagnetic interactions and other two tungsten modules optimised for hadronic interactions.

The hadronic calorimeter provides jet energy, position and E_{T}^{miss} measurements. Figures 2.12 and 2.13 shows the jet momentum and E_T^{miss} resolution performance against pile-up in the 2012 data and simulation.

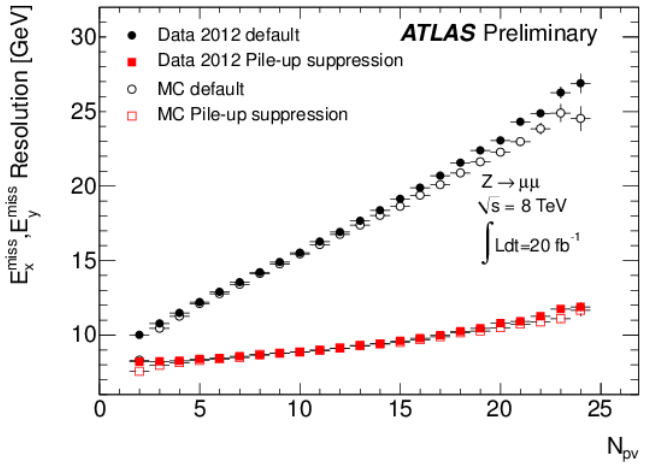

FIGURE 2.13: Resolution of x and y missing ET components as a function of the number of primary vertices for data and MC in $Z \rightarrow \mu\mu$ candidates. The resolution after pile-up suppression, based on the ratio of the sum p_T of the tracks associated to the primary vertex and all tracks, is also shown.

2.2.4 Muon spectrometer

The Muon Spectrometer is located in the outer part of the ATLAS detector. It is designed to detect charged particles going through the barrel and end-cap calorimeters and measure their momentum in the pseudo-rapidity $|\eta|$ <2.7 range. The detection principle is based on the magnetic deflection of muon tracks in the large superconducting toroid magnets trough high-precision tracking chambers. The magnetic bending is performed as following:

- Over the $|\eta|$ <1.4 range the muon tracks are bent by the large barrel toroid.
- In the 1.6 < $|\eta|$ <2.7 range, the magnetic bending is provided by two smaller magnets placed into both ends of the barrel toroids.
- In the 1.4 < $|\eta|$ <1.6 region (so-called transition region), the muon track deflection is performed by a mixture of the two fields (barrel and end-caps).

The magnetic field created in the whole configuration is mostly orthogonal to the muon trajectories, while minimising the degradation of resolution due to multiple scattering.

The tracks in the barrel are measured in chambers arranged in three cylindrical layers around the beam axis. For the transition region and end-caps the chambers

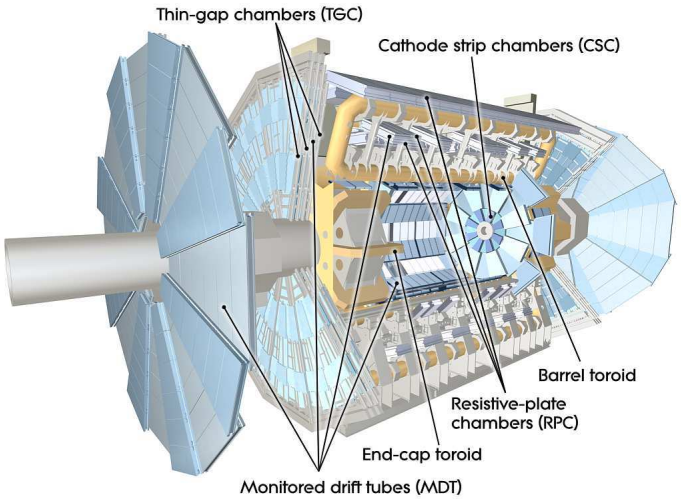

FIGURE 2.14: Cut-away view of the ATLAS muon system [60].

are installed in three layers perpendicular to the beam. The purpose of this tracking chambers is to determine the coordinate of the track in the bending plane.

The precision momentum measurement is performed by the Monitored Drift Tube chambers (MDTs) covering the $|\eta|$ <2.7 region (except in the innermost end cap layer where the coverage is up to $|\eta|$ <2.0). They consist of three to eight layers of drift tubes operating at 3 bar of absolute pressure, with an average resolution of 80 μm per tube, or about 35 μm per chamber. The MDTs combine high measurement accuracy, predictability of mechanical deformations and simplicity of construction.

In the 2.0< $|\eta|$ <2.7 forward region, Cathode Strip Chambers (CSC) are used to perform the innermost tracking due to their higher rate capability and time resolution. They are multi-wire proportional chambers with cathode planes segmented into strips in orthogonal directions, allowing both coordinates to be measured from the induced charge distribution.

To achieve an excellent resolution the locations of the MDT wires and CST strips along a muon trajectory has to be known better than 30 μm. For this, a high precision optical alignment system monitors the positions and internal deformations of the MDT chambers.

The expected resolution on the transverse momentum p_{T} achieved by the muon spectrometer at a p_{T} of 1 TeV is $\frac{\sigma_{p_T}}{p_T} = 10\%$. Their momentum resolution is expected to be best at around 100 GeV (3%) and goes to 4% at low momenta due to muons

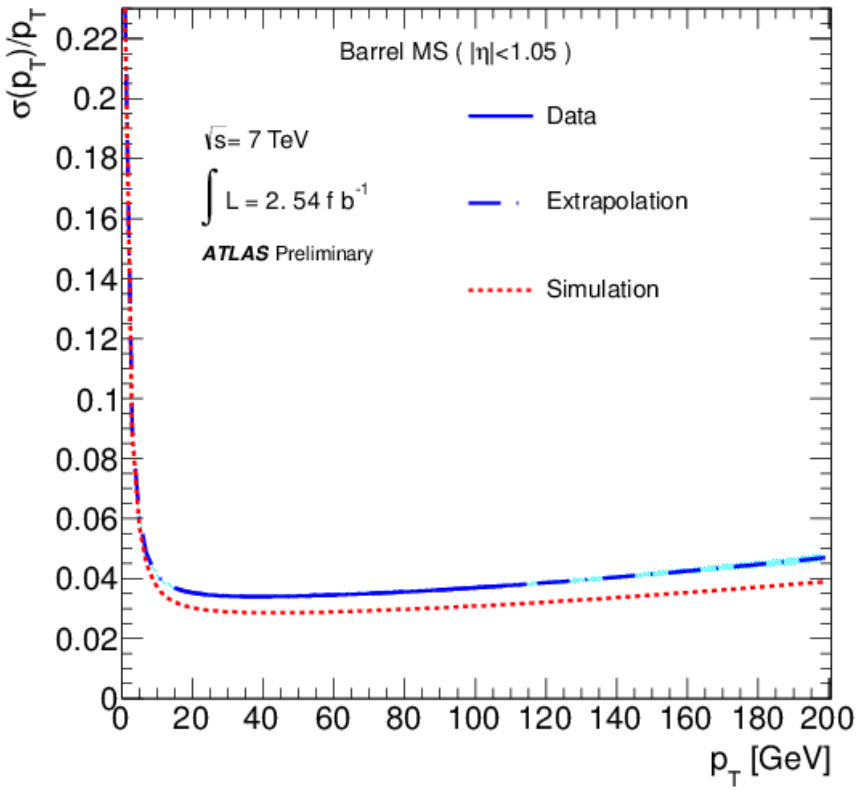

FIGURE 2.15: Resolution curve extracted from MS parameters in collision data and simulation as a function of the muon p_T, for the barrel region. The solid blue line shows determinations based on data, the dashed blue line shows the extrapolation to p_T range not accessible in this analysis and the dashed red line shows the determinations from simulation. The measurement is performed using 2.54 fb^{-1} of 7 TeV data [72].

losing energy in their pass by the calorimeters [73]. Figure 2.15 shows the momentum resolution measured in 2.54 fb^{-1} of 7 TeV data from $Z \to \mu\mu$ decays.

2.2.5 Trigger system

The ATLAS trigger system is divided into the different sub-systems. It has three distinct levels: L1, L2 and the event filter. Each level refines the decisions made by the previous one, applying additional selection criteria.

L1 trigger:

The L1 trigger selects high p_{T} muons, electrons, photons, jets and τ leptons decaying into hadrons. It also triggers for large missing energy. This selection variates with the different sub-systems. Calorimeter selections are based on reduced-granularity information from all the calorimeters. Muons are identified using trigger chambers in the muon spectrometer. Events passing the L1 selection are transferred to the stages of the detector specific electronics to be reconstructed.

In each event selected by the L1 trigger, a Region-of-Interest (RoI) is defined, which consist of geographical coordinates η and ϕ. This information is used later by the high-level triggers.

The L1 trigger is designed to reduce the event rate from 40 MHz to 75 kHz in nominal conditions.

L2 trigger

The L2 trigger uses the RoI information to perform selections using the full granularity and precision available in the detector data. It reduces the trigger rate to approximately 3.5 kHz. If the event passes the L2 selection it is sent to the next trigger level.

Event filter

The event filter (EF) reduces the ever rate to roughly 200 Hz. The selection is very close to offline analysis procedures (performing physics reconstruction close to the offline analyses but looser), processing in a rate of about 4 seconds/events. The output and recording rate at ATLAS for the L1, L2 and EF trigger as a function of the luminosity for a 2012 run are shown in Figure 2.16.

Depending on the triggers that an event has passed, it can be classified in different streams, which are built to separate interest events for different analyses in different datasets (there are muon, electron, jet, minimum bias streams, etc). Then, a trigger chain is built defining the sequence of algorithms and quality selections for a trigger object. The available trigger chains are defined in terms of a trigger menu, that is

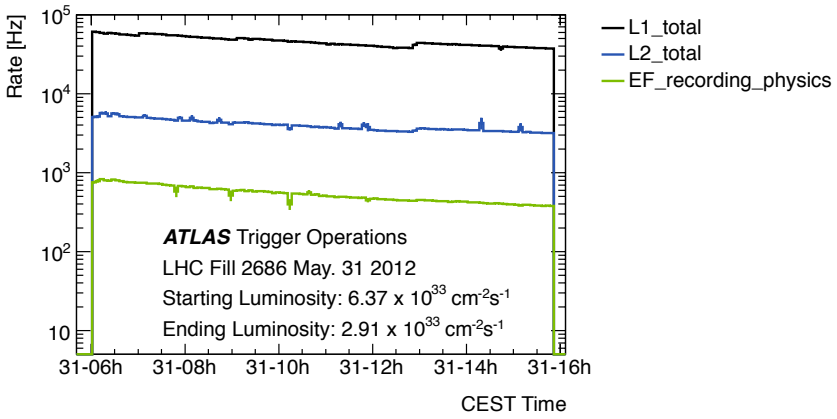

FIGURE 2.16: Output and recording rates at ATLAS for the L1, L2 and EF trigger as a function of the luminosity for a 8 TeV run [76].

defined considering the LHC luminosity and the physics program for the data-taking period.

Events passing a given trigger chain in a trigger menu are arranged in time units called *luminosity blocks* (LB). They correspond typically to a couple of minutes of data tacking. The beam condition, detector status and trigger configuration are stored for each LB, and they can be used in analysis needing time-dependent information as the luminosity calculation. The set of LB between the start and end of a data-taking period is called a *run*. Runs are grouped into *periods* where all runs share the same general detector conditions, machine configuration and trigger menus.

Chapter 3

The ATLAS electromagnetic calorimeter

Contents

As mentioned in the previous chapter, the ATLAS electromagnetic calorimeter consists of sampling detectors where layers of an absorber (a dense material used to degrade the energy of the incident particle, lead in the ATLAS case) and an active medium (in this case Liquid Argon provides the detectable ionisation signal) are alternated. The ionisation signal produced by an electromagnetic shower in the LAr gaps is collected by electrodes located in the middle of the gaps. These electrodes are set at a high voltage, and the absorbers are at ground, creating an electric field that allows the measurement of ionisation current. The electrodes and absorbers are bent into an accordion shape, allowing in this way to have several active layers in depth.

This Chapter is structured in four sections. First, a general overview of the physics of electromagnetic calorimetry is presented in Section 3.1. Then, in Section 3.2, a description of the main characteristics of the ATLAS EMCAL is reviewed, including the energy measurement from the ionisation signal (Section 3.3). Finally, a study on the effect of resistors in the electrodes in the High Voltage system (HV) and its impact on the energy measurement is presented in Section 3.4. The latter corresponds to the only personal contribution presented in this chapter.

3.1 Physics of electromagnetic calorimetry

3.1.1 Electromagnetic showers

Calorimeters are instrumented blocks of material in which particles are fully absorbed and their energy converted to a measurable quantity [77]. A shower of secondary particles with progressively degraded energy is created through the interaction of the incident particle with the material. The energy deposited by these secondary charged particles in the calorimeter is used to measure the incident particle energy.

For energies larger than 10 MeV, electrons mainly lose energy in interaction with matter by emitting radiation (Bremsstrahlung). In this range, electron-positron pairs are produced by the photon interaction with the absorber material. The combination of both processes produces an electromagnetic shower, where a cascade of

particles grows until the electron component falls below a critical energy ε, where the energy is dissipated by collisions with the atoms and molecules of the material causing ionisation and thermal excitations and not by creation of other particles. The quantity ε can be defined in the following way for solid (gases):

$$\varepsilon = \frac{610(710)MeV}{Z + 1.24(0.92)}, \tag{3.1}$$

where Z is the atomic number of the material.

Particles from an electromagnetic shower (electrons and photons) interact with matter through a few well understood QED processes, and can be parametrized with a few simple empirical functions. The main features as longitudinal and lateral sizes of the shower can be described with one parameter that depends on the characteristic of the material: the radiation length X_0, defined as

$$X_0(\mathrm{g/cm^2}) \simeq \frac{716.4\mathrm{g.cm^{-2}A}}{\mathrm{Z(Z+1)\ln(286/\sqrt{Z})}}, \tag{3.2}$$

where A is the atomic weight of the material. The radiation length represents the average distance x that an electron needs to travel in a material in order to reduce its energy to $1/e$ of its initial energy E_0,

$$\langle E(x) \rangle = E_0 e^{-x/X_0}. \tag{3.3}$$

A photon beam with initial intensity I_0, gets its intensity reduced by a factor of $1/e$ after traveling a distance $x = \frac{9}{7}X_0$:

$$\langle I(x) \rangle = I_0 e^{-7x/9X_0}. \tag{3.4}$$

The last two equations show that the physical context of the shower development is common to both electrons and photons, and is independent of the material type if expressed in terms of X_0, allowing to describe the electromagnetic showers as simple functions of X_0. For instance the shower transverse size, integrated over the full depth, is given by the Molière radius, which can be approximated by

$$R_{\mathrm{M}}(\mathrm{g/cm^2}) \simeq 21\mathrm{MeV}\frac{\mathrm{X_0}}{\varepsilon(\mathrm{MeV})}. \tag{3.5}$$

The Molière radius represents the average deflection of electrons at the critical energy ε after traversing one radiation length. An average of 90% of the shower energy is contained in a cylinder of radius 1 R_{M}.

Other characteristics of the shower shapes, such as mean longitudinal profile, shower maximum (the depth at which the largest number of secondary particles is produced), can be also described as functions of X_0 and ε and are further explained in [77].

3.1.2 Energy resolution

The total ionisation signal is proportional to the number of secondary charged particles created in the shower caused by an incident particle. For a given energy of the incident particle, the total number of electron-positron pairs in the shower can fluctuate statistically, therefore the final reconstruction energy is also subject to statistical fluctuations. This leads to the relative standard deviation for the energy to be:

$$\frac{\sigma(E)}{E} \propto \frac{1}{\sqrt{E}}. \tag{3.6}$$

To get a realistic model of a calorimeter, other effects beside the statistical one have to be taken into account (mechanical imprecision, electronic noise, etc). The energy resolution can be written in a more general way as:

$$\frac{\sigma(E)}{E} = \frac{a}{\sqrt{E}} \oplus \frac{b}{E} \oplus c. \tag{3.7}$$

The first right hand term in Eq. 3.7 is called the "stochastic term", the second the "noise term" and the last one is the "constant term". The relative importance of each contribution depends on the energy of incident particle. These contributions are discussed next:

1. The stochastic term accounts for fluctuations related to the development of the electromagnetic shower. In sampling calorimeters as the ATLAS EMCAL, the energy deposited in the active medium fluctuates event by event because the active layers are interleaved with absorber layers. In this case the thickness

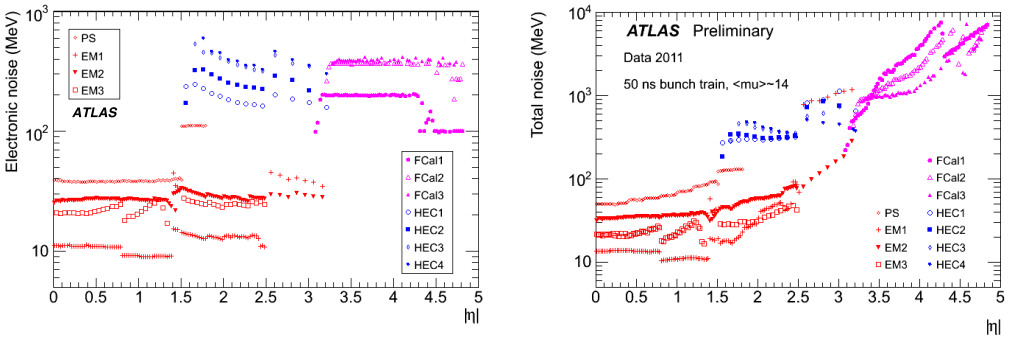

FIGURE 3.1: Electronics (left) and Total noise (electronics plus pile-up, right) as a function of $|\eta|$ for the different sub-systems of the LAr from data [79].

of the layers contributes to the also called "sampling term", which shares the same functional dependence on energy as in 3.6. This term is expected to be 10% in the ATLAS EMCAL. More information can be found in [78].

Another parameter of sampling calorimeters is the sampling fraction, and is given by

$$f_{\text{samp}} = \frac{E^{\text{LAr}}_{\text{mip}}}{E^{\text{LAr}}_{\text{mip}} + E^{\text{Pb}}_{\text{mip}}} \tag{3.8}$$

where E_{LAr} and E_{Pb} indicate the energies deposited by an incident minimum-ionising particle in the active medium (LAr) and in the lead absorber part of the detector respectively.

2. The noise term accounts for noise produced by the electronic readout chain, and pile-up noise. Techniques like optimal filtering are used to minimise the electronic noise in the calorimeter. Given that the contribution goes as $1/E$, the noise term becomes important at low energies but is negligible at higher energies. Figure 3.1, shows the total noise as a function of $|\eta|$ for the different sub-systems of the calorimeter obtained from data. The total noise is in the order on 10-30 MeV. For comparison, electronics noise only from commissioning before collisions is also shown. For $|\eta| > 2.5$, the noise is completely dominated by pileup noise. For $1.5 < |\eta| < 2.5$, the impact of pileup noise on the first and second layer of the EMCAL is also visible, as well as the impact on the pre-sampler for $|\eta| < 1.5$ [79].

3. The constant term refers to contributions that degrade the energy measurement and are independent of the energy of the incoming particle. Contributions to the constant term can be caused by material non-uniformity in gaps

and absorber shapes, imperfections in the mechanical structure and readout system (a consequence of radiation damage, temperature gradients, ageing of the detector), and others.

There are additional contributions to the energy resolution that can cause a smearing in the energy measurement:

- Energy in the EM calorimeter is reconstructed through "cell clusters". Lateral leakage occurs when a fraction of the shower energy is lost outside this cluster. More information about cluster algorithm can be found in [80]), and this topic will be further discussed in Chapter 4.
- The amount of material in front of the calorimeter (inner detector, cryostat, etc) degrades the energy measurement. In ATLAS, the pre-sampler (PS), is located between the ID and the calorimeter and helps estimating the energy lost caused by this material effect.
- The energy measurement is also degraded by showers developing in inactive areas as cracks and dead or transition regions (i.e barrel to end-cap transition).

3.2 Geometry

As stated before, the ATLAS EM calorimeter is a sampling LAr calorimeter where the absorber and active layers are alternated and disposed perpendicular to the direction of incident particles. The absorbers and electrodes are shaped in an accordion geometry, that provides natural full coverage in ϕ and a fast extraction of the signal at the rear or at the front of the electrodes [81] as well as a very uniform performance in terms of linearity and resolution in ϕ. In the barrel, the accordion waves are axial and run in ϕ. In the end-caps, the waves are parallel to the radial direction and run axially. A high voltage is applied to the electrodes, whereas the absorbers are set to ground. The value of this HV is set to 2000 V in the barrel and varies with η in the end-caps (a detailed description of the HV system is presented in Section 3.4). The geometry of electrodes and the HV settings can be seen in Figure 3.2.

The absorbers are made of lead plates with two glued stainless-steel sheets of 0.2 mm thick. The lead plates in the barrel have a thickness of 1.53 mm for $|\eta|$ <0.8 and

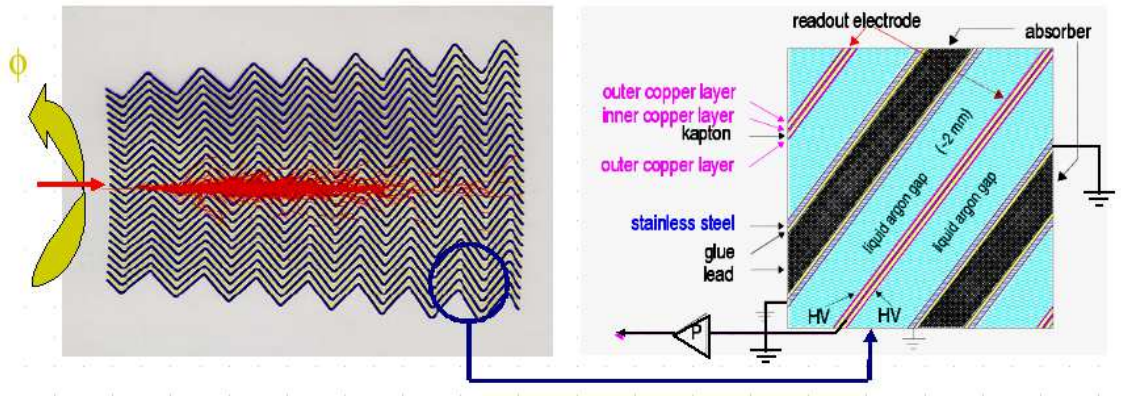

FIGURE 3.2: Schematic view of the electrode/gap structure of the ATLAS EM calorimeter.

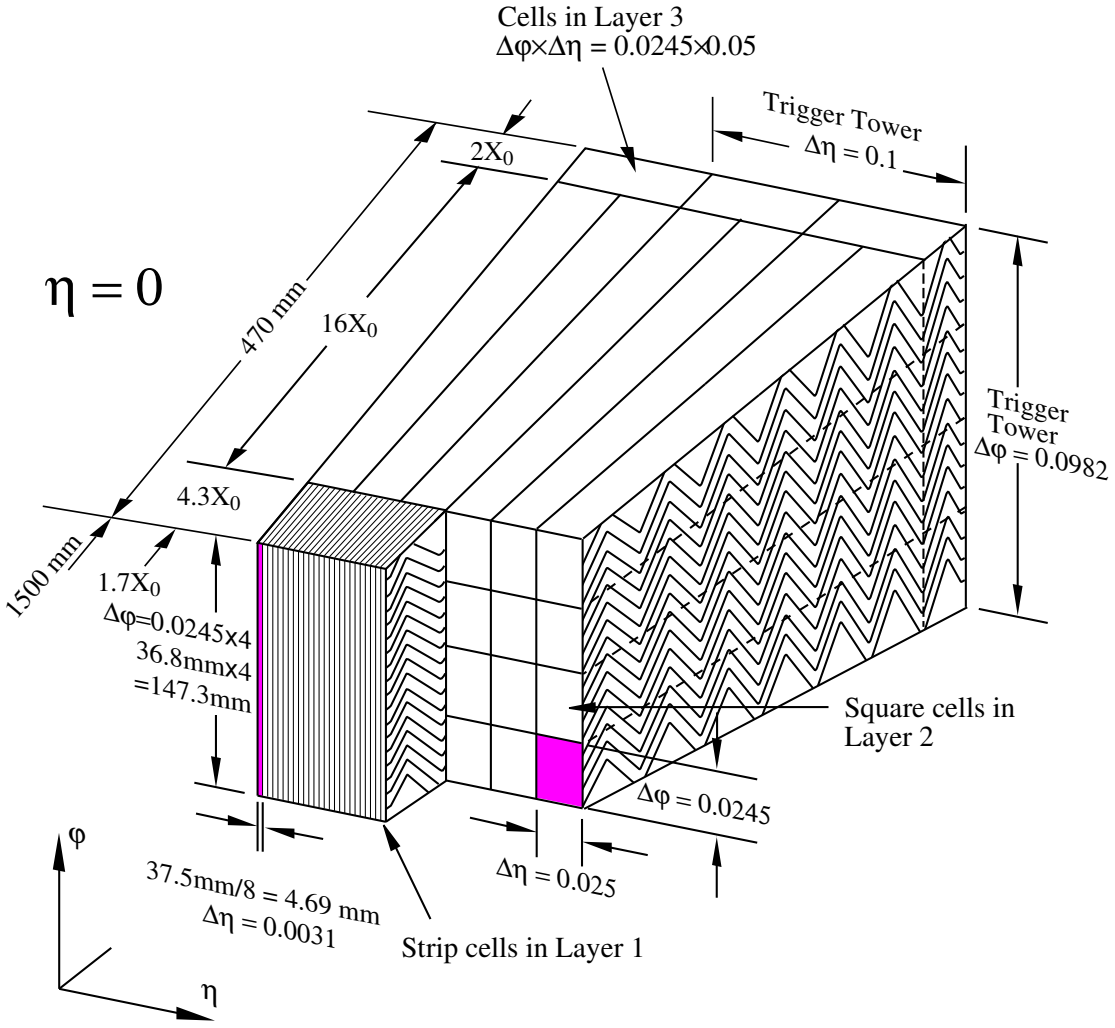

FIGURE 3.3: Sketch of a barrel module where the different layers are clearly visible with the ganging of electrodes in phi. The granularity in η and ϕ of the cells of each of the three layers and of the trigger towers is also shown [60].

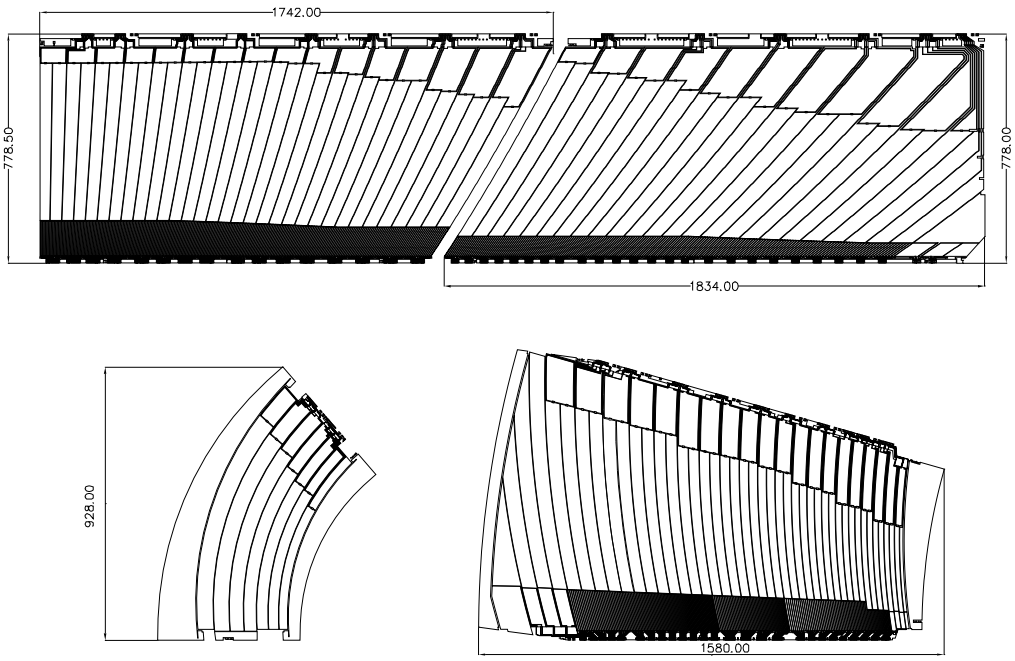

FIGURE 3.4: Layout of the signal layer for the four different types of electrodes before folding. The two top electrodes (types A and B) are for the barrel and the two bottom electrodes are for the end-cap inner (left, type C) and outer (right, type D) wheels. Dimensions are in millimetres. The drawings are all at the same scale. The two or three different layers in depth are clearly visible [60].

1.13 mm for $|\eta| > 0.8$. In the end-caps, the plate thickness are of 1.77 for $|\eta| < 2.5$ and 2.2 mm for $|\eta| > 2.5$.

The electrodes are divided longitudinally in three layers. As shown in Figure 3.3, the first layer is finely segmented along η, the second layer collects the largest fraction of the electromagnetic shower energy, and the third layer collects the tail of the shower and is less segmented in η. In the barrel, the electrodes are split into two, further named types A and B, which have an area of 2 m^2 each. Type A covers the $|\eta| < 0.8$ region, and electrode B $|\eta| > 0.8$. In the end-caps the inner wheel has electrodes type C, and the outer wheel type D.

The readout electrodes located in the gaps between the absorbers consist of three copper layers insulated by two layers of polyimide. The two outer layers are at high voltage potential and the inner one is used for reading out the signal via capacitive coupling [60, 82]. The segmentation of the calorimeter in η and in depth is obtained by different patterns in each electrode layer. The segmentation in ϕ is obtained by grouping together the appropriate number of electrodes.

Barrel

In the barrel EMCAL, two half barrels are centred around the z-axis with a 3.2 m length each. The barrel is complemented with the LAr PS, placed in front of its inner surface. Each half barrel is made of 1024 accordion shaped absorbers and electrodes with the characteristics described above, and is divided in 16 modules. The total thickness of a module is at least 22 radiation lengths (X_0).

The PS provides shower sampling in front of the active EM calorimeter and inside the barrel cryostat. It is made of 64 identical azimuthal sectors (32 in each half barrel). It is composed of eight modules of different size with a length increasing with η.

End-Caps

The EMEC calorimeters are two wheels, each in one side of the EMB. In the transition region between the barrel and end-caps, the amount of material in front of the calorimeter is of several X_0. Due to this effect and in order to improve the energy measurement in this region, the LAr pre-sampler is implemented in front of the calorimeter covering the range between $1.5 < |\eta| < 1.8$.

Each end-cap wheel consists of two co-axial wheels, which are further divided into eight wedge-shaped modules. Each end-cap contains 768 absorbers interleaved with readout electrodes in the outer wheel, and 256 absorbers in the inner wheel with the same configuration.

The number of interaction lengths X_0 in front and in the EM calorimeter is shown in Figure 3.5.

3.3 Ionisation signal and energy reconstruction

The LAr signal is generated by ionisation electrons drifting in the LAr gap under the electrical field created by the high voltage between electrodes and absorbers, and is collected in the electrodes. The ionisation current has a triangular shape, and its peak is proportional to the energy released in the LAr:

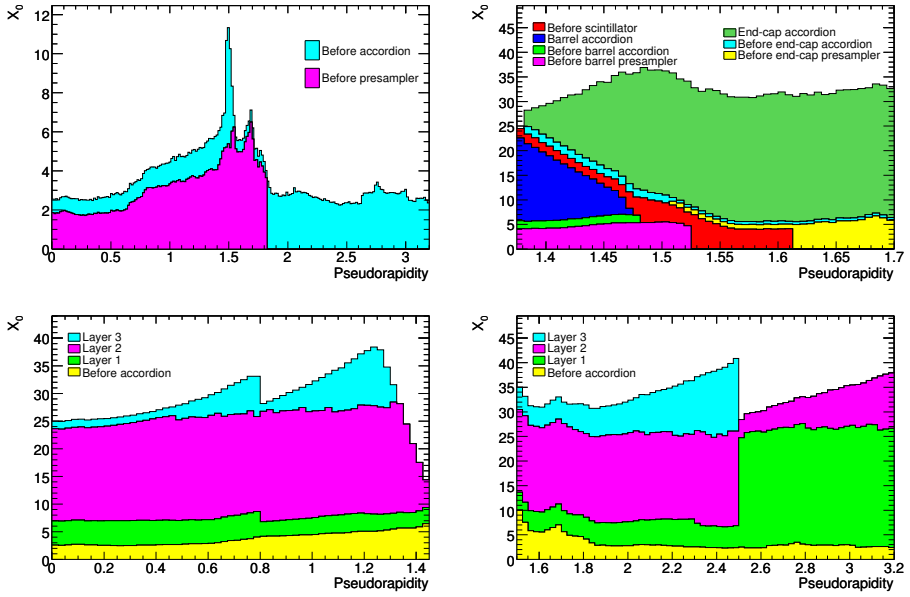

FIGURE 3.5: Cumulative amounts of material, in units of radiation length X_0 and as a function of $|\eta|$, in front of and in the electromagnetic calorimeters. The top left-hand plot shows separately the total amount of material in front of the pre-sampler layer and in front of the accordion itself over the full η-coverage. The top right-hand plot shows the details of the crack region between the barrel and end-cap cryostats, both in terms of material in front of the active layers (including the crack scintillator) and of the total thickness of the active calorimeter. The two bottom figures show, in contrast, separately for the barrel (left) and end-cap (right), the thicknesses of each accordion layer as well as the amount of material in front of the accordion. [60].

$$I(t) = \frac{Q_0}{t_\mathrm{d}} \left(1 - \frac{t}{t_\mathrm{d}}\right) , \quad \text{for } 0 \leq t \leq t_\mathrm{d} , \tag{3.9}$$

where t_d is the average time of electrons in the LAr (about 450 ns) and Q_0 is the total charge deposited in the LAr at t=0. This signal is transmitted by an electronic card in the *Front End Board* (FEB) detailed in Figure 3.6.

Passing through the FEB's, the triangular signal is pre-amplified to obtain a signal superior to the electronic noise level and is shaped with a bipolar filter $CR - RC^2$. The triangular input current pulse from the detector and the shaped output pulse from the FEB in the case of a barrel EMCAL cell are shown in Figure 3.7.

The shaped signals are sampled at the LHC bunch crossing frequency (nominal of 25 ns) and usually 5 samples are digitalised by an *Analog-to-Digital Converter* (ADC) and used for the signal reconstruction.

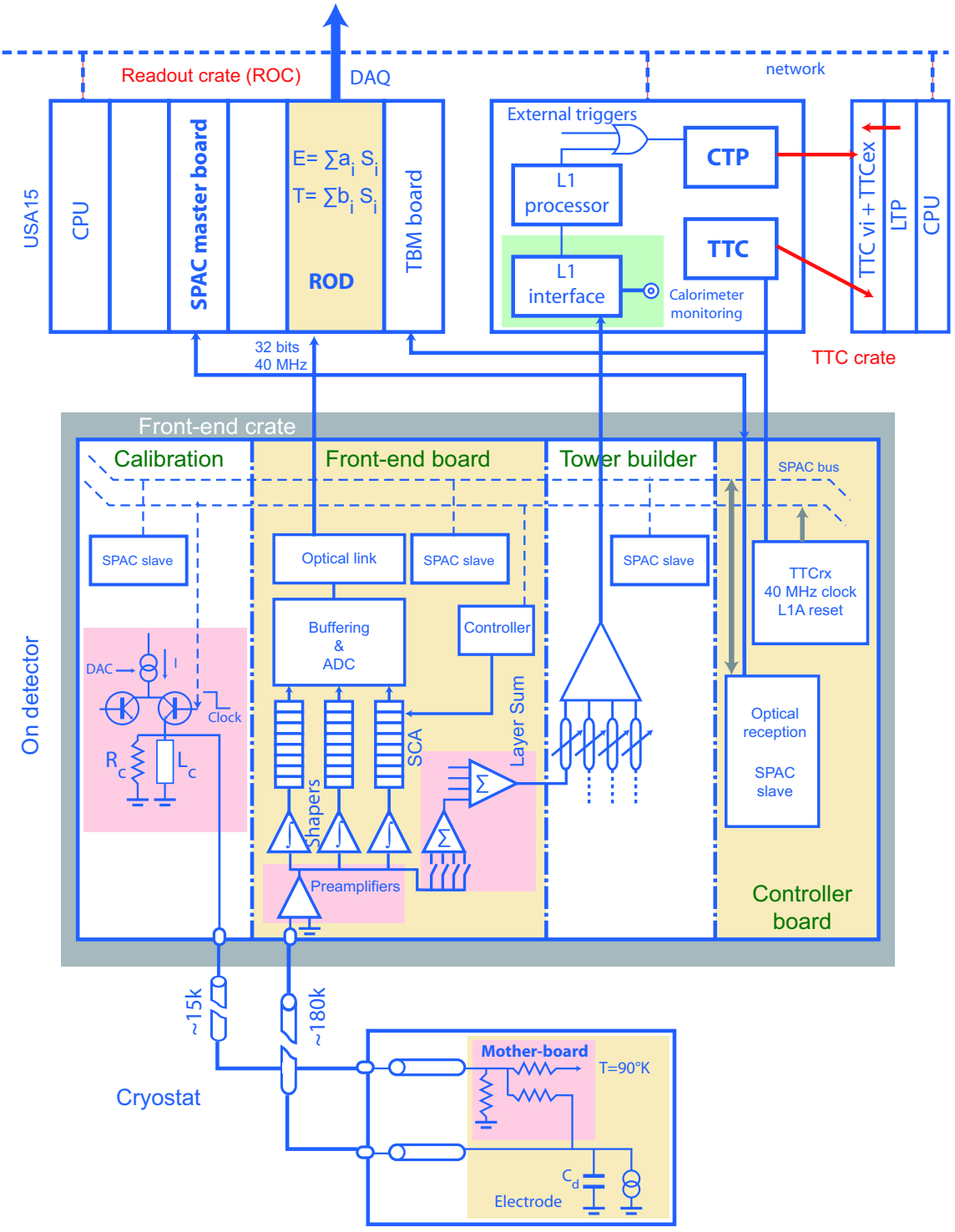

FIGURE 3.6: Block diagram of the LAr readout electronics [60].

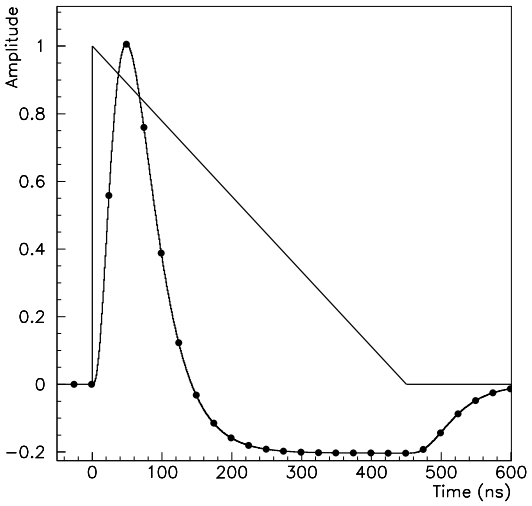

FIGURE 3.7: Amplitude versus time for a triangular pulse of the current in a LAr barrel electromagnetic cell and of the FEB output signal after bi-polar shaping. Also indicated are the sampling points every 25ns [60].

In order to meet the large dynamic range requirements for the expected physics signals, for each channel the signal is split into three overlapping linear gain scales (*low, medium and high*) on the ratio of 1/9/93. Low gain is used for high energies from 400 GeV to 4 TeV, the medium is for energies between 40 and 400 GeV and the high gain for low energies up to 40 GeV.

The energy is computed in the readout drivers (ROD's), that are responsible for receiving, digitally processing and formatting the data coming from the FEB's, and are located in the ATLAS counting room. The ROD's also perform various data-integrity checks and higher-level monitoring tasks. Only for a restricted number of channels (above the energy threshold), the 5 samples are transmitted, in addition to the energy, time and quality.

From these samples two important quantities are deduced, using the Optimal Filtering Technique. One is the signal maximum amplitude ($A_{\max}$) which is proportional to the energy deposited in the cell, and the other is the time shift (Δt) of the signal maximum amplitude with respect to a reference value. The are defined as:

$$A_{\max} = \sum_{j=1}^{N_{\text{samples}}} a_j(s_j - p), \tag{3.10}$$

$$\Delta t = \frac{\sum_{j=1}^{N_{\text{samples}}} b_j(s_j - p)}{A_{\text{max}}}, \tag{3.11}$$

where p is the pedestal value of the corresponding read-out channel, and a_{j} and b_{j} are the Optimal Filtering Coefficients (OFC), and are determined to minimise the dispersion in A_{max} and τ coming from electronics and pile-up noise. More information on the Optimal Filtering Technique can be found in [83].

In order to reconstruct the cell energy from the amplitude A_{max}, several steps have to be followed. They can be explained with the following formula:

$$E_{\text{reco}} = F_{\mu A \to \text{MeV}}.F_{DAC \to \mu A}.\frac{1}{M_{\text{phys}}/M_{\text{cali}}}R.A_{\text{max}}, \tag{3.12}$$

where $F_{\mu\text{A}\to\text{MeV}}$ and $F_{\text{DAC}\to\mu\text{A}}$ are two conversion factors:

- $F_{\mu\text{A}\to\text{MeV}}$ is the conversion factor between the current collected by the readout electrode and the energy deposited in the LAr. Some factors can affect it, as the temperature, variation of the HV, pollution, etc.
- $F_{\text{DAC}\to\mu\text{A}}$ takes into account calibration board specifics. The R factor converts to the DAC settings (*Digital-to-Analog Converter*) of the board, and is determined on a calibration pulse instead of a ionisation pulse.

The energy is corrected by a factor $\left(\frac{1}{M_{\text{phys}}/M_{\text{cali}}}\right)$ accounting for the difference between responses of a calibration and ionisation signal corresponding to the same input current. All the constants in the last equation except from the $F_{\mu\text{A}\to\text{MeV}}$, are determined by calibration runs, on a cell by cell basis [84].

3.4 HV energy corrections due to electrode resistors in the EM calorimeter

As described in Section 3.3, the LAr HV system is designed to feed the EMCAL gaps with an electric field that induces the drift of ionisation electrons activated by charged particles traversing the calorimeter. The energy measurement is performed through this drift ionisation current.

For redundancy, the two sides of the calorimeter electrodes are fed by independent HV lines. In this way, if one side of an electrode is not powered, half of the signal is still collected.

The increase of signal with HV is mainly due to the variation of drift velocity, as shown in Figure 3.8. The dependence is moderate: for example, 77% of the signal is collected when decreasing the HV to half of its nominal value [60].

3.4.1 High voltage distribution

Due to the gap size variation across the calorimeter, the HV should be varied accordingly in a continuous way to keep the detector response independent of η. In reality the HV is set by steps in η sectors:

- In the EMB, the accordion-shaped electrodes are set along the radial direction. Each electrode side of a sector is supplied by a HV line. Each sector is $\Delta\eta \times \Delta\phi$=0.2 $\times$ 0.2, with a total of 32 electrodes in ϕ. A voltage of +2000 V is applied in the entire barrel.
- In the EMEC the electrodes are set in a radial arrangement like a bicycle wheel. Each side of all the electrodes in a constant sector of $\Delta\phi$=0.2 and a varying region of $\Delta\eta$ form 0.1 to 0.4, are fed by a HV line (see Figure 3.9).

3.4.2 High Voltage corrections

In order to obtain an optimal measurement of energy, corrections due to the HV settings are applied. These corrections are divided in two categories:

3.4.2.1 η-dependent corrections

For ease of construction, the HV in the end-caps is set by steps, leaving a residual η-dependence of the response that has to be corrected for. This correction is performed by weighting the energy of each cell depending on its η position and its HV sector (l), by:

$$E^{\text{cell}}_{\text{HV}-\text{corr}}(\eta, l) = E^{\text{cell}}.\frac{\beta^l}{1+\alpha^l.(\eta-\eta^l_{\text{center}})}, \tag{3.13}$$

where η^l_{centre} is the η-value at the centre of the HV sector l. The coefficients α^l and β^l are HV correction parameters and are estimated by fitting inside each HV sector a linear dependence of the energy with η. The estimation of this correction was performed with test beam and Monte Carlo data, and is explained in detail in [85].

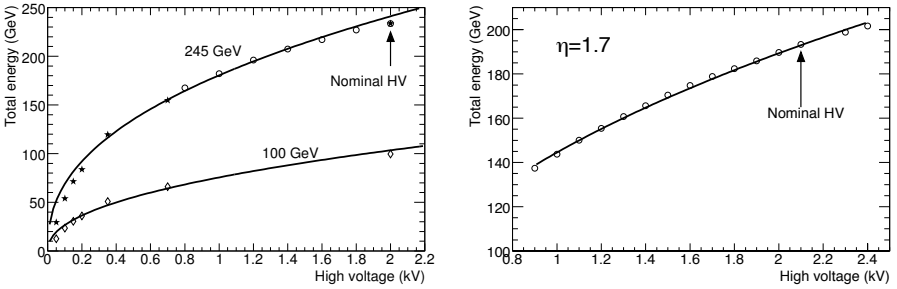

FIGURE 3.8: The measured electromagnetic cluster energy as a function of the applied high voltage. The results obtained with a barrel module (left), are shown for 245 GeV electrons (open circles), 100 GeV electrons (open diamonds) and for the 100 GeV results at the nominal voltage of 2 kV scaled to the corresponding result at 245 GeV (stars). The results obtained with an end-cap module (right) are shown for 193 GeV electrons. The curves correspond to fits with a functional form $E_{\text{tot}} = a \times V^b$ [60].

3.4.2.2 Corrections for reduced or missing HV

As shown in Figure 3.8, the energy measurement can be affected by a non nominal HV value, so corrections should be applied when one or more HV lines are off or

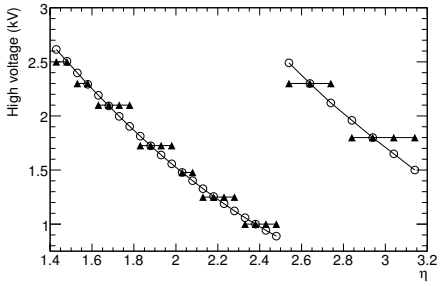

FIGURE 3.9: HV distribution as a function of $|\eta|$ for the EMEC. A uniform calorimeter response requires a HV which varies continuously as a function of $|\eta|$, as shown by the open circles. This has been approximated by a set of discrete values shown as full triangles [60].

at a lower voltage. Test beam measurements have shown that the measured energy is proportional to V^b (where b is equal to 0.38 in the barrel and 0.39 in the end-caps [85]). Therefore, when the two HV sides of an electrode group is reduced by the same amount, the corrected energy for this group would be [86]:

$$E_{\text{corr}} = E_{\text{meas}}.\left(\frac{V_{\text{nom}}}{V_{\text{op}}}\right)^b. \tag{3.14}$$

In the more general case when the two HV lines feeding an electrode are at two different operative voltages V_{op1} and V_{op2}, the correction to the energy would become:

$$C = \frac{E_{\text{corr}}}{E_{\text{meas}}} = \frac{2}{\left(\frac{V_{\text{op1}}}{V_{\text{nom}}}\right)^b + \left(\frac{V_{\text{op2}}}{V_{\text{nom}}}\right)^b}. \tag{3.15}$$

Currently, the corrections are defined by Eq. 3.15, which only assumes that the operational voltage is the one measured in the HV power supply. Now, the resistors in the electrodes can also affect the voltage by a voltage drop. A simulation-based study performed in 2004 [82] found a 0.3% voltage drop caused by resistors in the electrodes and currents coming from minimum bias events at the designed luminosity of $1 \times 10^{34}\text{cm}^{-2}\text{s}^{-1}$.

In this Section, the real effect of resistors in the feedthroughs and the electrodes is studied, by using the measured return currents (currents read from the HV line) and HV operation values from the HV system in data taking periods.

From Eq. 3.15, including the return currents (I) and effective resistances (ER) of the HV line (R) the correction becomes:

$$C' = \frac{E_{\text{corr}}}{E_{\text{meas}}} = \frac{2}{\left(\frac{V_{\text{op1}} - I_1 R_1}{V_{\text{nom}}}\right)^b + \left(\frac{V_{\text{op2}} - I_2 R_2}{V_{\text{nom}}}\right)^b}. \tag{3.16}$$

The voltage drop due to the resistors in a HV line "i" is evaluated as:

$$V_{\text{drop}_\text{i}} = \frac{I_\text{i} R_\text{i}}{V_{\text{op}_\text{i}}}. \tag{3.17}$$

Taking into account the effect of the resistances, the relative change in the correction is the following :

$$\frac{\Delta C}{C} = \frac{C' - C}{C}. \tag{3.18}$$

From Equations 3.15 and 3.16, the corrected energy becomes:

$$E'_{\text{corr}} = E_{\text{corr}} \left(1 + \frac{\Delta C}{C}\right). \tag{3.19}$$

The effect of resistors on the corrections is evaluated for all HV lines, even is their nominal correction is equal to 1 (the relative change is measured).

3.4.3 Resistance Model

The effective resistance R_{i} affecting a HV line i, has three contributions: the resistors in the feedthroughs, the HV wire resistance and the electrode resistance.

3.4.3.1 The resistors in the feedthroughs and HV wire

The warm HV lines are transferred to the liquid argon cryostats by the HV feedthroughs. The HV wire passes by an RC filter before being finally distributed to the calorimeter electrodes. Taking into account the currents (in the order of a few μA) and the value of the resistors (100 kΩ) the voltage drop is expected to be in the order of mV [86].The 130 m long HV wire has a 147 Ohm/km resistance per length. The voltage drop due to this is thus negligible.

3.4.3.2 The resistors in the electrode barrel

For simplicity, discrete detector-oriented coordinates ($i\eta$ and $i\phi$) are used. They are distributed along the calorimeter as shown in Table 3.1.

TABLE 3.1: Detector-oriented coordinates $i\eta$ and $i\phi$ in the barrel and their range in each region of the electrode.

	Pre-Sampler	Front	Middle	Back
$i\eta$	$0< i\eta <60$	$0< i\eta <447$	$0< i\eta <55$	$0< i\eta <26$
$i\phi$	$0< i\phi <63$	$0< i\phi <63$	$0< i\phi < 255$	$0< i\phi < 255$

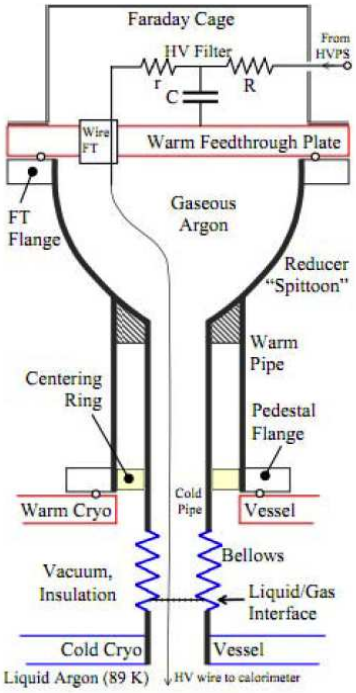

FIGURE 3.10: Schematic of a HV feedthrough. The value of the resistor r is 1 kΩ and R is approximately 100 kΩ [86].

Granularity in $i\eta$ and $i\phi$

The back and middle sampling pads to the HV bus on the back side of the electrodes are connected by series of HV resistors. On each side of the electrodes with η <0.8 (electrode A), 16 pairs of HV resistors are connected to 16 HV lines.

In each of the wheels (A and C), 16 modules containing 64 electrodes are arranged radially. The $i\phi$ coordinate for the HV lines is varied from 0 to 255 in the back layer. Due to the $i\phi$ granularity, one HV line is connected to 4 different electrodes located in the same $i\eta$ region.

3.4.3.3 Resistors value from the EM database

The values of electrode resistance are obtained from the EM database for the set of barrel electrodes with η <0.8. In a simplified model [87], it is assumed that the back layer dominates the total effective resistance (Figure 3.11). Resistance measurements were taken in 2001 after bending the electrodes, at room temperature, before being immersed in liquid argon. In order to estimate the values of the resistances after cooling down, several readings were performed. The results are documented in [82]

FIGURE 3.11: Pair of high-voltage distribution resistors (upper) connecting the HV bus to the back sampling or directly to the middle cells by narrow copper traces. Both pictures are from a bent B electrode but representative of all other types [82].

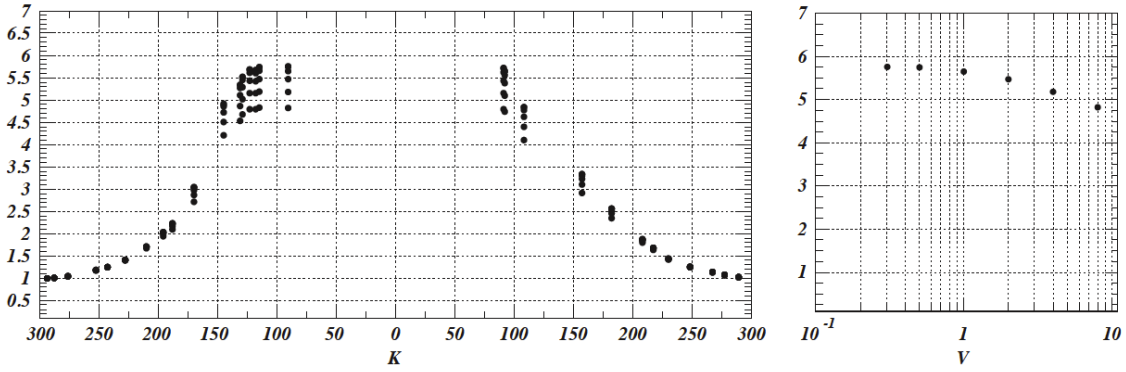

FIGURE 3.12: Left: evolution of the resistance between ambient and LAr temperatures. The measurements were performed while cooling down and warming up again and are normalised at room temperature. Right: ratio R(T=90 K)/R(T=300 K) and its dependence on the voltage used to measure it [82].

and represented in Figure 3.12. The database resistance values are corrected by a warm-to-cold global factor of 5.1, for the final HV correction.

3.4.3.4 Calculating the effective resistance for a HV line

Each resistance in the electrode corresponds to an $i\eta$ bin. For each bin, four electrodes build an $i\phi$ bin connected in parallel. For a HV line located in i$\eta = l$ and i$\phi = m$, its corresponding effective resistance is:

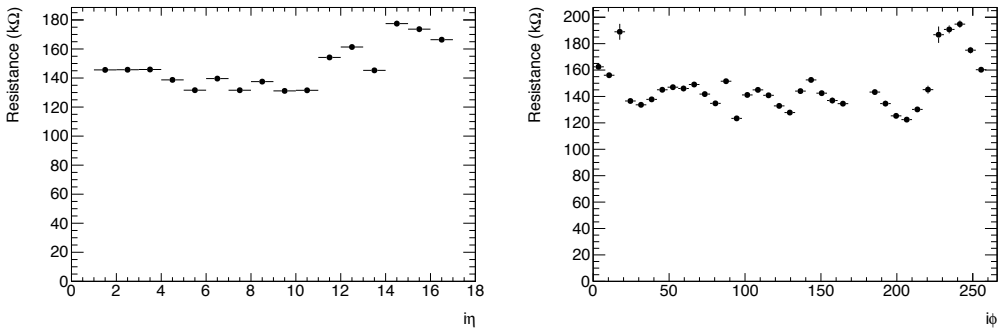

FIGURE 3.13: Left: Profile of resistance for each electrode A as a function of its $i\eta$ coordinate. Right: Profile of resistance for the electrode A as a function of its $i\phi$ coordinate. These values are obtained assuming that the resistance in the back of the electrode dominate the resistance measurement.

$$R_{\text{eff}}(l,m) = \frac{1}{\sum_{N_{\text{electrode}}=4m}^{4m+3} 1/R(i\eta = l, N_{\text{electrode}})} \tag{3.20}$$

where $N_{\text{electrode}}$ stands for electrode number. The effective resistance per HV line and as a function of its coordinates are in Figures 3.13 and 3.14.

For simplicity, a constant probe value of the resistance is used for the HV correction analysis:

$R_{\text{eff}} = 150$ kΩ

In the barrel $0.8 < |\eta| < 1.4$ region (Electrode B), the resistance values from the electrodes were not found in the database. As a consequence, the same probe value obtained for the $0 < |\eta| < 0.8$ region is used.

3.4.3.5 The resistors in the End-Cap electrodes

Similarly to the electrode B in the barrel, the End-Cap resistance values in the database are not found. Therefore, a different resistance model is used [88]. In this model, the effective resistance of a HV line is calculated taking into account all resistances in every layer of the electrodes. The values of each resistance are based on measurements performed during the electrode assembling, and the results vary with $|\eta|$. The final probe values of the ER in the End-Cap are shown in Table 3.2.

In summary:

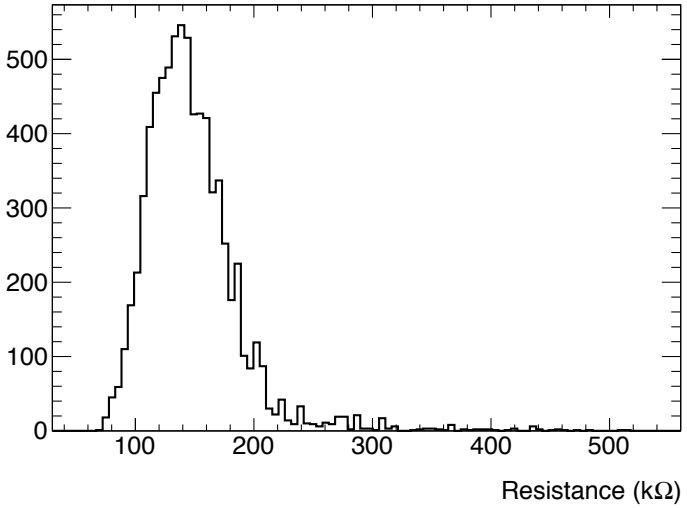

FIGURE 3.14: The distribution of effective resistances, integrated over $i\phi$ and $i\eta$, for electrodes type A.

TABLE 3.2: The effective resistances of HV line, for the nine $|\eta|$ regions in the End-Cap.

η Region	R_{eff} (kΩ)
1.375< $|\eta|$ <1.5	700
1.5< $|\eta|$ <1.6	1700
1.6< $|\eta|$ <1.8	600
1.8< $|\eta|$ <2.0	500
2.0< $|\eta|$ <2.1	1100
2.1< $|\eta|$ <2.3	600
2.3< $|\eta|$ <2.5	1100
2.5< $|\eta|$ <2.8	600
2.8< $|\eta|$ <3.2	500

- For the barrel, a simplified model is used, assuming that the back layer resistance dominates the total ER. Resistance values are obtained from the EM database for the electrodes A, and a probe value of ER is chosen for the analysis (150 kΩ) in the whole barrel. In Section 3.4.7, the sensitivity to the actual value of the resistance is studied, and shown to be small.

- For the end-caps, a different model is used. All resistances in the electrode are used for the ER calculation. Table 3.2 indicates the ER values for nine different η regions.

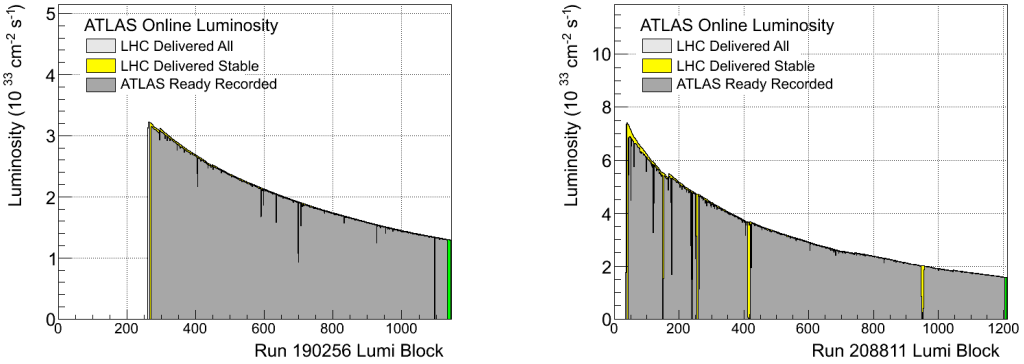

FIGURE 3.15: Instantaneous luminosity for chosen run in 2011 (left) and 2012 (right).These runs were selected because they span larger values of instantaneous luminosities.

3.4.4 Detector information: Return currents and Operational voltage

The return currents, operational voltage and instantaneous luminosity are read from the COOL database [89]. The mapping for HV lines to detector regions is done using the LArTranslator database. To test the corrections C and C' (nominal and modified by the resistor effect), two long runs in 2011 (run 190256) and 2012 (run 208811) were used to map detector information (return currents and operational voltage) from high to low instantaneous luminosity (Figure 3.15). These runs were selected because they span large values of instantaneous luminosities. The voltage drop and HV corrections are evaluated in separate detector regions: barrel and the 9 end-cap regions quoted in Section 3.4.3.5.

The nominal voltage varying in the detector region is summarised in Table 3.3 .

3.4.5 HV corrections due to the electrode resistance in the Barrel

In order to evaluate the change in the HV correction, and after introducing the resistance element in the calculation, the return currents for several different lumi-blocks were used as an input. The distribution of currents scales with the luminosity, and the spread increases as can be seen in Figures 3.16 and 3.17. The distribution of the operational voltage remains unchanged during the whole run. Figures 3.18 show the mean values of current for all cells and 3.19 the voltage drop (from Equation 3.17),

TABLE 3.3: Operational Voltage for 10 η regions in the EMCAL.

η Region	V_{op} (V)
$0< \lvert\eta\rvert <1.475$	2000
$1.375< \lvert\eta\rvert <1.5$	2500
$1.5< \lvert\eta\rvert <1.6$	2300
$1.6< \lvert\eta\rvert <1.8$	2100
$1.8< \lvert\eta\rvert <2.0$	1700
$2.0< \lvert\eta\rvert <2.1$	1400
$2.1< \lvert\eta\rvert <2.3$	1250
$2.3< \lvert\eta\rvert <2.5$	1000
$2.5< \lvert\eta\rvert <2.8$	2300
$2.8< \lvert\eta\rvert <3.2$	1800

as functions of the luminosity for the quoted runs in 2011 and 2012. The currents show a linear dependence with luminosity, growing by a ~ 1.5 factor from the lowest and highest luminosity in 2011, and almost by a ~ 4 factor in 2012 (current slopes in both years are compatible). The 2012 run presents a unexplained "glitch" of current readout at a single high luminosity lumi block. This feature is not likely to be a frequent event, as currents in the barrel where checked for a few other 2012 runs, none reproducing the "glitch" effect.

For the 2012 peak luminosity, the highest voltage drop due to the resistances is 0.04%. The relative change in the corrections in Eq. 3.18 is evaluated as a function of the luminosity (Figure 3.20). Due to the linear dependence of currents with luminosity, the relative change in corrections follow the same linear behaviour, but the effect is small (a 0.02% increase in the correction, at the highest luminosity point in 2012). In order to extrapolate the effect of the resistance in the corrections to high luminosities, a linear fit is performed to the profile. Extrapolating to a $1 \times 10^{34} cm^{-1} s^{-1}$ luminosity, the increase in the corrections would be:

$$\frac{\Delta C}{C} = 0.029\% \text{ (from 2012 fit result)},$$
$$\frac{\Delta C}{C} = 0.027\% \text{ (from 2011 fit result)}.$$

with a typical error of $\pm 0.001\%$ arising from the dispersion in the currents included in the profile.

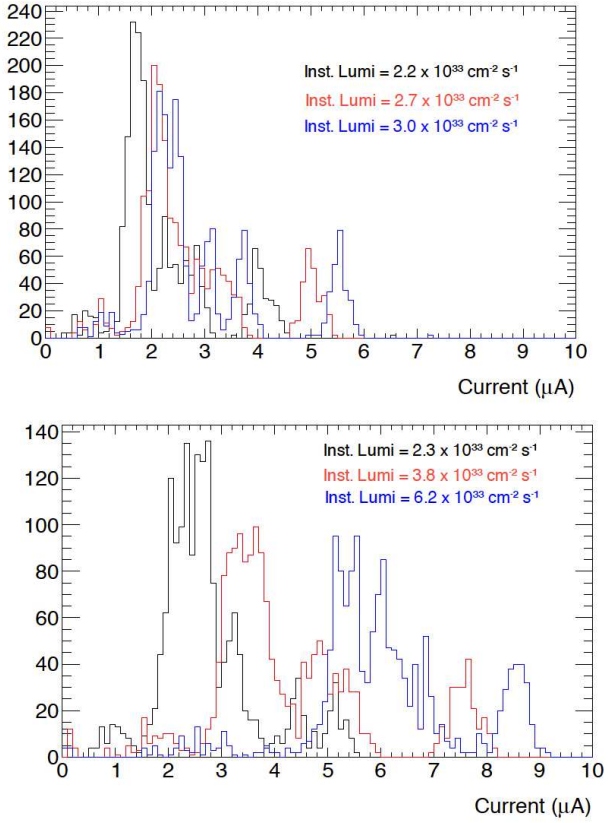

FIGURE 3.16: Distribution of the return currents for three values of instantaneous luminosity for 2011 (top) and 2012 (bottom)

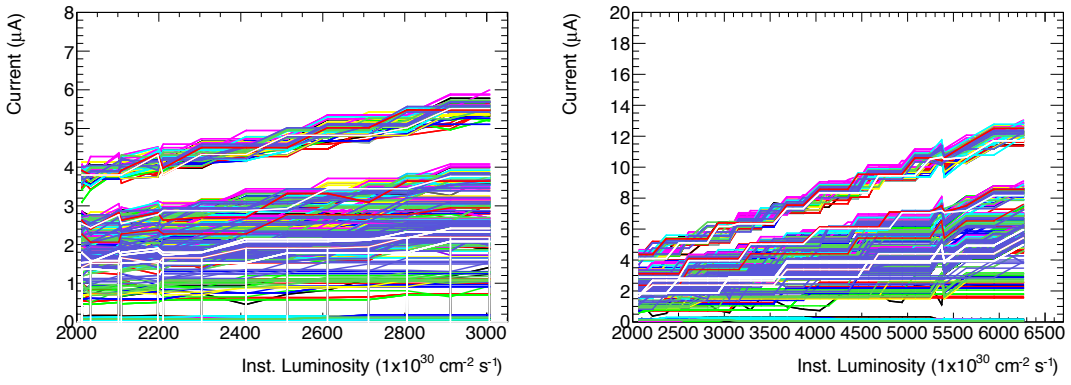

FIGURE 3.17: Return currents of every HV line in the barrel as a function of instantaneous luminosity for 2011 (left) and 2012 (right). Each line represents the evolution of the return current in a HV line with the luminosity.

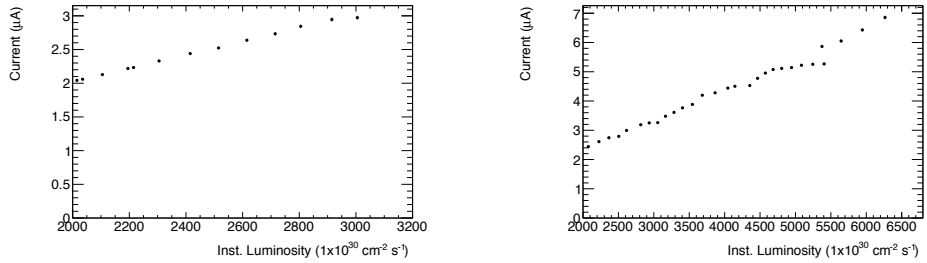

FIGURE 3.18: The mean value of the return current of the totality of HV lines, as a function of instantaneous luminosity for 2011 (left) and 2012 (right).

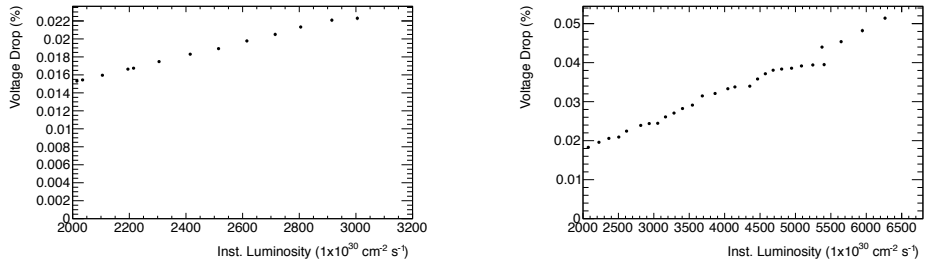

FIGURE 3.19: The mean value of voltage drop, as a function of instantaneous luminosity for 2011 (left) and 2012 (right).

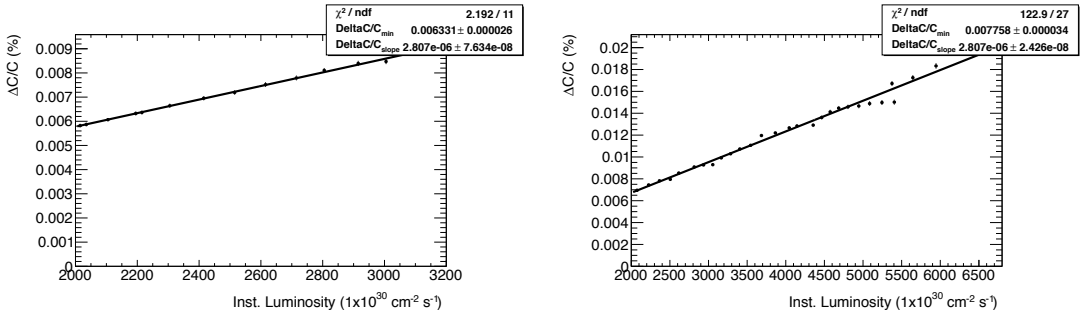

FIGURE 3.20: Mean value of the relative change of HV corrections as a function of instantaneous luminosity for 2011 (left) and 2012 (right).

3.4.6 HV corrections due to the electrode resistance in the End-Cap

In the end-caps the HV system is different from the barrel. The HV nominal values and the resistance model vary with η. The voltage drop for the maximal 2012 luminosity, and the extrapolation to $1 \times 10^{34} cm^{-1} s^{-1}$ of the relative change in the corrections for each region in η are presented in Figures 3.21, 3.22 and summarised in Table 3.4.

The extrapolated results are in most cases one order of magnitude larger than in the barrel, with the extreme example in the $2.3 < |\eta| < 2.5$ region, where the relative difference in the corrections gets to a maximum value of 1.2% and the voltage drop at the highest point in 2012 is 19.0 V. There are a couple of factors that dominate the end-cap result: the resistance model used in the calculation is up to one order of magnitude larger than in the barrel (see Table 3.2), and the currents values increase at forward regions of $|\eta|$.

η region	$\frac{\Delta C}{C}$ (%) at $1 \times 10^{34} cm^{-1} s^{-1}$
1.375< $\|\eta\|$ <1.5	0.04
1.5< $\|\eta\|$ <1.6	0.15
1.6< $\|\eta\|$ <1.8	0.15
1.8< $\|\eta\|$ <2.0	0.32
2.0< $\|\eta\|$ <2.1	0.43
2.1< $\|\eta\|$ <2.3	0.58
2.3< $\|\eta\|$ <2.5	1.21
2.5< $\|\eta\|$ <2.8	0.40
2.8< $\|\eta\|$ <3.2	0.72

TABLE 3.4: Relative change in the HV corrections for various end-cap regions in 2012.

3.4.7 Sensitivity to the hypothesis used on the resistance models

The new corrections and voltage drops are calculated with two different resistance hypothesis for the barrel and End-Caps. In the barrel, the hypothesis that the ER of the HV line is 150 kΩ, is obtained assuming that the back resistance in the electrode dominates the total ER. In the end-caps, the hypothesis takes into account all the resistances in the electrode to calculate the ER. These two approaches provide different final results: The End-Cap ER can be roughly from 3 to 11 times larger than the ones on the barrel. Considering that there is no easy way to directly measure the ER [87], a study of sensitivity of the final corrections to the resistance model is performed.

The sensitivity of the correction to the resistance, while expected to be small, can be tested by defining a modified correction:

$$C'(\varepsilon) = \frac{2}{\left(\frac{V_{\text{op1}} - I_1 R_1 (1+\varepsilon)}{V_{\text{nom}}}\right)^b + \left(\frac{V_{\text{op2}} - I_2 R_2 (1+\varepsilon)}{V_{\text{nom}}}\right)^b}, \tag{3.21}$$

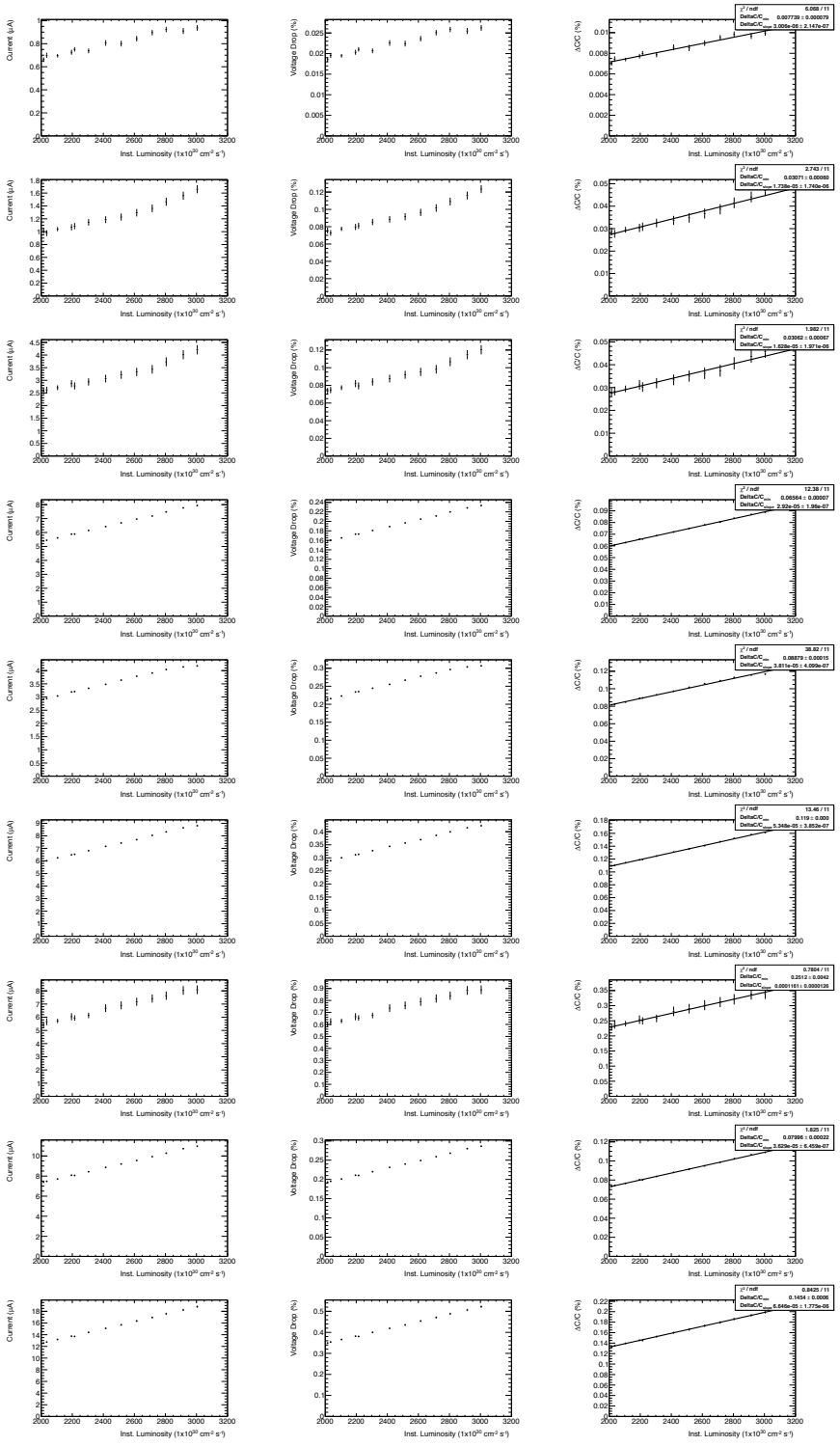

FIGURE 3.21: Currents (first column), Voltage drop (second column) and Relative change of the HV correction (third) as a function of the luminosity, for the 9 End-Cap η regions (9 rows) in 2011.

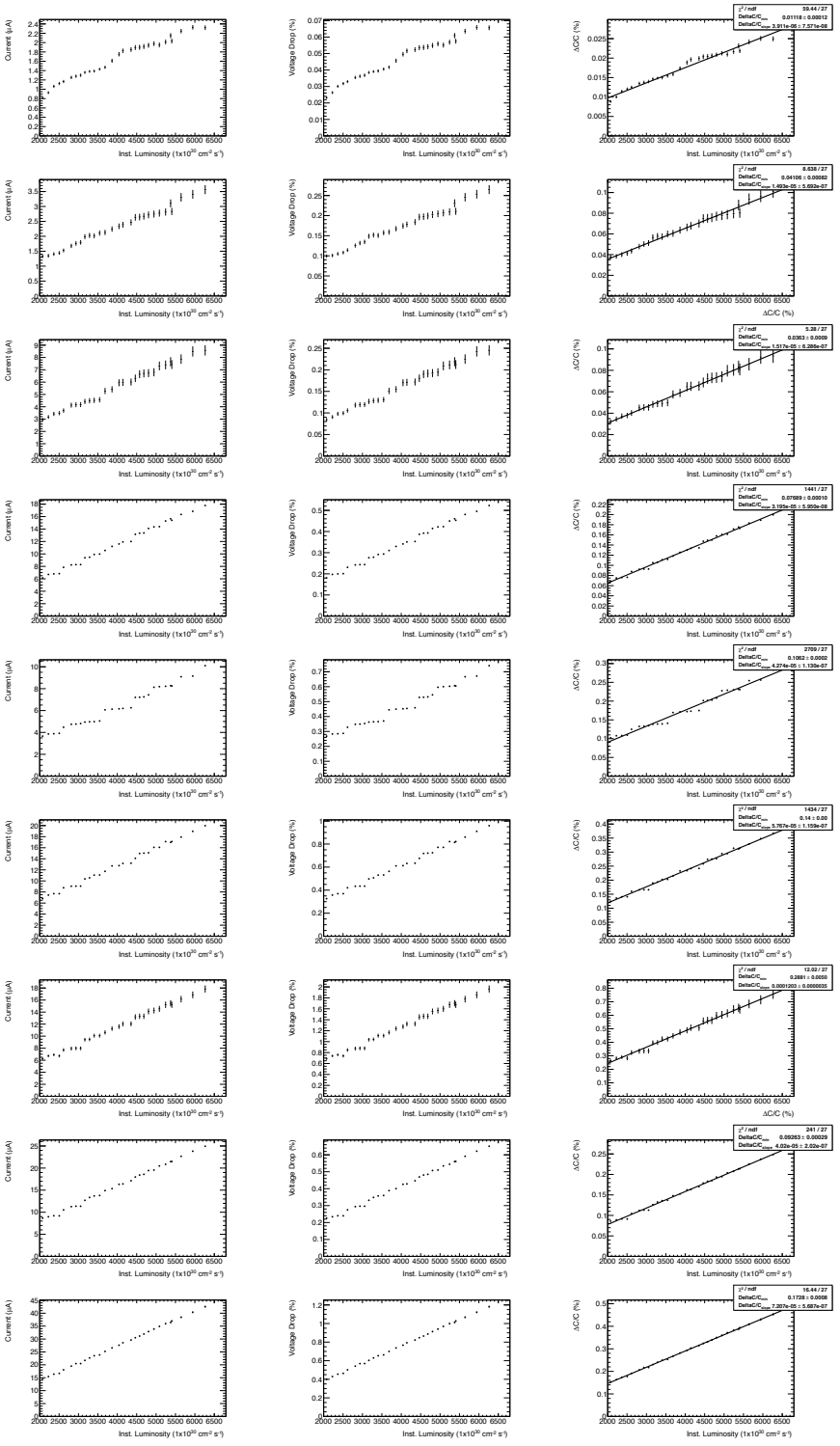

FIGURE 3.22: Currents (first column), Voltage drop (second column) and Relative change of the HV correction (third) as a function of the luminosity, for the 9 End-Cap η regions (9 rows) in 2012.

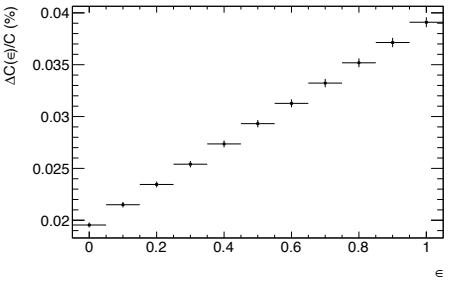

FIGURE 3.23: Mean value of the relative change in C' and C'(ε) corrections as a function of the resistance variation ε, to test the sensitivity to the resistance value, at a fixed luminosity of 6.260 $\times 10^{33} cm^{-2} s^{-1}$ in the barrel.

and scanning the resistance variation range in the $0 < \varepsilon < 1$ range (that is, from nominal up to $2 \times R$), at a fixed luminosity, and evaluating (Figure 3.23):

$$\frac{\Delta C_{\varepsilon}}{C} = \frac{C'(\varepsilon) - C}{C}. \tag{3.22}$$

Using the barrel hypothesis with ER=150 kΩ, even in the extreme case that the resistance values were wrong by one order of magnitude (ε=9), the relative change of the correction, when extrapolating to a luminosity of $1 \times 10^{34} cm^{-1} s^{-1}$, would at most reach 0.3%.

3.4.8 Study on the distribution of currents

Figure 3.16 suggests the presence of different sub-populations in the current distribution, and some of these sub-populations show a larger increase with luminosity, as is observed in Figure 3.17. A specific distribution from the barrel return currents taken in the 2012 run with a single instantaneous luminosity of $5.08 \times 10^{33} cm^{-1} s^{-1}$ is chosen to study these sub-population (Figure 3.24 and 3.25).

Figure 3.25 shows the currents in function the $i\phi$ and $i\eta$ coordinate of HV lines. All current sub-populations are uniformly distributed in $i\phi$. On the other hand, the distribution of currents is split in seven contiguous $i\eta$ blocks, as the higher values of current correspond to high $i\eta$ values ($i\eta > 16$ corresponding to the electrodes B and $|\eta| > 0.8$), while the lower ones are located at $i\eta < 16$ corresponding to the electrodes A and $|\eta| < 0.8$. This effect can be due to the higher density of particle flux in the forward regions.

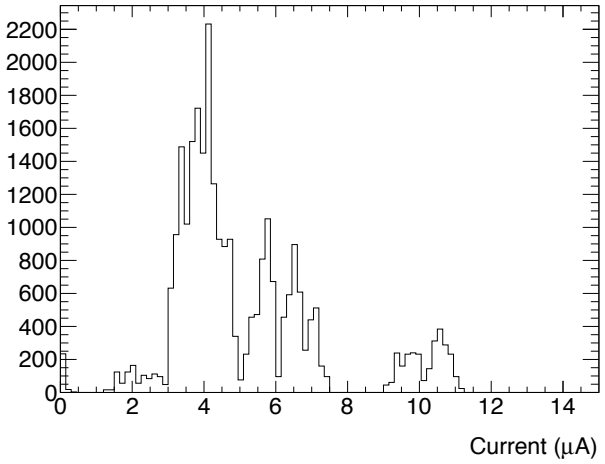

FIGURE 3.24: Distribution of the return currents in the barrel for the instantaneous luminosity $5.08 \times 10^{33} cm^{-1}s^{-1}$. Several sub-populations are observed: Region I: 0 to 3 μA. Region II: 3 to 5 μA. Region III: 5 to 6 μA. Region IV: 6 to 8 μA. Region V: 8 to 10 μA. Region VI: 10 to 14 μA.

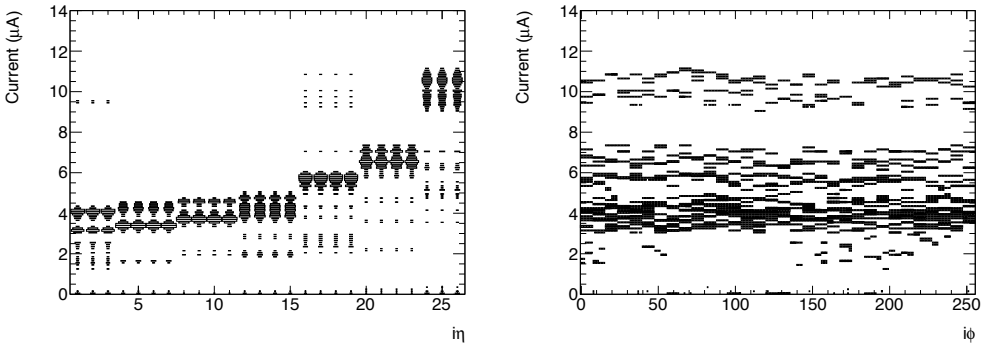

FIGURE 3.25: Return current in the barrel for the instantaneous luminosity $5.08 \times 10^{33} cm^{-1}s^{-1}$ as a function of its $i\eta$ (left) and $i\phi$ (right) coordinates.

Due to the sub-population effect in the barrel, the sample is divided in two regions: $i\eta$ <=16 (electrodes A), and $i\eta$ >16 (electrodes B). The profiles of the currents, voltage drop and relative change in the correction for both cases can be seen in Figure 3.26. The mean value of currents for electrodes A is lower than for electrodes B, and their increase with luminosity show a different pattern in each case (the slope is larger for electrodes B than A). The relative change in the corrections at high luminosity is therefore calculated for these two regions. Extrapolating to luminosity of $1 \times 10^{34} cm^{-1}s^{-1}$, one finds

$$\frac{\Delta C}{C}_{\text{ElectrodesA}} = 0.023\% \pm 0.001\%,$$
$$\frac{\Delta C}{C}_{\text{ElectrodesB}} = 0.043\% \pm 0.002\%.$$

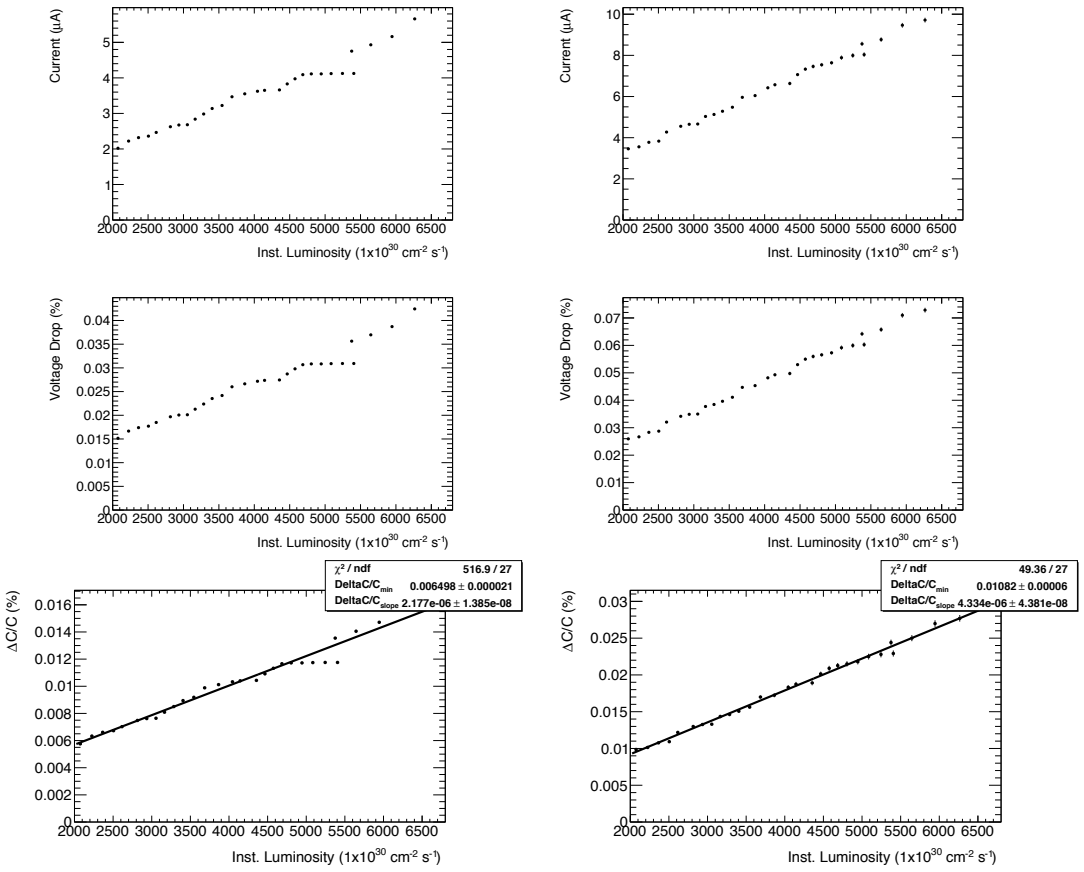

FIGURE 3.26: Return currents (first row), Voltage Drop (second row) and Relative change in the corrections (third row) as a function of the luminosity, for the electrodes A (left) and the electrodes B (right).

3.4.9 Conclusions

The effect of electrode resistors and return currents in the HV system on the energy corrections is studied. To account for their resistances, a probe value of 150 kΩ is used in the whole barrel (both electrodes A and B). For the End-Cap, a different resistance model is used, that takes into account all resistances on the electrodes to calculate the ER seen by a HV line. The effect in the end-cap is one order of magnitude larger than in the barrel, as the resistance values are considerably larger, and the values of currents are larger with η. The results are summarised in Table 3.5.

For 2011 and 2012 data, the results are compatible and the changes in corrections are found to be small in most of the cases. After extrapolating to high luminosities ($1 \times 10^{34} cm^{-1} s^{-1}$), the relative corrections in the barrel are still small (from 0.02 to 0.04%). The effect is more pronounced in the end-cap where the largest change would occur in the $2.3 < |\eta| < 2.5$ region, where a change of about 1.2% compared

to the nominal corrections values is observed (0.8% in the highest luminosity point in the 2012 run).

As described in Eq. 3.19, this relative change found in the correction would also imply a similar increase in the corrected energy in that region. Even if in most of the regions the effect is small, the larger factors observed in some of the end-cap regions should be accounted for and eventually corrected. The in-situ calibration (explained in detail in Chapter 4) takes into account the differences while computing η-dependent energy scale factors, which are calculated by comparing the $Z \to e^+e^-$ peak in data and MC. However, the in-situ calibration is static in time, while the relative change in the corrections vary with luminosity. Therefore it accounts for an average correction (not dependent on the luminosity).

Another strategy, to validate the results presented in this Chapter and to extract direct corrections, would be to measure the $Z \to e^+e^-$ peak as a function of the luminosity and in the instance of any difference being seen, extract a luminosity-dependent correction factor. The latter case needs high statistics that would imply to merge many different runs, this would need similar machine conditions in each of the included runs to be viable. Further studies would need to be undertaken to better understand the feasibility of such procedure.

η region	$R_{\text{eff}}(k\Omega)$	V_{drop} (V) at highest 2012 lumi	$\frac{\Delta C}{C}$ (%) at $1 \times 10^{34} cm^{-1}s^{-1}$
$\lvert\eta\rvert$ <0.8	150	0.8	0.02
0.8< $\lvert\eta\rvert$ <1.375	150	1.4	0.04
1.375< $\lvert\eta\rvert$ <1.5	700	1.65	0.04
1.5< $\lvert\eta\rvert$ <1.6	1700	6.3	0.15
1.6< $\lvert\eta\rvert$ <1.8	600	5.0	0.15
1.8< $\lvert\eta\rvert$ <2.0	500	10.2	0.32
2.0< $\lvert\eta\rvert$ <2.1	1100	10.8	0.43
2.1< $\lvert\eta\rvert$ <2.3	600	11.0	0.58
2.3< $\lvert\eta\rvert$ <2.5	1100	19.0	1.21
2.5< $\lvert\eta\rvert$ <2.8	600	13.8	0.40
2.8< $\lvert\eta\rvert$ <3.2	500	21.6	0.72

TABLE 3.5: Summary of results : HV corrections and voltage drops, for various eta regions.

Chapter 4

Photon Performance

Contents

In the ATLAS detector, a precise reconstruction of electrons and photons is provided in the $|\eta| < 2.47$ region, where the EMCAL has a good granularity and the inner detector contributes with tracking information. This chapter describes how the photons are reconstructed, identified and their energy is calibrated in ATLAS. Furthermore, the contents described in this chapter do not reflect any personal contribution, and aim at providing background for Chapters 5, 6 and 7 which involve photons.

The photon identification, reconstruction as well as other aspects involving photon performance described in this chapter, are developed based on Monte Carlo simulations, and validated and refined using collision data.

4.1 Photon Reconstruction

Electromagnetic clusters are reconstructed using a "sliding window" algorithm where electron and photon reconstruction is seeded by a *preliminary set of pre-clusters* in the EM calorimeter with size 3×5 units of 0.025×0.025 in $\eta \times \phi$ space (based on the granularity of the second layer of the calorimeter), and total $E_{\mathrm{T}} > 2.5$ GeV. The rectangular *pre-clusters* are positioned to maximise the quantity of energy within the cluster. After these *pre-clusters* have seeded the reconstruction, the *electromagnetic clusters* are built. The optimal cluster size depends on the particle being reconstructed and the region in the calorimeter; for example, the presence of material upstream in the calorimeter can cause photon conversion and hence the cluster size has to be amplified in the barrel (3x7) to account for the opening angle of the electron-positron pair in ϕ due to the magnetic field. In the EMEC all photons are reconstructed with clusters of 5x5 cells. More information about the clustering algorithm can be found in [80].

To classify a cluster as an electron, a converted photon or a unconverted photon, the reconstruction tries to find a matching track with a momentum p compatible with the cluster energy. In the case where no track is matched, the cluster is treated as unconverted photon. In the case of a matching track coming from a conversion vertex, the cluster is treated as converted photon. Most converted photons are initially treated as electron candidates, until a matching conversion vertex candidate is assigned to them, and they are *recovered* from the electron classification. The recovery of converted photon candidates described in [90].

The converted photons are classified depending on the number of conversion pair tracks assigned to them. One-track conversions are due to conversions decaying asymmetrically (either the electron or the positron has a very low energy), or late conversions where the two tracks are essentially merged and only one track is reconstructed and matched to the cluster. In the two-track conversion, the two track momenta are not very different from each other (the hard-to-soft momentum ratio

is less than a factor of 4), each track is extrapolated to the calorimeter and matched to the same cluster (Figure 4.1).

Two-track conversions are mostly observed at low conversion radius (R_{conv}), whilst the one-track are mostly reconstructed at larger R_{conv}, especially inside the TRT. More details about photon reconstruction can be found in [90] and [91].

Overall MC photon reconstruction efficiencies before and after recovery as a function of true η and p_{T} are shown in Figure 4.2.

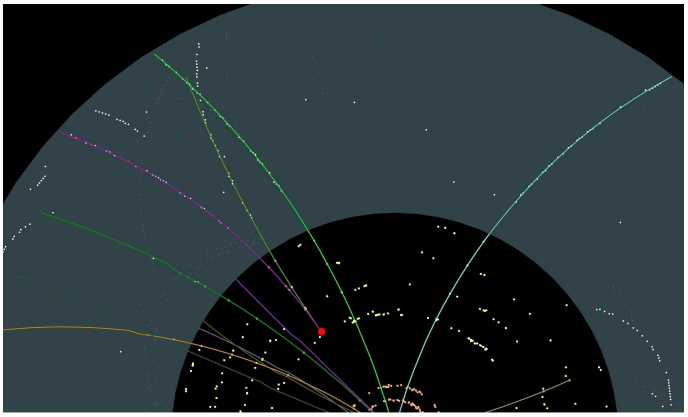

FIGURE 4.1: Display of a two silicon tracks conversion candidate.The conversion occurs on the 1st SCT layer. Both tracks have TRT extensions. The second track (on the right) has visible signs of bremsstrahlung losses as it propagates through the TRT. Both tracks show high threshold TRT hits (3 and 11 respectively).

4.2 Photon Calibration

The calibration of the EMCAL is performed in several steps:

- First the "electronic calibration" [92], converts the raw signal extracted from each cell into a deposited energy; the method used in this step is explained in detail in Section 3.3.
- The second step deals with clusters, where the energies deposited in each layer of a cluster are summed and an energy-weighted position is calculated. In this step there are some considerations taken into account: A ϕ modulation is created due to the accordion geometry (the amount of absorber material crossed by a particle varies with ϕ). A bias in the measured position ("S-shape") due to the finite granularity of cells in η and a modulation in energy

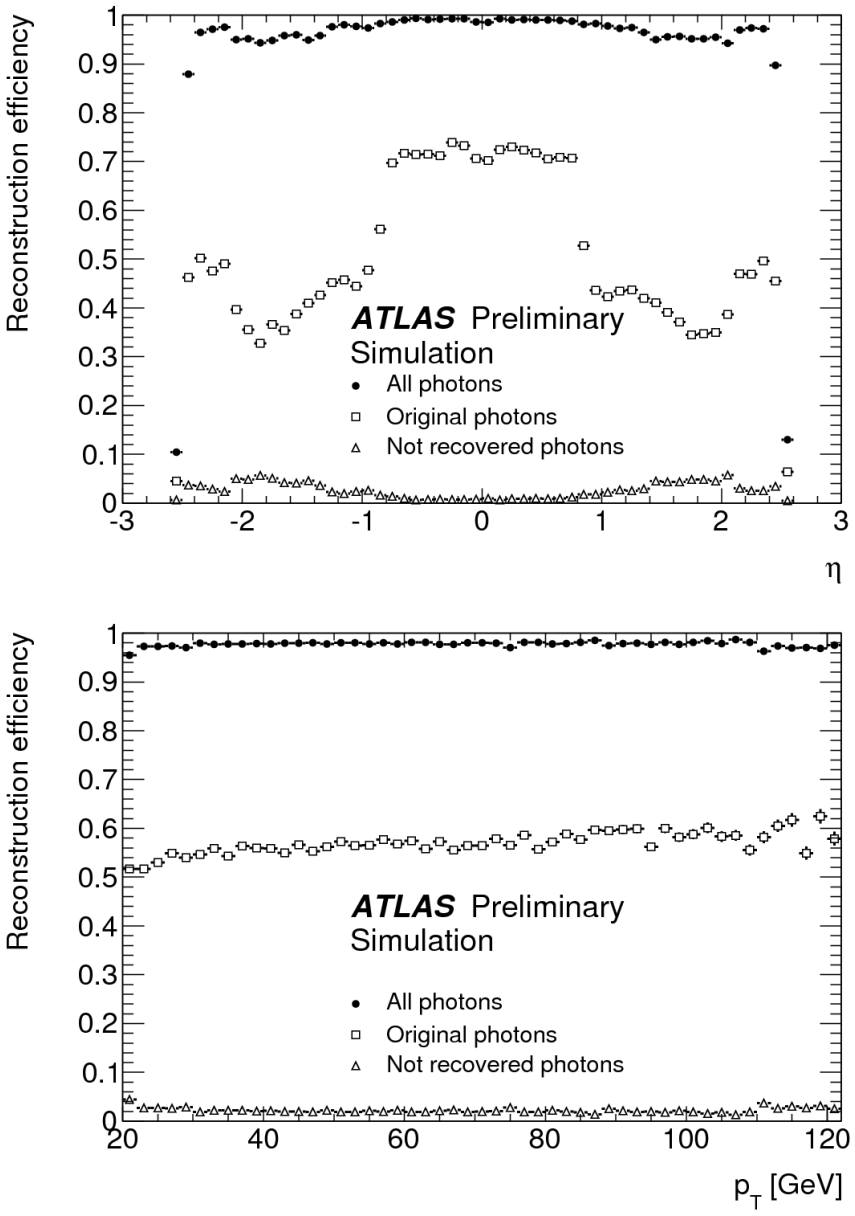

FIGURE 4.2: Overall photon reconstruction efficiencies before and after recovery as a function of true η (top) and p_{T} (bottom) [90].

is created due to the shower not being completely contained in the η cluster window. A particle created from a vertex away from the origin will intersect the calorimeter at a slightly different η in each layer. All these considerations bring corrections to be applied to the position of the cluster measured in each layer. The position measurements are combined to define the shower impact point in the calorimeter, and are used to correct the total energy for modulations in η and ϕ [91].

- The energies deposited in each layer are combined. In this step, the calibration

hits method is used, which is based in simulation to correct for energy losses in each layer, correlating them with measured observables. In this step the corrections are determined as a function of η.

- At last, an in-situ calibration using physics events recorded by ATLAS is performed (electron pair from Z boson decays), where the absolute energy scale is determined and an inter-calibration in all the different calorimeter regions is performed.

This chapter describes in detail the simulation-based calibration hits corrections to the energy layers and the in-situ calibration using Z boson decays into electrons.

4.2.1 Monte Carlo Energy Calibration

In this method the total energy is calculated from the energy in the individual layers and pre-sampler. It uses special simulations (mono-energetic single photons or electrons) in which the energy deposit is recorded in all detector material, such as active (for example the LAr between the electrodes of the Accordion), inactive (for example the absorbers of the Accordion) and even the dead materials (solenoid, cryostat, etc). This allows to correlate the energy deposited in the inactive materials, with measured energies in the following layers.

This method provides a modular way to to calibrate electrons and photons by decoupling the corrections for the energy lost in front, in and besides the calorimeter, and is performed separately for converted and unconverted photons. The method is described in detail in [93].

The reconstructed energy of an electromagnetic object (either electron or photon) is the following:

$$\begin{aligned} E_{e/\gamma} = &\left[a\left(E_{cal},\eta\right) + b\left(E_{cal},\eta\right) E_{ps} + c\left(E_{cal},\eta\right) E_{ps}^{2}\right. \\ &\left. + \frac{s_{cl}(X,\eta)}{f_{out}(X,\eta)} \sum_{i=1}^{3} E_i \times \left(1 + f_{leak}\left(X,\eta\right)\right)\right] \times \left(F\left(\eta,\phi\right)\right), \end{aligned} \tag{4.1}$$

where:

- $E_{e\gamma}$ in the electron/photon energy.

- E_{ps} is the energy deposited in the active material of the pre-sampler.
- η is the cluster barycentre, corrected for the "S-shape" effect.
- a, b, c are coefficients parametrized in terms of the energy deposited by a particle in the calorimeter (E_{cal}) and η. The coefficient c is only used in the end-cap and set to 0 in the barrel. In the region without pre-sampler ($|\eta| > 1.8$), the three first E_{ps} dependent terms term in Equation 4.1 are replaced by:
$$a\left(E_{cal},\eta\right)+b\left(E_{cal},\eta\right)X+c\left(E_{cal},\eta\right)X^{2}, \tag{4.2}$$
- X is the longitudinal barycentre or shower depth, defined by:
$$X=\frac{\sum_{i=1}^{3}E_{i}X_{i}+E_{ps}X_{ps}}{\sum_{i=1}^{3}E_{i}+E_{ps}}, \tag{4.3}$$
where E_i are the energies deposited in each of the calorimeter layers (i) in a given cluster, and X_i is the longitudinal depth, expressed in radiation lengths, of compartment "i", computed on the centre of the detector.
- $s_{cl}\left(X,\eta\right)$ is the Accordion sampling factor in the cluster.
- $f_{out}\left(X,\eta\right)$ is the correction for the energy deposited in the calorimeter outside the cluster.
- $f_{leak}\left(X,\eta\right)$ is the correction for the energy deposited behind the calorimeter.
- $F\left(\eta,\phi\right)$ is the energy correction depending from the impact point inside a cell (energy modulation).

As discussed in the previous chapter, the energy resolution is defined by the formula 3.7, which contains a noise term, a sampling term resulting from the sampling fluctuations and a constant term. The overall constant term consists of local, short-range, and long range constant terms. The local constant term is due to the imperfection of corrections for longitudinal and lateral leakage and ϕ modulation. The short-range constant term is a sum of contributions from mechanics (such as absorber and liquid gap tolerances) and calibrations (amplitude accuracy, readout stability and difference between calibration and physics signals). The long-range constant term includes the effects from time-dependence of charge measured in liquid, high voltage variation and temperature gradients.

Figure 4.3 shows the linearity of the response found in MC (ratio between the reconstructed and the true photon energy) for unconverted and converted photons as a function of pseudo-rapidity and at different energies after applying the MC calibration. For unconverted photons, the deviation from linearity is less than 0.5% at almost all values of $|\eta|$. For converted photons, the deviation from linearity is within1% over most of the simulated samples, reaching +1.5% at low energies in the $1.7< |\eta| < 2.2$ region, where the effect of the upstream material is more pronounced.

In Figure 4.4, the energy resolution (σ/E) as a function of $|\eta|$ is shown for unconverted and converted photons, for different photon energies in MC. The resolution deteriorates as a function of the number of radiation lengths in front of the EM calorimeter. This effect is particularly visible for the converted lower-energy photons and is due to the combined effect of the bremsstrahlung radiation and the magnetic field [94].

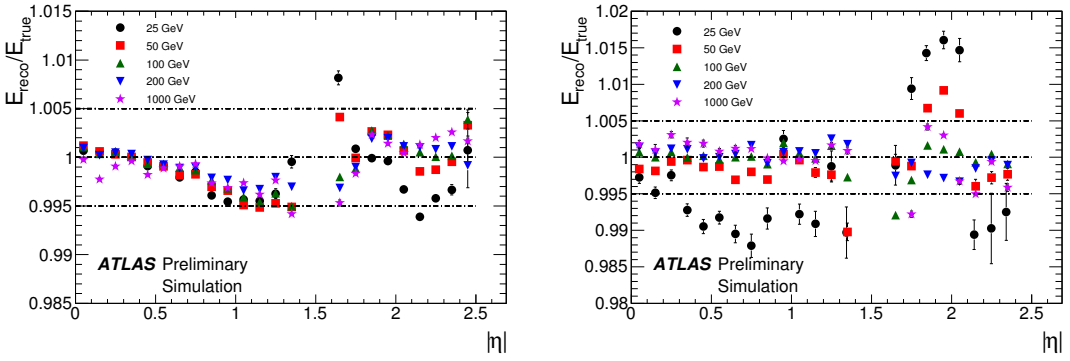

FIGURE 4.3: Expected linearity of response of the EMCAL for unconverted photons (left) and converted photons (right) as a function of pseudo-rapidity. [94].

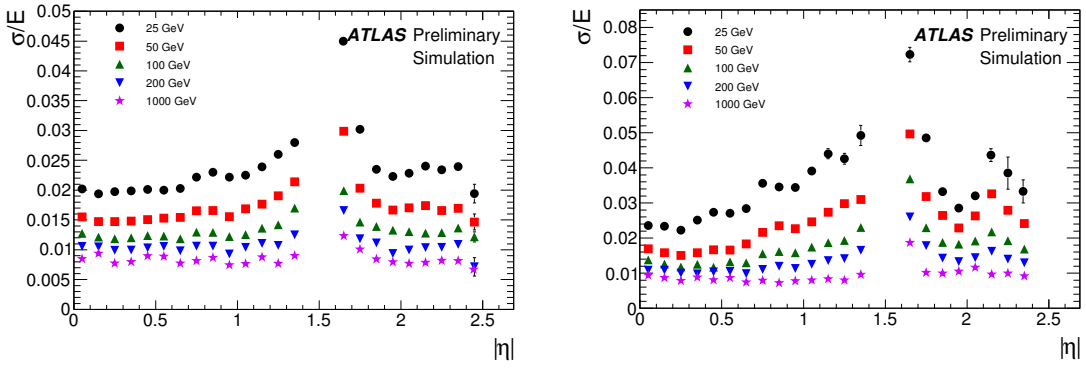

FIGURE 4.4: Expected fractional energy resolution of the EM calorimeter for unconverted photons (left) and converted photons (right) as a function of pseudo-rapidity. [94].

4.2.2 In-situ calibration with Z $\rightarrow e^+e^-$ events

Electron pairs from Z boson decays provide a sample with two electromagnetic objects, which are kinematically correlated. This correlation can be used to correct for some long-range non-uniformities, such as HV variations due to localised calorimeter defects, LAr temperature variations and impurities, mechanical deformation and material in front of the calorimeter. The method consists in constraining the di-electron invariant mass to the well-known Z boson line-shape and has as a goal to provide the absolute calorimeter electromagnetic energy scale with an accuracy of approximately 0.1%. More information can be found in [95].

For a given region "i", the long range non-uniformity can be parametrized modifying the measured electron energy as:

$$E_i^{reco} = E_i^{true}(1 + \alpha_i), \tag{4.4}$$

where E_i^{reco} is the reconstructed electron energy in the region "i", E_i^{true} is the true electron energy and α_i the electron energy scale correction factor. The invariant mass M_{ij} of two leptons found in two different regions i and j is given by the following expression:

$$M_{ij} = \sqrt{2E_iE_j(1 - cos\theta)}, \tag{4.5}$$

where E_i and E_j are the energy of the two electrons, and θ is its separation angle measured by the tracker. Neglecting second order terms and assuming that the angle between electrons is perfectly known, the effect on the di-electron invariant mass is:

$$M_{ij}^{reco} = M_{ij}^{true}(1 + \beta_{ij}/2), \tag{4.6}$$

where $\beta_{ij} = \alpha_i + \alpha_j$.

To determine $\alpha_{i,j}$, β_{ij} is extracted by minimising the following log-likelihood:

$$-lnL_{tot} = \sum_{i,j} \sum_{k=1}^{N_{ij}^{events}} -\ln L_{ij} \left(\frac{M_k}{\left(1 + \frac{\beta_{ij}}{2}\right)} \right), \tag{4.7}$$

where the indices i, j denote the regions considered for the calibration with one of the electrons from the $Z \to e^+e^-$ decay being in region i and the other in region j, N_{ij}^{events} is counts all the selected $Z \to e^+e^-$ events with electrons in regions i and j. M_k is the di-electron invariant mass of the event of the event k, and $L_{ij}(m)$ is the probability density function quantifying the compatibility of an event with the Z line-shape.

The α values extracted in 2010 are shown in Figure 4.5 and detailed in [96]. They were recomputed in 2011 and additional corrections of the order of 0.5% in the barrel and 1% in the end-cap were applied to the electrons. Then in 2012, a small correction (a few per mil) was included in the energy scale correction factors (so-called "scales"). The in-situ energy calibration is static with time, as shown in Figures 4.6, no energy scale dependence on time or pile-up is observed (the stability is at the 3×10^{-4} level).

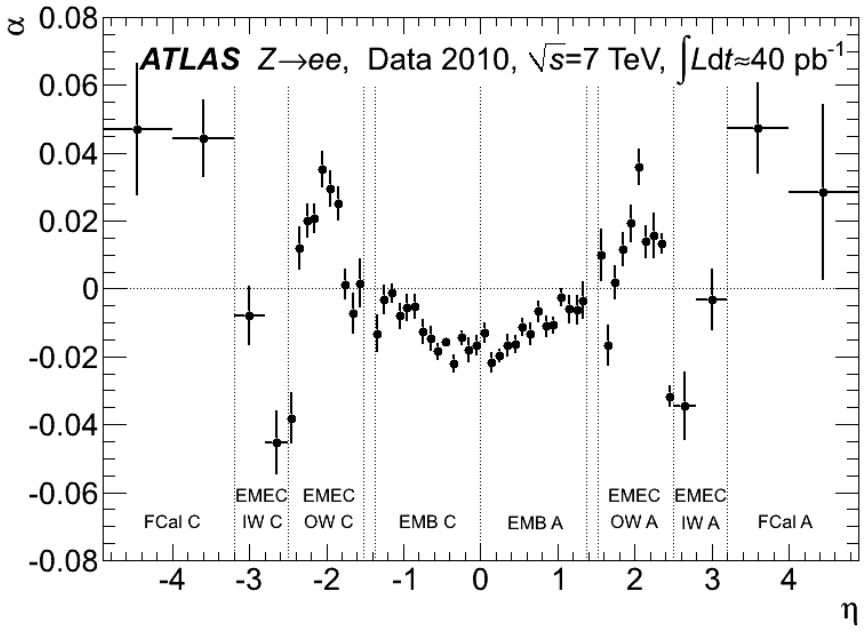

FIGURE 4.5: The energy-scale correction factor as a function of the pseudo-rapidity of the electron cluster derived from fits to $Z \to e^-e^+$ data and. The uncertainties are statistical only [96].

The energy resolution can also be measured using the $Z \to e^-e^+$ invariant mass distribution. The distribution is fitted with a Breit-Wigner convoluted with a Crystal Ball function (these functions are defined in Section 5.3.2). The Breit-Wigner width is fixed to the PDG Z width, and the experimental resolution is described by the Crystal Ball function. The resolution parameters are extracted from the fit to

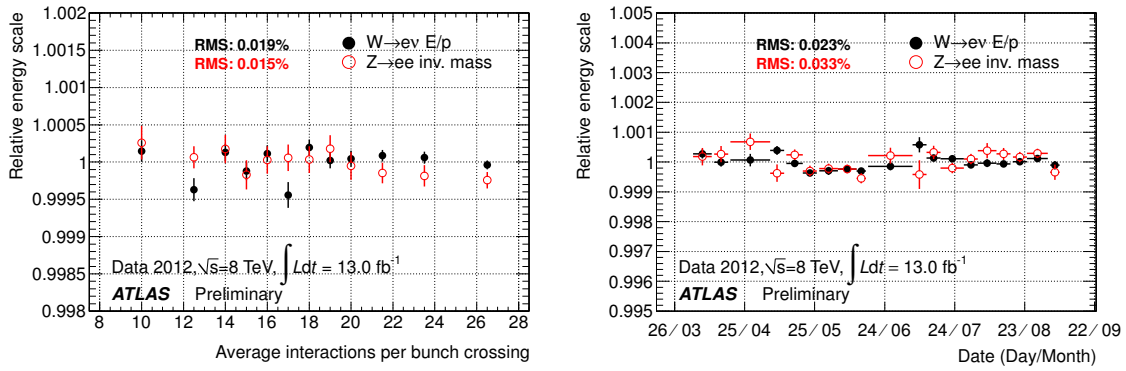

FIGURE 4.6: Electron energy response stability with μ left and with time (right) in 2012 data [97].

the invariant mass, where it is assumed that the sampling term that dominates the electron resolution is well described by the data. The effective constant term that includes both the calorimeter constant term and the effect of inhomogeneities due to possible additional material can be extracted with the following formula:

$$c_{data} = \sqrt{2\left(\left(\frac{\sigma}{M_Z}\right)^2_{data} - \left(\frac{\sigma}{M_Z}\right)^2_{MC} + c^2_{MC}\right)}, \tag{4.8}$$

where c_{MC} is the residual constant term in the MC, M_Z is the Z mass and σ the resolution of the Crystal Ball function. Figure 4.7 shows the invariant mass distributions of the $Z \to e^-e^+$ decays. In all cases the components of the experimental resolution are always slightly worse than those predicted by MC (in this case, the MC resolution has zero constant term), as indicated in the plots.

4.2.3 Systematic uncertainties associated to the electron and photon energy scales

The energy of the photons is calibrated with the in-situ scales described previously. The different sources of systematics that affect photon energy scale (ES) calibration are related to the uncertainties in the electrons ES measurement and the extrapolation from electron to photon in the calibration. These uncertainties are discussed in the following, and are based in [74, 99].

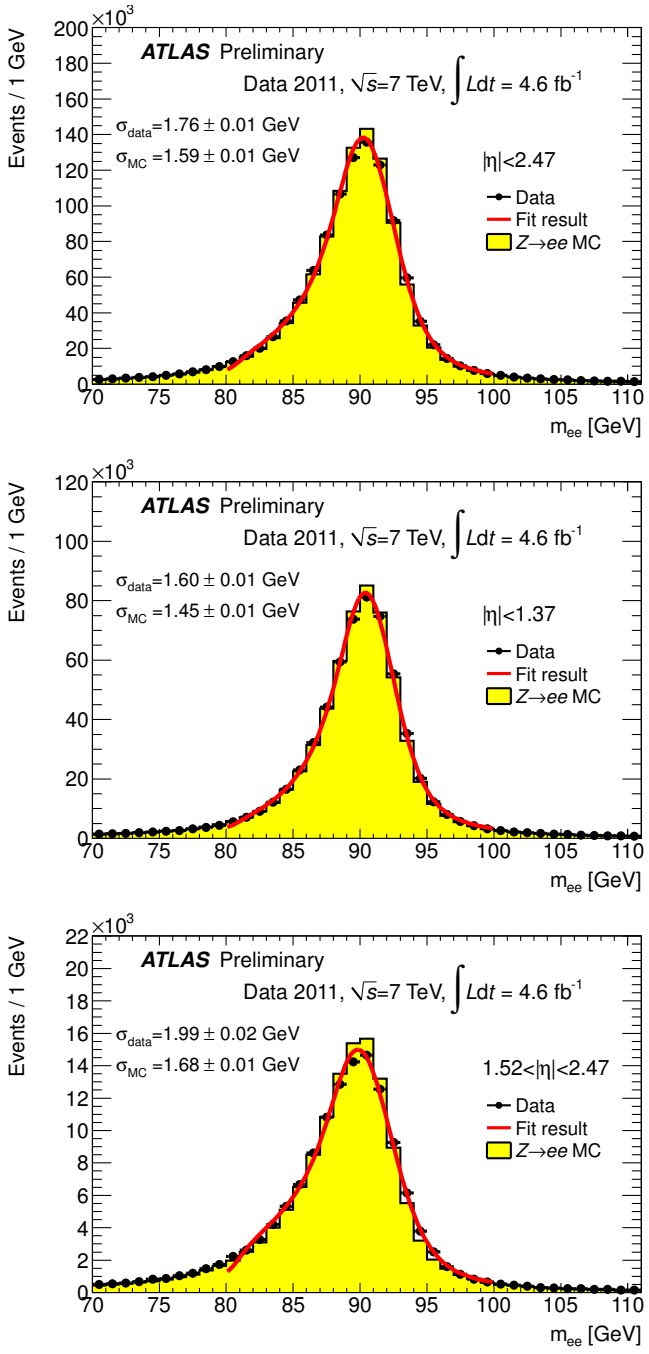

FIGURE 4.7: Reconstructed di-electron mass distributions for Z $\rightarrow e^-e^+$ decays for different pseudo-rapidity regions after applying the baseline Z $\rightarrow e^-e^+$ calibration. The transition region 1.37< $|\eta|$ <1.52 is excluded. The data (full circles with statistical error bars) are compared to the signal MC expectation (filled histogram). The fits of a Breit-Wigner convolved with a Crystal Ball function are shown (full lines). The Gaussian width (σ) of the Crystal Ball function is given both for data and MC simulation. Note that the MC resolution constant term is zero [98].

Material uncertainties

The uncertainty in the knowledge of the quantity of material in front of the EMCAL affects the electron energy measurement since the deposit energy in any other material is not considered in the MC-based energy calibration described in Section 4.2.1. Nevertheless, if there is extra upstream material in data with respect to MC, it should be absorbed in the energy scale factors extracted from the in-situ calibration. However, given that the E_{T} spectrum of electrons from Z decays have a mean value around 40 GeV, there is a residual uncertainty for the other E_{T} values (mainly for low E_{T} electrons, for which material effects have a more important influence).

The residual uncertainty is estimated in two steps. First the in-situ $Z \rightarrow e^{+}e^{-}$ scale factors are extracted with a dedicated MC sample using a geometry model with additional material in front of the calorimeters. Second, the non-linearity is measured using MC truth information by comparing the mean value of the $E_{\mathrm{reco}}/E_{\mathrm{truth}}$ distributions between the nominal MC and the one with additional material in bins of electron E_{T}. The systematic uncertainty varies from -2% to +1.2%, and is parametrized as a function of E_{T} for the different η regions.

Pre-sampler ES uncertainties

The MC calibration uses the measured pre-sampler energy to correct for energy lost upstream of the active EM calorimeter, making the calibration sensitive to the pre-sampler ES. In the in-situ calibration only one overall scale is extracted, therefore any differences between the pre-sampler and total EMCAL ES are explicitly corrected. An upper limit on the pre-sampler ES uncertainty is extracted by comparing the energy deposited in the pre-sampler by electrons from $W \rightarrow e\nu$ decays between data and MC. It is about $\pm 5\%$ in the barrel and $\pm 10\%$ in the end-cap regions (with $|\eta| < 1.8$).

The impact on the electron energy scale due to the uncertainty on the pre-sampler ES variates with η (due to the η dependent material distribution in front of the calorimeter) region, and E_{T} (given that the fraction of energy deposited in the pre-sampler decreases with increasing E_{T}). The extrapolation to different E_{T} regions is performed using electrons from MC simulation. The largest uncertainty is $\pm 1.4\%$, found for the $1.52 < |\eta| < 1.8$ region, and $E_{\mathrm{T}} = 1$ TeV (due to the large extrapolation from the electrons E_{T} mean value of 40 GeV to this energy).

Method uncertainties

Uncertainties related to the method used in the in-situ $Z \rightarrow e^+e^-$ calibration as the background fit and range are evaluated by tightening the electron selection (therefore using a cleaner electron sample), and variating the fit range. The resulting uncertainty associated to the background is $\pm 0.1\%$ in the barrel region and reaches $\pm 1\%$ in the forward region, while the uncertainty associated to the chosen fit range it is $\pm 0.1\%$ in the barrel region and grows to $\pm 0.6\%$ in the forward region.

A possible bias in the method is evaluated by repeating the fit procedure on simulated data, resulting in a systematic uncertainty of $\pm 0.1\%$ ($\pm 0.2\%$) in the central (forward) region. In addition, alternative fit methods are tested and were compared on data which agree within $\pm 0.1 - \pm 0.5\%$($\pm 0.8 - \pm 1.0\%$). This is added as an additional uncertainty due to possible biases of the method.

There are other extra sources of uncertainties associated to the electron ES such as calorimeter electronic calibration and cross- talk (uncertainties of $\pm 1\%$ and $\pm 2\%$ relative to the middle layer for cells in the strip and back layers of the calorimeter respectively), non-linearities in the readout electronics ($\pm 0.1\%$), pile-up (0.1%), and an extra uncertainty associated to low E_{T} electrons ($\pm 1\%$ for electrons with $E_{\mathrm{T}} =$ 10 GeV, decreasing linearly to $\pm 0\%$ for $E_{\mathrm{T}} = 20$ GeV). These uncertainties, added to the material, pre-sampler and method uncertainties, gives as a result an overall systematic uncertainty on the electron energy scale is a function of E_{T} and η.

In Figure 4.8, the overall uncertainties are shown for two η-regions. For central electrons ($|\eta| < 2.47$), the uncertainty varies from $\pm 0.3\%$ to $\pm 1.6\%$. The systematic uncertainties are smallest for $E_{\mathrm{T}} = 40$ GeV (usually below $\pm 0.4\%$). For low E_{T} electrons (less than 20 GeV) the uncertainty grows linearly with decreasing E_{T} and slightly exceeds $\pm 1\%$ at $E_{\mathrm{T}}=$ 10 GeV. For forward electrons ($2.5 < |\eta| < 4.79$, the uncertainties are from $\pm 2\%$ to $\pm 3\%$.

Propagation of systematic uncertainties to photons

The systematic uncertainties associated to the in-situ calibration discussed above are common between electrons and photons, except the ones related to the pre-sampler ES and the material uncertainties, which have different impact with respect to electrons due to the differences in the development of electromagnetic showers initiated by electrons or photons in the EMCAL.

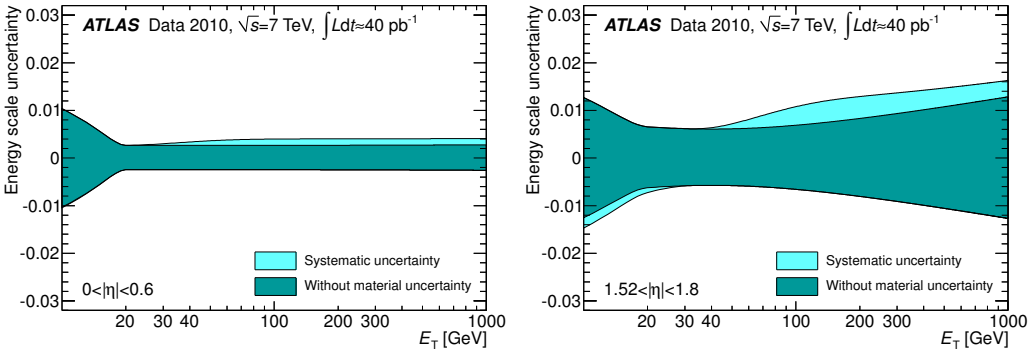

FIGURE 4.8: Total systematic uncertainty on the electron energy scale (left) for the region $|\eta| < 0.6$ which has the smallest uncertainty, and (right) for $1.52 < |\eta| < 1.8$ which has the largest uncertainty within the central region. The uncertainty is also shown without the contribution due to the amount of additional material in front of the EM calorimeters [74].

- Pre-sampler ES uncertainty for photons: The pre-sampler ES uncertainties associated to photons is estimated by two approaches. The first approach is similar to the one used for electrons, but the uncertainty that matters in this case is the bias on the photon energy with respect to the bias for electrons with $E_{\mathrm{T}} = 40$ GeV. The second approach uses events from $Z \to e^+e^-$ MC, where the pre-sampler energy has been artificially increased by 5% in the barrel and 10% in the end-caps. Scale factors are extracted by comparing this sample with nominal MC, and then applied to a simulated sample of photon + jet events. The corrected photon energies for the photon+jet samples are compared to their true energies and the difference is taken as the systematic uncertainty induced by the pre-sampler ES uncertainty on the photon scale. This uncertainty is a function of η and E_{T} and varies from 0 to 1.4%.

- Material uncertainty for photons: To account for the uncertainty in the amount of material in the front of the calorimeter, scale factors are extracted from $Z \to e^+e^-$ events with distorted geometry (where extra upstream material is added). The scales are applied to the photon of MC photon + jets samples, which have been simulated with the same distorted geometry. The distributions of the reconstructed energy between the distorted and nominal samples are compared and the differences are taken as the systematic uncertainty associated to the material uncertainty. This uncertainty varies from 0.3% to 1%.

4.3 Photon Identification

The primary source background for photons (fake photons) comes from jets that contain photons from neutral hadron decays, such as $\pi^0 \rightarrow \gamma\gamma$. In order to separate real photons from fakes coming from jets, several discriminant variables that use information from the calorimeter and inner detector are defined. Cuts in these variables are optimised to provide a high efficiency in real photon and high rejection of fakes.

In the EMCAL, photon showers are narrow, well-contained objects, while showers from jets are wider and can deposit a fraction of their energy in the HCAL. Information of longitudinal and transversal shower shapes are used to discriminate photons from jets. In the following, variables containing such information are described.

Variables using the first layer of the EMCAL

The fist EMCAL layer uses strips and provides a very fine granularity in η. This information can be used to identify substructures in the showers and distinguish between isolated photons and photons from π^0 decays (see Figure 4.9).

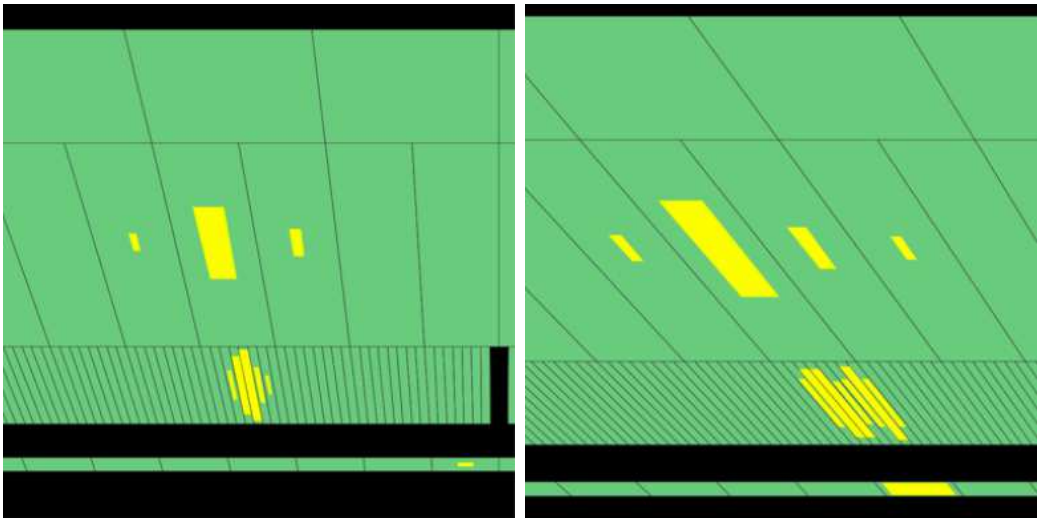

FIGURE 4.9: Separation of direct photons vs high Et π^0 shower shapes in the EMCAL. The narrow shower shape in the first layer correspond to a photon (left) and the structure with peaks from two close photons coming from a π^0decay [100].

- $\Delta E_{\rm s}$: For $\pi^0 \to \gamma\gamma$ decays, two local maxima are often found in the first layer. The following two variables are constructed using the information from the identified second maximum, to quantify the presence of a second peak:

$$\Delta E_{\rm s} = E_{\rm max2} - E_{\rm min}, \tag{4.9}$$

  where E_{max2} is the energy associated with the second maximum and E_{min} is the energy reconstructed in the strip with the minimum value, found between the first and second maxima.

- R_{max2} : The second largest energy deposit normalised to the cluster energy is defined as:

$$R_{max2} = \frac{E_{max2}}{1 + 9 \times 10^{-3} E_{\rm T}/GeV}, \tag{4.10}$$

  where $E_{\rm T}$ is the transverse energy of the cluster in the EMCAL.

- F_{side}: The fraction of energy deposited outside the shower core of three central strips, is defined as:

$$F_{side} = \frac{E(\pm 3) - E(\pm 1)}{E(\pm 1)}, \tag{4.11}$$

  where the variable $E(\pm n)$ is the energy deposit in $\pm n$ strips around the strip with the highest energy.

- w_{s3}: The shower width over the three strips around the one with the maximal energy deposit, defined as:

$$w_{s3} = \sqrt{\sum E_i \times (i - i_{max})^2 / \sum E_i}, \tag{4.12}$$

  where the index i is the strip identification number, i_{max} the index of the most energetic strip, and E_i the energy deposited in the strip i.

- w_{stot}: The shower width over the strips that cover 2.5 cells of the second layer.

Variables using the second layer of the EMCAL

Electromagnetic showers deposit most of their energy in the second layer of the EMCAL. Thus, a set of variables that measure the shape of these showers are defined:

- Real photons deposit most of their energy in a $\Delta\eta \times \Delta\phi = 3 \times 7$ window. Two lateral shower shape variables are defined by the ratio of the reconstructed energy (E) in $\Delta\eta \times \Delta\phi$ windows with different sizes, as described the following:

$$R_\eta = \frac{E_{3\times7}}{E_{7\times7}}, \tag{4.13}$$

and

$$R_\phi = \frac{E_{3\times3}}{E_{3\times7}}. \tag{4.14}$$

- The lateral width in η is calculated in a window of $\Delta\eta \times \Delta\phi = 3 \times 5$ cells using the energy weighted sum over al cells:

$$w_\eta = \sqrt{\frac{\sum(E_c \times \eta_c^2)}{\sum E_c} - \left[\frac{\sum(E_c \times \eta_c)}{\sum E_c}\right]^2}, \tag{4.15}$$

where E_c is the energy deposited in each cell, η_c the position of the cell.

Variables for hadronic leakage

Real photons deposit their energies primarily in the EMCAL while fake photons from jets contain hadrons that could penetrate deeper into the calorimeter deposing sizeable energy in the first compartment of the HCAL. To quantify this the following variable is used:

$$R_{\rm had} = \frac{E_{\rm T}^{\rm had}}{E_{\rm T}}, \tag{4.16}$$

where E_T^{had} is the energy deposited in the HCAL and $E_{\rm T}$ is the transverse energy in the EM cluster. In the $0.8 < |\eta| < 1.37$ region, the energy deposited in the whole hadronic calorimeter is used, while in the other pseudo-rapidity intervals only the leakage in the first layer of the hadronic calorimeter is used.

By comparing distributions of discriminant variables in data and MC, some small differences are observed. To correct for this differences, the MC distributions are shifted by a factor equal to the observed difference. Figure 4.10 shows the distribution of the variables using the second layer of the EMCAL (R_η (top), R_ϕ and w_η) for unconverted and converted photons with $E_{\rm T} > 20$ GeV selected from $Z \to ll\gamma$

events obtained from the 2012 data sample and compared to simulated $Z \to ll\gamma$ events and for fake photons from hadronic jets in Z($\to \ell\ell$)+jets (the simulation has been corrected by the discriminant variables differences previously discussed).

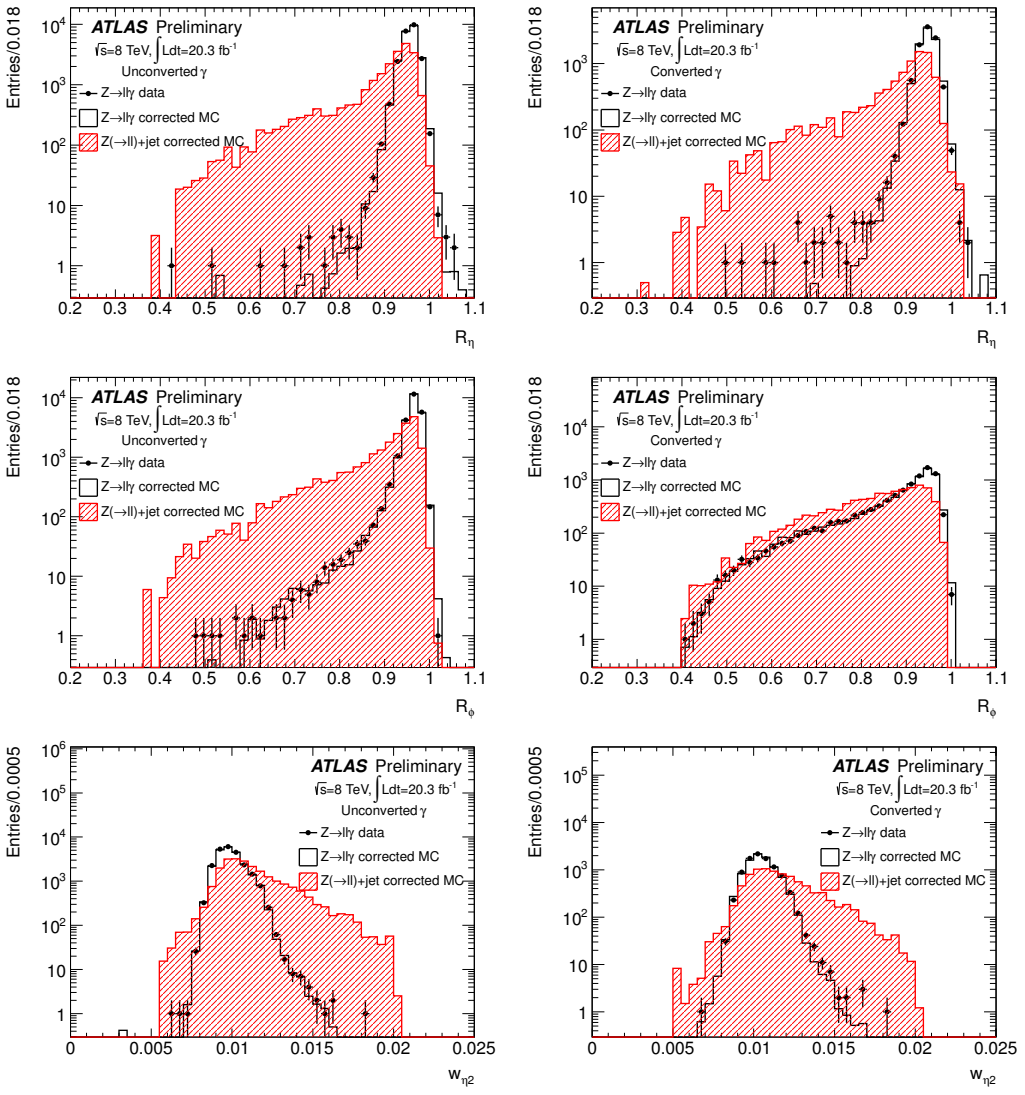

FIGURE 4.10: Distribution of the calorimetric discriminating variables R_η (top), R_ϕ and w_η for unconverted (left) and converted (right) photon candidates with $E_{\mathrm{T}} > 20$ GeV and $|\eta| < 2.37$ (excluding $1.37 < |\eta| < 1.52$) selected from $Z \to ll\gamma$ events obtained from the 2012 data sample (dots). The distributions for true photons from simulated $Z \to ll\gamma$ events (black hollow histogram) and for fake photons from hadronic jets in Z($\to \ell\ell$)+jets (red hatched histogram) are also shown. Photon isolation is required on the photon candidate but no criteria on the shower shape are applied. The photon purity of the data sample is about 99% [101].

4.3.1 Loose selection

Electron and photons share a set of common loose cuts in the shower-shape variables of the second layer (R_η, w_2) and hadronic leakage. These cuts are set for trigger purposes and show relatively small differences between converted and unconverted photons [90].

4.3.2 Tight selection

The tight selection is optimised to reduce the most dangerous background coming from photons decaying from isolated π^0. Consists of tighter cuts to the variables used in the loose selection plus an additional cut on the variable R_ϕ, and cuts on the first layer variables that provide good $\pi^0 - \gamma$ separation ($F_{side}, \Delta E_s, R_{max2}$, w_{s3} and w_{stot}). The cuts are optimised separately for converted and unconverted photons, taking into account that the electromagnetic deposit is different in both cases. They provide an identification efficiency of about 85% for photon candidates with transverse energy of $E_{\mathrm{T}} > 40$ GeV and a corresponding background rejection factor of about 5000 [102, 103]. The cut-based selection criteria does not depend on the photon candidate E_{T}, but vary as a function of η to take into account variations associated to the total thickness of material in front of the calorimeter and its geometry[1].

During the physics analysis of 7 and 8 TeV, different sets of tight identification cuts are used:

- 7 TeV analyses: A cut based selection is first used with an efficiency of photon reconstruction and identification variating from 65% to 90% between $25 < E_{\mathrm{T}} < 80$ GeV. Later, an alternative neural-net based selection is developed and tuned to achieve a similar jet rejection than the cut-based selection but with higher efficiency, the neural-net method finally replaces the cut-based selection.
- 8 TeV analyses: The cut based selection is re-optimised for robustness against pile-up by relaxing requirements on shower shapes more susceptible to pile-up, and tightening others. The photon efficiency is similar to the ones obtained with the 7 TeV cut-based selection.

[1]The $|\eta|$ acceptance of the photon identification is $|\eta| < 2.37$, excluding the region where $1.37 < |\eta| < 1.52$.

4.4 Photon Isolation

In order to further discriminate real photons from its main background of fakes coming from jets, on top of the photon identification criteria, the photon candidates are required to be isolated from the hadronic activity characteristic of a jet with a leading light meson. The activity surrounding a photon can be measured by the ID, in the so-called "track isolation" and in the calorimeter with the "calorimetric isolation". Both methods are explained next.

4.4.1 Calorimetric Isolation

A calorimetric isolation estimator ($E_{\mathrm{T}}^{\mathrm{cone}}$) is constructed from the transverse energy in a cone of half opening angle ΔR (usually 0.4 but it varies among the analyses) around the photon candidate direction, where the energy of the photon is excluded. Corrections to the isolation energy from the EM object are applied, to take into account the object out-of-core energy leakage, underlying event[2] and pile-up. The contribution from the pile-up, underlying event is subtracted in event-by-event basis.

The isolation can be based on the electromagnetic and hadronic calorimeter cells or on topological clustering[3]. The calorimeter isolation based on topological cluster is less-sensitive to pile-up as can be observed in Figure 4.11. This is achieved by consistently using topological cluster energies for both the raw isolation and the ambient energy density corrections. More information on topological isolation can be found in [104] and [105].

4.4.2 Track Isolation

The tracking isolation is computed with the scalar sum of the transverse momentum p_{T} of the tracks reconstructed around a photon candidate within a distance ΔR (ΔR being the $\eta - \phi$ distance between the track direction at the vertex and the cluster centroid, its typical value 0.3 but it varies among analyses). The tracks considered

[2]The underlying event represents all the activity resulting from a proton-proton interaction that is not associated with the hard interaction process

[3]The basic idea of topological clustering is to group into clusters neighbouring cells that have significant energies compared to the expected noise and are designed to follow the shower development taking advantage of the fine segmentation of the ATLAS calorimeters. Details on these algorithms can be found in [80].

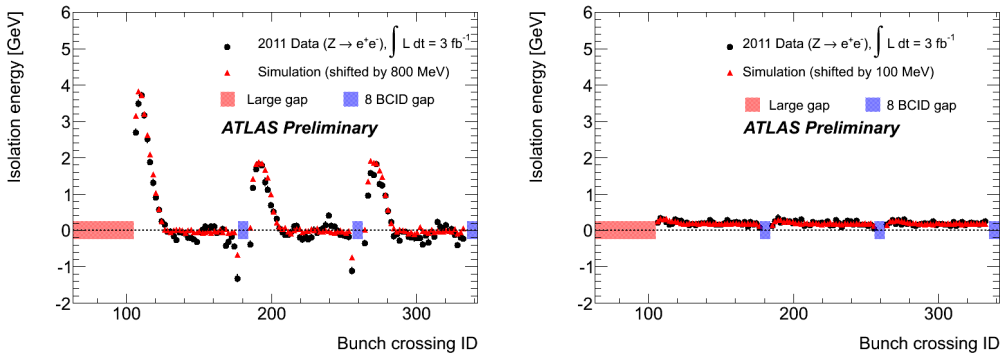

FIGURE 4.11: The mean of a binned Crystal Ball likelihood fit to the isolation distribution for electrons from Z decays is shown as a function of the bunch crossing identifiers. Based calorimeter isolation is shown on the left and in the topological isolation on the right [105].

in the computation are required to have a p_{T} >1 GeV (these cuts rejects a large amount of tracks from the underlying event and pile-up). In the case of conversion the conversion tracks are excluded from the sum through a minimal threshold in the ΔR cut.

The tracking isolation has both advantages and disadvantages compared to the calorimetric isolation. Whilst calorimetric isolation includes information for both neutral and charged particles, track isolation only considers information of charged particles, making the jet rejection from the track isolation potentially worse than the calorimetric one. However, track isolation can be more stable against pile-up, this is due to the fact that it does not suffer from the out-of-time pile-up that affects the calorimeter. Nevertheless, in order to have a track isolation which is robust against pile-up, the primary vertex has to be correctly identified, to force the isolation to only consider tracks associated to it. Choosing the correct primary vertex can be straight-forward in the case of electrons or muons but not in the case of photons, where the sufficiently precise identification of the primary vertex is only achieved with early conversions (with hits in the silicon tracker). This would lead to a photon track isolation that is not robust against increasing of pile-up. In the analyses presented in this thesis, only the calorimetric isolation is used.

Chapter 5

Study of Radiative Z Decays

Contents

5.1 Introduction

A good performance of the EMCAL is crucial for many important physics studies in ATLAS, particularly in Higgs analyses such as $H \to \gamma\gamma$ and $H \to Z\gamma$, where both searches and measurements of properties are performed. In both analyses, the invariant mass is computed via reconstruction of particles in the final state, hence a precise knowledge of kinematical quantities of final particles is absolutely critical. In the $\gamma\gamma$ channel a narrow resonance is looked over a large background, therefore photon energy resolution plays a very important role; a good control of the photon energy scale is imperative for the Higgs mass measurement in this channel.

As presented in Chapter 4, the in-situ calibration applied to photons comes from $Z \to e^+e^-$ decays. The electron and photon behaviour is not identical, therefore an electron to photon extrapolation has to be performed using MC simulation [91], and a systematic uncertainty is associated to it. A data-driven validation to the standard calibration is highly recommended to assure the best EMCAL performance, and is the purpose of the study of Z radiative decays discussed in this Chapter.

This chapter describes the extraction of the photon energy scales from a sample of Radiative Z decays performed in 7 and 8 TeV data. In Section 5.2, the Z production in Initial and Final State Radiation are described. The methods used to extract the photon energy scales are presented in Section 5.3, the data and MC samples as well as the event selection are described in Sections 5.4 and 5.5. The results obtained with the 7 TeV and 8 TeV data sample are shown in Sections 5.6 and 5.7, respectively[1]. Finally, a discussion of the method and results is found in Section 5.8.

5.2 Z production in Initial and Final State Radiation

The main diagrams contributing to the SM $pp \to Z\,(\ell^+\ell^-)\,\gamma + X$ processes, where ℓ is either an electron or a muon, are shown in Figure 5.1. The two production modes are:

[1]The 7 TeV analysis was performed in collaboration by two separated groups: Tokyo for the $Z \to ee\gamma$ decays mode, and LPNHE-Paris for the $Z \to \mu\mu\gamma$ channel. As a consequence, for the 7 TeV analysis only the muon final stated is discussed in the context of this thesis, and results in the electron channel are taken as a reference and comparison points (the 7 TeV results are fully documented in [2]). In contrast, for the 2012 analysis both the electron and muon final states were studied, and are presented in this document.

Initial State Radiation (ISR), where the Z boson is created together with a radiated photon, and Final State Radiation (radiative Z decays), that occurs when the photon is radiated by one of the leptons in the final state through Bremsstrahlung. In Figure 5.2, a $Z\gamma$ event candidate recorded by ATLAS in 2010 is displayed.

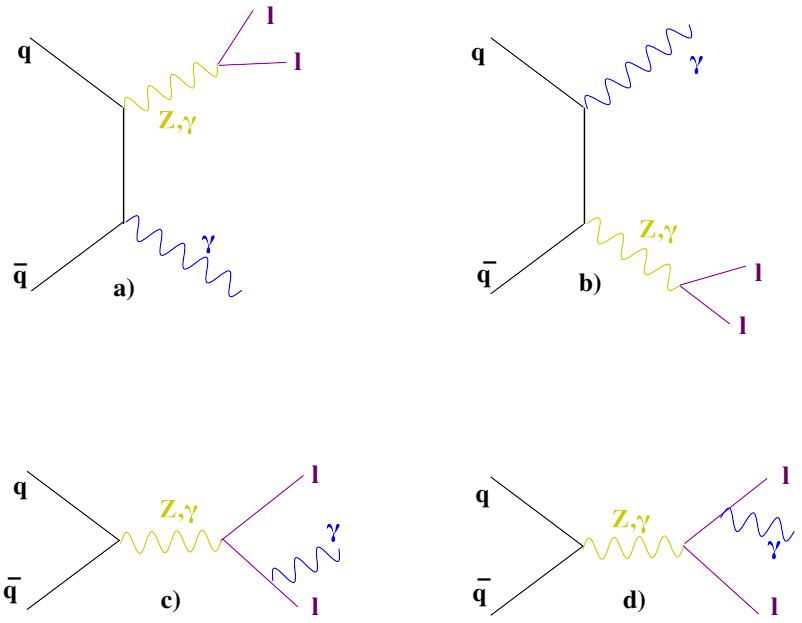

FIGURE 5.1: Feynman diagrams for the SM $pp \to Z\gamma$ productions. The top diagrams a) and b) are Initial State Radiation. The bottom diagrams c) and d) are Final State Radiation.

Each of these two processes can be identified by comparing the two- and three-body invariant mass distributions. In the ISR process, the two-body invariant mass is described by the Z line-shape, whilst the total invariant mass is larger than 91 GeV due to the addition of the photon energy to the lepton pair. The opposite case occurs for FSR, where the Z line-shape is followed by the three-body invariant mass. This can clearly be seen in the scatter plot of the two-body versus the three-body invariant mass in the muon decay channel presented in Figure 5.3.

Isolated photons from Z radiative decays (FSR) in the electron and muon decay channels are studied in this chapter. The kinematics of the final objects can be easily reconstructed and as they follow the Z line-shape, are easy to identify in data, and provide a sample with small background contamination, from which the in-situ photon energy scales can be extracted. The ISR process will be discussed later in Chapter 7, given that it is the main background for the $H \to Z\gamma$ search.

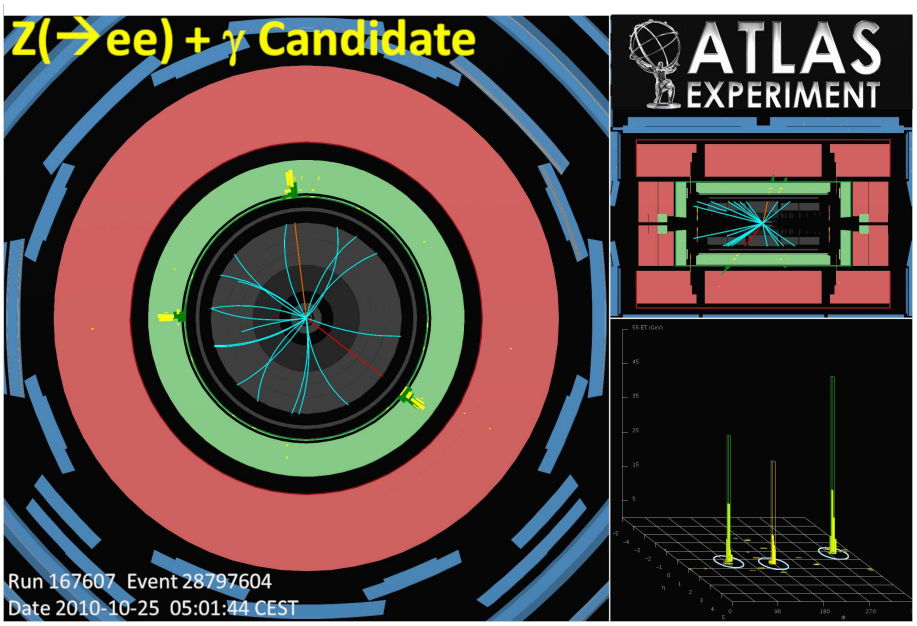

FIGURE 5.2: Candidate for a Z→ e^+e^- decay, with the Z boson produced in association with a photon, collected on 28 October 2010. The Z boson candidate invariant mass is 91 GeV. The two electrons and the photon are well isolated.

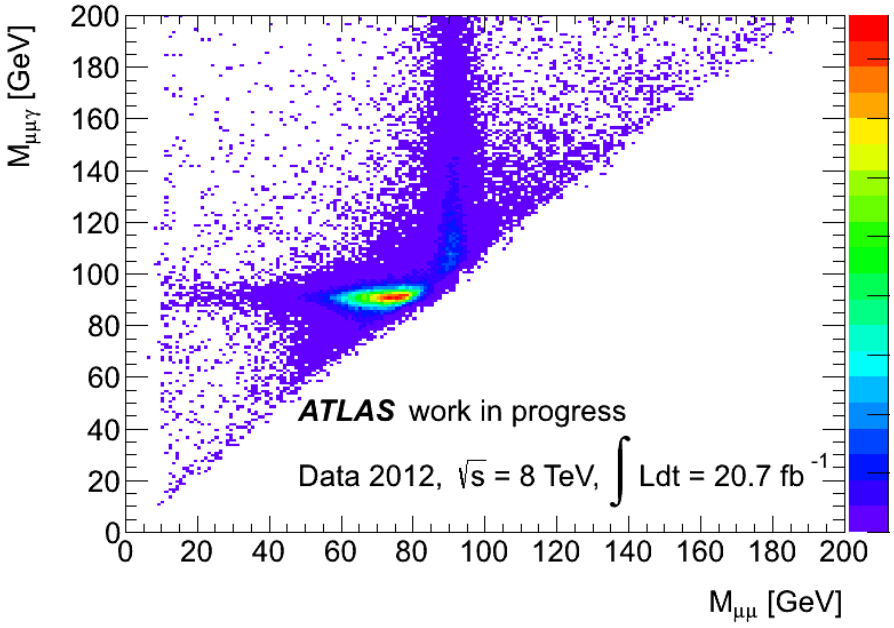

FIGURE 5.3: Scatter plot of the two-body invariant mass $m_{\mu\mu}$ as a function of the three-body invariant mass $m_{\mu\mu\gamma}$ for Zγ decays in the muon channel. The vertical pattern shows the ISR contribution with $m_{\mu\mu} \sim m_{\mathrm{Z}}$ while the horizontal pattern shows the FSR candidate where $m_{\mu\mu\gamma} \sim m_{\mathrm{Z}}$.

5.3 Measurement of the Photon Energy Scale

The goal of this study is to extract the photon energy scales in data directly from the clean photon sample from FSR events, in order to validate the standard EMCAL calibration .

For an η or p_{T} region i, after applying both the MC-based and data-driven Z$\rightarrow e^{-}e^{+}$ in-situ corrections to the photon energy scales[2], as explained in Chapter 4, any residual mis-calibration between data and MC can be parametrized as:

$$E_i^{\mathrm{MC}} = E_i^{\mathrm{data}}/(1+\alpha_i), \tag{5.1}$$

where E_i^{MC} and E_i^{data} are the corrected photon energies in region i, for MC and data respectively, and α_i measures the residual mis-calibration in the photon energy scale (ES). The α_i energy-scale factors are extracted by comparing the three-body invariant mass distributions in data and MC in the following way:

1. The photon energy in data is shifted by α_i and the three-body invariant mass is recalculated.

2. The recalculated invariant mass distribution is compared to MC. The value of α_i that provides the best agreement in the distributions of data and MC is the residual mis-calibration in the ES, which henceforth will be referred to as the "photon energy scale". This agreement is quantified separately by two methods: the so-called "χ^2" and "Double Ratio" methods, both described in the next sections.

In the following, the analysis performed over the 4.7 fb-1 of data with a 7 TeV centre-of-mass collision energy, recorded in the March-November 2011 period, is referred to as "the 2011 analysis" or the "7 TeV analysis". The "2012 analysis" or "8 TeV analysis" uses the 20.7 fb^1 of 8 TeV data recorded in 2012.

[2]The photon energies in MC are smeared to reproduce the resolution observed in data from Z$\rightarrow e^{-}e^{+}$ events.

5.3.1 The χ^2 Method

For each value of α in data, a χ^2 is calculated by binning the three-body invariant mass histograms in an 80 to 100 GeV interval, according to the following:

$$\chi^2 = \sum_{j=1}^{N_{\text{bins}}} \frac{\left(N^{\text{data}}_{\ell\ell\gamma,j} - N^{\text{MC}}_{\ell\ell\gamma,j}\right)^2}{(\sigma^{\text{data}}_{\ell\ell\gamma,j})^2 + (\sigma^{\text{MC}}_{\ell\ell\gamma,j})^2}, \tag{5.2}$$

where j is the bin label, N_{bins} (total number of bins) is equal to 20, $N_{\ell\ell\gamma,j}$ are the number of events in each bin, and $\sigma_{\ell\ell\gamma,j}$ their corresponding Poisson uncertainties. The set of resulting χ^2 values as a function of α_i, is fitted around its minimum to a parabola, parametrized as:

$$\chi^2(\alpha) = \frac{(\alpha - \alpha_{\text{min}})^2}{\sigma^2_\alpha} + \chi^2_{\text{min}}, \tag{5.3}$$

where α_{min} is the value of α that minimises the function, σ_α is the error on α, and χ^2_{min} the χ^2 minimum value. All these parameters are floated in the fit. The photon energy scale is thus $(\alpha_{\text{min}} \pm \sigma_\alpha)$.

The χ^2 method was initially used in the analysis of 2011 data. As this method is found to be more sensitive to the lepton energy uncertainties, it is then kept as a cross-check to the Double Ratio method, that is the main method used in the analysis of 2012 data and is described in the next section.

5.3.2 The Double Ratio Method

In this method, the mean value of the three-body invariant mass distributions in data and MC are compared explicitly. For different values of α, the recomputed distribution is fitted in data, and the α-dependent double-ratio R is calculated:

$$R(\alpha) = \frac{\langle m(\ell\ell\gamma(\alpha))_{\text{data}}\rangle \,/\, \langle m(\ell\ell)_{\text{data}}\rangle}{\langle m(\ell\ell\gamma)_{\text{MC}}\rangle \,/\, \langle m(\ell\ell)_{\text{MC}}\rangle}, \tag{5.4}$$

where $\langle m(\ell\ell\gamma)\rangle$ and $\langle m(\ell\ell)\rangle$ are the fitted mean values of the three-body and two-body invariant masses, respectively.

The ratio in data is set to cancel out the lepton scale uncertainties, but the different kinematics could shift the radiative peak with respect to the non-radiative one.

Hence the double-ratio: any such kinematic bias is cancelled out by dividing the above by the same ratio in MC.

As illustrated in Figure 5.4, the value of α that provides the best agreement in these distributions with $R(\alpha) = 1$ is the photon energy scale.

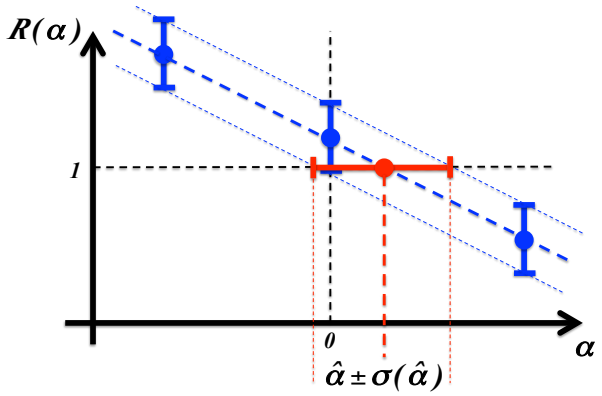

FIGURE 5.4: Schema of the Double Ratio Method. The photon energy scale is $\hat{\alpha}$, with $R(\hat{\alpha})$=1.

Fitting strategy

The unbinned distribution is fitted with a composite model of a function (V) for the Z line shape, and a wide gaussian (wGA) (with parameters μ_{wGA} as the mean value and σ_{wGA} as the resolution) to model the outliers and the small background, all functions of the invariant mass $m_{\ell\ell\gamma}$.

The complete probability density function (PDF) is thus defined as :

$$\mathcal{P}(m_{\ell\ell\gamma}) = f_V \times V(m_{\ell\ell\gamma}) + (1 - f_V) \times wGA(m_{\ell\ell\gamma}), \tag{5.5}$$

with f_{V} as the fraction of events belonging to the V species.

The extended likelihood function with the complete PDF $\mathcal{P}$(V+wGA), for the "n" events, coming from a Poisson distribution with a mean value equal to κ_{ev}, is:

$$\mathcal{L} = \frac{{\kappa_{ev}}^n e^{-\kappa_{ev}}}{n!} \prod_i^{\mathrm{n}} \mathcal{P}(m_{\ell\ell\gamma}; a_1 ... a_m), \tag{5.6}$$

where $a_1 ... a_m$ are the parameters that maximise the likelihood and are extracted from the fit. These parameters depend of the choice of the V function used to model the Z peak, which is the convolution a Breit-Wigner with a resolution function. The Breit Wigner (BW) function is defined as:

$$BW(m_{\ell\ell\gamma}) = \frac{2}{\pi} \frac{\Gamma_{BW}^2 \mu_{BW}^2}{(m_{\ell\ell\gamma}^2 - \mu_{BW}^2)^2 + m_{\ell\ell\gamma}^4 (\Gamma_{BW}^2 / \mu_{BW}^2)}, \tag{5.7}$$

with μ_{BW} is the pole mean value and Γ_{BW} its width. The Breit-Wigner is convolved with one of the following functions:

1. A gaussian function:

$$GA(m_{ll\gamma}) = \frac{1}{\sigma_{GA}\sqrt{2\pi}} e^{-\frac{(m_{ll\gamma} - \mu_{GA})^2}{2\sigma_{GA}^2}} \tag{5.8}$$

   where μ_{GA} is the central value of the gaussian and σ_{GA} its width.

2. A Crystal Ball function:

$$CB(m_{\ell\ell\gamma}) = N \cdot \begin{cases} \exp\left(-t^2/2\right), & \text{for } t > -\alpha, \\ \left(\frac{n_{\mathrm{CB}}}{|\alpha_{\mathrm{CB}}|}\right)^{n_{\mathrm{CB}}} \cdot \exp\left(-|\alpha_{\mathrm{CB}}|^2/2\right) \cdot \left(\frac{n_{\mathrm{CB}}}{|\alpha_{\mathrm{CB}}|} - |\alpha_{\mathrm{CB}}| - t\right)^{-n_{\mathrm{CB}}}, & \text{otherwise}, \end{cases} \tag{5.9}$$

   where $t = (m_{\ell\ell\gamma} - \mu_{\mathrm{CB}})/\sigma_{\mathrm{CB}}$, with μ_{CB} as the distribution mean value, σ_{CB} represents invariant mass resolution. The non-Gaussian tail is parametrized by n_{CB} and α_{CB}. N is a normalisation parameter.

For the 7 TeV analysis the V function is defined as:

$$V = BW \otimes GA, \tag{5.10}$$

this convolved function is also called a Voigtian, in which the BW width is fixed to the PDG value (2.49532 GeV [106]). There are two parameters of the V function which are let free in the fit: its mean value $\mu_V = \mu_{BW}$ and the resolution $\sigma_V = \sigma_{GA}$.

The total PDF $\mathcal{P}$ is fitted on events in the mass range of 60 to 120 GeV (both in the 7 and 8 TeV analyses) to extract the total total unknown parameters (κ_{ev}, f_{V}, μ_{V}, σ_{GA}, μ_{wGA}, σ_{wGA}).

For the 8 TeV analysis, a Crystal Ball function was instead used to convolve the Breit-Wigner, as the larger statistics showed the need to address a proper modelling of the leakage tails, which are mainly present in the electron channel:

$$V = BW \otimes CB, \tag{5.11}$$

the BW width is again set to the PDG value, and the tail parameter n_{CB} is fixed to 10. The unknown parameters for the V function are the Z pole mean value ($\mu_V = \mu_{BW}$), the resolution ($\sigma_V = \sigma_{CB}$) and the tail parameter ($\alpha_V = \alpha_{CB}$). These and the rest of parameters from the total PDF $\mathcal{P}$ (κ_{ev}, f_{V}, μ_{wGA}, σ_{wGA}) are extracted from the extended maximum likelihood fit.

5.4 Data and MC samples

Collision data are compared to MC simulations. The generated events pass through the full ATLAS detector simulation [107] based on Geant4 [108], that provides data compatible with 2011 and 2012 data reprocessing, corresponding to LHC running with 50 ns bunch spacing. Pile-up is also included in the simulation. The MC samples are re-weighted to reproduce the distribution of mean number of interactions per bunch crossing observed in data, and the size of the luminous beam-spot.

Simulation samples at $\sqrt{s} = 7$ TeV

Samples with a Z boson decaying into a muon pair are generated with PYTHIA6 [109], without any additional kinematic filters at the generation or simulation stage. PYTHIA simulates at leading order (LO) all aspects of the physical process; both perturbative (hard scatter matrix element calculation) and non perturbative as Parton Density Functions (PDFs), fragmentation and hadronization.

Simulation samples at $\sqrt{s} = 8$ TeV

For the 7 TeV analysis, the only suitable MC sample produced at LO is PYTHIA. In contrast, for the 8 TeV analysis the simulated $Z\gamma$ events are generated with SHERPA 1.4.1 [110–112], using the CT10 family of PDFs calculated at next-to-leading order (NLO) [113]. There are differences between the SHERPA generator

and the PYTHIA used in 2011, for example SHERPA calculates the interference term between the ISR and FSR diagrams. Separate samples are produced for the $ee\gamma$ and $\mu\mu\gamma$ final states. Up to three additional partons are produced in the hard scattering processes, with matrix elements implemented at LO.

Data Samples

The determination of the photon scale using the Z boson in the di-muon decay mode and one photon in final state radiation uses all proton-proton of 2011 data (4.7 fb^{-1}) for the 7 TeV analysis. All 2012 data for the muon and electron decay channel is used in the 8 TeV analysis (20.7 fb^{-1}).

5.5 Event Selection

Two samples are extracted in data and MC, one specific sample of a Z decay with radiation (two leptons and a photon) and one inclusive sample of di-lepton final state. Events are selected by requiring two oppositely charged isolated leptons (electrons or muons) and a photon, such that the three-body invariant mass is close to the Z mass peak.

Combined muons (CB) are reconstructed by combining the two independent measurements of the Inner Detector (ID) and the Muon Spectrometer (MS) using the parameters of the reconstructed tracks and their covariance matrices (the so-called STACO reconstruction [114]); the selection criteria are detailed in Table 5.1. The momentum of the muons is corrected in MC to better reproduce the data. In this correction the ID, MS and CB momentum is smeared and a scale correction is applied. No correction is applied to data. The corrections applied to MC have been calculated from the comparison of the Z line-shape in data and MC, as described in [115].

Electrons and photons are reconstructed and calibrated as described in Chapter 4, their selection criteria are detailed in Tables 5.2 and 5.3. All reconstructed objects are fully calibrated, which means that the energy of electrons and photons are smeared in MC and scaled in data. In addition, the converted photon energy is corrected by a calibration explained in Chapter 6. Photons with p_{T} >15 GeV are measured in the 7 TeV analysis, and this cut is relaxed to p_{T} >10 GeV for the 8

TeV analysis. The difference in the lepton p_{T} cut between the 7 and 8 TeV is purely circumstantial, as changing the p_{T} threshold does not affect the final photon scale.

In order to eliminate the ISR contribution and constrain the FSR events, a rectangular cut is performed in the $m_{\ell\ell} - m_{\ell\ell\gamma}$ plane. A ΔR cut between the photon and its closest lepton is applied to eliminate contamination of the photon cluster (with a shower in the electron channel or a MIP [3] deposit in the muon case) that might be produced by the lepton. Details about these cuts are found in Table 5.4.

The average photon purity in both samples is estimated from MC and is about 97% (loose photons) in 2011, and 98% in 2012. The main source of background events are Z +jets, where the jet contains photons from neutral hadron decays, such as $\pi^0 \rightarrow \gamma\gamma$.

Events in the $Z \rightarrow \mu\mu\gamma$ and $Z \rightarrow ee\gamma$ channels are analysed separately. The consistency of results in both channels allows to have a combination into a single measurement.

Muons		
Category	7 TeV analysis	8 TeV analysis
Trigger	EF_mu18_MG || EF_mu18_MG_medium || EF_mu40_MSonly_barrel_medium	EF_mu24i_tight || EF_mu36_tight || EF_2mu13 || EF_mu18_tight_mu8_EFFS
General Cuts:	* Muons with a Z position $\lvert Z_{\mathrm{PV}}\rvert$ <10 mm to the primary vertex	
	* Pseudo-rapidity region in $\lvert\eta\rvert$ <2.4	
Identification:	* Tight Identification criteria	
Isolation:	* Ptcone30/P_t < 0.15	
p_{T} min:	$p_{\mathrm{T}} > 15$ GeV	$p_{\mathrm{T}} > 20$ GeV
ID Cuts:	* Pixel b layer hit except the extrapolated muon track passes by an un-instrumented or dead area of the b-layer	
	* N^o pixel hits+N^o crossed dead pixel sensors > 1 * N^o SCT hits+N^o*crossed* dead SCT sensors > 5	* N^o pixel hits+N^o crossed dead pixel sensors > 0 * N^o SCT hits+N^o crossed crossed dead SCT sensors > 4
	* N^o pixel holes+N^o SCT holes < 3	
Muons with $0.1 < \lvert\eta\rvert < 1.9$:	*N^o TRT hits(nTRTh)+N^o TRT outliers hits(nTRToh)>5(nTotal) * nTRToh/nTotal > 0.9	
Rest of muons:	* If nTotal >5 then nTRToh/nTotal > 0.9	

TABLE 5.1: Selection criteria applied on muon candidates, for the 2011 and 2012 analyses.

[3] MIPs stands for minimum ionising particles.

Electrons		
Category	7 TeV analysis	8 TeV analysis
Trigger	EF_el20_medium || EF_el22_medium || EF_el22vh_medium1	EF_2e12Tvh_loose1 || EF_e24vhi_medium1 || EF_e60_medium1
General Cuts:	* Electrons with a Z position $\|Z_{\text{pv}}\|$ <10 mm to the primary vertex * Pseudo-rapidity region $\|\eta\| < 1.37$ or $1.52 < \|\eta\| < 2.37$	
Identification:	* isEM Medium++ and object quality (OQ) criteria	
Isolation:	* $E_{Tcone20}/p_T < 0.15$ and $p_{Tcone20}/p_T < 0.2$	
p_{T} min:	$p_{\text{T}} > 15$ GeV	$p_{\text{T}} > 20$ GeV
ID Cuts:	*$\|d_0\|/\sigma_{d0} < 10$ where $\|d_0\|$ is the impact parameter	

TABLE 5.2: Selection criteria applied on electron candidates, for the 2011 and 2012 analyses.

Photons		
Category	7 TeV analysis	8 TeV analysis
General Cuts:	Pseudo-rapidity region $\|\eta\| < 1.37$ or $1.52 < \|\eta\| < 2.37$	
Identification:	Loose photons and OQ criteria	Tight photons and OQ criteria
Isolation:	$E_{Tcone40} < 5GeV$ (cell based)	$E_{Tcone40} < 4GeV$ (topo based)
p_{T} min:	$p_{\text{T}} > 15$ GeV	$p_{\text{T}} > 10$ GeV

TABLE 5.3: Selection criteria applied on photon candidates, for the 2011 and 2012 analyses.

Category	7 and 8 TeV analysis
Z FSR events	
$m_{\text{ll}}(ISRcut)$ $m_{\text{ll}\gamma}(FSRcut)$ Electrons Muons	Two opposite-charge leptons and one photon passing their respective cuts
	45 GeV $< m_{ll} <$85 GeV
	80 GeV $< m_{ll\gamma} <$120 GeV
	$\Delta R > 0.4$ from the photon to the closest electron. $\Delta R > s0.2$ from the photon to the closest muon.
Z events for normalisation	
m_{ll}	Two opposite-charge leptons passing their respective cuts
	60 GeV $< m_{ll} <$120 GeV

TABLE 5.4: Details about the selection of Z events, including FSR events in 2011 and 2012 analyses.

5.6 Results at $\sqrt{s} = 7$ TeV

In the muon channel, 5041 radiative Z candidate events are selected in data, corresponding to:

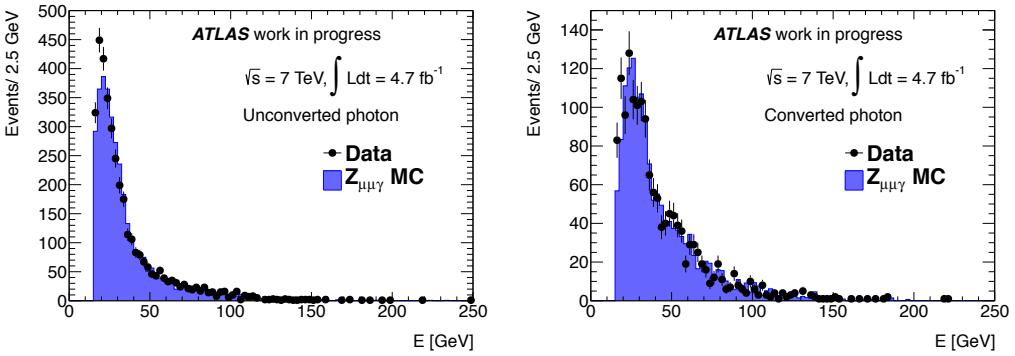

FIGURE 5.5: The energy spectrum of photon candidates passing the selection in the muon channel superimposed over the MC, shown separately for unconverted (left) and converted (right) photon candidates. The plot contains candidates from pp data collected at $\sqrt{s} = 7$ TeV in 2011 corresponding to 4.7 fb^{-1}.

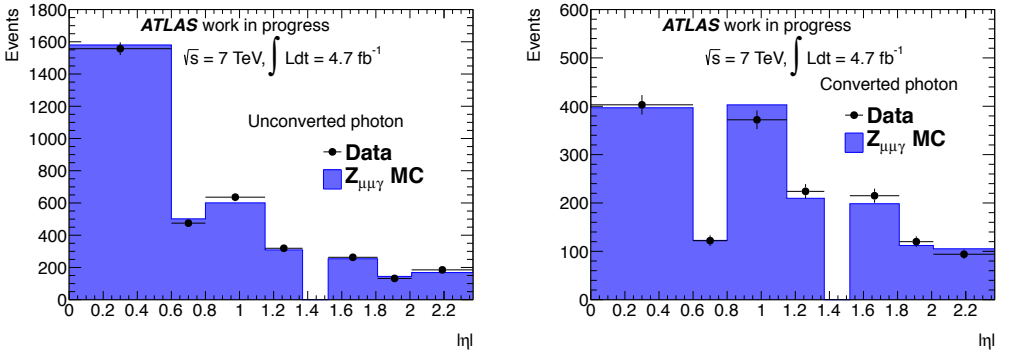

FIGURE 5.6: The pseudo-rapidity distribution for photon candidates passing the selection in the muon channel superimposed over the MC, shown separately for unconverted (left) and converted (right) photon candidates. The plot contains candidates from pp data collected at $\sqrt{s} = 7$ TeV in 2011 corresponding to 4.7 fb^{-1}.

- 3516 (4811) unconverted photons in data (MC), and
- 1525 (2036) converted photons in data (MC). Converted photons represent (30 ± 0.65)% of the data sample, which is in good agreement with MC expectations.

The energy spectrum of the radiative photons decreases rapidly with increasing energy, as illustrated in Figure 5.5. Figure 5.6 shows that unconverted photons tend to be central: more than 40% of these events are at $|\eta| < 0.6$, that is the region with the smallest amount of material upstream of the calorimeter, in the whole acceptance region of the calorimeter. The comparison of three-body invariant masses in data and MC is shown in Figure 5.7. The data is fairly well modelled by the MC in the distributions.

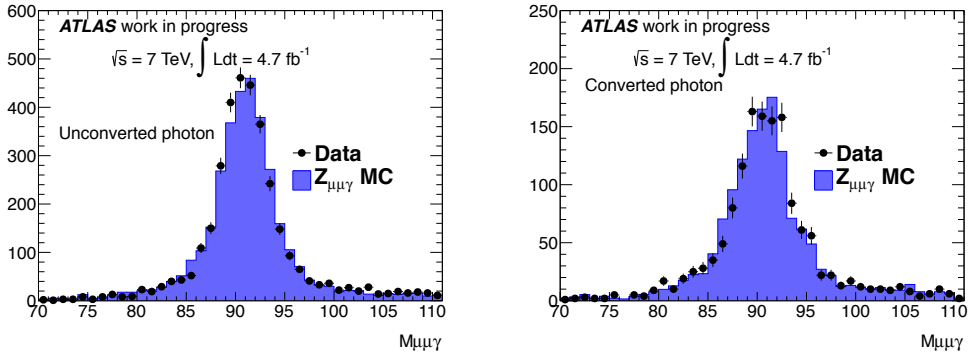

FIGURE 5.7: Invariant mass distribution of events passing the selection in the muon channel superimposed over the MC, shown separately for unconverted (left) and converted (right) photon candidates. The plot contains candidates from pp data collected at $\sqrt{s} = 7$ TeV in 2011 corresponding to 4.7 fb^{-1}.

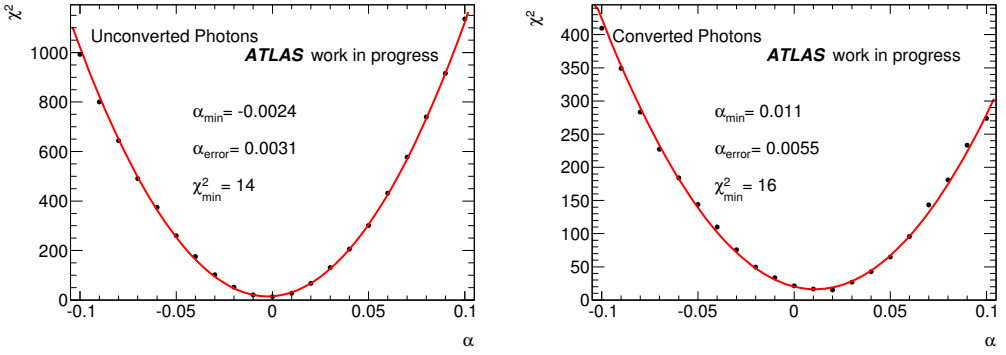

FIGURE 5.8: Results of the χ^2 method : the change in χ^2 as a function of the energy scale α, for unconverted (left) and converted (right) photons.

5.6.1 Evaluation of the photon Scales

The photon scale for unconverted and converted photons was determined by the two methods explained previously. Due to the low statistics of the sample, only two categories are considered: unconverted and converted photons.

χ^2 Method The photon scales obtained with the χ^2 method are presented in Figure 5.8. The scale α is found to be (-0.002 ± 0.003) for the unconverted case and $(+0.011 \pm 0.006)$ for the converted category. The quoted errors are only statistical.

Double Ratio Method The resulting fits of the $\mu\mu\gamma$ invariant mass distributions of data and MC are shown in Figure 5.9 for unconverted photons and Figure 5.10 for converted photons. The fits of the di-muon mass distribution in data and MC are in Figure 5.11. The double ratio of the mean value fit results are shown in

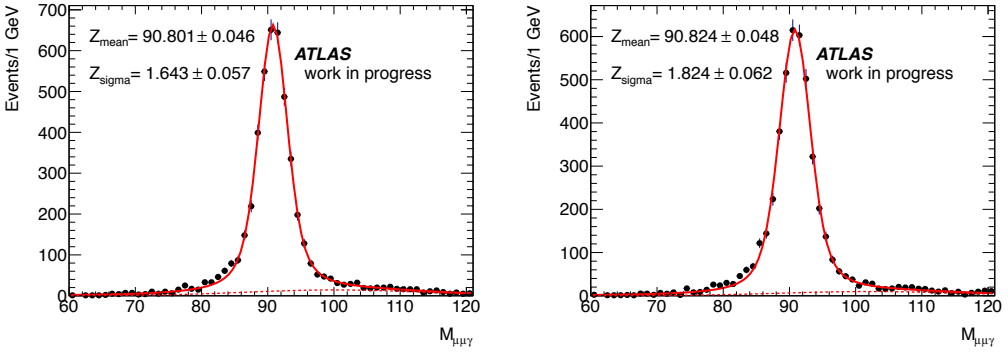

FIGURE 5.9: The fitted distribution of three-body mass spectrum, for selected radiative FSR Z events with unconverted photons, both in data (left) and MC (right).

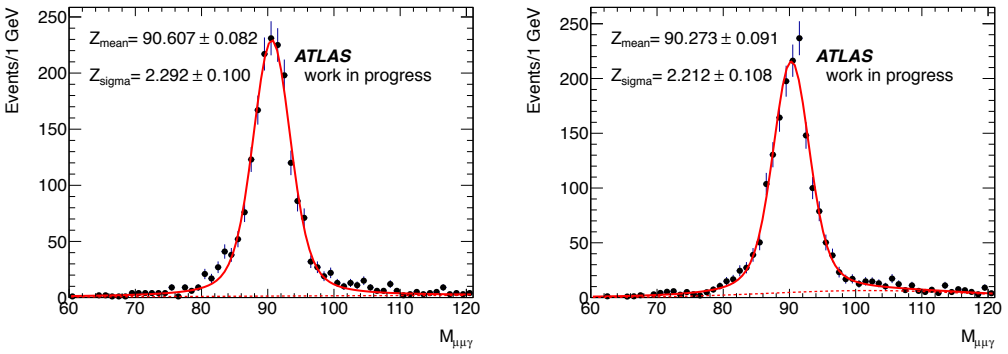

FIGURE 5.10: The fitted distribution of three-body mass spectrum, for selected radiative FSR Z events with converted photons, both in data (left) and MC (right).

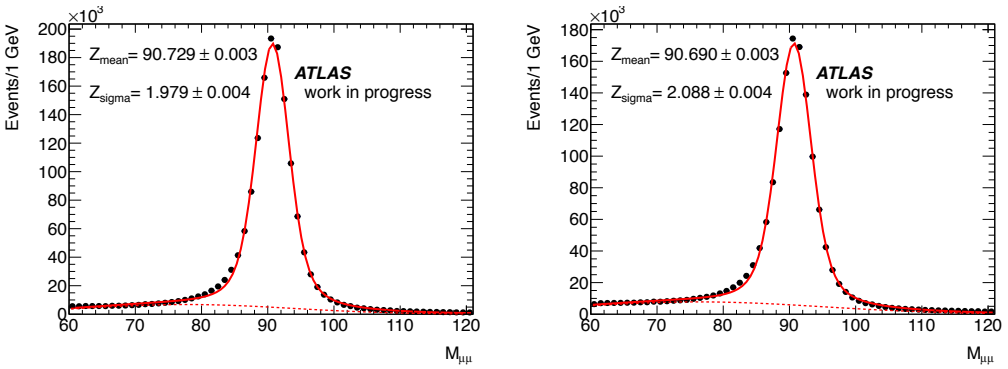

FIGURE 5.11: The fitted distribution of two-body mass spectrum, for selected non-radiative Z events, both in data (left) and and MC (right).

Figure 5.12. The extracted values of α are (-0.003 ± 0.003) for the unconverted case, and $(+0.013 \pm 0.006)$ for the converted category (errors are only statistical).

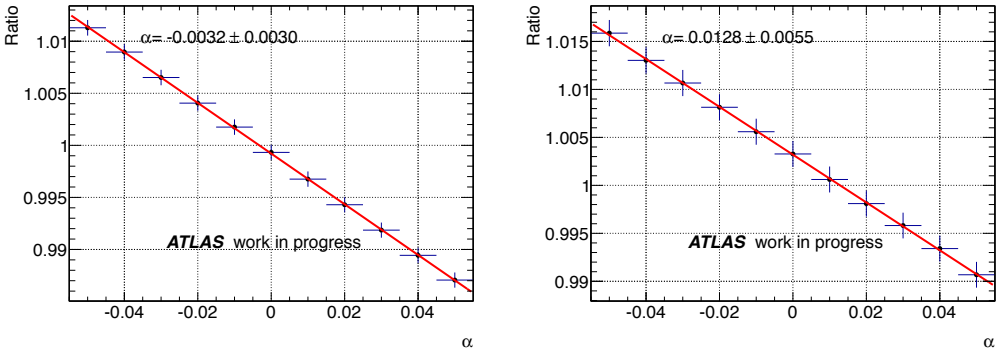

FIGURE 5.12: Ratio of fitted mean values as a function of α for unconverted photons (left) and converted photons (right).

5.6.2 Systematic uncertainties

There are different potential sources of systematic uncertainties to the energy scale: lepton energy scale and smearing, selection acceptance, background contamination, and fitting model. Among all these sources, the predominant is the uncertainty due the lepton scale.

Systematics from lepton momentum scale It is expected to be the dominant systematic uncertainty for this analysis, for both muon and electron channels. The momentum uncertainty of combined muons is obtained from the $Z \to \mu\mu$ absolute mass scale in a similar procedure to the one used for $Z \to e^+e^-$ electron scales where the Z peak mean value is compared as described in 4.2.2. A global scale uncertainty is found to be about 0.2% [99].

In this analysis, the systematic uncertainty for the muon momentum scale is obtained by shifting the muon p_{T} by $\pm 0.2\%$ (following standard recommendations from muon performance [116]) and reevaluating the photon scale (Figure 5.13 and 5.14). The systematic is evaluated as the difference between the photon scales, obtained with and without the muon momentum scale shift.

The systematic uncertainty on α from the muon scale is found to be 0.25 % for the Double Ratio method and 0.7% for the χ^2 method. As expected, the Double Ratio method is more robust against this systematics.

The electron channel was analysed by the Tokyo group. For this channel, the selected sample contains 2690 events with unconverted photons, and 1079 events with

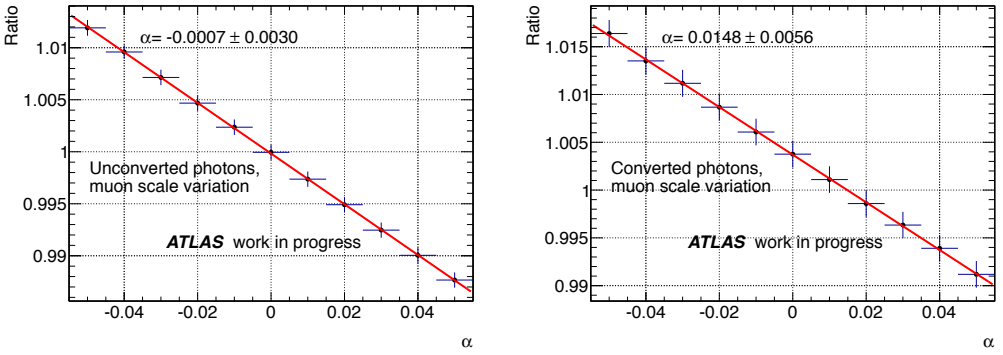

FIGURE 5.13: Ratios of fitted mean values without correcting the muon scale as a function of α for unconverted photons (left) and converted photons (right).

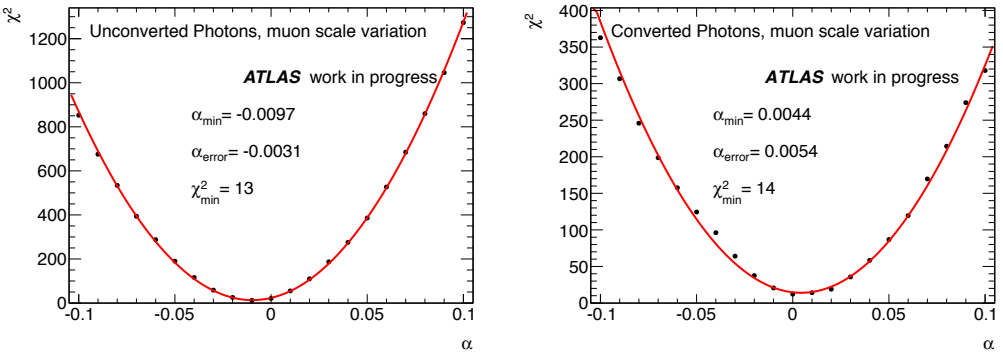

FIGURE 5.14: Results of the χ^2 method for unconverted (left) and converted (right) photons without correcting the muon scale.

converted photons. The details of these analyses are found in [2], and only the results are quoted in this thesis.

The results of the electron and muons channels are presented in Table 5.5. For the unconverted photon case there is a good agreement between both channels, within their uncertainties, but a discrepancy between the results of $Z \to \mu\mu\gamma$ and $Z \to ee\gamma$ is found in the converted photon scales, and is discussed in Section 5.6.3.

Photon scales		
Method	Unconverted	Converted
Muon channel results		
Double Ratio	- 0.003 ± 0.003 (stat.) ± 0.003 (sys.)	+ 0.013 ± 0.006 (stat.) ± 0.003 (sys.)
χ^2	- 0.002 ± 0.003 (stat.) ± 0.007 (sys.)	+ 0.011 ± 0.006 (stat.) ± 0.007 (sys.)
Electron channel results		
Double Ratio	+ 0.006 ± 0.004 (stat.) ± 0.005 (sys.)	- 0.017 ± 0.009 (stat.) ± 0.004 (sys.)
χ^2	+ 0.001 ± + 0.004 (stat.) ± 0.004 (sys.)	- 0.014 ± 0.007 (stat.) ± 0.009 (sys.)

TABLE 5.5: Photon scales for the two channels $Z \to \mu\mu\gamma$ and $Z \to ee\gamma$.

5.6.3 Additional studies on the converted photon scale

In order to understand the discrepancies in the converted photon scales, additional studies are performed. In the electron channel several causes are investigated, i.e possible electron contamination, electron-photon mis-identification, kinematic cut bias, all documented in [2]. The checks performed in the muon channel are presented next.

5.6.3.1 Effect of possible mis-modeling in muon momentum linearity

As stated before, the nominal analysis uses STACO muons, that combine an ID track and a MS track. These combined muons could suffer from a small non-linearity due to energy losses that would occur between the ID and MS measurement. In the hypothetical case where the method used to extract the photon energy scale does not cancel out correctly the muon energy scale, a non-linearity in the muon momentum could affect the photon scale. To test this potential source of non-linearity, the invariant mass was reconstructed using only inner detector information from the STACO muons, and the photon energy was reevaluated. For this cross-check, the same events that pass the nominal selection are used. The ID muon momentum is smeared and scaled as described in Section 5.5.

In Tables 5.12 and 5.13 the resulting photon scales are quoted. In both the χ^2 and the Double Ratio methods, the photon scales are compatible with the nominal result for converted and unconverted photons reported in the previous section in Table 5.5.

$$\alpha_{\chi^2} = \begin{cases} +0.0000 & \pm 0.0032\,(\text{stat.}) \quad (\text{unconverted}) \\ +0.0096 & \pm 0.0057\,(\text{stat.}) \quad (\text{converted}) \end{cases} \tag{5.12}$$

$$\alpha_{\text{Ratios}} = \begin{cases} -0.0001 & \pm 0.0031\,(\text{stat.}) \quad (\text{unconverted}) \\ +0.0113 & \pm 0.0058\,(\text{stat.}) \quad (\text{converted}) \end{cases} \tag{5.13}$$

5.6.3.2 Study of potential muon energy contamination in the photon cluster

The effect of a possible contamination from muons in the photon energy deposit is investigated. The cut at $\Delta R > 0.2$ between the photon and its closest muon is set

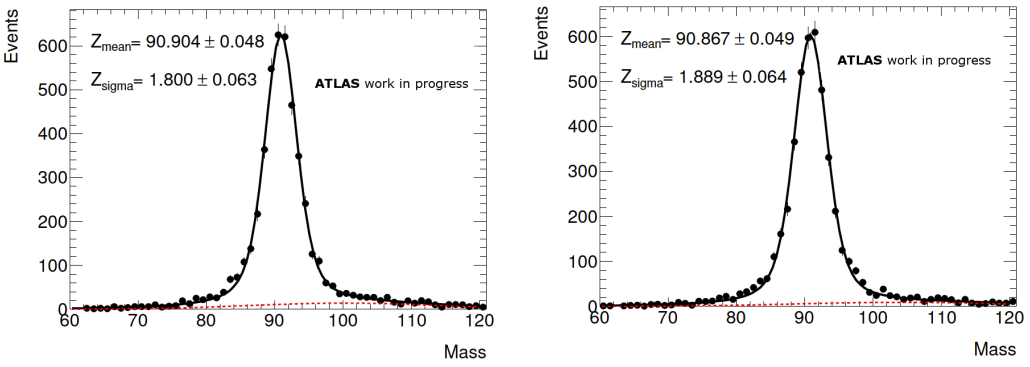

FIGURE 5.15: The fitted distributions of three-body invariant mass spectrum, for selected radiative FSR Z events where the photon is unconverted. The muons are reconstructed using only the ID information. The data sample is on the left and the MC on the right.

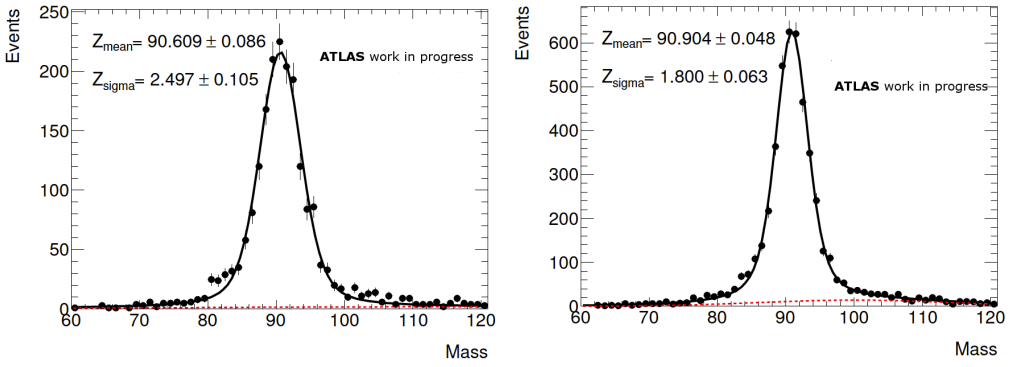

FIGURE 5.16: The fitted distributions of three-body invariant mass spectrum, for selected radiative FSR Z events where the photon is converted. The muons are reconstructed using only the ID information. The data sample is on the left and the MC on the right.

to decrease the potential effect of muon leaking energy into the photon cluster, and thus biasing the photon energy.

Figure 5.17 shows the difference between the measured muon momentum in the MS and the ID as a function of the photon energy for both categories of conversion. In case of leakage of muon energy in the photon clusters, a correlation should be visible. As no correlation is observed in Figure 5.17 (the correlation factor is about 0.025 both in for the unconverted and converted sample), the possibility of muon contamination introducing a bias in the photon energy scale is dismissed.

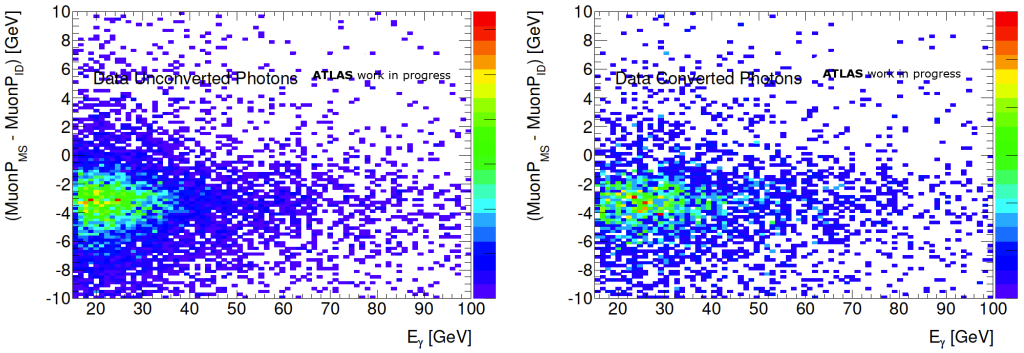

FIGURE 5.17: Difference between the measured muon momentum in the MS and ID as a function of the photon energy for unconverted (left) and converted (right) photons.

5.6.4 Discussion

The energy scale for unconverted and converted photons is evaluated using Z radiative events for the muon and electron channels, using the complete dataset at 7 TeV. Two different methods are applied to ensure robustness of the results.

For each channel, both methods offer consistency in the results. For unconverted photons, both channels give a photon scale consistent with no mis-calibration.

In the converted case, a disagreement in the scale is found between the electron and muon channels. The difference in both results is $\Delta\alpha(e-\mu) = (-0.030 \pm 0.013)$ for the ratio method, corresponding to some 2.3 standard deviations. Several studies were performed in order to understand this discrepancy: possible electron/muon contamination in the photon sample, effects of kinematic cuts, possible mis-modelling of lepton linearity and energy uncertainty, etc. None of these studies could explain the observed effect. Hence the most likely origin of this discrepancy is a statistical fluctuation.

Results using the 7 TeV sample are dominated by statistics. Improved studies and categorisations to a more complete analysis of the photon energy scale are a benefit of the larger statistics in the 2012 dataset. The analysis of this dataset is presented next.

5.7 Results at $\sqrt{s} = 8$ TeV

The 2011 analysis was a preliminary study of photon energy scales. The scope was limited by statistics, and the scales could only be extracted in two photon categories. In 2012, the integrated luminosity is about four times larger, and the photon p_{T} threshold was lowered to 10 GeV, which increases significantly the statistics (about 8 times larger than the 2011 sample). With such a data sample, the photon energy scales can now be measured in several bins of p_{T} and pseudo-rapidity, for unconverted and converted photons with one and two reconstructed tracks separately, in both the $Z \to ee\gamma$ and $Z \to \mu\mu\gamma$ channels. Finally, the measurements are combined into a final photon scale. This measurement is done for fully calibrated photons, and for photons where the $Z \to e^+e^-$ in-situ scales are removed, in order to compare the photon scales directly to MC and not only to the electron Z$\to e^+e^-$ scales.

The events passing the selection criteria detailed in Tables 5.1, 5.2 and 5.3 are the following: in the muon channel, 39379 radiative Z candidate events are selected, where 16.45 ± 0.18% of the data events are one-track converted photons and 6.73 ±0.12% are two-track converted photons; in the electron channel 21810 radiative Z candidate events are selected, with similar ratios in the conversion categories as in the muon channel. All the numbers of selected events, both on data and MC are shown in Table 5.6.

Converted photons are approximately 24% of the total sample in both channels. For the reconstruction of the 8 TeV data, the tracking, vertex and matching to clusters are improved to ensure that the reconstruction of converted photons is more robust against pile-up [117]. This change is reflected in the decrease of conversion rate from 30% in the 7 TeV sample to 24% in the 8 TeV samples. The one-track conversion case dominates the conversion sample, with 70% of the events. Figure 5.18 shows the total "conversion fraction" (defined as the ratio of number of converted photons to the total number of photon candidates) in different η regions for data and MC. As expected, the conversion fraction is smaller in the central region ($|\eta| < 0.6$), where the amount of material before the calorimeter is lower ($|\eta| < 0.6$). In this region the converted photons are only 15% of the sample, while in the transition region it increases up to 40%. This is observed to be in agreement both in data and MC.

The conversion fraction is also evaluated as a function of pile-up. Figure 5.19 shows the total conversion fraction as a function of the average interactions per bunch

crossing. An increase is clearly observed in the relative fraction of conversion categories[4], the one-track converted photon fraction is shown to grow as the pile-up increases. On the other hand the two-track conversion fraction shows the opposite pattern. In a high pile-up environment, the probability of matching one track from an underlying process to a photon cluster increases, which is not exactly the case with the two-track conversions, where the photon cluster would have to be matched to two tracks sharing a conversion vertex coming from an underlying process. This trend is also observed in MC.

In Figure 5.20, the radial distribution of the reconstructed conversion vertices (so-called radius of conversion: R_{conv} as defined in Section 4.1), is shown for the two conversion categories, for photons from both $Z \to \mu\mu\gamma$ and $Z \to ee\gamma$. Both data and MC distributions are in agreement, the vertices reconstructed in each of the three pixel layers are clearly visible in the distribution where $R_{\text{conv}} < 200\ mm$. Then, the pattern of SCT layers is exposed in the $200 < R_{\text{conv}} < 600\ mm$ range, and finally the vertex reconstruction in the TRT system is observed at $R_{\text{conv}} > 600\ mm$. Photons are reconstructed as one-track converted photons when the conversion decay is "asymmetric" (one of the conversion tracks has $p_{\text{T}} < 0.5$ GeV and is not reconstructed), or the conversion occurs so late than the two tracks are merged. Most of these conversions occur inside the TRT which has a limited ability of distinguishing hits from the two tracks, and thus reconstructs only one. Two-track conversions occur upstream and are well reconstructed by the first SCT or pixel layers.

Radiative Z candidates selected events				
	Unconverted	Converted one-track	Converted two-track	Total
Muon channel				
Data	30247	6481	2651	39379
MC	61334	13740	5606	80680
Electron channel				
Data	16598	3672	2054	22324
MC	32956	7237	4039	44232

TABLE 5.6: Selected events in data and MC for the 8 TeV analysis.

Relevant kinematic distributions for the analysis of photon scales, such as photon energy and lepton transverse momentum, pseudo-rapidity and three-body invariant mass, are built for all candidates in data, and superimposed to the SHERPA MC for comparison, and done separately in the $Z \to \mu\mu\gamma$ and $Z \to ee\gamma$ channels. The

[4]The relative fraction of conversion categories is defined as the fraction of the number of photons in a converted category with respect to total number of photons.

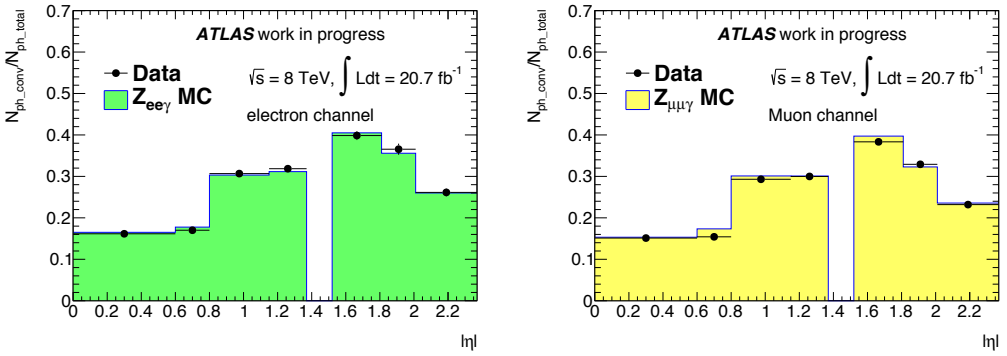

FIGURE 5.18: Photon conversion fraction in different η regions, for the electron (left) and muon (right) channels.

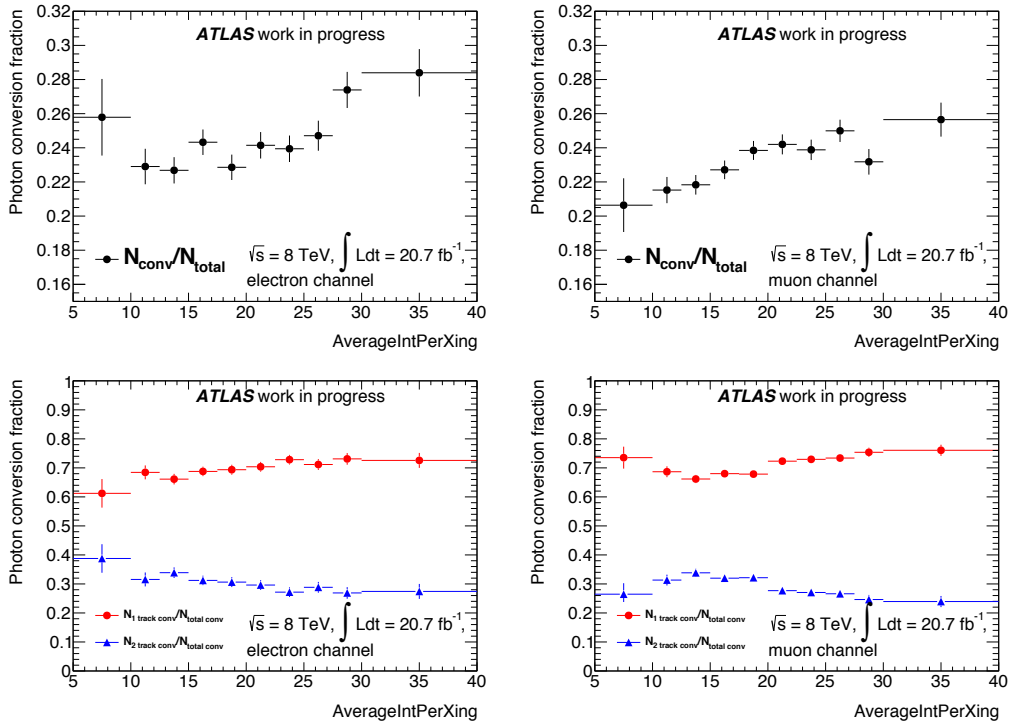

FIGURE 5.19: Photon conversion fraction as a function of the average interactions per bunch crossing in data for the electron (left) and muon (right) channels, for total conversions (top), and one- and two-track conversion (bottom).

photon transverse energy in each of the conversion categories, their pseudo-rapidity are shown in Figure 5.21, 5.22 respectively. The transverse momentum of the leptons is shown in Figure 5.23 and their pseudo-rapidity in 5.24. The MC shows a good agreement with data. Background events as Z plus jets passing the selection are mainly distributed at low p_{T} regions (less than 15 GeV), lowering the purity in this region.

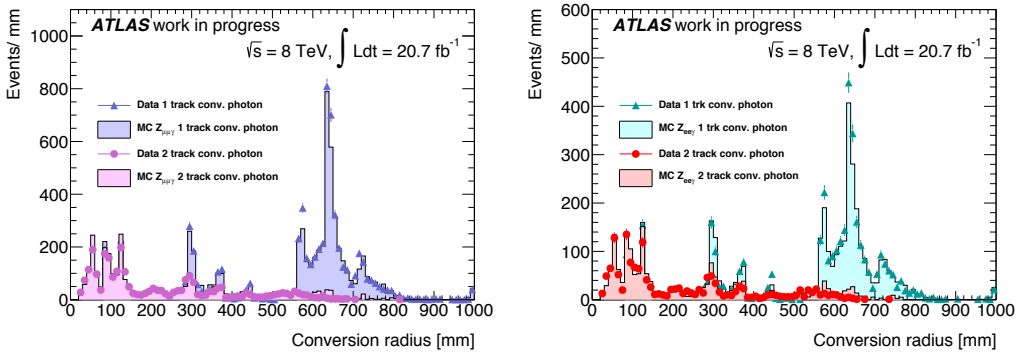

FIGURE 5.20: Radius of conversion for converted photons with one and two reconstructed tracks. Photons from $Z \to ee\gamma$ are on the left plot, and from $Z \to \mu\mu\gamma$ on the right.

5.7.1 Photon Categorisation and evaluation of the photon scales

As explained in Section 5.3, the extraction of photon scales in 2012 data is performed using the Double Ratio Method, as this was shown to be more robust against lepton systematics and small statistics.

The three-body invariant mass distribution is fitted using an analytic model, composed of a Breit-Wigner function convoluted with a Crystal Ball for the Z peak, and a wide gaussian. The latter component is included to improve the description of the tails, and model the small background component. With more statistics, this model is an improvement with respect to the model used in 2011, as it provides a more accurate treatment of leakage tails. This fact becomes important in fitting mass distributions in the electron channel, where the leakage tails are accentuated by having three objects reconstructed in the calorimeter. The fitted distributions for unconverted, converted one-track and two-track photons are shown in Figure 5.25 for both data and MC. The fitted distributions of di-lepton invariant masses, used for the normalization are shown in Figure 5.26. The fitted functions are in good agreement in data and MC in most cases of three- and two-body invariant mass. The main exception is the two-track conversion category in the electron channel, where the fitted distributions differ: the fitted mean value is shifted by -320 MeV in data with respect to MC, and its resolution on data is 14 % narrower.

First, the scales are extracted for the three conversion categories. Results in both $Z \to \mu\mu\gamma$ and $Z \to ee\gamma$ are shown in Figure 5.27 (only statistical uncertainties are shown). As the fitted functions in data and MC hinted (Figures 5.25), the scales

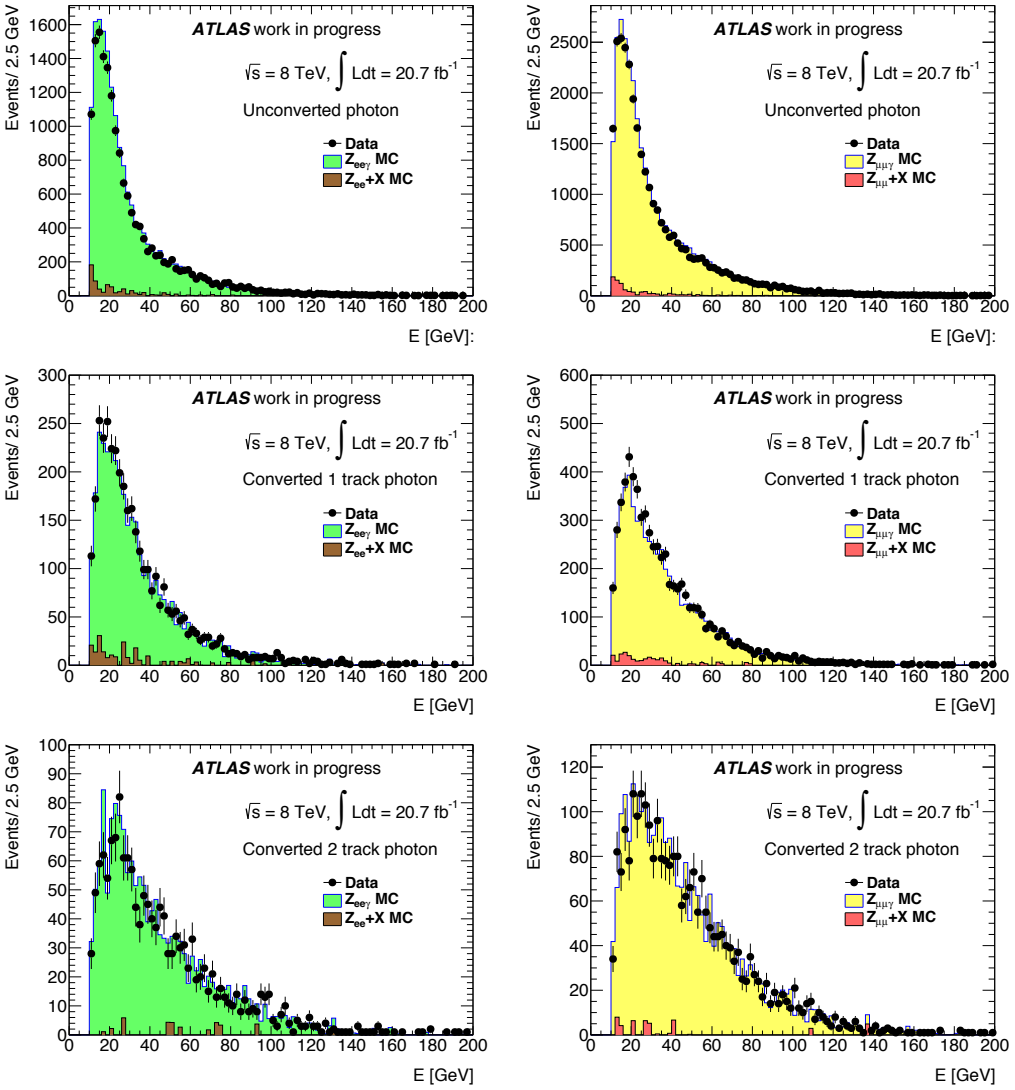

FIGURE 5.21: The energy spectrum of photon candidates passing the selection in the electron (left) and muon (right) channels, superimposed over MC, separately shown for unconverted (top),one-track (medium) and two-track (bottom) photon candidates. The plots contain candidates from pp data collected at $\sqrt{s} = 8$ TeV in 2012 corresponding to 20.7 fb^{-1}.

for unconverted and one-track converted photons agree in both channels, and are compatible with no mis-calibration in these categories. In the two-track conversion category, the muon channel gives a scale fairly compatible with zero, whilst in the electron channel the data is off by -2% with respect to MC, the difference follows the same trend as the one found in 2011 (but in the 2011 sample the conversion category included one- and two-track conversions).

Owing to the increase in statistics, a more detailed study of the photon scales is performed. The scales are extracted in η and p_{T} bins for the three conversion

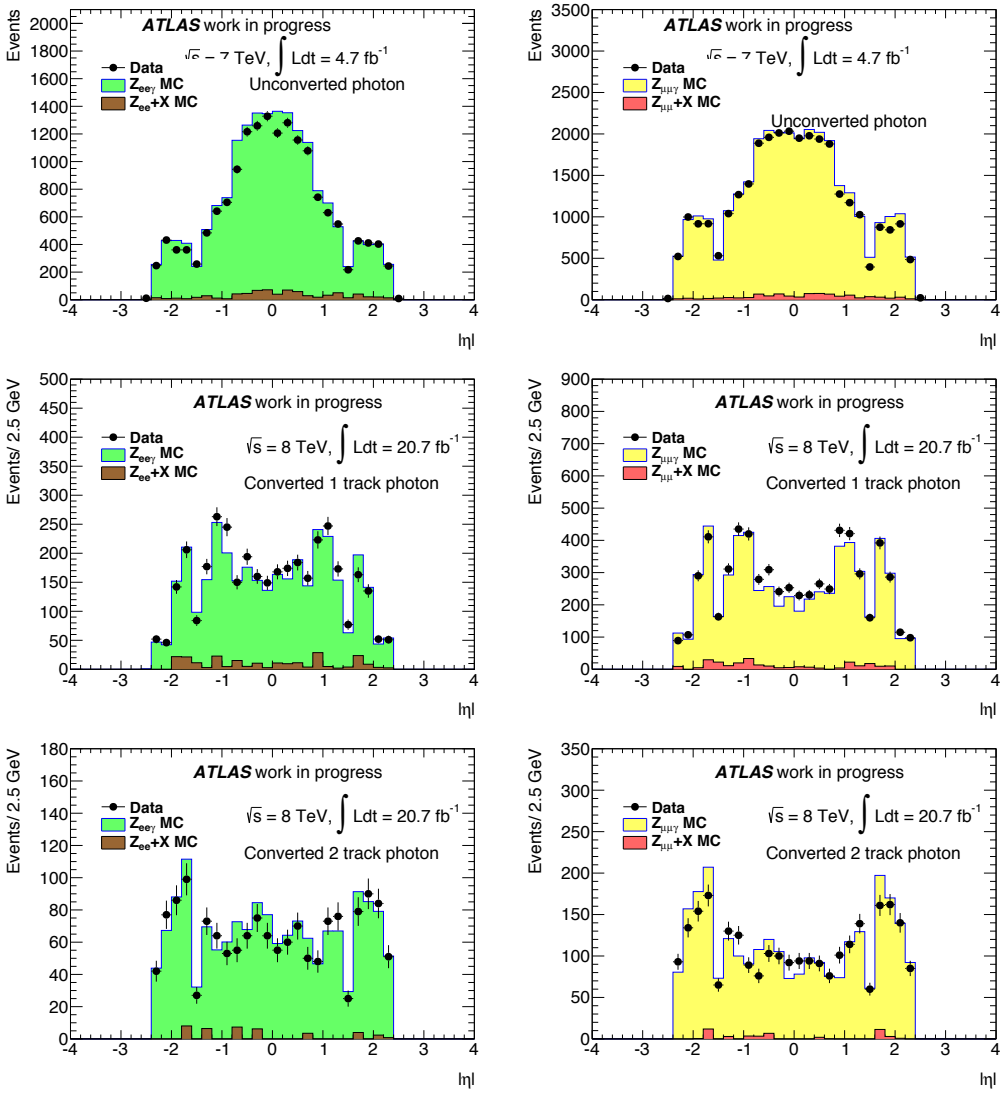

FIGURE 5.22: Pseudo-rapidity distribution of the photon candidates passing the selection in the electron (left) and muon (right) channels superimposed over the MC, separately shown for unconverted (top) one-track (medium) and two-track (bottom) converted photon candidates. The plot contains candidates from pp data collected at $\sqrt{s} = 8$ TeV in 2012 corresponding to 20.7 fb^{-1}.

categories, and in each channel independently, allowing to check for potential miscalibrations in specific detector and p_{T} regions. The p_{T} and η bins are chosen to take into account detector-oriented regions, adapting them to cuts used in physics analyses (i.e in the H$\rightarrow \gamma\gamma$ analysis), and ensuring sufficient statistics for a stable result. The p_{T} and η bins are set as following:

p_{T} bins : $\{10, 15, 20, 30, 100\}$
$|\eta|$ bins : $\{0.0, 0.6, 1.37, 1.52, 1.88, 2.37\}$

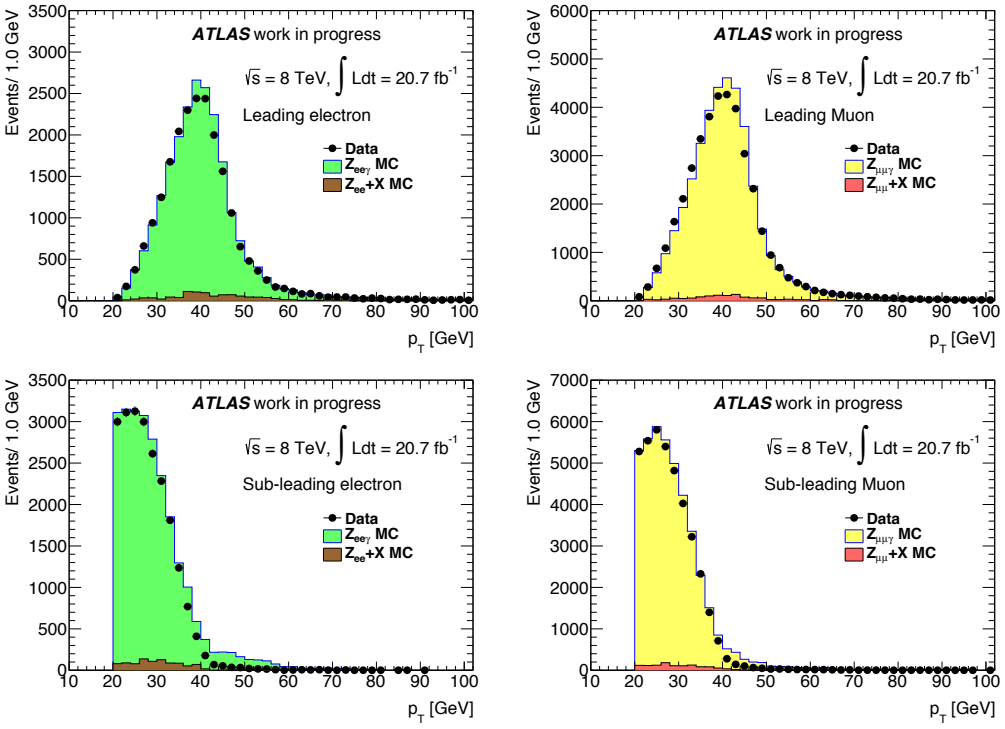

FIGURE 5.23: Transverse momentum spectrum of the leptons passing the selection in the electron (left) and muon (right) channels superimposed over MC. The plot contains candidates from pp data collected at $\sqrt{s} = 8$ TeV in 2012 corresponding to 20.7 fb^{-1}.

The fitted values of the most relevant PDF parameters of the model: the peak mean value (μ_{V}), its resolution (σ_{CB}), and the mean value of the wide gaussian (μ_{GA}) are shown in Figures 5.28, 5.29, 5.30 and 5.31, as function of the η and p_{T} bins described above, and for both data and MC in both channels,

Figures 5.28 and 5.29 show that both the Crystal Ball mean values present a growing dependency with increasing p_{T}, this behaviour is found both in data and MC and follows the same trends. As a consequence, the photon scales have a flat behaviour with p_{T}. The signal resolution is compatible in data and MC. The fitted mean value of the wide gaussian modelling the background also grows with increasing p_{T} in both data and MC with a similar trend, validating the background model used for the scales extraction.

5.7.2 Systematic uncertainties

The sources of systematic uncertainties to the photon energy scale analysis are the same as the ones in the analysis at 7 TeV described in Section 5.6.2. The two

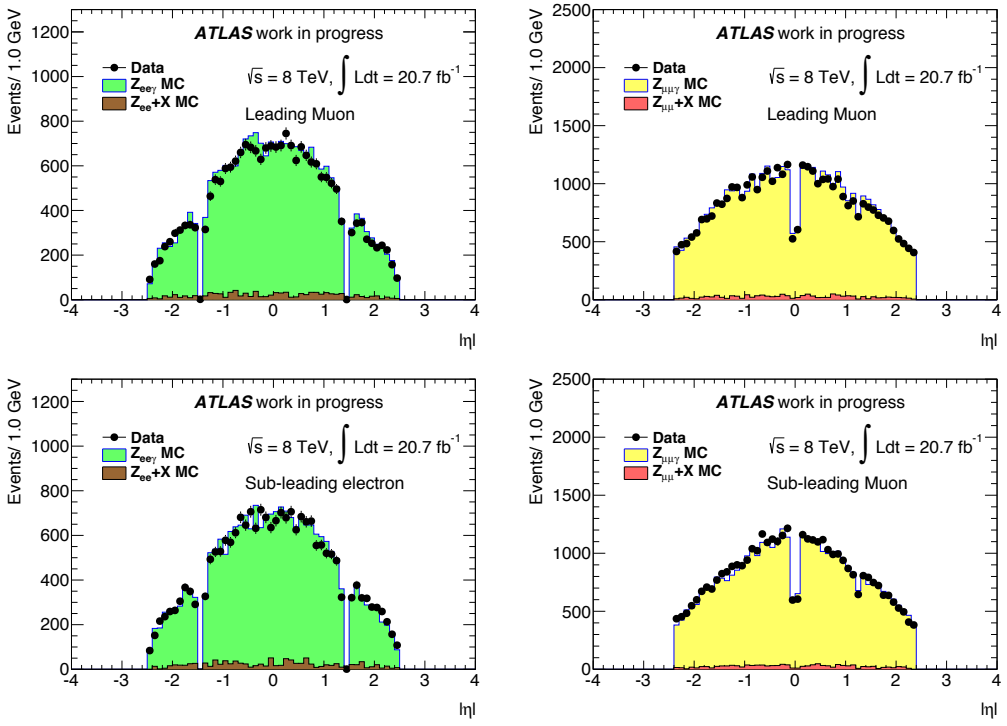

FIGURE 5.24: Pseudo-rapidity distribution of the leptons passing the selection in the electron (left) and muon (right) channels superimposed over MC. The plot contains candidates from pp data collected at $\sqrt{s} = 8$ TeV in 2012 corresponding to 20.7 fb^{-1}.

predominant systematic uncertainties are the following: uncertainty on the lepton energy scale and uncertainty on the fit model, and are assigned to the photon scale measurement.

Uncertainties from muon energy scale and muon energy resolution

A total of three systematic uncertainties variations are applied: muon scale, ID resolution and MS resolution. The evaluation uses a slightly different approach with respect to the 7 TeV analysis where the muon momentum is shifted by a global value. In the present case, the muon momentum in MC is shifted in each event by a variation that depends of the measured ID, MS and combined momentum as recommended by the Muon Combined Performance group [118]. This is done for both the momentum scale and the resolution. The scales are recomputed and the differences with respect to the nominal are summed in quadrature for a final systematic uncertainty is bellow $\pm 0.05\%$ and thus negligible.

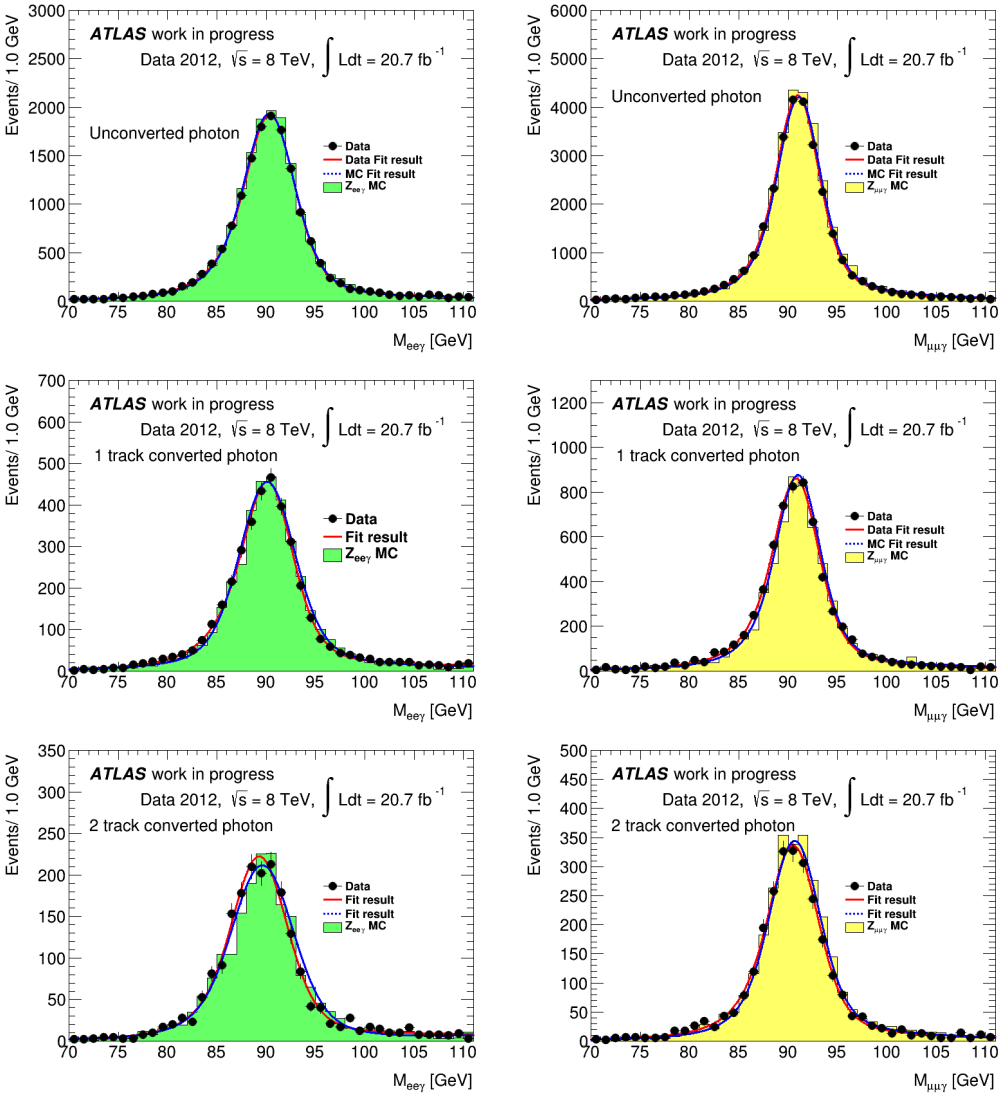

FIGURE 5.25: The distributions of three-body invariant mass, for events passing the selection in the electron (left) and muon channel (right), superimposed over the MC. The fits of a Breit-Wigner convolved with a Crystal Ball function are shown, separately for unconverted (top), one-track (medium) and two-tracks (bottom) converted photon candidates.

Uncertainties from electron energy scale and electron energy resolution

The systematic uncertainties on electron energy are the Z scale uncertainties (statistics, method and choice of generator), pre-sampler scale uncertainty, and material uncertainty. They are varied independently for each electron in MC, the scales are recalculated and the variations are summed in quadrature. The final uncertainty is $\pm 0.39\%$.

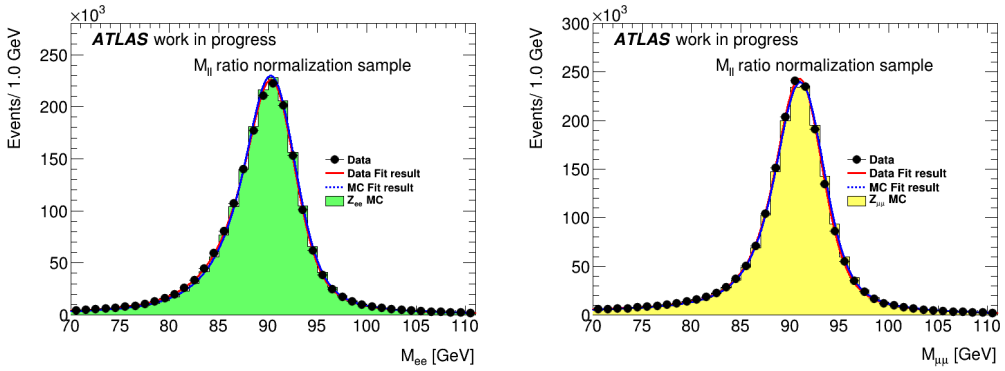

FIGURE 5.26: Di-lepton invariant mass distribution used for the Double Ratio method normalisation in the electron (left) and muon channel (right) superposing data over the MC. The fits of a Breit-Wigner convolved with a Crystal Ball function are shown.

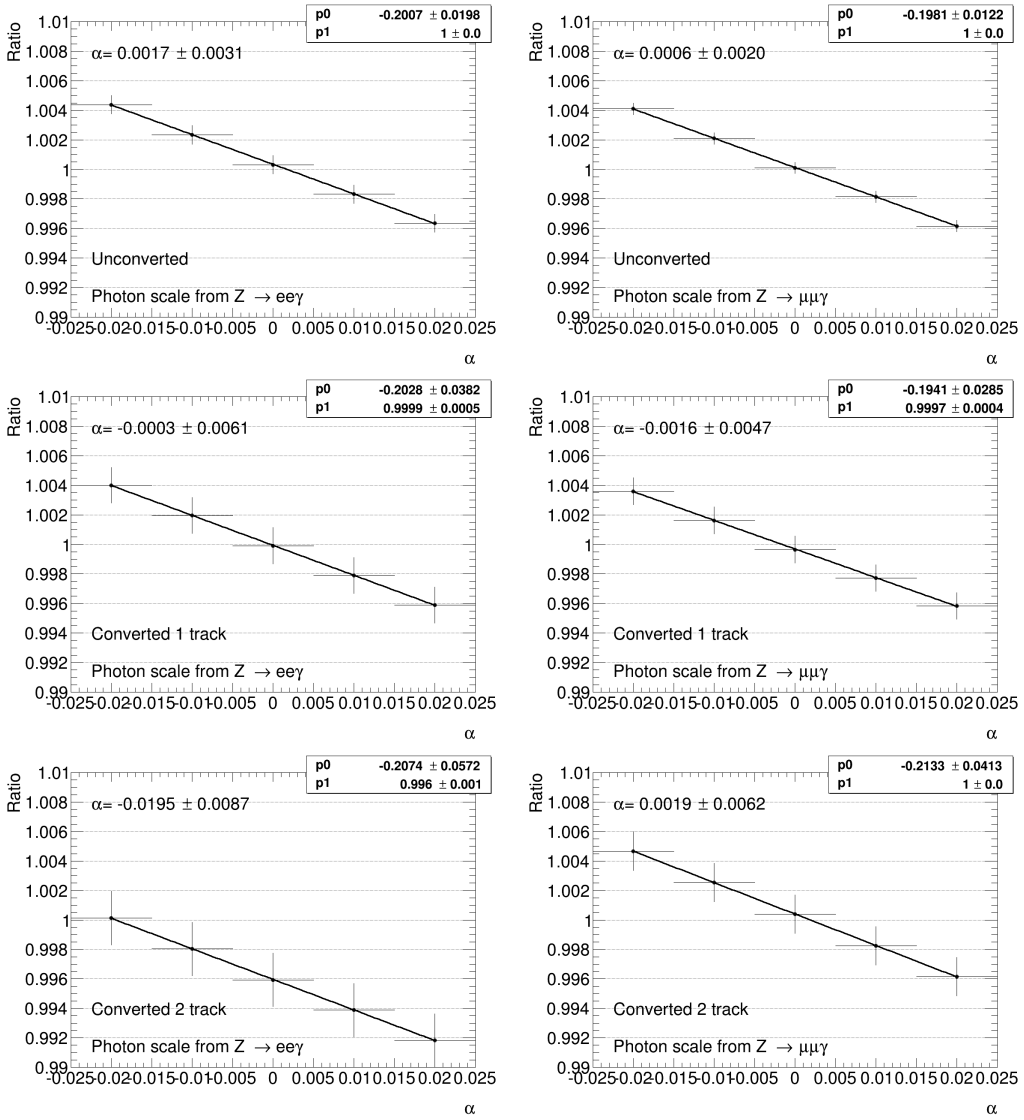

FIGURE 5.27: The Double Ratio as a function of α for the three photon conversion categories extracted from the $Z \to ee\gamma$ (left) and $Z \to \mu\mu\gamma$ channel (right). Errors are only statistical.

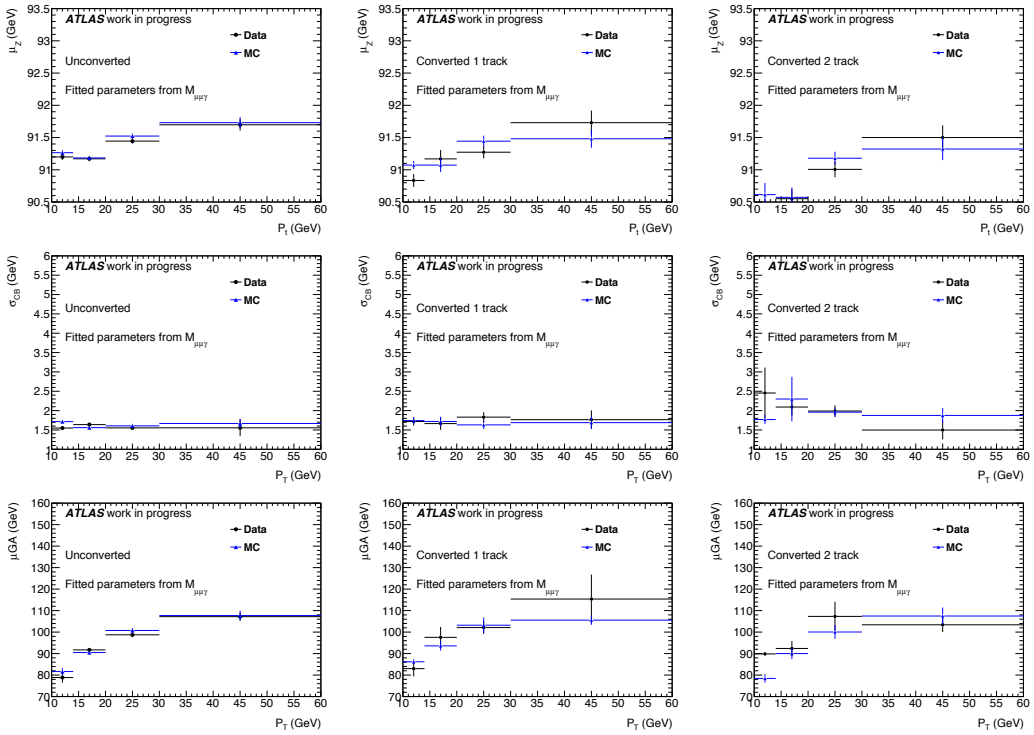

FIGURE 5.28: Fitted value of the peak mean μ_{V} (first row), resolution σ_{CB} (second row) and wide gaussian mean value μ_{wGA} (last row) in the four p_{T} bins, for unconverted (left), converted one-track (middle) and converted two-track (right) photons the $m_{\mu\mu\gamma}$ distribution.

Uncertainties from the fit range

To assign a systematic uncertainty to the fit range used for the scale determination, different fit ranges are tested. For this, 5000 toys are generated from the nominal shape extracted from fits to data. The toy datasets are generated in each of the conversion categories in the η and p_{T} bins. The standard PDF is fitted to the toys in different mass ranges as [60,120] (nominal), [60,130] and [70,110] GeV.

The fitted mean value of the Crystal Ball in each range for all the categories is shown in Figure 5.32 as a function of p_{T} and 5.33 in η. In most cases, the optimal range where μ_{CB} is fitted with the best precision is the nominal one.

The difference of the fitted mean value in the different ranges is less than 100 MeV (in 91 GeV) in most of the cases. Therefore a systematic uncertainty of $\pm 0.1\%$ due to the fit model and range is assigned to the photon scale.

In summary, in the muon channel the total systematics are in the order of 0.1% and is dominated by the fit range uncertainties (the muon scales uncertainties are

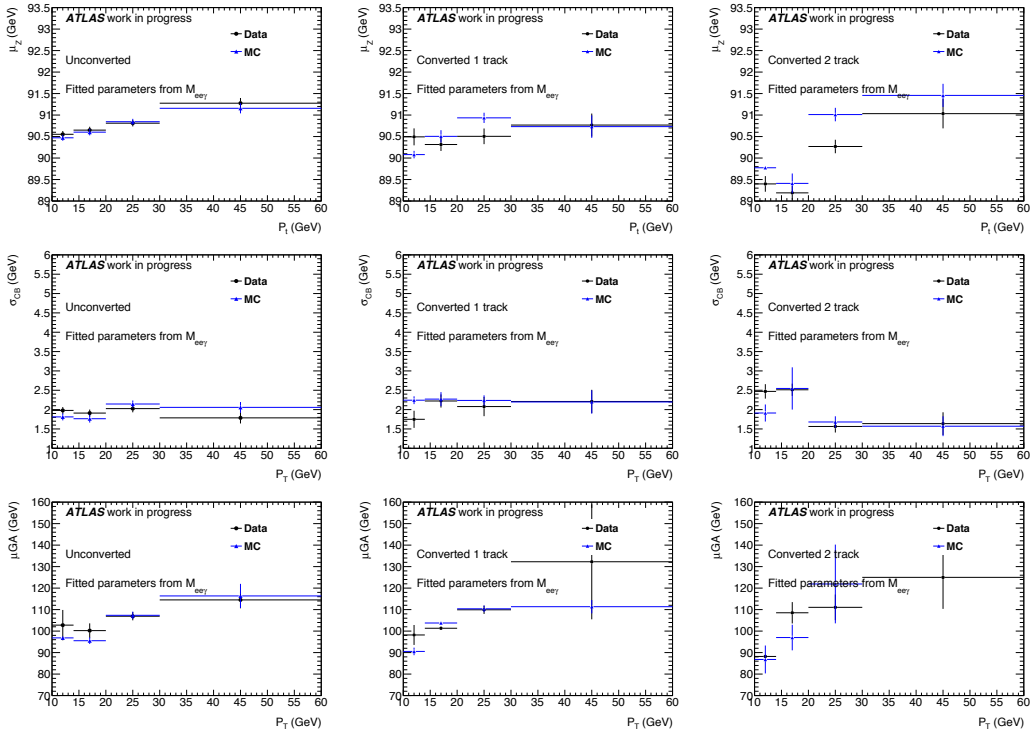

FIGURE 5.29: Fitted value of the peak mean μ_{V} (first row), resolution σ_{CB} (second row) and wide gaussian mean value μ_{wGA} (last row) in the four p_{T} bins, for unconverted (left), converted one-track (middle) and converted two-track (right) photons from the $m_{\mathrm{ee}\gamma}$ distribution.

negligible). The statistical uncertainties are ±0.2% (unconverted), ±0.5% (one-track converted) and ±0.6% (two-track converted) for the inclusive cases . The η and p_T based categories suffer of higher statistical uncertainties (in a ±0.3% to ±0.5% range in the unconverted case up to a ±0.9% - ±1.6% range in the two-track converted categories). In both inclusive and categorised cases the total uncertainties (statistical and systematics) are dominated by the statistical errors.

In the electron channel, the dominant systematic is the uncertainty on the electron scale (±0.39% from a total of ±0.41% including the uncertainty associated to the fit range). The statistical uncertainties in the inclusive cases are ±0.3% (unconverted), ±0.6% (one-track converted) and ±0.9% (two-track converted). In the categorised scales the statistical uncertainties are correspondingly larger, from ±0.4% to ±0.7% in the unconverted case and from ±1% to ±1.9% in the two-track converted categories. Only the unconverted inclusive scales are dominated by the systematic uncertainties, in all other cases the dominant uncertainty is statistical.

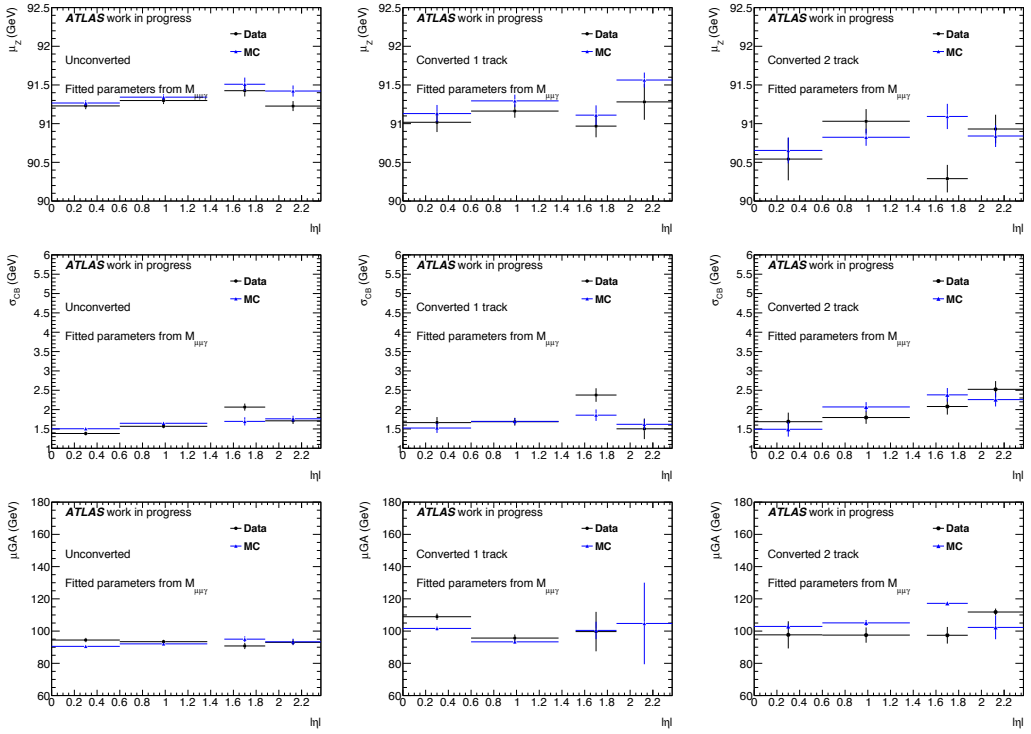

FIGURE 5.30: Fitted value of the peak mean μ_{V} (first row), resolution σ_{CB} (second row) and wide gaussian mean value μ_{wGA} (last row) in the four η bins, for unconverted (left), one-track (middle) and two-track (right) converted photons from the $m_{\mu\mu\gamma}$ distribution.

5.7.3 Photon scales and combined results from both channels

In Figures 5.34 and 5.35, the photon energy scales, extracted separately in the electron and muon channel, are presented. The errors in the plots include both the statistical and systematic components, summed in quadrature (as discussed in the previous section, the categorised scales are dominated by statistical uncertainties). In general, most scales are within one standard deviation from perfect calibration. For unconverted and one-track converted photons, the muon and electron channels are in good agreement. Again for the two-track converted photons, a difference between the electron and muon channel is observed; for the inclusive scale, this disagreement is around 1.8σ.

The results in both channels are combined into one measurement in the following way:

$$\alpha_{\mathrm{combined}} = \frac{\alpha_{\mathrm{el}}/\sigma^2_{\mathrm{el}} + \alpha_{\mathrm{mu}}/\sigma^2_{\mathrm{mu}}}{1/\sigma^2_{\mathrm{el}} + 1/\sigma^2_{\mathrm{mu}}}. \tag{5.14}$$

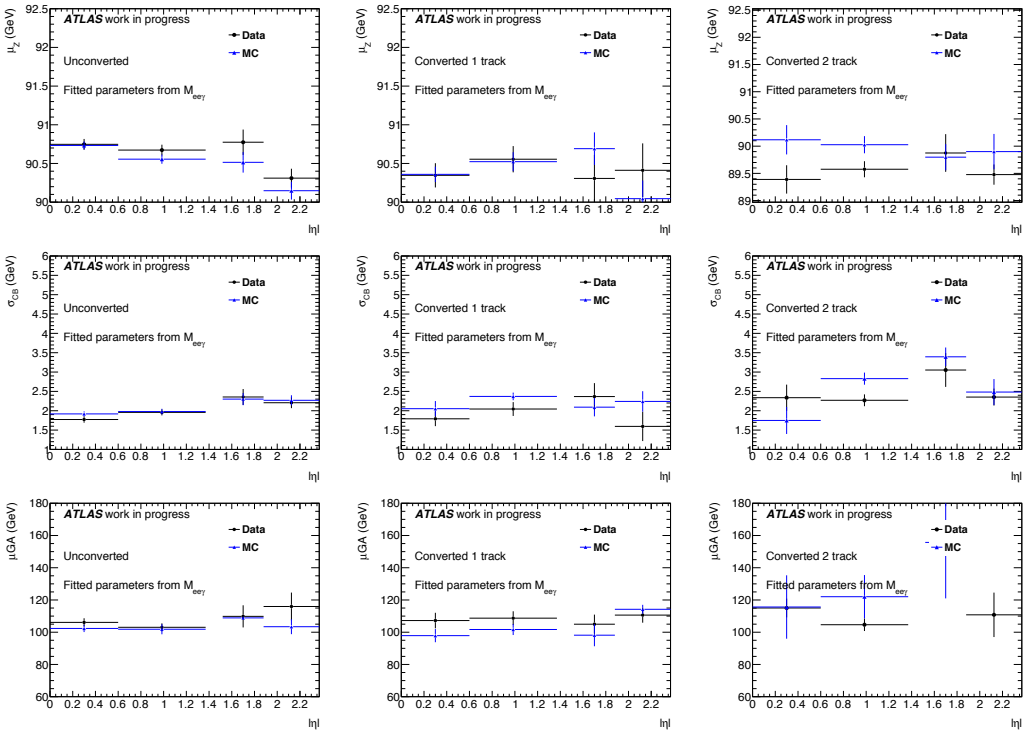

FIGURE 5.31: Fitted value of the peak mean μ_{V} (first row), resolution σ_{CB} (second row) and wide gaussian mean value μ_{wGA} (last row) in the four η bins, for unconverted (left), one-track (middle) and two-track (right) converted photons from the $M_{\mathrm{ee}\gamma}$ distribution.

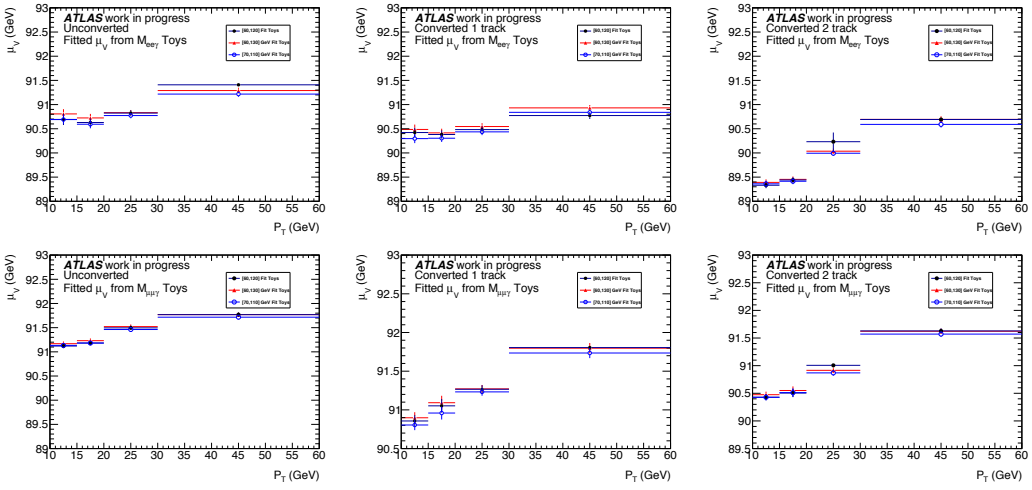

FIGURE 5.32: Fitted mean value of the Z peak μ_{V} in three different fit ranges as a function of the photon p_{T} for the electron (top) and muon (bottom) channels. The fit is performed to 5000 toy datasets generated from the nominal shape extracted from data, in different mass ranges as [60,120] (nominal), [60,130] and [70,110] GeV.

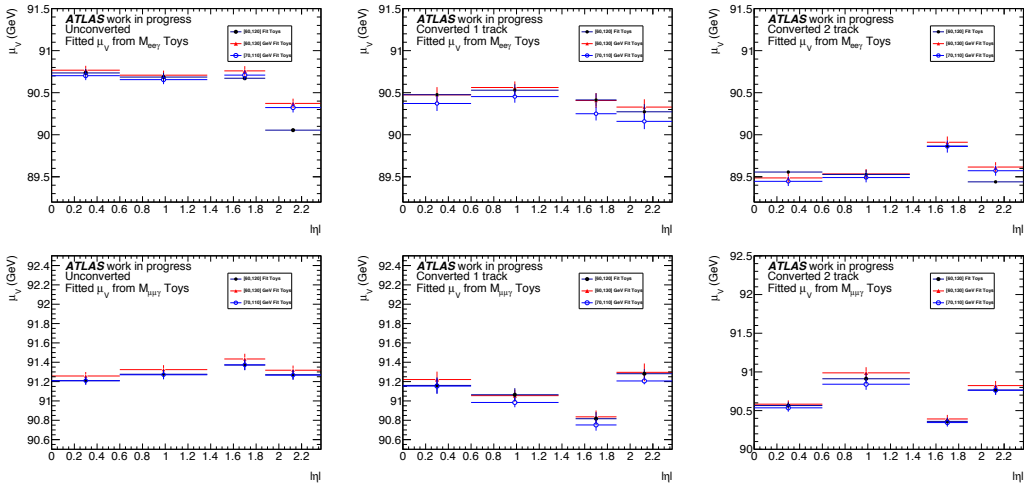

FIGURE 5.33: Fitted mean value of the Z peak μ_V in three different fit ranges as a function of the photon $|\eta|$ for the electron (top) and muon (bottom) channels. The fit is performed to 5000 toy datasets generated from the nominal shape extracted from data, in different mass ranges as [60,120] (nominal), [60,130] and [70,110] GeV.

where α are the scales in each channel, and σ their corresponding errors. At this stage, the uncorrelated uncertainties as the lepton scales and the statistical uncertainty are added in quadrature in each σ for the average (the shared correlated error from the fit range cancels out in the weighted average estimation).

The statistical, and the lepton scale uncertainties are uncorrelated between the channels and are combined as such ($1/\sigma^2_{\text{uncorr}} = \sum_i 1/\sigma_i^2$). The fit range uncertainties are treated as 100% correlated among the muon and electron channel .The final uncertainty is obtained by adding in quadrature the combined uncorrelated and correlated uncertainties.

The final scales are shown in Figures 5.36 and 5.37. The photon scales are shown for fully-calibrated photons, where both MC and $Z \to e^+e^-$ in-situ calibration is applied (sample used in this chapter), and are compared to the scales of photons where only the MC calibration is applied (no $Z \to e^+e^-$ in-situ scales), in order to check the real effect of this calibration, and the true scale to MC.

The combined photon scales show an overall good behaviour. There is no obvious sign of energy non-linearity, and most of the scales are within one and a half standard deviation from zero. The two-track converted photons, has an inclusive scale of (-0.44 $\pm$ 0.52)%, but a significative mis-calibration is observed in the 1.55< $|\eta|$ < 1.88 transition region of about $(-3.0 \pm 1.1)\%$.

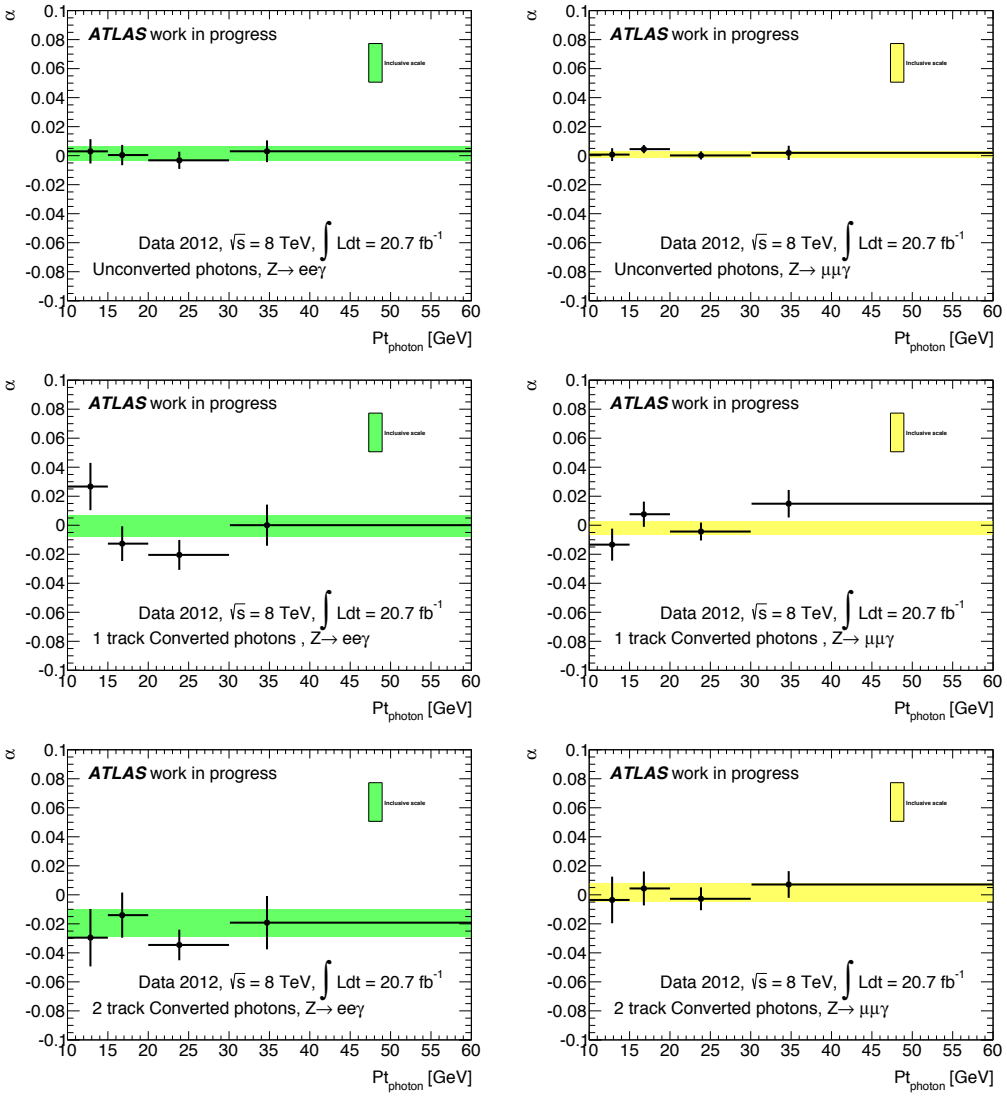

FIGURE 5.34: Photon energy scales as a function of the photon p_{T} extracted from the electron (left) and muon (right) channel. The scales are shown for unconverted photons (top), one-track (middle) and two-track (bottom) converted. The filled bands are the inclusive scale value for each category. Errors are both statistical and systematic, summed in quadrature.

The systematic uncertainty used in ATLAS physics analyses, associated to the photon energy scale in the current calibration due to the Z scale uncertainties, presampler scale, material uncertainty, and the electron to photon extrapolation is about 0.6% for photons with $p_{\mathrm{T}} > 20$ GeV, and grows up to more than 1.5% for low energy photons and photons in the transition region of the calorimeter [2] . The measurements performed with the 8 TeV data presented in this chapter show to be mostly within these uncertainties.

When the $Z \to e^+e^-$ in-situ calibration is not applied, the scales are not significantly different to the fully calibrated ones. For unconverted and one-track converted

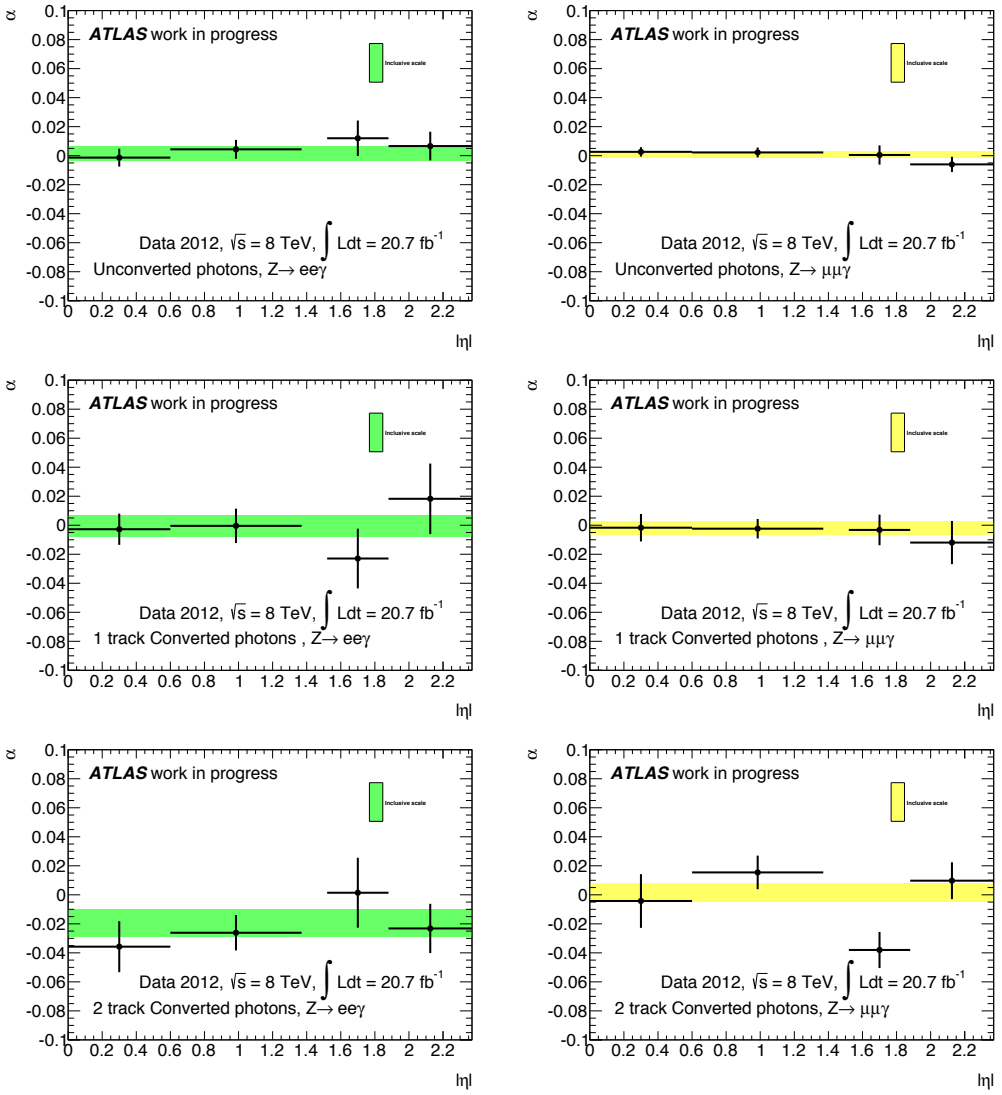

FIGURE 5.35: Photon energy scales as a function of the photon $|\eta|$ extracted from the electron (left) and muon (right) channel. The scales are shown for unconverted photons (top), one-track (middle) and two-track converted (bottom). The filled bands are the inclusive scale value for each category. Errors are both statistical and systematic summed in quadrature.

photons the difference is almost negligible (much less than one standard deviation), while for two-track converted photons the effect of the $Z \to e^+e^-$ scales is found to be more important, with differences that reach almost one standard deviation in some bins.

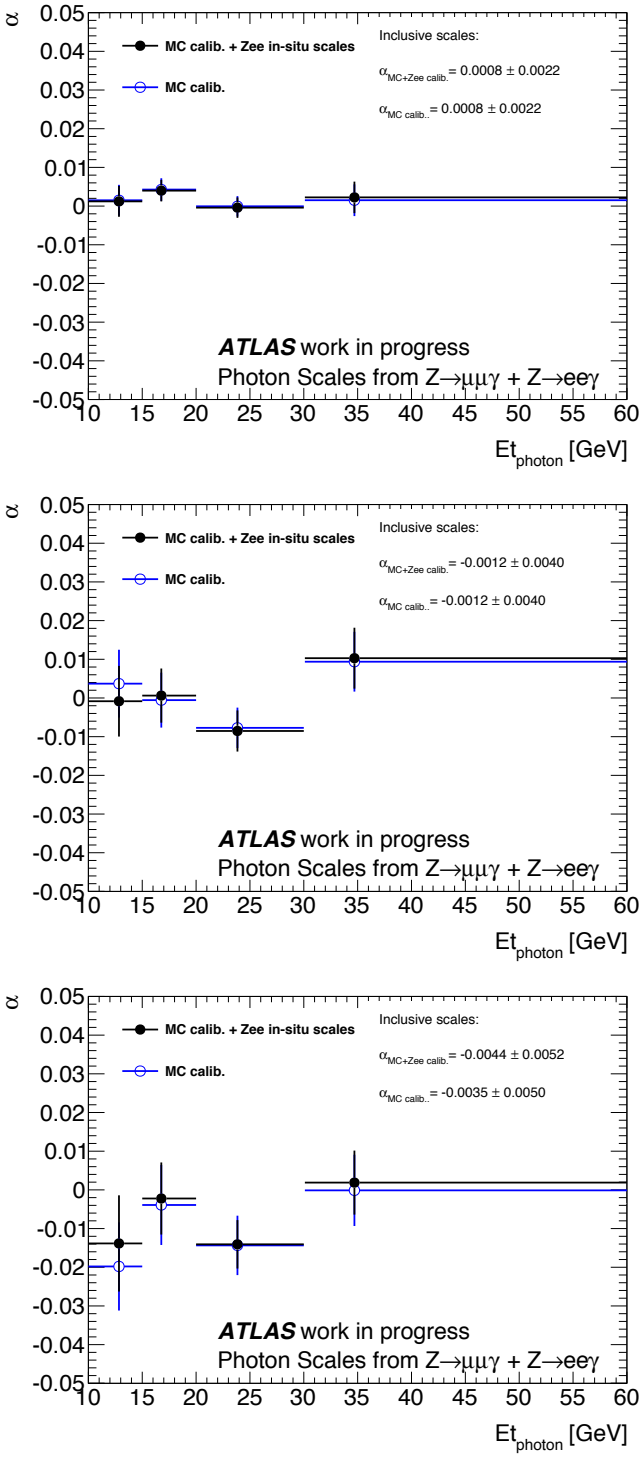

FIGURE 5.36: Combined photon energy scales as a function of the photon p_{T} extracted from the electron and muon channel. The scales are shown for unconverted photons (top), one-track (middle) and two-track converted (bottom). The scales are extracted for photons calibrated with both the in-situ $Z \to e^+e^-$ scales and MC calibration (black filled circles) and photons with only the MC based calibration (blue circles).

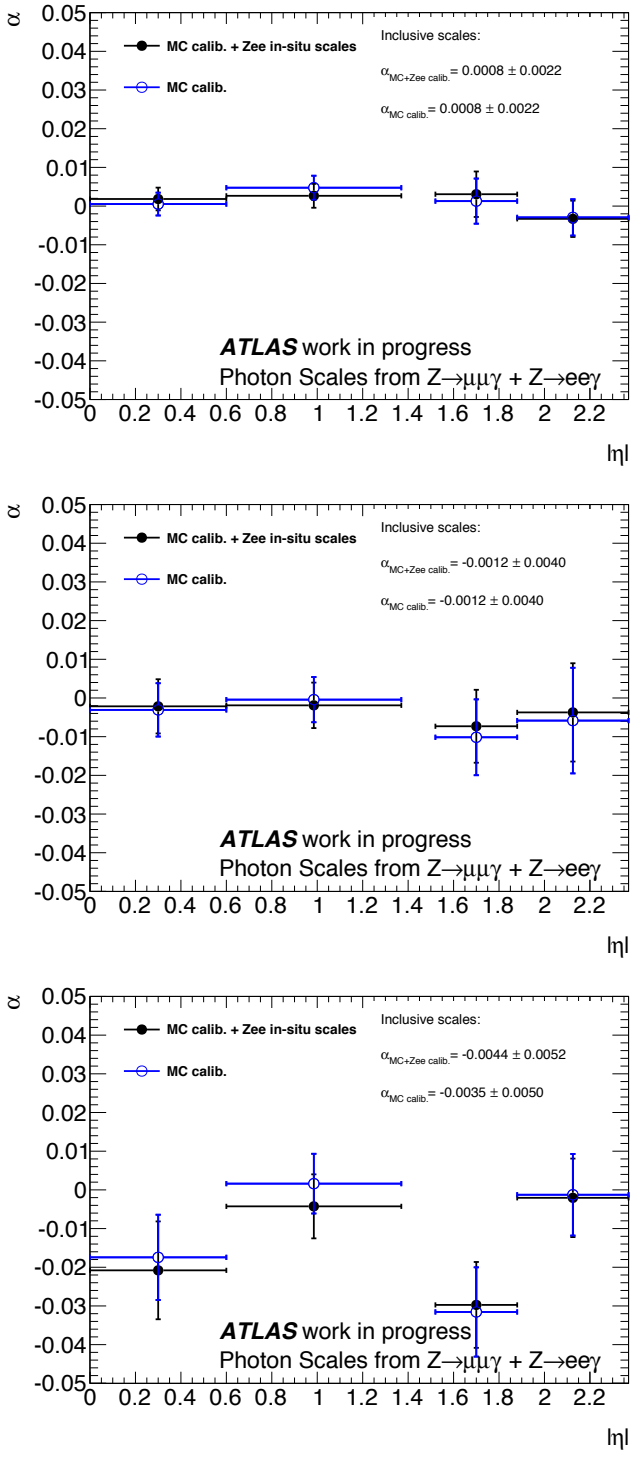

FIGURE 5.37: Combined photon energy scales as a function of the photon $|\eta|$ extracted from the electron and and muon channel. The scales are shown for unconverted photons (top), one-track (middle) and two-track converted (bottom). The scales are extracted for photons calibrated with both the in-situ $Z \to e^+e^-$ scales and MC calibration (black filled circles) and photons with only the MC based calibration (blue circles).

5.8 Conclusions

The radiative Z decays are a high purity photon data sample with an energy range in the order of tens of GeV; the sample is used to determine the photon energy scales, and validate the nominal photon calibration, based in MC and $Z \to e^+e^-$ electron to photon extrapolated energy scales. A first preliminary analysis is performed using the 2011 data sample at 7 TeV with a total luminosity of 4.7 fb^{-1}. A more complete study is done using the 8 TeV sample collected in 2012 with 20.7 fb^{-1}.

The results of the 7 TeV analysis are dominated by statistics. The photon energy scale is evaluated for unconverted and converted photons, in the muon and electron channels. Two different methods are applied to assure robustness of the results, where the double ratio shows to be the best method against systematic uncertainties due to the lepton energy scale. The complete analysis is documented in [2].

The 2012 sample at 8 TeV is eight times larger, owing both to the total integrated luminosity and a lower threshold in the photon p_{T}. The increase of statistics concedes the possibility of further categorisations in conversion, photon energy and detector region. Finally the photon scales are evaluated in different p_{T} and η bins for photons in the unconverted, converted one-track and two-track categories. The scales are extracted separately in the electron and muon channels, and combined into a single measurement. Most of the scales in the various categorisations are at less than one and a half standard deviations from zero (the uncertainties vary from 0.2% to 1.3% depending on the photon conversion and the category), and the results are in good agreement with the nominal systematic uncertainties associated to the photon energy scales. The combined results are presented in Tables 5.7 and 5.8. The documentation for this analysis is in the final stages of editing.

Photon scales (%)			
Pt. bin	Unconverted	Converted one-track	Converted two-track
10 GeV$< p_{\mathrm{T}} <$15 GeV	+ 0.12± 0.40	- 0.08 ± 0.91	- 1.38 ± 1.24
15 GeV$< p_{\mathrm{T}} <$20 GeV	+ 0.40 ± 0.28	+ 0.06 ± 0.70	- 0.22 ± 0.93
20 GeV$< p_{\mathrm{T}} <$30 GeV	- 0.04 ± 0.26	- 0.85 ± 0.53	- 1.41 ± 0.63
$p_{\mathrm{T}} >$30 GeV	+ 0.22 ± 0.41	+ 1.02 ± 0.79	- 0.19 ± 0.83

TABLE 5.7: Combined scales for fully calibrated photons in different p_{T} bin for all conversion categories. The scales are in percentage.

A sample where the photon is not corrected by the $Z \to e^+e^-$ in-situ scales is also used to compare their effect on photon calibration, and to have an extraction of

Photon scales (%)			
η bin	Unconverted	Converted one-track	Converted two-track
$\|\eta\| < 0.6$	+ 0.18 ± 0.29	- 0.22 ± 0.70	- 2.08 ± 1.26
$0.6 < \|\eta\| < 1.37$	+ 0.26 ± 0.31	- 0.19 ± 0.59	- 0.42 ± 0.83
$1.55 < \|\eta\| < 1.82$	+ 0.31 ± 0.59	- 0.73 ± 0.94	- 2.97 ± 1.11
$1.82 < \|\eta\| < 2.37$	- 0.33 ± 0.47	- 0.37 ± 1.27	- 0.21 ± 1.01

TABLE 5.8: Combined scales for fully calibrated photons in different η bin for all conversion categories.The scales are in percentage.

the real photon scales (i.e. not relative to electrons). The difference with the full calibrated scales is found to be small.

Even if the $Z \to \ell\ell\gamma$ is a pure photon sample from which the photon energy scales can be directly extracted, the total combined sample (combined muon and electron channels) with 20.7 fb^{-1} at 8 TeV, is about 50 times smaller than the available $Z \to e^+e^-$ sample used for the current in-situ calibration of the EMCAL. This statistical limitation increases the difficulty of extracting scales with a proper granularity in η as shown in Figure 4.5 (the samples can be divided into just a few bins for each conversion category to assure the stability of the fit). Therefore, a sample 50 times larger is needed to compete with the current statistical uncertainties of the $Z \to e^+e^-$ calibration, and it would mainly concern low p_T photons.

As discussed in Section 4.2.3, for current ATLAS physics analyses involving photons, the systematic uncertainty associated to the photon energy scale takes into account uncertainties due to the material upstream of the calorimeter, the pre-sampler energy scale, $Z \to e^+e^-$ in-situ calibration methods and an electron to photon extrapolation due to the different development of electromagnetic showers initiated by electrons or photons in EMCAL. This procedure is adequate for photons with transverse momentum similar to the electrons from the Z decay, where the systematic uncertainty is about 0.3% (at 40 GeV), but for softer photons (p_{T} less than 20 GeV), the systematic uncertainty due to the extrapolation to lower energy ranges becomes large (going to almost 2%). The measurement done in this Chapter is robust enough to deliver a new systematic scale uncertainty for low p_{T} photons in ATLAS. This subject is currently in discussion within ATLAS.

Chapter 6

Signal studies for the H$\rightarrow \gamma\gamma$ search

Contents

6.1 Introduction

The search for the Higgs boson decaying into two photons in the low mass range ($110 < m_{\mathrm{H}} < 150$ GeV), was one of the benchmark analyses for detector design and performance in ATLAS. Despite its low branching fraction (in the order of 10^{-3}), the sensitivity in this channel is the highest for Higgs masses below 125 GeV, due to the clean signature and good mass resolution, which is a benefit from the excellent EMCAL performance.

The analysis strategy is based on the di-photon invariant mass ($m_{\gamma\gamma}$) as main discriminant variable, built by a photon pair with well measured energies and directions. For the search, the $m_{\gamma\gamma}$ range is scanned, and a narrow resonance is looked for, over a large QCD combinatorial background. The background is composed of pairs of photons, associated production of photons with jets, and processes with several jets in the final state. For the latter two backgrounds, the jets are mis-identified as single photons. An extended unbinned maximum-likelihood fit is performed to extract the signal and background event yields and determine the sensitivity of the search and significance of the potential signal.

For this analysis, a number of studies were performed to investigate the photon performance in the MC and to improve the way the $H \to \gamma\gamma$ signal is modelled for the final statistical analysis. These personal contributions are presented in this chapter in a roughly chronological order. First, an early study in event categorisation, described in Section 6.5, led to investigate the energy scale and resolution of the photons coming from signal MC presented in Section 6.6. The data-driven photon energy scale measurements presented in Chapter 5 are strongly related to these studies.

The need for an interpolation of the signal invariant mass PDF for the search, induced a proposal for a global signal resolution model. This is an analytical function (of m_{H}) that provides a full description of the signal in the whole mass range. This model is also a personal contribution to the $H \to \gamma\gamma$ analysis, and is developed in Section 6.7, and used in the discovery described in Section 6.8 and published in [3], where an excess of events is observed at m_{H}=126.5 GeV leading to the observation of

a Higgs boson-like particle. In Section 6.9, the properties of the new found particles are studied using the full dataset of the first run of the LHC[1].

6.2 Signal simulation samples

Monte Carlo simulated samples are produced with the full ATLAS detector simulation [107] based on Geant4 [108], providing experimental conditions compatible with the 7 TeV and 8 TeV data for hypothetical Higgs masses (m_{H}) from 100 to 150 GeV in 5 GeV steps. Samples are generated separately for each of the Higgs production modes: gluon-gluon fusion (ggF), Vector Boson Fusion (VBF), Higgs-strahlung (WH, ZH) and associated production with a $t\bar{t}$ pair (ttH). Event weights are applied to the MC samples to reproduce the pile-up distribution, and the spread of the z position of the primary vertex observed in data.

Simulations for the ggF and VBF processes are generated with POWHEG interfaced with PYTHIA, for parton showers and their hadronization, and to simulate the underlying event. The remaining samples (WH,ZH and ttH) are generated with PYTHIA (PYTHIA6 [109] is used for the 7 TeV samples and PYTHIA8 [119] for the 8 TeV ones).

For the ggF samples at 7 TeV, event weights are applied to match the Higgs boson transverse momentum distribution with the one resulting from higher order calculations [120]. Also in this process, a reweighting is done in both 7 and 8 TeV samples to correct for destructive interference between $gg \to \gamma\gamma$ and $gg \to H \to \gamma\gamma$ processes [121].

The studies presented next are performed with different MC samples, which simulate the data-taking periods of 2010, 2011 and 2012. These will be referred as to MC10, MC11 and MC12 respectively.

[1]It is important to clarify that the analyses presented in Sections 6.8 and 6.9 correspond to the contributions of several people working in the $H \to \gamma\gamma$ analysis in ATLAS. As will be described along the chapter, personal contributions to these results are restricted to the signal modelling.

6.3 Photon selection

The aim of this analysis is the search for a resonance in events with two photons that match a set of quality criteria. Events that pass a di-photon trigger are selected as data for the analysis. The trigger used for the 7 TeV data requires two clusters in the EMCAL with at least 20 GeV of transverse energy, while in the 8 TeV data, the trigger E_{T} threshold is increased to 35-20 GeV for the leading and sub-leading clusters, respectively. Events are required to contain at least two photon candidates in the $|\eta| < 2.37$ detector region, excluding the transition region between barrel an end-cap ($1.37 < |\eta| < 1.52$). Photons are reconstructed and calibrated in data and MC as explained in Chapter 4, and are required to have E_{T} >40 GeV and E_{T} >30 GeV for the leading and sub-leading photon respectively (it was initially 25-25 GeV in early data analyses). In addition, to suppress the jet background, photons are required to pass the tight identification (upstream of this requirement, the photon shower shapes are corrected in MC to improve the agreement with the data shower shapes) and an isolation criteria, requiring the isolation energy to be less than 4 GeV in a ΔR <0.4 cone. More details about this background rejection methods are found in Chapter 4.

6.4 Invariant mass reconstruction

The di-photon invariant mass is evaluated starting from the photon energies measured in the EMCAL and their directions with the following expression:

$$M_{\gamma\gamma} = \sqrt{2E_{\mathrm{T}}^{1}E_{\mathrm{T}}^{2}\left[\cosh(\eta_1 - \eta_2) - \cos(\phi_1 - \phi_2)\right]}, \tag{6.1}$$

where E_{T} are the transverse energies of the two photons, η their pseudo-rapidities and ϕ the azimuthal angles. The η of the photon is measured by the photon cluster barycenter of the second layer of the calorimeter, assuming that the photon has been originated in the geometrical centre of the detector. As the last statement is not necessarily true (the *pp* interactions in ATLAS are spread along the z-axis with an RMS of about 50 mm), the photon pseudo-rapidity is corrected by their longitudinal position z of their origin defined as primary vertex (PV).

The PV of a photon pair is identified by combining the following information in a global likelihood:

- The flight direction of the photons. It is determined by using the longitudinal segmentation of the EMCAL (calo-pointing). The cluster barycentre in the first and second layers are combined, and a straight line is fitted, determining the photon z position as the interception of the fitted line with the beam axis [91]. The independent vertex position measurements for both photons are then combined.
- The average beam spot position.
- The sum of $|\vec{p_{\mathrm{T}}}|^2$ of the tracks associated with each reconstruction vertex.
- The conversion vertex (only used in 2011 data in the calo-pointing procedure).

As shown in Figure 6.1, applying the PV η correction improves the mass resolution. The largest improvement is achieved by the calo-pointing technique, which is very close to the final likelihood result and to the optimal mass resolution obtained by choosing the true PV.

For signal, the di-photon invariant mass distribution at a fixed Higgs boson mass has been traditionally described by a sum of two functions: A Crystal Ball function (CB): a gaussian core with a power-law tail modelling energy leakage, and a small wide Gaussian component (GA) modelling the distribution outliers and improving the description of the tails of the distribution [91]. Both functions are defined in Chapter 5. The PDF parameters are the Crystal Ball mean value μ_{CB}, the di-photon invariant mass resolution σ_{CB}, the CB tail parameters n_{CB} and α_{CB}, the wide gaussian mean value μ_{GA} and resolution σ_{GA}, and the fraction of the Crystal Ball component f_{CB} on the PDF. The di-photon invariant mass distribution at 8 TeV, as fitted with the Crystal Ball plus Gaussian model, is shown in Figure 6.2.

FIGURE 6.1: The di-photon mass distribution for $H \to \gamma\gamma$ signal events, for different algorithms used to determine the longitudinal vertex position of the event. The use of calorimeter information, labelled as "Calo pointing" is fully adequate to reach the optimal achievable mass resolution labelled as "True vertex". The likelihood described in the text, combining with tracking information, provides similar mass resolution [117].

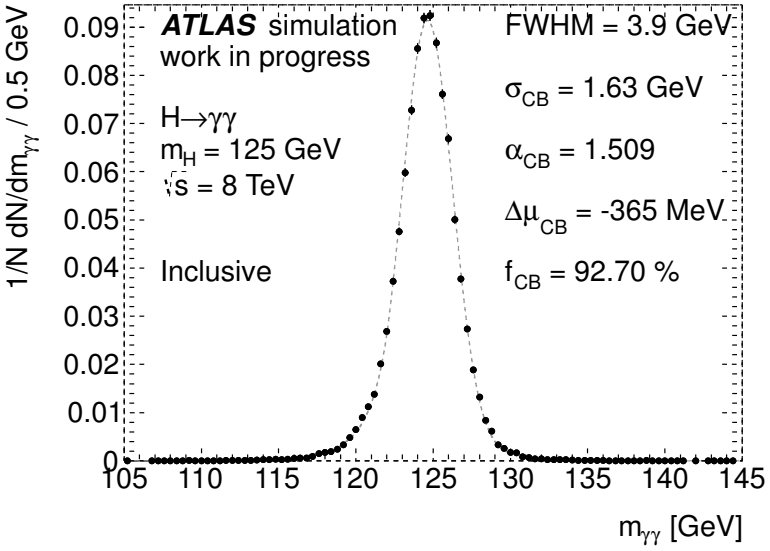

FIGURE 6.2: Reconstructed inclusive invariant mass distribution for a simulated signal of m_H=125 GeV in MC12 for which a smearing has been applied to the photons energy, to account for differences in the $Z \to ee$ mass resolutions between data and MC. The result of the fit is superimposed. The core component of the mass resolution, σ_{CB}, is 1.64 GeV and the FWHM of the distribution is 3.94 GeV.

TABLE 6.1: Description of categorisation by photon conversion status. The first digit in the category nomenclature corresponds to the conversion status of the leading photon, and the second to the sub-leading photon.

Cat.	Leading γ	Sub-leading γ
Cat. 0-0	Unconverted	Unconverted
Cat. 0-1	Unconverted	One-track converted
Cat. 0-2	Unconverted	Two-track converted
Cat. 1-0	One-track converted	Unconverted
Cat. 1-1	One-track converted	One-track converted
Cat. 1-2	One-track converted	Two-track converted
Cat. 2-0	Two-track converted	Unconverted
Cat. 2-1	Two-track converted	One-track converted
Cat. 2-1	Two-track converted	Two-track converted

6.5 Early study in photon categorisation

Event categorisation is a common approach to increase the sensitivity of an analysis searching for a potential signal. The events are separated into exclusive categories with different discriminating power (i.e differences in resolutions and signal-to-background ratios). The first ATLAS result in the $H \to \gamma\gamma$ channel is an inclusive analysis due to the low statistics of 40 pb^{-1} [122] which corresponds to the 2010 dataset. With the increase on statistics in the 2011 dataset, different categorisations are investigated.

In the early categorisation study presented in this section, the categories are oriented into the photon reconstruction, based on the conversion status of the photons. The shape of the signal invariant mass is studied in each of these categories. These studies are performed in MC10[2] with a signal sample for a hypothesised Higgs with m_{H} of 120 GeV, which simulates the signal with conditions corresponding to the 2010 data-taking. In Figure 6.3, it is shown that the unconverted photons dominate in the sample. As photon reconstruction is different for unconverted, converted one-track and converted two-track photons, potential differences in the mass resolution are studied. The di-photon invariant mass distribution is fitted to the signal PDF for each of the nine possible configurations of conversion status of each photon (see Table 6.1).

[2]The MC10 samples were the only samples available at the moment, the study was performed in sight of the 2011 analysis.

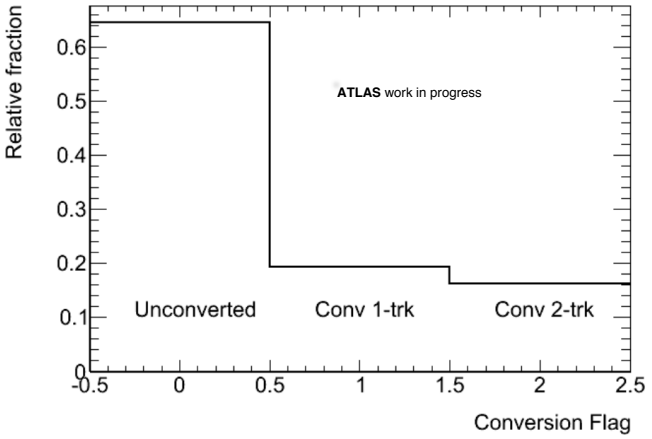

FIGURE 6.3: Relative fraction of the three conversion categories for a H → γγ sample with a m_{H} of 120 GeV with MC10 reconstruction.

In Figure 6.4, the fitted values for the μ_{CB}, σ_{CB} and α_{CB} parameters are shown, for each of these nine categories. Some main features are observed:

- A difference in resolution is found among the categories with unconverted and the ones with converted photons (a 70% relative change in resolution from 0-0 to 2-2). The resolution is worst when the sub-leading is converted (suggesting that the largest impact on the resolution is carried by the sub-leading photon). The category with the worst resolution is the 2-2. The resolution for the inclusive MC10 sample at m_H= 120 GeV is about 1.7 GeV which is 160 MeV wider than the best category (0-0), and 740 MeV narrower than the 2-2 category.

- The Crystal Ball fitted mean value (μ_{CB}) changes among the categories. The more pronounced shifts are observed when the sub-leading is a two-track converted photon (the largest shift is found in the 2-2 category). An opposite sign shift is observed when both photons are one-track converted. The difference between categories 1-1 and 2-2 is found to be about 2%, which is not negligible compared with an average resolution of 1.7 GeV at MC10.

- For categories with two-track conversion photons, the contribution of non-gaussian tails is more pronounced (as indicated by the small α_{CB} value). For the 0-0 and 1-0 categories, the leakage tail is significantly smaller.

These features show that there are differences in the MC energy scale and resolution among the three type of photons, which led to investigate the photon performance in the $H \to \gamma\gamma$ samples. These studies are performed in MC11 and presented next.

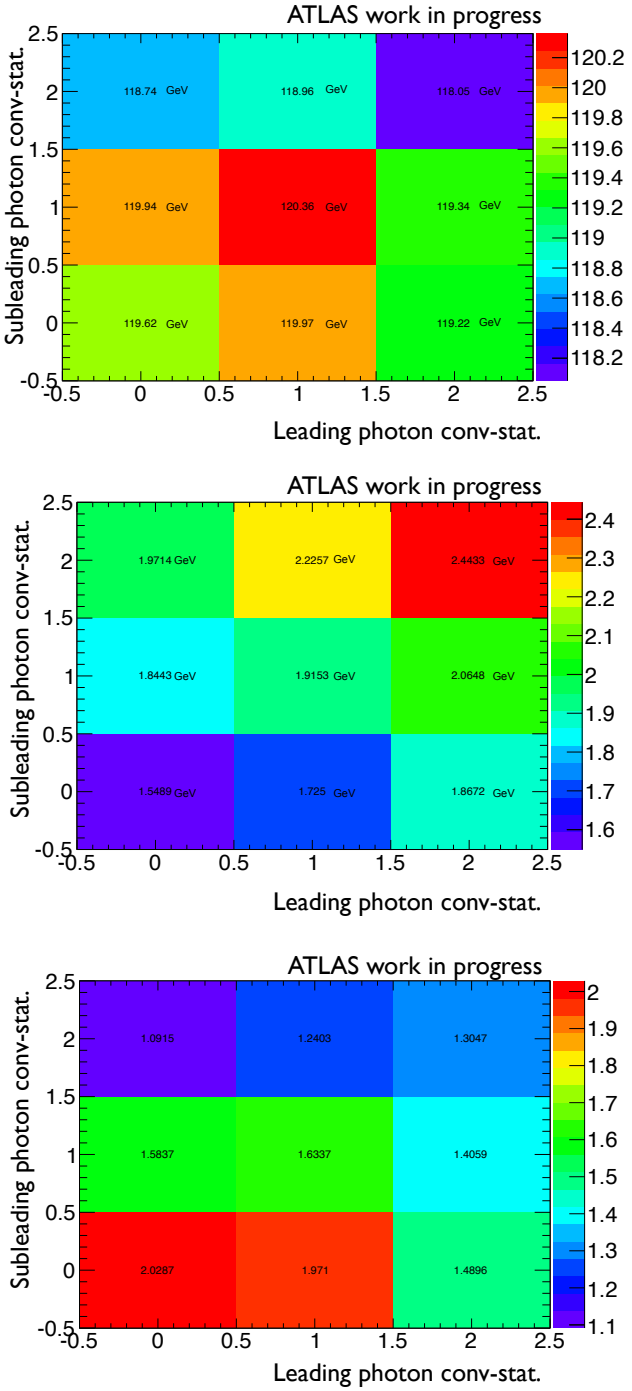

FIGURE 6.4: The values of the signal PDF parameters, fitted to invariant mass distributions of the Higgs signal with mass of 120 GeV (with MC10 reconstruction), for nine categories based on the conversion status of each photon. In the upper figure the fitted mean value of the Crystal ball (μ_{CB}) is shown, in the middle the resolution (σ_{CB}) and in the bottom the tail parameter α_{CB}.

6.6 MC photon energy response

Tight and isolated photons with $p_{\mathrm{T}} > 20$ GeV from the signal MC samples are used for this study. In order to test the photon energy response and resolution in MC, a variable "Δ" (which is the relative change of reconstructed p_T with respect to the true MC p_T) is defined for each of the three different conversion categories for p_{T} and $|\eta|$ bins.

$$\Delta = \frac{p_{\mathrm{T}}^{reco} - p_{\mathrm{T}}^{true}}{p_{\mathrm{T}}^{true}}. \tag{6.2}$$

The Δ distribution is evaluated in 5 GeV p_{T} bins from 20 to 100 GeV, and for different calorimeter regions, from $0 < |\eta| < 2.37$, excluding the $1.37 < |\eta| < 1.52$ transition region in the calorimeter.

To study the photon energy response linearity, the mean value of the Δ distribution is fitted with a gaussian in an asymmetric restricted range between -1.5σ and +2.0 σ (shown as an example in Figure 6.5). The asymmetric fit range is defined through an iterative fit procedure, and is set to avoid biasing the fitted peak values by potential asymmetries in the distribution due to energy leakage.

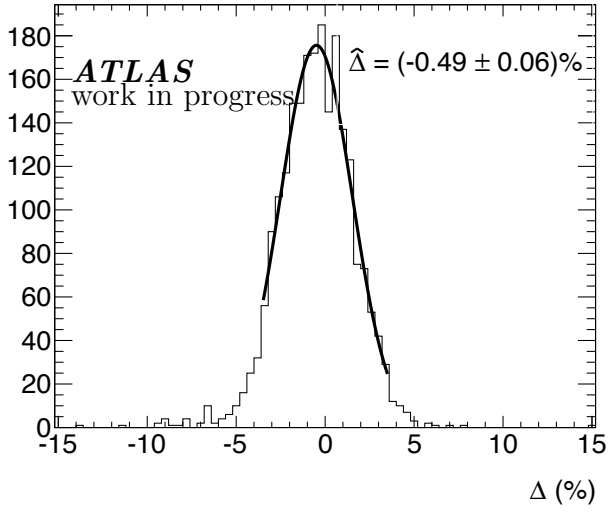

FIGURE 6.5: Illustrative plot of the gaussian fit in an asymmetric restricted range between -1.5σ and +2.0σ to the Δ distribution (see Equation 6.2). The Δ distribution corresponds to unconverted photons with 20 GeV$< p_T <$ 25 GeV in the $0.0 < |\eta| < 0.1$ range.

The fitted mean values as a function of p_{T} are shown in Figure 6.6 for all the different $|\eta|$ bins. The behaviour in each of the conversion categories is different:

- For unconverted photons, the photon energy response within each $|\eta|$ bin is quite stable as a function of p_{T}, with differences below 0.5%. In contrast, the energy response can differ by up to 1% among $|\eta|$ bins.
- For converted photons, the photon energy response tend to increase as a function of p_{T}, and differ by up to several percent among $|\eta|$ bins; these variations are significantly more pronounced for two-track converted photons.

A similar behaviour to the mean value from the Δ distribution is found in the mean value of the shower shape variable R_{ϕ} that gives the ratio of the energy reconstructed in 3x3 cells to the energy in 3x7 cells as defined in Chapter 4 (Figure 6.7).

The correlation between the Δ and R_{ϕ} patterns can be illustrated with Figure 6.8, where two potential sources of mis-calibration for converted photons are sketched. The front energy loss is due to the amount of material between the conversion point and the calorimeter. The out-of-cluster effect could be caused by the magnetic field opening, making the separation between the electron-positron pair larger than the sliding window used for the cluster reconstruction (this occurs mainly in converted photons with a small R_{conv}). As a consequence, a fraction of the total energy is deposited in calorimeter cells which are not part of any reconstructed cluster. This effect is also evident in the R_{ϕ} variable. The effect of front energy loss is a function of the detector region, and the out of cluster effect depends on the radius of conversion and energy of the original photon: the earlier the conversion of a low p_{T} photon, the largest the opening of the conversion products before arriving to the calorimeter. These effects are clearly correlated with the trends observed in two-track converted photon.

6.6.1 Performance studies on the converted photon calibration tool

To correct for the non-linearities observed in converted photons in the MC, a calibration algorithm was built and implemented by the Milano Group to correct the energy. The LPNHE group contributed to the validation of this new calibration. The

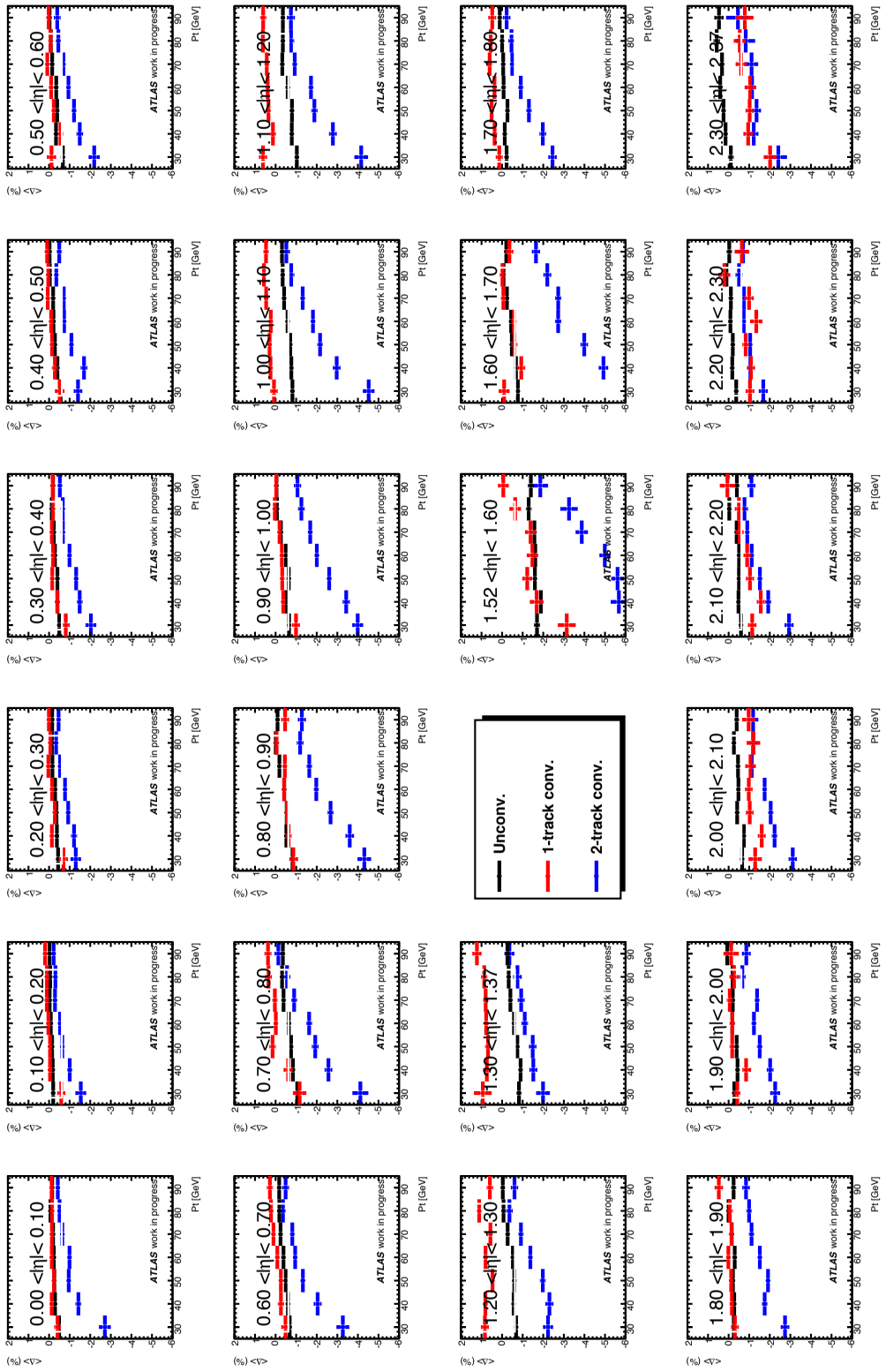

FIGURE 6.6: The fitted mean value of the Δ distribution, as a function of the photon p_{T}, for different η regions of the detector. The distribution is fitted to a gaussian in a restricted range.

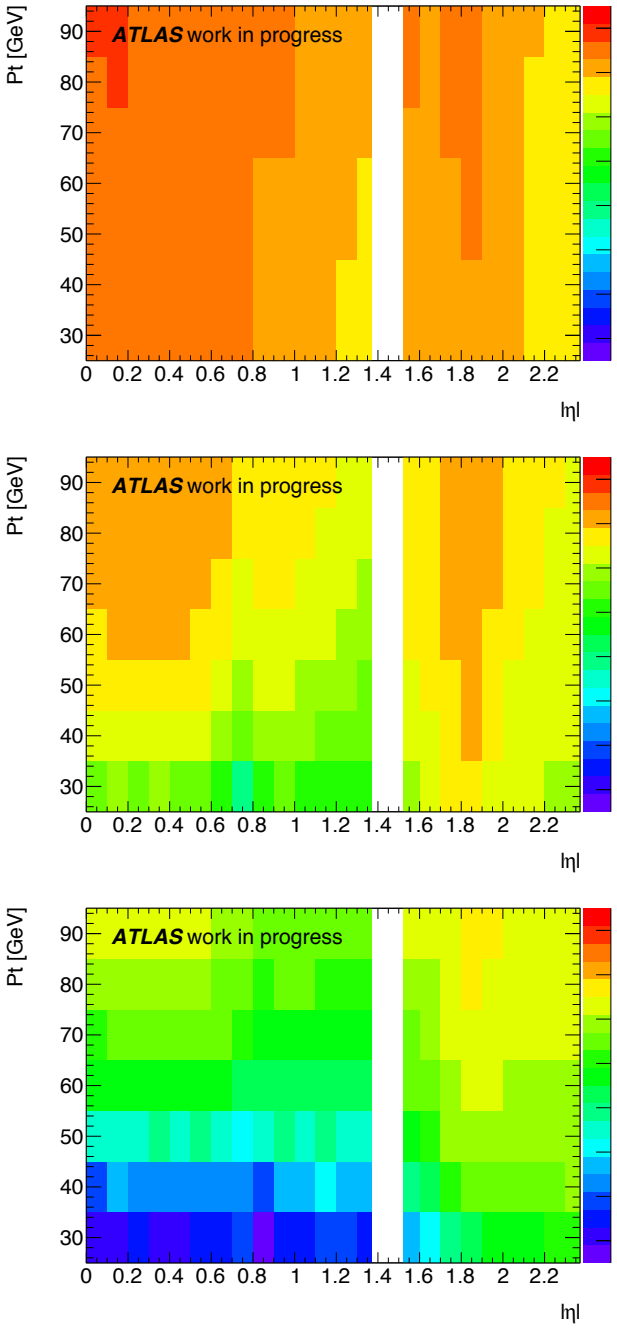

FIGURE 6.7: Mean value of the R_ϕ distribution in p_{T} and η bins for the three types of photon conversion categories, unconverted (top), one-track converted (middle), two-track converted(bottom).

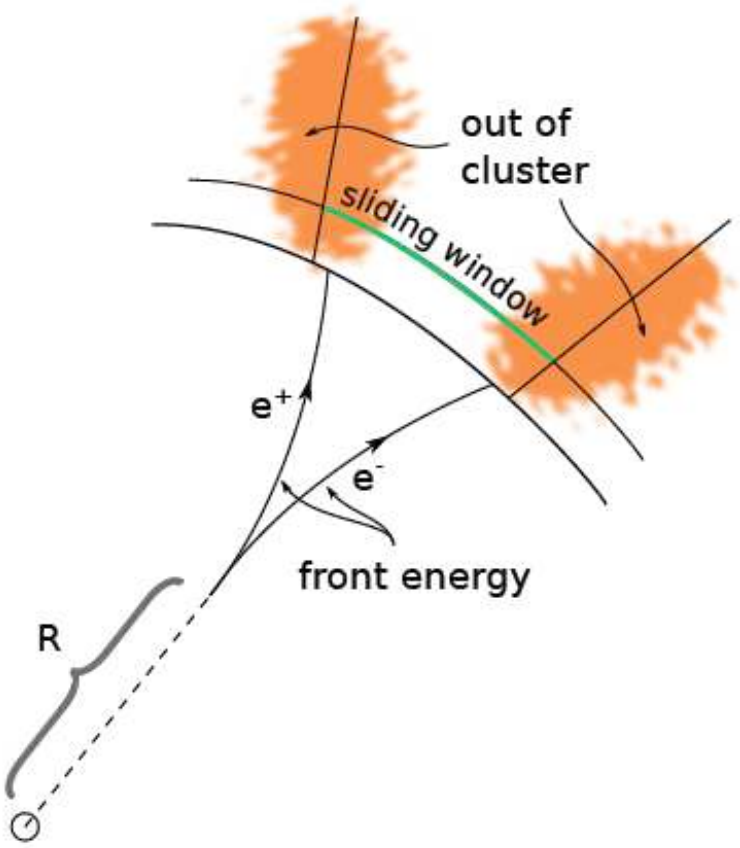

FIGURE 6.8: Schema of sources of mis-calibration in converted photons. Two effects are shown, the front energy loss and the out of cluster effect.

algorithm takes as inputs the photon pseudo-rapidity, the energy after the standard calibration and the true radius of conversion, with no distinction of one-track and two-track converted photons, and returns a factor to obtain an improved calibration with good linearity. More information can be found in [123]. This calibration is optimised in MC simulations with single particles (photons) with a flat $|\eta|$ distribution. The performance of the tool is tested on the $H \to \gamma\gamma$ MC samples.

The energy correction factors vary between 0.97 and 1.1, and are large for low conversion radius, low photon energy and for high pseudo-rapidity. In Figure 6.9, the fitted mean value of the Δ distribution after the correction is shown for all different $|\eta|$ bins. The inter-calibration is significantly improved by the converted photon calibration tool with respect to the original Figure 6.6. There is also a clear improvement in the p_{T} linearity, with still some smaller non-linearity issues remaining in a few $|\eta|$ bins.

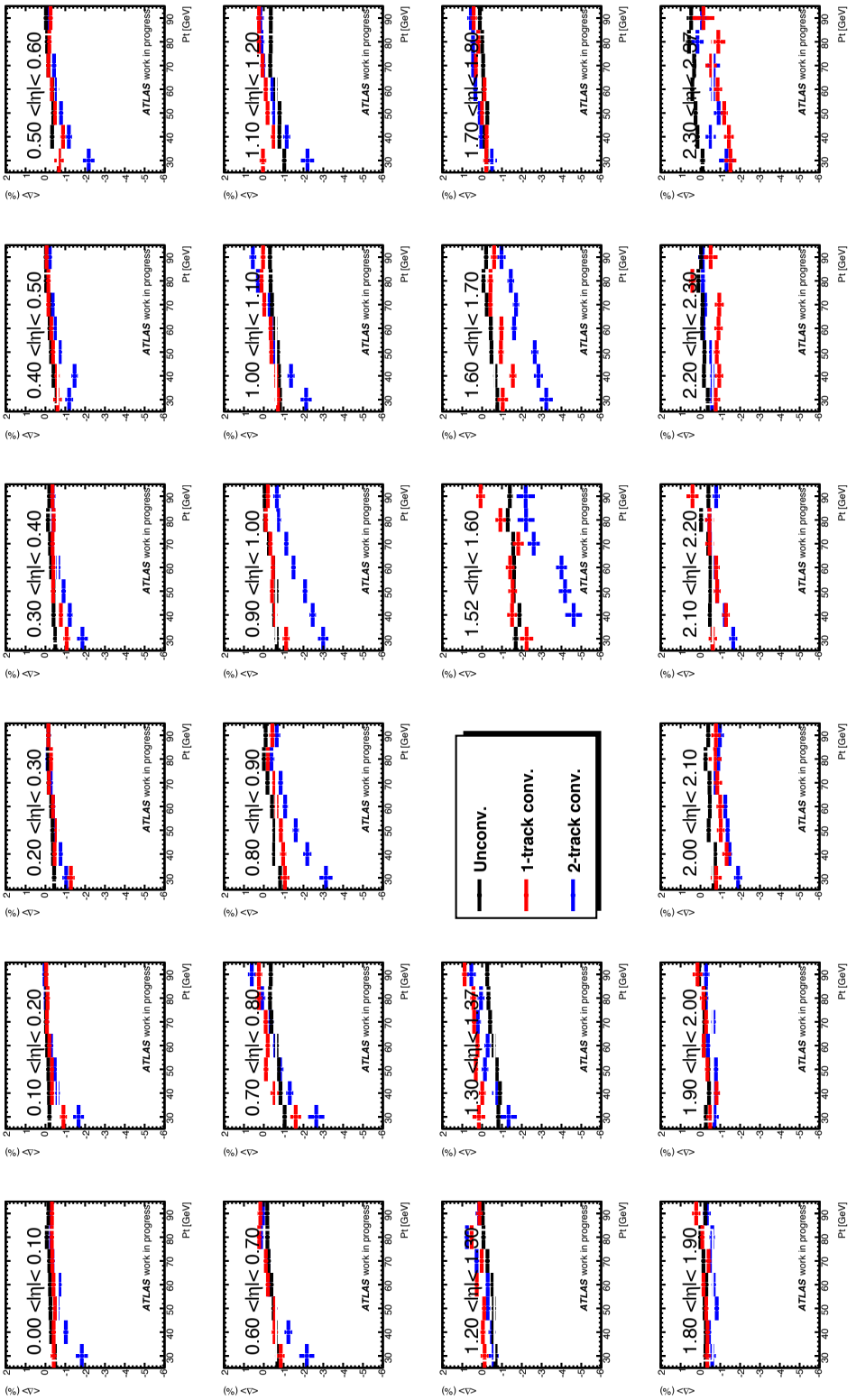

FIGURE 6.9: Fitted mean value of the Δ distribution corrected by the converted photon calibration tool, as a function of the photon p_{T}, for different η regions of the detector. The distribution is fitted to a gaussian in a restricted range.

Parameter.	Before Correction	After Correction.
Pairs of one-track converted photons		
α_{CB}	1.61 ± 0.40	1.51 ± 0.30
f_{CB}	0.772 ± 0.066	0.789 ± 0.061
μ_{CB} [GeV]	119.852 ± 0.098	119.558 ± 0.098
σ_{CB} [GeV]	1.78 ± 0.11	1.71 ± 0.11
σ_{GA} [GeV]	4.28 ± 0.39	4.29 ± 0.41
Pairs of two-track converted photons		
α_{CB}	0.82 ± 0.13	0.88 ± 0.12
f_{CB}	0.99 ± 0.21	0.90 ± 0.20
μ_{CB} [GeV]	118.30 ± 0.20	119.17 ± 0.14
σ_{CB} [GeV]	2.27 ± 0.18	2.23 ± 0.18
σ_{GA} [GeV]	3.20 ± 3.1	3.23 ± 0.84

TABLE 6.2: Fitted parameters of the signal PDF for two cases: Invariant mass built with pairs of one-track converted photons and pairs of two-track converted photons. The change between the parameters after implementing the correction is presented.

In order to test the impact of this converted photon calibration on the $H \to \gamma\gamma$ invariant mass, the converted photon energies are corrected with the improved radius-dependent calibration and the invariant mass distribution is recalculated as explained in Section 6.4. The inclusive MC11 sample of ggF with a Higgs mass of 120 GeV is used. Two extreme cases are tested, when the two photons are either with one-track or two-track conversions. The distributions with and without the corrections are fitted to the signal PDF, and the changes in the parameters and the overall shape are evaluated.

In Figure 6.10, the two resulting PDFs are superposed for the two instances. In the case where the two photons are one-track converted, the resolution improves by 4% and the distribution mean value is shifted by -300 MeV. In the case of two track converted photons the improvement is more pronounced, the resolution is 2% narrower, and the leakage tails are reduced by 7%. The mean value is shifted by +800 MeV, approaching it to the mean value of the unconverted sample (the same happens with the one-track converted peak although the shift has an opposite sign). More details about changes in the PDF parameters with corrections are found in Table 6.2.

Following the results of good performance of the tool shown in this study, the tool is used in the $H \to \gamma\gamma$ analysis [117], and recommended to be used by all other physics

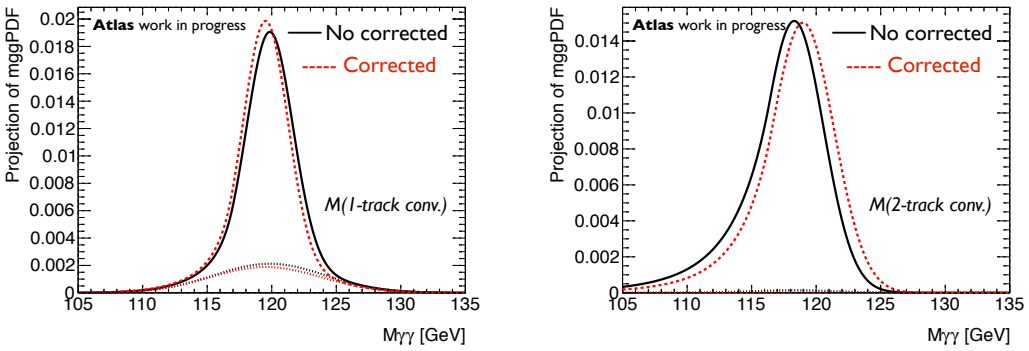

FIGURE 6.10: Invariant mass PDF of the H→ γγ signal in MC11 with (red) and without (black) the converted photon energy correction. The signal for pairs of one-track converted photons (left) and two-track converted photons (right) is shown.

analyses concerning photons. The idea of extracting the photon energy scale from data using Z radiative decays as presented in Chapter 5, is a continuation of these studies.

6.7 Global signal model

6.7.1 Resolution model

As stated in Section 6.4, the signal shape for a fixed m_{H} is described with a function that is the sum of a Crystal Ball function, plus a small wide Gaussian component:

$$\begin{aligned} R\left(m_{\gamma\gamma}\right) &= f_{CB} CB\left[m_{\gamma\gamma}; \mu_{CB}, \alpha_{CB}, \sigma_{CB}, n_{CB}\right] \\ &+ \left(1 - f_{CB}\right) GA\left[m_{\gamma\gamma}; \mu_{GA}, \sigma_{GA}\right]. \end{aligned} \tag{6.3}$$

The resolution model R is a function of 7 free parameters with large correlations (Figure 6.11). In the model, each parameter is highly correlated with all others (up to 99%). This fact suggests the implementation of a simpler parametrisation with a reduced number of free parameters.

A model of the Higgs signal valid in the mass range from 100 to 150 GeV is needed to perform the search in this region. The signal MC samples are generated in 5 GeV steps of the Higgs mass, therefore an interpolation of the invariant mass PDF

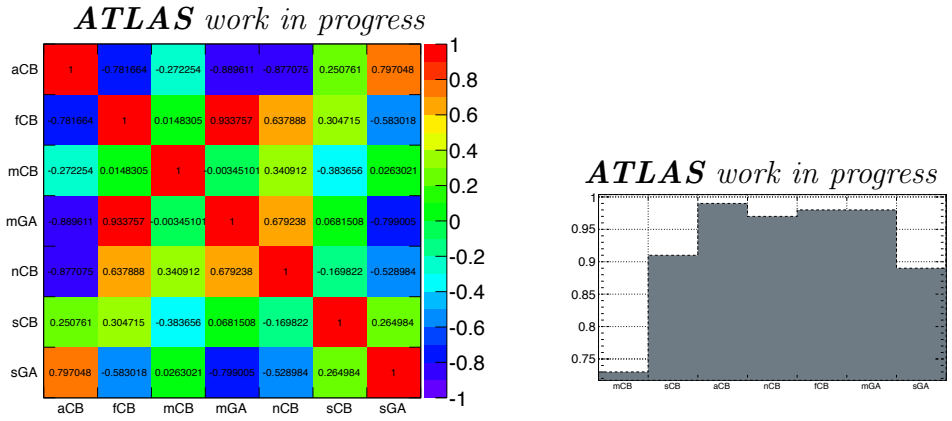

FIGURE 6.11: Correlation matrix (left) and global correlations (right) of the 7 free parameters in the resolution model R of a Crystal Ball and a wide Gaussian fitted on a MC11 sample with $m_H = 125$ GeV.

is needed for the scan in the whole mass range. In the early data analyses [122, 124–126], the resolution for arbitrary mass values was evaluated by assuming a"piecewise" linear interpolation of the parameters between adjacent MC mass points separated by 5 GeV, building a model with 7×11 parameters corresponding to the shape in every mass point. This is a valid approach, but sensitive to fluctuations in the description of shape, especially in the case where the sample could be split into many categories.

The global resolution model is an analytical function of the Higgs mass, with a full description of the signal in the whole mass range. It is assumed that the resolution follows a "self-similar" dependence with mass, i.e. its core peak should be displaced with mass, and its width should scale monotonically with mass as shown in Figure 6.12. The fact that the standard CB+GA function is degenerate (global correlations that are often $> 90\%$) is also exploited by implementing a simpler parametrisation with the minimal number of free parameters needed to achieve a good description of the $m_{\gamma\gamma}$ distribution.

From the available signal MC samples at different mass points, the parameters that depend on the nominal Higgs boson mass m_{H} are identified and both global and mass dependent parameters are extracted from a simultaneous fit. The monotonous, smooth dependence of the photon mass resolution, is exploited by this method, identifying the relevant parameters that carry the information for shape and sensitivity.

The first step to build the global resolution model is to identify which parameters are irrelevant to the overall shape and can be fixed in the fit. In view of the large global correlations, these parameters can be dispensed with, without compromising

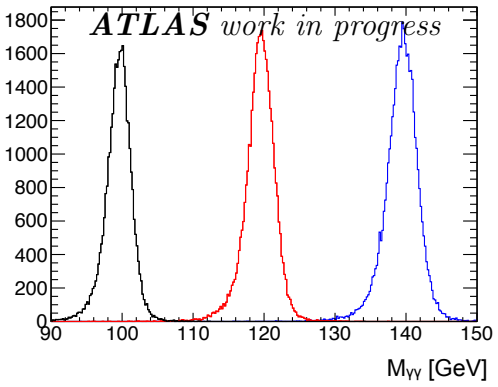

FIGURE 6.12: Reconstructed invariant mass distributions for hypothesised Higgs masses of m_{H} =100 GeV, m_{H} =120 GeV and m_{H} =140 GeV with MC11.

the goodness of the fit or the signal description. The parameters investigated are the tail parameter n_{CB} and the mean value of the wide gaussian μ_{GA}:

- In Figure 6.13 the signal PDFs extracted from a MC11 ggF sample at m_H = 125 GeV are shown for different values of n_{CB} fixed in the fit. No significant differences in the shape are found. Comparing the negative tails a small difference is observed between the PDFs with $n_{CB} = 5$ and $n_{CB} = 10$, the difference between $n_{CB} = 10$ and $n_{CB} = 25$ is completely negligible. These results imply that the n_{CB} can be safely fixed in the fit.

- Figure 6.14 shows a comparison of the signal PDFs for two hypotheses of the μ_{GA} parameter. In one instance μ_{GA} is free in the fit, and in the second is forced to be equal to μ_{CB}. Some small differences are observed in the tails in masses far away from the main core, which remains unchanged. Forcing $\mu_{GA} = \mu_{CB}$ appears to be a valid approach.

To model the "self-similar" behaviour of the signal invariant mass resolution with m_H, parameters dependent on the invariant mass are investigated. The signal mass resolution is a complex function of the photons energy and position resolution. The EMCAL energy resolution presented in Equation 3.7 suggests that the mass resolution should follow a quadratic dependence of the mass. Nevertheless, when performing the simultaneous fit the quadratic dependence is found to be to be compatible with zero, and is considered as such in the global model:

$$\sigma_{CB}(m_H) = \sigma_{CB_{125\ \mathrm{GeV}}} + \Delta_{\sigma CB_{\mathrm{slope}}} \times (m_H - 125\ \mathrm{GeV}). \tag{6.4}$$

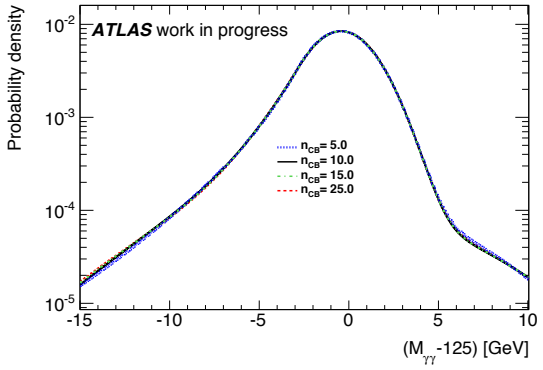

FIGURE 6.13: Signal PDFs extracted from a MC11 ggF sample with $m_H = 125$ GeV for shapes using different values of the tail parameter n_{CB}.

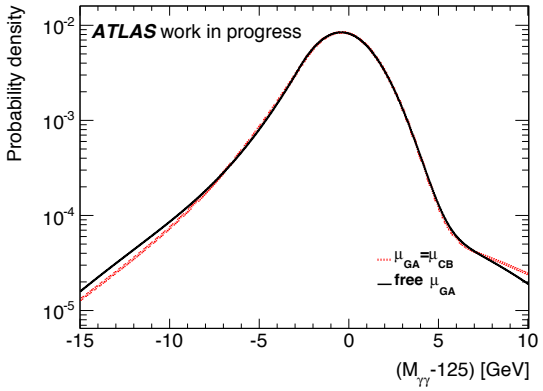

FIGURE 6.14: Signal PDFs extracted from a MC11 ggF sample with $m_H = 125$ GeV for different hypotheses of the μ_{GA} parameter. In one case the mean value of the gaussian is unconstrained, and in a second case it is forced to be equal to the mean value of the Crystal Ball.

Equation 6.4, in an empirical result. As shown in Section 6.5, the sub-leading photon dominates the mass resolution, the E_{T} spectrum of sub-leading photon of a Higgs $\rightarrow \gamma\gamma$ decay varies from a mean value of 40 to 70 GeV depending of m_{H}, at which point the photon resolution is dominated by the constant term. This fact justifies the observed approximation to a linear functionality of the mass resolution with m_H. Both $\sigma CB_{125\mathrm{GeV}}$ and $\Delta_{\sigma CB_{\mathrm{slope}}}$ are extracted from the simultaneous fit. In addition, to force the "self-similarity", the relative width of the core and the outlier components is set to a constant value ($\kappa = \sigma_{GA}/\sigma_{CB}$), that is extracted from the fit.

In a similar way to the resolution, the shift between the Crystal Ball mean value and the true Higgs mass ($\Delta\mu_{CB} = \mu_{CB} - m_H$) its assumed to follow a linear dependence with the mass:

$$\Delta\mu_{CB}(m_H) = \Delta\mu_{CB_{125GeV}} + \Delta\mu_{CB_{\text{slope}}} \times (m_H - 125 \text{ GeV}), \tag{6.5}$$

the $\Delta\mu_{CB_{125GeV}}$ and $\Delta\mu_{CB_{\text{slope}}}$ parameters are extracted from the simultaneous fit. The other parameters (f_{CB}, α_{CB}) are set to a single global value for all mass points and the mean value of the outliers (GA) is set to be the same as the CB, finally the parameter n_{CB} is fixed to 10, as discussed previously, without this having any significant cost in the goodness of the fit or the description of the signal shape.

In total, 8 parameters (2 shape parameters with a linear dependence on the Higgs boson mass and 4 global parameters), are extracted from a single fit to all available Monte Carlo samples, and are sufficient to provide a robust parametrisation of the invariant mass PDF at any Higgs boson mass. In Figure 6.15, the projection of the global fit result superposed to every MC mass point is shown.

6.7.1.1 Resolution Model per Production Process

The global fit of the resolution function is performed on all MC samples for the different production processes, weighted by their SM cross-sections. It is also possible to split the signal component into separate sub-components for each production process, so the strength of each process can be fitted separately. A first evaluation of the global resolution model is performed for each of the processes: ggF, VBF, associated production (WH and ZH) and ttH.

In Figure 6.16, the projection of the global fit performed exclusively to each production mode at 120 GeV is shown. A difference in the resolution between the different processes is observed, for example the difference between the main production mode ggF mass resolution and the VBF mass resolution is about (65.6 ± 8.6) MeV (the VBF resolution is narrower as the photons are more central than the ones from the ggF). In the analysis that will be presented in this Chapter, a multiple categorisation in $|\eta|$, energy regions and other variables is applied to increase the sensitivity of finding a potential Higgs signal. These categorisations could reduce the differences between shapes among the processes.

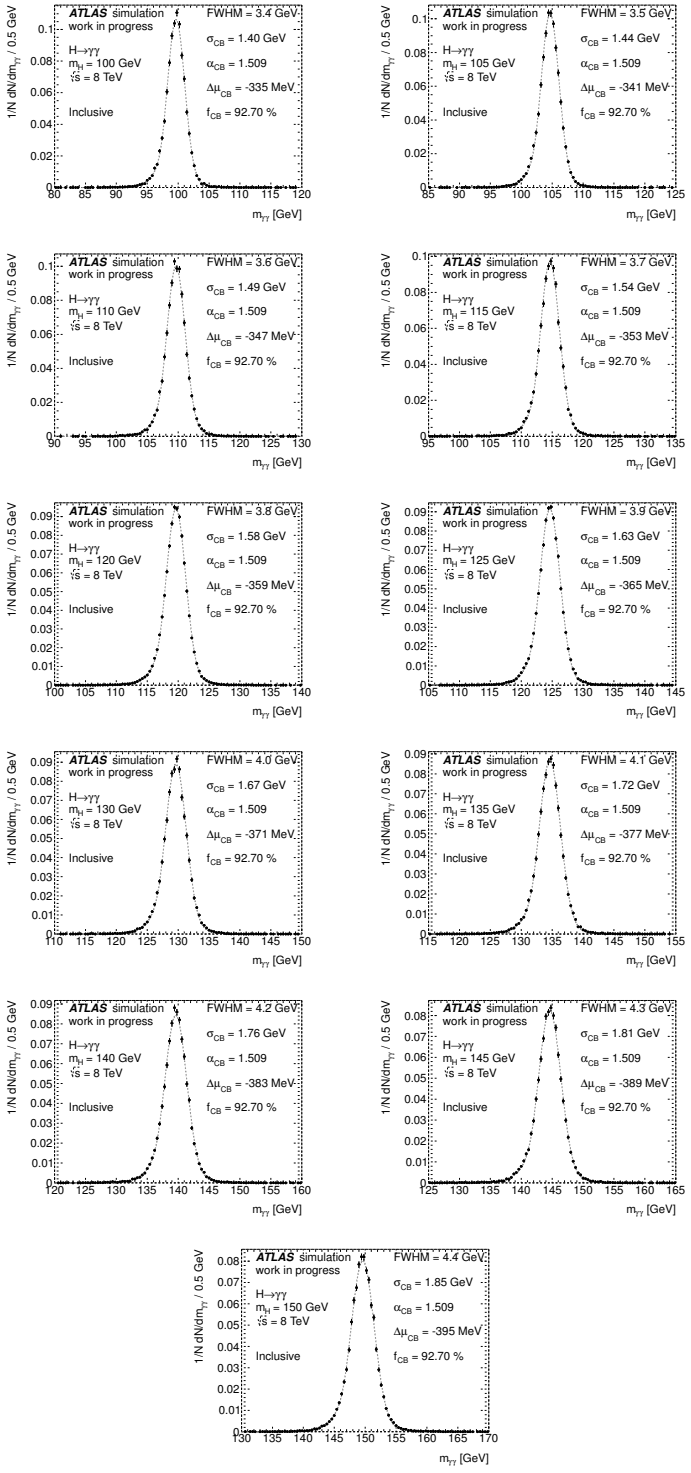

FIGURE 6.15: Reconstructed invariant mass distributions from the signal processes and the projection of the global fit in all available MC mass points at 8 TeV. In the figures, the plotted invariant mass increases from 100 GeV to 150 GeV in 5 GeV steps. The parameters appearing in the figures are the evaluation of the global function at that mass point.

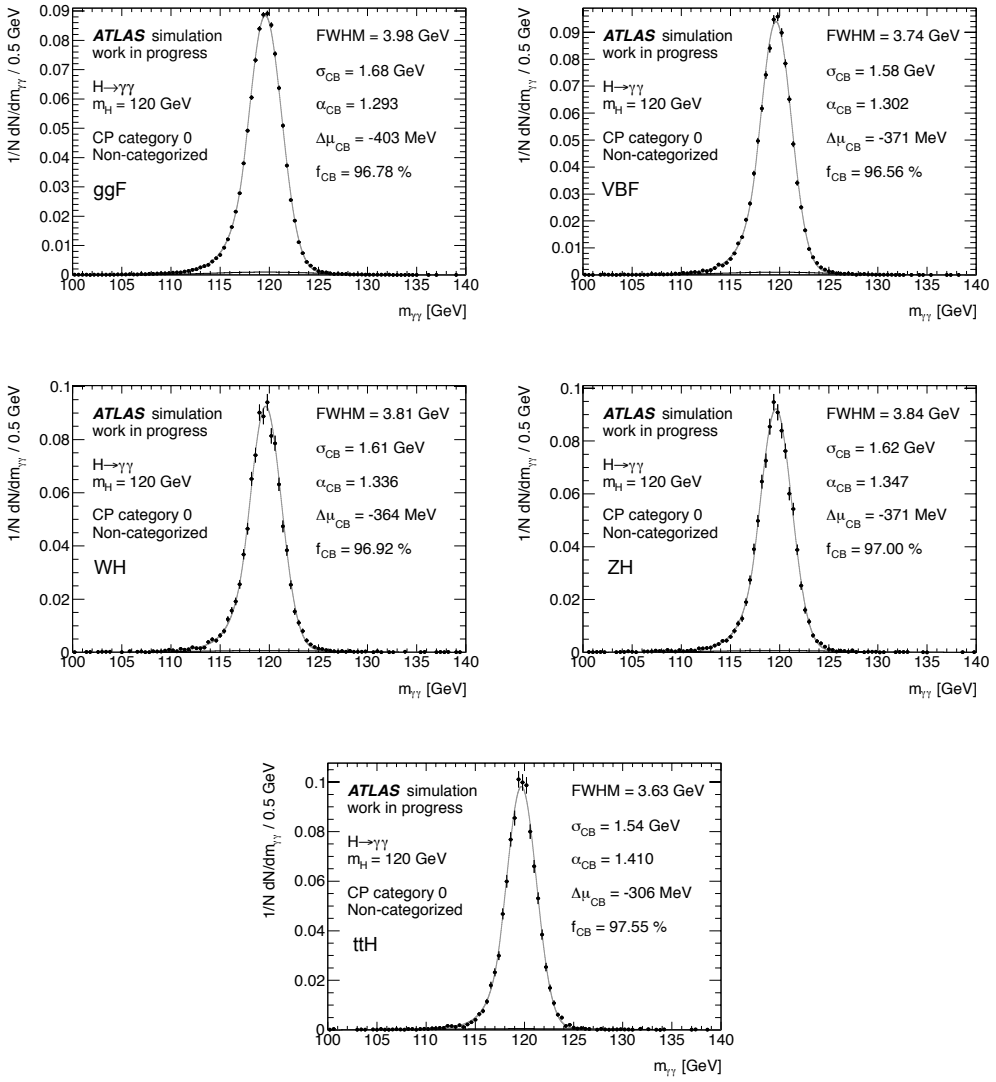

FIGURE 6.16: Reconstructed invariant mass distributions and the projection of the global fit at 120 GeV for the signal processes ggF, VBF, WH, ZH and ttH at 8 TeV.

6.7.2 Analytical parametrisation for the signal expected yields

To perform the final statistical analysis, not only a parametrisation of the signal shape in the search mass range is needed, but also the expected signal yields are needed to be parametrised as a function of m_H in accordance to the SM Higgs boson prediction.

The expected signal yields at a certain m_{H} are calculated from the following formula:

$$N_{\mathrm{i}}(m_H) = \sigma_i(m_H) \times \mathcal{B}_{\mathrm{H}\to\gamma\gamma}(m_H) \times \varepsilon_{\mathrm{i}}(m_H) \times \int \mathcal{L}dt, \tag{6.6}$$

where

1. $\int \mathcal{L}dt$ is the integrated luminosity of the data sample,
2. $\sigma_i(m_H)$ is the SM Higgs boson production cross-section for a Higgs boson of mass m_H, in the production process i (ggF, VBF, ..),
3. $\mathcal{B}_{\mathrm{H}\to\gamma\gamma}(m_H)$ is the branching fraction for the decay to $\gamma\gamma$ of a SM Higgs boson of mass m_H,
4. $\varepsilon_{\mathrm{i}}(m_H)$ is the selection efficiency for $H \to \gamma\gamma$ events.

where both the Higgs cross-section and branching fraction are taken from [127] and [128].

In the search mass range ($m_{\gamma\gamma}$) from 100 GeV to 150 GeV, the expected signal yields can be parametrized by a third order polynomial in the form:

$$N(m_{\gamma\gamma}) = N_{125\mathrm{GeV}}\left[1 + \lambda_{\mathrm{lin}}\frac{(m_{\gamma\gamma}-125\mathrm{GeV})}{25\mathrm{GeV}} + \lambda_{\mathrm{sqrt}}\frac{(m_{\gamma\gamma}-125\mathrm{GeV})^2}{(25\mathrm{GeV})^2} + \lambda_{\mathrm{cubic}}\frac{(m_{\gamma\gamma}-125\mathrm{GeV})^3}{(25\mathrm{GeV})^3}\right], \tag{6.7}$$

where $N_{125\mathrm{GeV}}$ is the total yield at 125 GeV, and λ_{lin}, λ_{sqrt} and λ_{cubic} are the first, second and third order terms in the polynomial. They are obtained from a fit to all MC points as shown in Figure 6.17. The fitted function reproduces correctly all the signal yields resulting from the MC output, the point with the largest deviation from the function (a fluctuation of less than 2σ) is the $m_H = 110$ GeV point where the yield would be underestimated by 2% with respect to the function.

6.8 Observation of a new particle in the search for the SM Higgs boson in the $\gamma\gamma$ channel

In this section, the ATLAS analysis leading to the observation of an excess of events in the H→ γγ channel is presented. Personal contributions as the Global Resolution Model, described in detail in the Section 6.7 are used in this analysis.

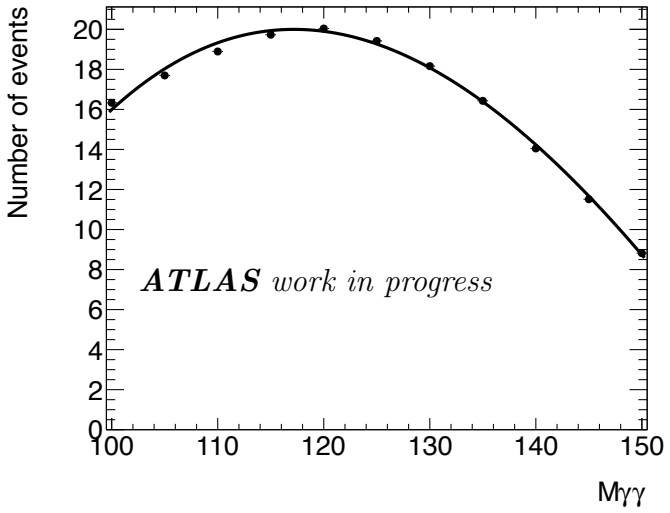

FIGURE 6.17: Expected SM signal yields parametrisation as a function of the $m_{\gamma\gamma}$ mass. The yields corresponds to the prediction at 1 fb^{-1} of 8 TeV data in the inclusive category.

For this search, the complete dataset at 7 TeV with 4.8 fb^{-1} of integrated luminosity and the first 5.9 fb^{-1} of the 8 TeV data is used. This analysis is fully documented in [3].

6.8.1 Categorisation

The events are separated into different categories with different mass resolutions and signal to background ratios. The categories are defined as a function of several variables:

- The conversion status of the photon candidates (photons are treated only as unconverted or converted).
- The pseudo-rapidity of the photons.
- The transverse momentum of the di-photon pair projected in the thrust axis (p_{Tt}). The di-photon thrust axis is defined as the difference between the two photon momenta (Figure 6.18), in the following way:

$$\hat{t} = \frac{\vec{p}_{\mathrm{T}}^{\,\gamma 1} - \vec{p}_{\mathrm{T}}^{\,\gamma 2}}{|\vec{p}_{\mathrm{T}}^{\,\gamma 1} - \vec{p}^{\,\gamma 2}|}, \tag{6.8}$$

where $\vec{p}_{\mathrm{T}}^{\gamma 1}$ and $\vec{p}_{\mathrm{T}}^{\gamma 2}$ are the transverse momentum of the two photon candidates in the ATLAS coordinate system. The transverse momentum of the di-photon system is defined as:

$$\vec{p}_{\mathrm{T}}^{\gamma\gamma} = \vec{p}_{\mathrm{T}}^{\gamma 1} + \vec{p}_{\mathrm{T}}^{\gamma 2}. \tag{6.9}$$

Finally the $\vec{p}_{\mathrm{Tt}}$ vector is calculated as follows:

$$\vec{p_{\mathrm{Tt}}} = \vec{p}_{\mathrm{T}}^{\gamma\gamma} - (\vec{p}_{\mathrm{T}}^{\gamma\gamma}.\hat{t}).\hat{t}, \tag{6.10}$$

$$\vec{p}_{\mathrm{Tt}} = |\vec{p}_{\mathrm{T}}^{\gamma\gamma} \times \hat{t}|. \tag{6.11}$$

The p_{Tt} turns out to be a good discriminant variable between signal and background. As shown in Figure 6.19, the Higgs p_{Tt} produced by ggF or VBF, is found to be larger than the background ($\gamma\gamma + \gamma$jet) one. A sample with an improved signal to background ratio can be obtained by cutting at a high p_{Tt} value.

- A 2-jet selection with a VBF-like signature; at least two jets are reconstructed using the anti-k_{t} algorithm [129] with a radius parameter R=0.4, in the $|\eta| <$ 4.5 region. The jets are required to have p_{T} >25 GeV in the whole η range for 7 TeV data, and in 8 TeV data, the p_{T} threshold is raised to more than 30 GeV for jets with $2.5 < |\eta| < 4.5$. To eliminate the contributions from jets coming from proton-proton interactions that are not associated with the primary vertex, a cut in the jet vertex fraction (JVF[3]), is set to 0.75 for all jets in the ID acceptance ($|\eta| < 2.5$). Finally, cuts motivated by the VBF topology are applied:
  - The difference in the pseudo-rapidity between the two jets is required to be larger than 2.8.
  - The di-jet invariant mass is asked to be larger than 400 GeV.
  - The azimuthal angle between the di-photon system and the di-jet system has to be larger than 2.6.

Finally, ten mutually exclusive categories are defined in this analysis. They are the following:

[3]JVF is the fraction of the sum of the p_{T} of the tracks belonging to the jet associated with the PV, with respect to the sum of p_{T} of the total tracks in the jet.

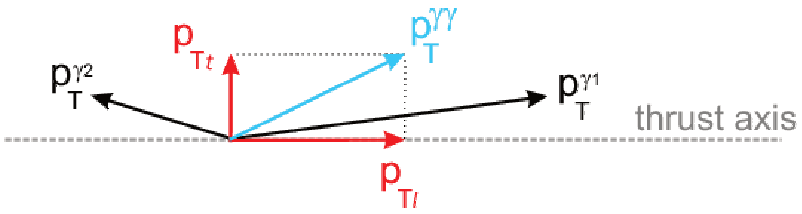

FIGURE 6.18: Sketch of the p_{Tt} definition.

FIGURE 6.19: Distribution of p_{Tt} in simulated events with Higgs boson production and in background events. The signal distribution is shown separately for gluon fusion (blue), and vector-boson fusion together with associated production (red). The background MC and the two signal distributions are normalised to unit area [3].

1. Unconverted central, low p_{Tt}: Both photon candidates are reconstructed as central unconverted photons ($|\eta|$ <0.75). The di-photon system p_{Tt} is lower than 60 GeV (low p_{Tt}).

2. Unconverted central, high p_{Tt}: Both photon candidates are reconstructed as central unconverted photons ($|\eta|$ <0.75). The di-photon system p_{Tt} is higher than 60 GeV (high p_{Tt}).

3. Unconverted rest, low p_{Tt}: Both photon candidates are unconverted and at least one photon has $|\eta|$ >0.75. The di-photon system has low p_{Tt}.

4. Unconverted rest, high p_{Tt}: Both photon candidates are unconverted and at least one photon has $|\eta|$ >0.75. The di-photon system has high p_{Tt}.

5. Converted central, low p_{Tt}: At least one of the photon is converted, and both are at $|\eta|$ <0.75. The di-photon system has low p_{Tt}.

6. Converted central, high p_{Tt}: At least one of the photon is converted, and both are at $|\eta|$ <0.75. The di-photon system has high p_{Tt}.

7. Converted rest, low p_{Tt}: At least one photon candidate is a converted photon. Both photon candidates are at $|\eta| < 1.3$ or $|\eta|$ >1.75, with at least one photon candidate has $|\eta| < 1.3$. The di-photon system has low p_{Tt}.

8. Converted rest, high p_{Tt}: At least one photon candidate is a converted photon. Both photon candidates are at $|\eta| < 1.3$ or $|\eta|$ >1.75, with at least one photon candidate has $|\eta| < 1.3$. The di-photon system has high p_{Tt}.

9. Converted transition: At least one photon candidate is a converted photon, and at leas one candidate is in the $1.3 < |\eta| < 1.37$ or $1.52 < |\eta|$ >1.75 regions.

10. 2-jets: The events passes the 2 jet selection described above. This category is rich in VBF (at 70% least of the signal in this category is from VBF).

6.8.2 Signal parametrisation

Expected signal yields

The expected efficiencies and yields of a Higgs boson signal are calculated as described in Section 6.7.2. The yields are evaluated for the different production processes and normalised to the total integrated luminosity of the data samples of 7 (4.8 fb^{-1}) and 8 TeV (5.9 fb^{-1}). In Table 6.3, the expected signal yields and selection efficiency for all production process and mass points are shown. The expected signal yields per category for each production process, and evaluated at $m_H = 126.5$ GeV are shown in Table 6.4.

Resolution model

The global resolution model is extracted from a simultaneous fit to all the MC samples as described in detail in Section 6.7. The multiple categorisation in η and p_{Tt} categories leaves small room for differences on shape among the PDFs for the processes, therefore a single process-inclusive PDF is extracted for every category, weighting every process contribution by the SM cross-section.

TABLE 6.3: Expected Higgs boson signal efficiency ε (including acceptance of kinematic selections as well as photon identification and isolation efficiencies) and event yield for $H \to \gamma\gamma$ assuming an integrated luminosity of $4.8\,\text{fb}^{-1}$ for the $\sqrt{s}$ =7 TeV data (top) and of $5.9\,\text{fb}^{-1}$ for the $\sqrt{s} = 8$ TeV data (bottom). Results are given for different production processes and in 5 GeV m_H steps.

		$gg \to H$		VBF		WH		ZH		ttH		Total
$\sqrt{s}$	m_H [GeV]	ε(%)	N_{evt}	ε(%)	N_{evt}	ε(%)	N_{evt}	ε(%)	N_{evt}	ε(%)	N_{evt}	N_{evt}
7 TeV	110	37.3	71.7	37.9	5.17	33.5	2.8	33.6	1.53	33.7	0.358	81.5
	115	39.5	73.8	40.1	5.5	34.9	2.8	35.5	1.5	34.9	0.4	84.0
	120	40.9	73.5	42.1	5.8	37	2.6	37	1.4	35.9	0.3	83.7
	125	42	70.9	43.8	5.8	38.1	2.4	38.4	1.3	37.2	0.3	80.8
	130	43.1	66.3	44.8	5.7	39.3	2.1	39.9	1.2	37.8	0.3	75.6
	135	43.1	59.8	46.9	5.3	40.7	1.8	40.8	1.0	38.7	0.2	68.3
	140	45.2	51.8	48.7	4.8	41.9	1.5	42.3	0.9	39.5	0.2	59.1
	145	45.8	42.3	49.8	4.1	42.5	1.2	43.6	0.7	40.5	0.2	48.4
	150	45.8	31.6	49.7	3.1	44.1	0.9	44.7	0.5	40.7	0.1	36.3
8 TeV	110	33.7	100.3	34.4	7.3	29.8	3.7	29.4	2.1	27.2	0.6	114.0
	115	35.5	103.5	36.1	7.9	30.5	3.6	32.3	2.0	27.8	0.6	117.6
	120	37.1	103.3	38	8.2	32.5	3.41	32.8	2.0	29.3	0.6	117.4
	125	38.2	99.96	39.5	8.2	33.8	3.14	34.1	1.8	29.7	0.5	113.7
	130	39	93.8	41.1	8	35.1	2.8	35.8	1.6	31	0.5	106.7
	135	40.4	84.9	42.2	7.5	35.6	2.4	36.6	1.4	32.1	0.4	96.7
	140	40.9	73.7	42.9	6.8	36.8	2.0	36.7	1.2	32.3	0.3	84.0
	145	41.5	60.4	43.2	5.7	37.8	1.6	38.3	0.9	33.5	0.3	68.9
	150	41.6	45.1	44.6	4.4	38.1	1.1	39.0	0.7	34.0	0.2	51.6

TABLE 6.4: Number of expected signal events per category at $m_H = 126.5$ GeV, at $\sqrt{s} = 7$ TeV (top) and $\sqrt{s} = 8$TeV (bottom) and breakdown by production process.

$\sqrt{s}$	Category	Events [N_{evt}]	$gg \to H$ [%]	VBF [%]	WH [%]	ZH [%]	ttH [%]
7 TeV	Inclusive	79.4	87.8	7.3	2.9	1.6	0.4
	Unconv. central, low p_{Tt}	10.5	92.9	4.0	1.8	1.0	0.2
	Unconv. central, high p_{Tt}	1.5	66.5	15.7	9.9	5.7	2.4
	Unconv. rest, low p_{Tt}	21.6	92.8	3.9	2.0	1.1	0.2
	Unconv. rest, high p_{Tt}	2.8	65.4	16.1	10.8	6	1.8
	Conv. central, low p_{Tt}	6.7	92.8	4.0	1.9	1.0	0.2
	Conv. central, high p_{Tt}	1.0	66.6	15.3	10.0	5.7	2.5
	Conv. rest, low p_{Tt}	21.1	92.8	3.8	2.0	1.1	0.2
	Conv. rest, high p_{Tt}	2.7	65.3	15.9	11.0	5.9	1.8
	Conv. transition	9.5	89.4	5.2	3.3	1.7	0.3
	2-jet	2.2	22.5	76.7	0.4	0.2	0.1
8 TeV	Inclusive	111.9	87.9	7.3	2.7	1.6	0.5
	Unconv. central, low p_{Tt}	14.2	94.0	4.3	1.7	1.0	0.3
	Unconv. central, high p_{Tt}	2.5	73.5	14.3	7.0	4.3	2.4
	Unconv. rest, low p_{Tt}	30.9	93.7	4.2	2.0	1.1	0.2
	Unconv. rest, high p_{Tt}	5.2	72.9	14.0	7.9	4.7	1.7
	Conv. central, low p_{Tt}	8.9	94	4.3	1.7	1.0	0.3
	Conv. central, high p_{Tt}	1.6	73.8	13.6	7.2	4.2	2.3
	Conv. rest, low p_{Tt}	26.9	93.8	4.2	2.0	1.1	0.2
	Conv. rest, high p_{Tt}	4.5	72.1	14.1	8.5	4.8	1.8
	Conv. transition	12.8	90.1	5.9	3.1	1.8	0.4
	2-jet	3.0	30.8	69.3	0.4	0.2	0.2

In Figures 6.20 and 6.21, the global fit projection evaluated at m_H=125 GeV and superimposed over the invariant mass distributions is shown for each category in the 7 TeV and 8 TeV samples respectively. In both samples, the category with the best resolution is the Unconverted central, high p_{Tt} category, with σ_{CB} =1.36 ± 0.01 (1.35 ± 0.01) GeV at 8 (7) TeV. In contrast, the worst resolution is in the Converted Transition category, with σ_{CB} =2.57 ± 0.02 (2.25 ± 0.02) GeV. In addition, a comparison plot of the two p_{Tt} type categories with different resolutions at 8 TeV is shown in Figure 6.22.

The numerical results of the global fit parameters that fulfil Equations 6.5, 6.4 in each of the categories in 7 and 8 TeV samples are shown in Table 6.5. The resolution seems to be similar in both cases, but the 8 TeV sample appears to be more gaussian than the 7 TeV one, as the α_{CB} value is systematically larger in most categories.

As discussed in Section 6.7.1, the global resolution model only needs two parameters depending on m_H: σ_{CB} and μ_{CB}, all other parameters (the tail parameter α_{CB}, the Crystal Ball fraction f_{CB} and the fraction between the main core and outliers k) are set to a single global value for all mass points. The parameter n_{CB} is set to 10 and fixed in the fit.

6.8.3 Background composition and modelling

In the 100 - 160 GeV mass range, 23788 di-photon candidates pass the selection described in Section 6.3, constituting the 2011 sample at 7 TeV. In the 8 TeV sample 35281 events are selected.

As stated before, the background has three main contributions: $\gamma\gamma$, γj and jj. Also, a small component of a Drell-Yan is present in the data sample. The different background components are estimated using data-driven techniques based on the photon identification and isolation criteria [130]. The Drell-Yan component is obtained from a sample of Z→ e^+e^- events where both electrons pass the photon selection. The measured composition of the selected sample is approximately 74%, 22%, 3% and 1% for the $\gamma\gamma$, γj and jj and Drell-Yan processes, respectively. These results are used to assess the background composition but are not used in the final statistical analysis.

For each category, the total background is estimated from data through a fit to the di-photon mass spectrum in the 100 - 160 GeV mass range. In the fit, a model with

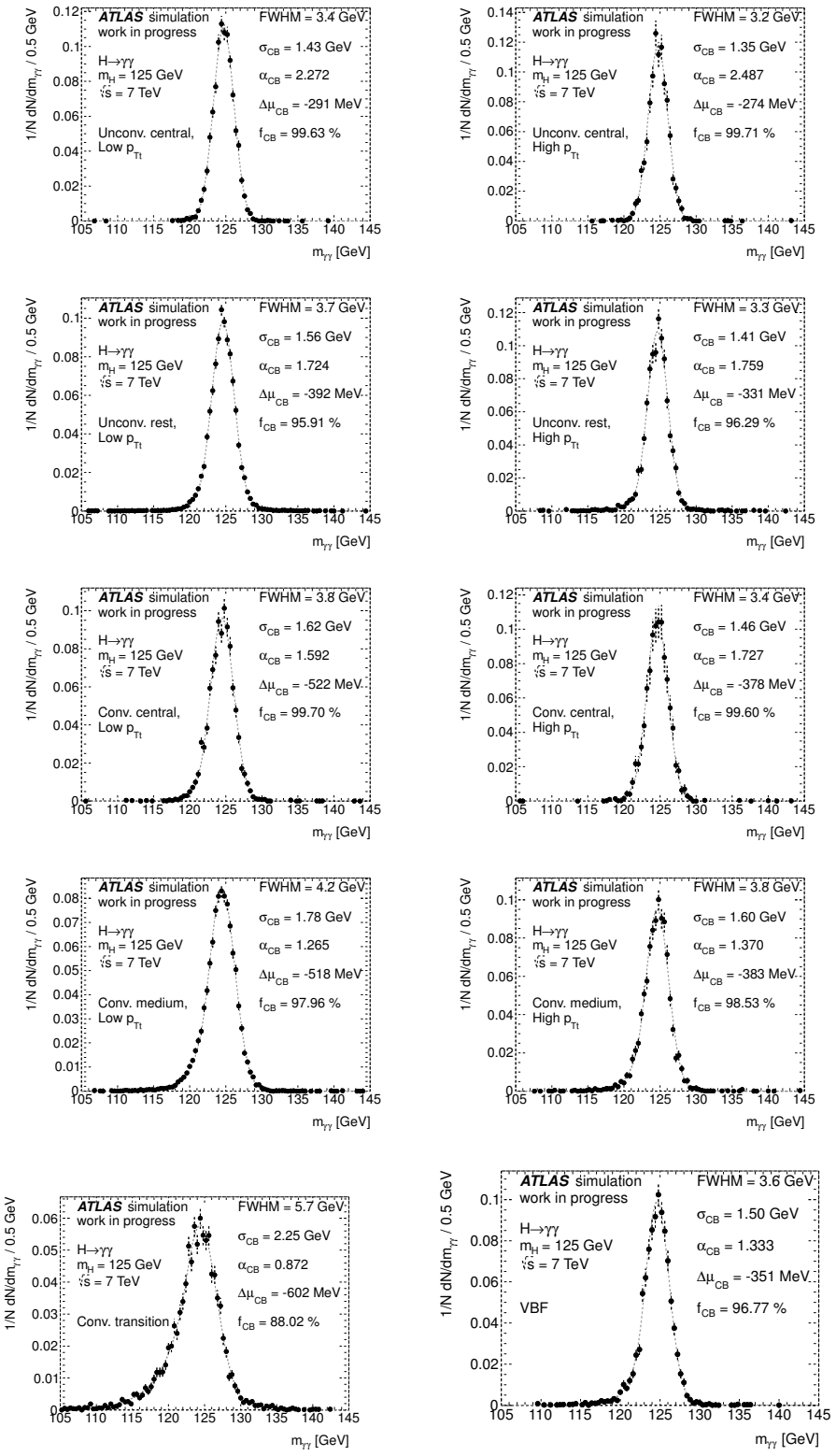

FIGURE 6.20: Reconstructed invariant mass distributions from the signal processes and the projection of the global fit at the MC 125 GeV mass point at 7 TeV for all categories. The parameters appearing in the figures are the evaluation of the global function at that mass point for each category.

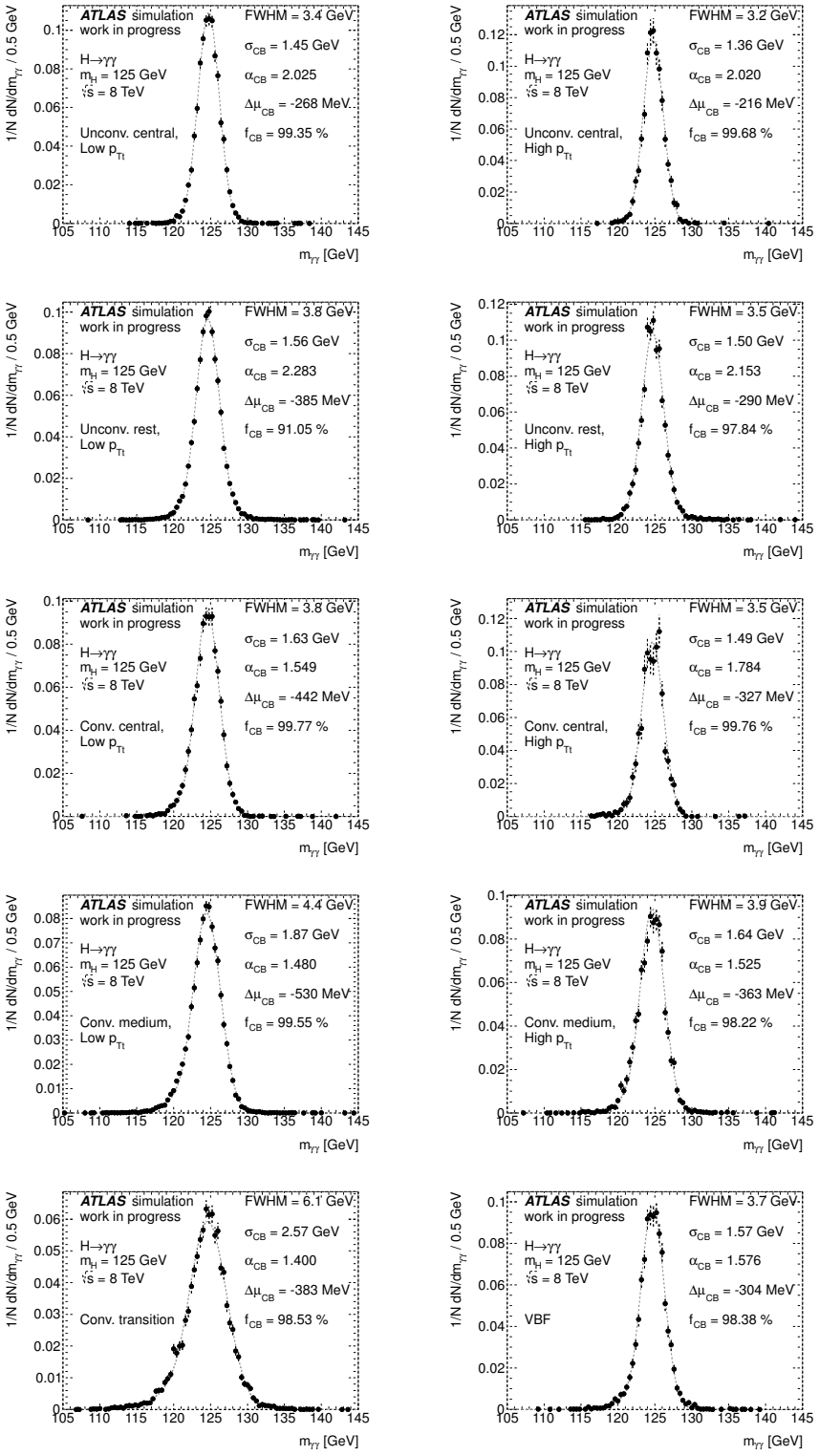

FIGURE 6.21: Reconstructed invariant mass distributions from the signal processes and the projection of the global fit at the MC 125 GeV mass point at 8 TeV for all categories. The parameters appearing in the figures are the evaluation of the global function at that mass point for each category.

TABLE 6.5: The numerical results of the global fit. The linear dependence of the $\mu_{\rm CB}$ shape parameter is given by $\mu_{\rm CB}(M) = M - 125 + \mu(125) + \Delta_\mu \times (M - 125)$; and similarly for the $\sigma_{\rm CB}$. The outlier mean value $\mu_{\rm GA}$ is set to $\mu_{\rm GA} = \mu_{\rm CB}$, and the width of the outlier component is set to $\sigma_{\rm GA} = \kappa_{\rm GA} \times \sigma_{\rm CB}$ with a single value for $\kappa_{\rm GA}$. Parameters with (*) are fixed in the fit, therefore no statistical errors.

Cat.	μ_{CB}(125 GeV) (MeV)	Δ_μ (MeV/GeV)	σ_{CB}(125 GeV) (GeV)	Δ_σ (MeV/GeV)	$\alpha_{CB}(125GeV)$ (%/GeV)	f_{CB} (%)	κGA
7 TeV							
Incl.	-387.6 ± 3.1	-2.156 ± 0.3102	1.614 ± 0.003	9.792 ± 0.18	1.256 ± 0.0052	96.27 ± 0.087	3.445 ± 0.036
CP1	-291.6 ± 6.0	-1.044 ± 0.600	1.433 ± 0.005	8.588 ± 0.320	2.273 ± 0.050	99.63 ± 0.05	3.56(*)
CP2	-274.5 ± 10.0	-2.590 ± 1.001	1.352 ± 0.008	9.154 ± 0.560	2.488 ± 0.170	99.71 ± 0.06	5.30(*)
CP3	-392.5 ± 5.3	-2.391 ± 0.530	1.556 ± 0.005	9.719 ± 0.250	1.724 ± 0.021	95.92 ± 0.19	3.29 ± 0.05
CP4	-331.2 ± 8.9	-2.006 ± 0.890	1.411 ± 0.008	9.621 ± 0.500	1.759 ± 0.041	96.29 ± 0.28	3.77 ± 0.11
CP5	-522.4 ± 9.8	-2.078 ± 0.980	1.619 ± 0.008	8.757 ± 0.540	1.592 ± 0.026	99.71 ± 0.08	4.55 ± 0.54
CP6	-378.9 ± 15.0	-2.254 ± 1.500	1.464 ± 0.013	8.632 ± 0.850	1.727 ± 0.052	99.61 ± 0.09	5.56(*)
CP7	-518.9 ± 6.9	-2.416 ± 0.690	1.781 ± 0.007	9.224 ± 0.410	1.266 ± 0.010	97.97 ± 0.16	2.63 ± 0.06
CP8	-383.4 ± 11,1	-2.880 ± 1.100	1.597 ± 0.010	11.150 ± 0.640	1.370 ± 0.021	98.54 ± 0.15	3.64 (*)
CP9	-602.3 ± 18.0	-0.943 ± 1.800	2.252 ± 0.022	12.990 ± 0.960	0.873 ± 0.013	88.02 ± 0.76	2.29 ± 0.04
CP10	-351.3 ± 10.0	-2.486 ± 1.100	1.505 ± 0.010	10.530 ± 0.590	1.333 ± 0.022	96.78 ± 0.30	4.06 ± 0.18
8 TeV							
Incl.	-365.1 ± 3.8	-1.202 ± 0.381	1.627 ± 0.005	9.123 ± 0.180	1.509 ± 0.010	92.71 ± 0.26	2.41 ± 0.02
CP1	-268.9 ± 8.1	-0.667 ± 0.810	1.447 ± 0.007	7.421 ± 0.400	2.026 ± 0.047	99.36 ± 0.12	3.06 (*)
CP2	-216.7 ± 16 .0	-1.975 ± 1.610	1.360 ± 0.013	8.893 ± 0.770	2.021 ± 0.092	99.69 ± 0.11	4.38 (*)
CP3	-385.8 ± 6.7	-2.487 ± 0.670	1.562 ± 0.008	9.027 ± 0.330	2.284 ± 0.120	91.05 ± 0.61	2.34 ± 0.03
CP4	-290.6 ± 12.0	-0.656 ± 1.200	1.501 ± 0.011	10.250 ± 0.650	2.154 ± 0.093	97.84 ± 0.20	4.69 (*)
CP5	-442.6 ± 13.0	-0.058 ± 1.300	1.627 ± 0.011	7.299 ± 0.590	1.549 ± 0.032	99.78 ± 0.06	4.49 (*)
CP6	-327.3 ± 24.0	0.447 ± 2.400	1.487 ± 0.020	8.538 ± 1.100	1.784 ± 0.092	99.76 ± 0.11	4.73 (*)
CP7	-530.9 ± 8.8	-1.327 ± 0.880	1.875 ± 0.008	9.524 ± 0.410	1.489 ± 0.017	99.56 ± 0.06	4.14 (*)
CP8	-363.6 ± 16.0	-1.943 ± 1.600	1.637 ± 0.016	11.100 ± 0.790	1.525 ± 0.037	98.22 ± 0.48	3.14 ± 0.27
CP9	-383.6 ± 18.1	1.353 ± 1.810	2.567 ± 0.016	15.46 ± 0.83	1.400 ± 0.022	98.53 ± 0.16	4.02 (*)
CP10	-304.8 ± 14.0	-2.751 ± 1.400	1.572 ± 0.013	11.40 ± 0.72	1.576 ± 0.040	98.39 ± 0.18	4.64 (*)

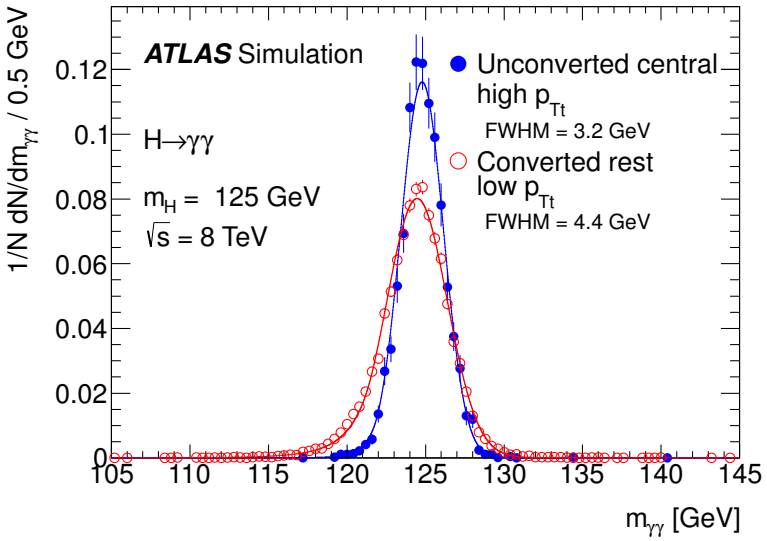

FIGURE 6.22: Invariant mass distributions for a Higgs boson with a hypothesised mass of 125 GeV, for the best-resolution category (σ_{CB}=1.4 GeV) shown in blue and for a category with lower resolution (σ_{CB}=1.9 GeV).

free parameters of background shape and normalisation is chosen for the different categories. The model is required to achieve a good compromise between limiting the size of a potential bias and keeping a good statistical power.

In order to determine the potential bias of a background selected model, studies are performed over large samples of MC background events, where the di-photon mass spectrum shapes are cross-checked with data control regions. The bias is estimated by performing a maximum likelihood fit using a model of background plus signal to these large simulation background only samples (the signal model is the SM expectation, with yields free in the fit). The bias is the largest absolute signal yield obtained in the fit, which is taken as an uncertainty on the background model. The bias is required to be less than 20% of the statistical uncertainty of the fitted signal yield. The model that has the best sensitivity for m_{H}=125 GeV and smaller bias is chosen as a background model in that category. In the final fit to the data, using the procedure explained in Appendix A, a signal-like term considering the found bias to the background model is included in the final likelihood function for each category.

Finally, three different functions are used to model the 10 categories: a fourth order

Bernstein polynomial function[4], an exponential function of a second order polynomial and a single exponential. The explicit models for each category, and their associated uncertainties are shown in Table 6.6. The background-only fits in each of the categories of the two data samples are shown in Figures 6.23 and 6.24. The inclusive mass spectrum combined with 2011 and 2012 data is shown in Figure 6.25.

TABLE 6.6: Systematic uncertainties in the number of signal events fitted due to the background parametrisation, given in number of events. Three different background parametrisation are used depending on the category, an exponential function, a fourth-order Bernstein polynomial and the exponential of a second-order polynomial [117].

Category	Parametrisation	Uncertainty $[N_{\text{evt}}]$	
		$\sqrt{s} = 7$ TeV	$\sqrt{s} = 8$TeV
Inclusive	4th order pol.	7.3	10.6
Unconverted central, low p_{Tt}	Exp. of 2nd order pol.	2.1	3.0
Unconverted central, high p_{Tt}	Exponential	0.2	0.3
Unconverted rest, low p_{Tt}	4th order pol.	2.2	3.3
Unconverted rest, high p_{Tt}	Exponential	0.5	0.8
Converted central, low p_{Tt}	Exp. of 2nd order pol.	1.6	2.3
Converted central, high p_{Tt}	Exponential	0.3	0.4
Converted rest, low p_{Tt}	4th order pol.	4.6	6.8
Converted rest, high p_{Tt}	Exponential	0.5	0.7
Converted transition	Exp. of 2nd order pol.	3.2	4.6
2-jets	Exponential	0.4	0.6

Having the signal and background models, the sensitivity to a Higgs boson signal at any mass for each category can be extracted. This is a function of the signal resolution and the signal to background ratios. In Table 6.7, relevant variables such as the expected number of signal and background, their ratio in a window around m_{H}= 126.5 GeV that would contain 90% of the signal events, and the observed number of events in this window are presented.

6.8.4 Systematic uncertainties

There are three sources of experimental systematic uncertainties to the analysis: uncertainty on the signal yield, uncertainties on the di-photon mass peak position

[4]The Bernstein polynomials of degree n are defined by $B_{\text{i,n}}(t) = \binom{n}{i} t^i (1-t)^{n-i}$, for i=0,1,..,n, where $\binom{n}{i} = \frac{n!}{i!(n-i)!}$. By induction, all Bernstein polynomials are non-negative for the interval $0 \leq t \leq 1$ [131].

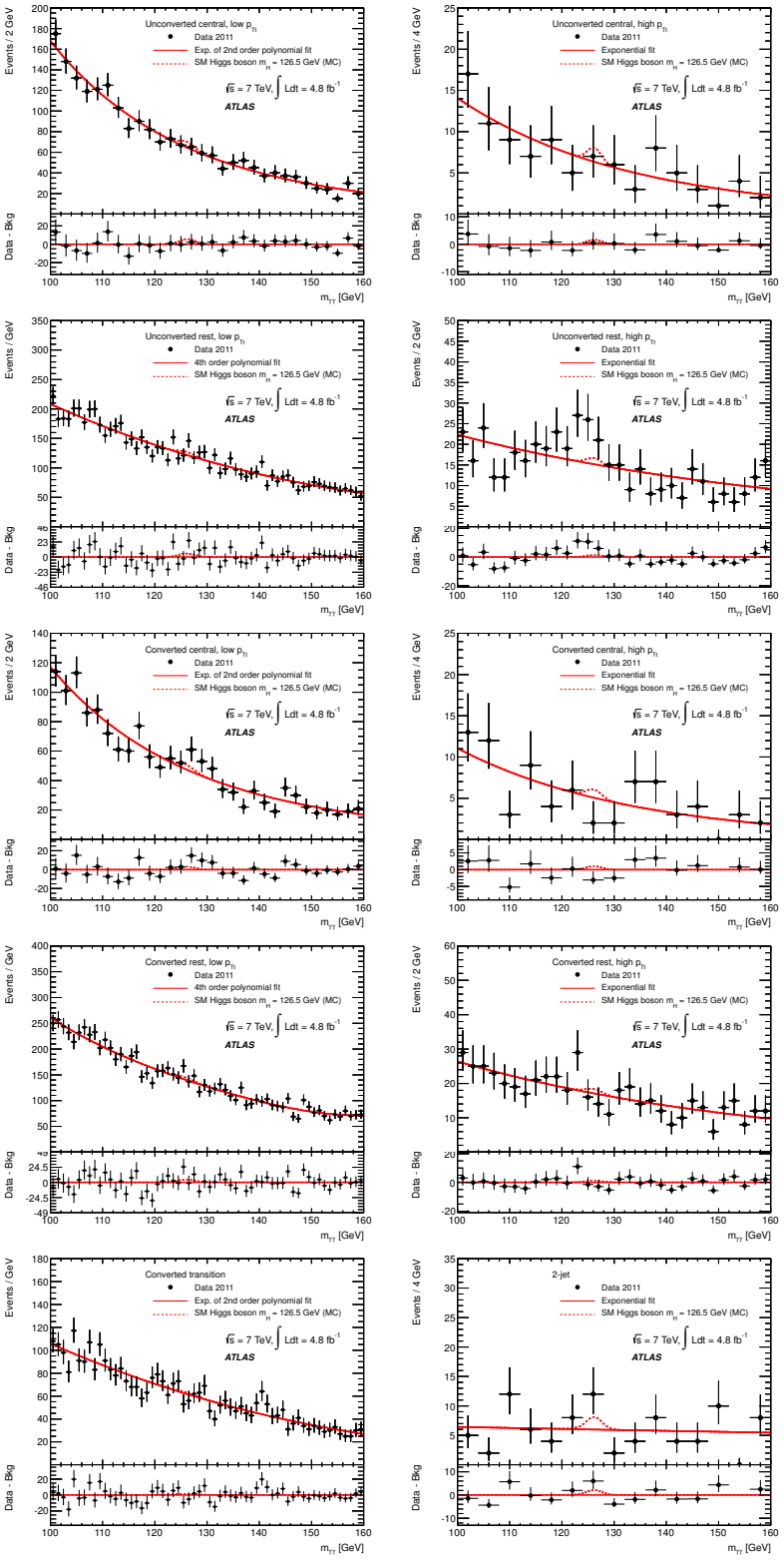

FIGURE 6.23: Background-only fits to the di-photon invariant mass spectra for the ten categories. The bottom inset displays the residual of the data with respect to the background fit. The Higgs boson expectation for a mass hypothesis of 126.5 GeV corresponding to the SM cross-section is also shown. All figures correspond to the $\sqrt{s} = 7$ TeV data sample [3].

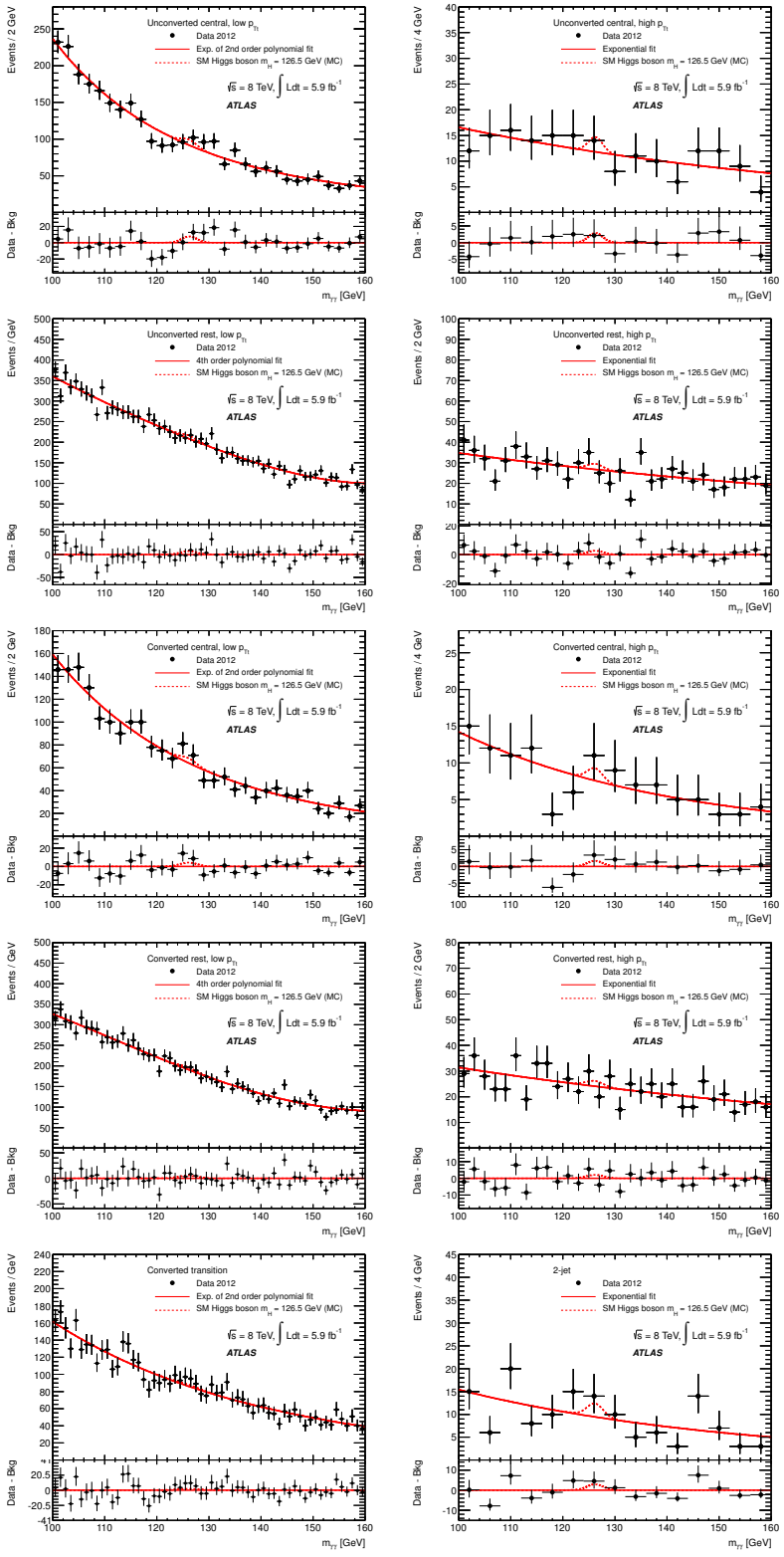

FIGURE 6.24: Background-only fits to the di-photon invariant mass spectra for the ten categories. The bottom inset displays the residual of the data with respect to the background fit. The Higgs boson expectation for a mass hypothesis of 126.5 GeV corresponding to the SM cross-section is also shown. All figures correspond to the $\sqrt{s} = 8$ TeV data sample [3].

TABLE 6.7: Number of expected signal S and background events B in mass a window around $m_H = 126.5$ GeV that would contain 90% of the expected signal events. In addition, σ_{CB}, the Gaussian width of the Crystal Ball function describing the invariant mass distribution [117], and the FWHM of the distribution, are given. The numbers are given for data and simulation at $\sqrt{s} = 7$ TeV (top) and 8 TeV (bottom) for different categories and the inclusive sample.

$\sqrt{s}$	Category	σ_{CB}	FWHM	Window [GeV]	Observed	S	B	S/B
7 TeV	Inclusive	1.63	3.84	122.94 - 129.28	2653	71.5	2557.6	0.028
	Unconv. central, low p_{Tt}	1.45	3.41	123.8 - 128.61	161	9.4	154.9	0.061
	Unconv. central, high p_{Tt}	1.37	3.22	123.96 - 128.48	7	1.3	7.2	0.181
	Unconv. rest, low p_{Tt}	1.57	3.71	123.36 - 128.85	700	19.5	669.7	0.029
	Unconv. rest, high p_{Tt}	1.43	3.36	123.68 - 128.65	57	2.5	37.7	0.066
	Conv. central, low p_{Tt}	1.63	3.84	123.12 - 128.83	166	6	136.4	0.044
	Conv. central, high p_{Tt}	1.48	3.48	123.58 - 128.66	2	0.9	6.4	0.141
	Conv. rest, low p_{Tt}	1.79	4.23	122.53 - 129.43	986	18.9	967.3	0.02
	Conv. rest, high p_{Tt}	1.61	3.8	123.12 - 129.11	48	2.5	51.2	0.049
	Conv. transition	2.27	5.52	120.24 - 131.55	709	8.5	703.9	0.012
	2-jet	1.52	3.59	123.26 - 129.03	12	2	8.7	0.23
8 TeV	Inclusive	1.64	3.88	123.14 - 129.12	3649	100.7	3584.8	0.028
	Unconv. central, low p_{Tt}	1.46	3.44	123.78 - 128.68	237	12.7	224.7	0.057
	Unconv. central, high p_{Tt}	1.37	3.24	123.98 - 128.59	16	2.3	13.6	0.169
	Unconv. rest, low p_{Tt}	1.58	3.73	123.42 - 128.8	1141	27.8	1122.5	0.025
	Unconv. rest, high p_{Tt}	1.52	3.57	123.66 - 128.76	75	4.7	68.3	0.069
	Conv. central, low p_{Tt}	1.64	3.86	123.16 - 128.95	207	8	186.6	0.043
	Conv. central, high p_{Tt}	1.5	3.53	123.61 - 128.74	13	1.5	9.7	0.155
	Conv. rest, low p_{Tt}	1.89	4.45	122.57 - 129.36	1311	24.2	1299.9	0.019
	Conv. rest, high p_{Tt}	1.65	3.9	123.18 - 129.09	71	4	71.3	0.056
	Conv. transition	2.59	6.1	121.36 - 130.88	849	11.5	821.2	0.014
	2-jet	1.59	3.74	123.38 - 129.01	19	2.7	13.3	0.203

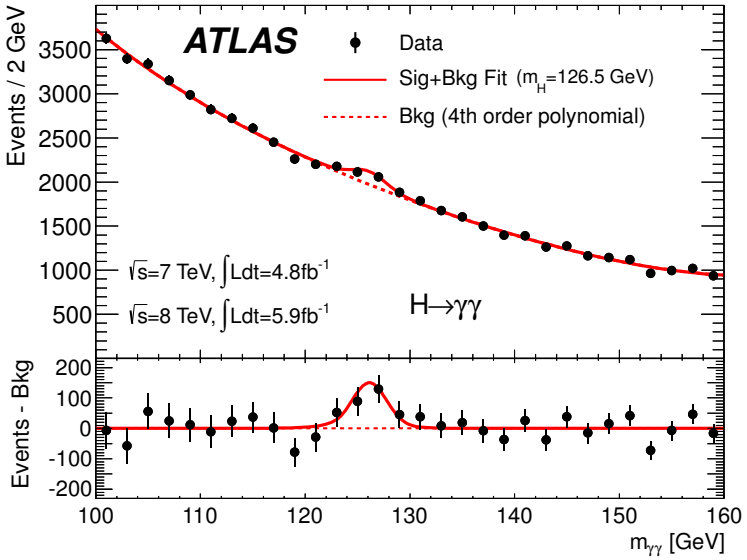

FIGURE 6.25: Invariant mass distribution of di-photon candidates for the combined 7 TeV and 8 TeV data samples. The result of a fit to the data of the sum of a signal component fixed to an hypothesised Higgs mass of 126.5 GeV and a background component described by a fourth-order Bernstein polynomial is superimposed. The bottom inset displays the residuals of the data with respect to the fitted background component [3].

and resolution, and the uncertainty on the background model. The latter is discussed in the previous section, and summarised in Table 6.6. The first two uncertainty sources related to the signal are explained next.

6.8.4.1 Systematic uncertainty on the expected signal yields

Several factors act as a source of systematic uncertainty on the calculation of the expected signal yield:

- **Theoretical uncertainties** on the Higgs boson production cross-section and branching fraction into $\gamma\gamma$. These uncertainties are taken from [127, 128] and [132] respectively. The uncertainties are related to the energy scales used for the fixed-order calculation, the uncertainty from the parton density function and the value of the strong coupling α_s used in the perturbative calculation.

- **Luminosity:** The systematic uncertainty on the total integrated luminosity is 1.8% for the 7 TeV data sample, and 3.6% for the 8 TeV data.

- **Trigger efficiency:** The uncertainty on trigger efficiency is found to be 1%.

- **Photon identification:** The photon identification uncertainty is obtained by comparing the efficiency obtained in MC and various data-driven methods based on $Z \to \ell\ell\gamma$ and $Z \to e^+e^-$. More information on these methods can be found in [102]. For the 7 TeV analysis, a neural-network is used to perform the photon identification, and an uncertainty of 4% is assigned to each photon, in most of η regions. The exceptions are for unconv. photons in the $1.52 < |\eta| < 1.81$ and $1.81 < |\eta| < 2.37$ regions, for which 5% and 7% uncertainties are assigned. In the 8 TeV sample the photon identification is performed by means of a cut-based analysis based on shower shapes, as discussed in Chapter 4. The systematic uncertainty from this approach is 5% for photons in the barrel, and 7% in the end-cap. The uncertainties are treated as fully correlated between the two photons, and have a relative value of 8.4% per event at 7 TeV and 10.8% at 8 TeV.

- **Isolation cut efficiency:** A relative shift of 80 MeV is found between the isolation distributions in data and MC for electrons from the $Z \to e^+e^-$ sample. This shift leads to an uncertainty in the isolation cut efficiency of 0.4% at 7 TeV and 0.5% at 8 TeV.

- **Photon energy scale:** The uncertainty on the photon energy scale leads to an uncertainty of 0.3% in the expected yields.

- **Pile-up effect:** The effect of pile-up on the signal yields is estimated by comparing samples with low and high pile-up conditions. The uncertainty is found to be 4%.

- **Uncertainty due to migration among categories:** There are several factors that could create migration of signal events between the categories, which are similar in the 7 TeV and 8 TeV analysis:

  1. *The Higgs kinematics:* These uncertainties could be caused by the uncertainty on the Higgs kinematics, which could create a migration in the categories of high and low p_{Tt}. The uncertainty is estimated by varying scales and PDFs used by HqT2 [133]. The uncertainty is found to be 9% on both data samples.

  2. *Conversion Fraction with pile-up:* As observed in Chapter 5, the conversion fraction grows with increasing pile-up, which could create a migration between the conversion categories. An uncertainty of 2% is assigned to this effect.

3. *Material effects:* The probability of conversion is a function of the upstream material in the calorimeter, so the uncertainty in the amount of material would cause migration among the conversion categories. The uncertainty is estimated by comparing the fraction of events in the different categories between nominal MC samples and samples generated with distorted material. An uncertainty of 4% is assigned this effect in the conversion categories.
4. *Primary vertex selection:* The probability of selecting a wrong primary vertex is very small and is neglected.
5. *Jet energy scale:* The energy scale is varied by its uncertainty and the migrations from the 2-jet category are quantified, the uncertainty is found to be 19% for the 2-jet category and 4% for the other categories.
6. *Underlying events:* Uncertainties due to the modelling of the underlying event are estimated by comparing different underlying event tunes in the simulation. It is found to be 6% for VBF and 30% for other processes in the 2-jet category.
7. *JVF modelling:* The uncertainty in the jet vertex fraction is obtained as the differences between data and MC, and is set to 12%.

All uncertainties, except the one on integrated luminosity are treated as fully correlated between the 7 TeV and 8 TeV analysis.

6.8.4.2 Systematic uncertainty on the mass resolution

The sources of uncertainty on the signal mass resolution are the following:

- **Uncertainty on the constant term:** As explained in Section 6.7.1, the calorimeter resolution is described by three terms. The dominant in this energy region is the constant term, which is about 1% in the barrel and between 1.2% to 2.1% in the end-caps. In order to estimate the systematic due to the uncertainty in this term, the constant term is varied within its uncertainty separately for the parts correlated and uncorrelated with the sampling term. An uncertainty of 12% in found.

- **Pile-up effect on energy resolution:** The FWHM of the signal peak is compared in samples of high and low pile-up environment. The uncertainty is 4%.

- **Electron to photon extrapolation:** As discussed in Chapter 4, the calorimeter energy resolution is estimated using Z→ *ee* events. An uncertainty due to the electron to photon extrapolation is obtained by assuming that the difference in the calorimeter response to electrons and photons is dominated by the upstream material. An in-situ $Z \rightarrow ee$ calibration is performed out of MC samples generated with distorted material and applied the $H \rightarrow \gamma\gamma$ samples. The uncertainties found are in the order of 6%.

The total resulting uncertainty on the mass resolution is 14%, which is applied to the width of the signal components (CB and GA). The systematics are treated as fully correlated between the 7 TeV and 8 TeV data.

6.8.4.3 Uncertainty on the invariant mass peak position due to the photon energy scale (ES)

Three sources of uncertainties contribute to the uncertainty on the mass peak position (the origin of these uncertainties are described in better detail in Section 4.2.3):

- **Pre-sampler energy scale:** The uncertainty in the pre-sampler energy scale is found to be 5% in the barrel and 10% in the end-caps, the uncertainty due to this fact is evaluated separately for barrel and end-caps candidates.

- **Uncertainties from material effects** are estimated when extrapolating the electron ES to photons. This is estimated separately for material volumes below and above $|\eta| = 1.8$.

- **In-situ calibration uncertainties:** the effect on the peak position of the multiple small uncertainties from the in-situ $Z \rightarrow ee$ calibration explained in Chapter 4 is evaluated.

A total of 0.6% of systematic uncertainty is assigned to the peak position, and therefore to the mass scale. As for all other uncertainties, they are treated as fully correlated between the 7 TeV and 8 TeV analyses.

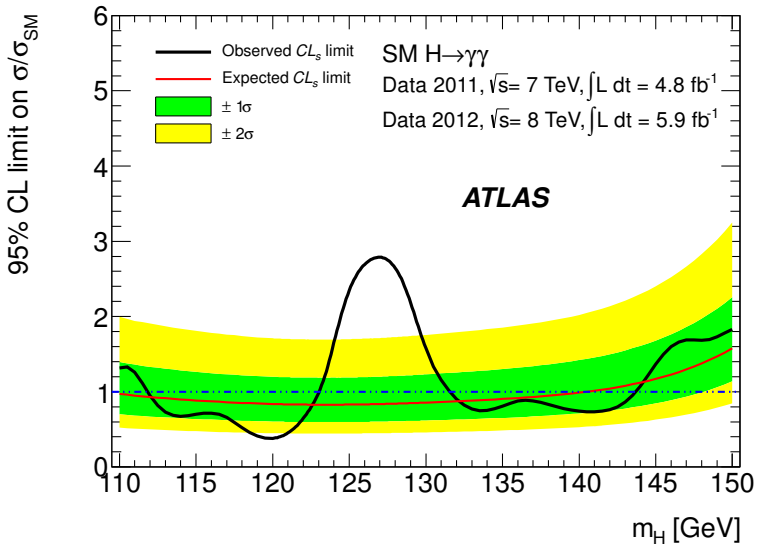

FIGURE 6.26: Expected and observed CLs limit on the normalised signal strength as a function of the assumed Higgs boson mass for the combined $\sqrt{s} = 7$TeV and $\sqrt{s} = 8$TeV analysis. The dark (green) and light (yellow) bands indicate the expected limits within ± 1 sigma and ± 2 sigma fluctuations, respectively [3].

6.8.5 Results

In Figure 6.25, the invariant mass spectrum is shown for the combined 7 TeV and 8 TeV datasets. An excess of events is observed around $m_{\mathrm{H}} = 126.5$ GeV. In order to characterise this excess, a statistical analysis based on an un-binned likelihood function constructed for each of the categories is performed to estimate exclusion limits, determine the significance of the excess, and evaluate a potential signal strength and mass range of this potential signal. A short summary of the statistical method is presented in Appendix A.

In Figure 6.26, the expected and observed exclusion limits on the Higgs boson production cross-section for the decay into two photons are presented. The mass regions of 112-123 and 132-143.5 GeV mass regions are excluded under the SM hypothesis at 95% of confidence level. In the 123-132 GeV region, it is not possible to exclude the SM hypothesis.

The compatibility of the selected events with the background-only hypothesis (p_0, see Appendix A), in the combination of 7 TeV and 8 TeV data is shown in Figure 6.27. The minimal value of $p_0 = 1.7 \times 10^{-6}$ is found at m_{H}=126.5 GeV. The local significance at that mass is 4.5σ, and the global significance (after the look-elsewhere effect, see Appendix A) is found to be 3.6σ.

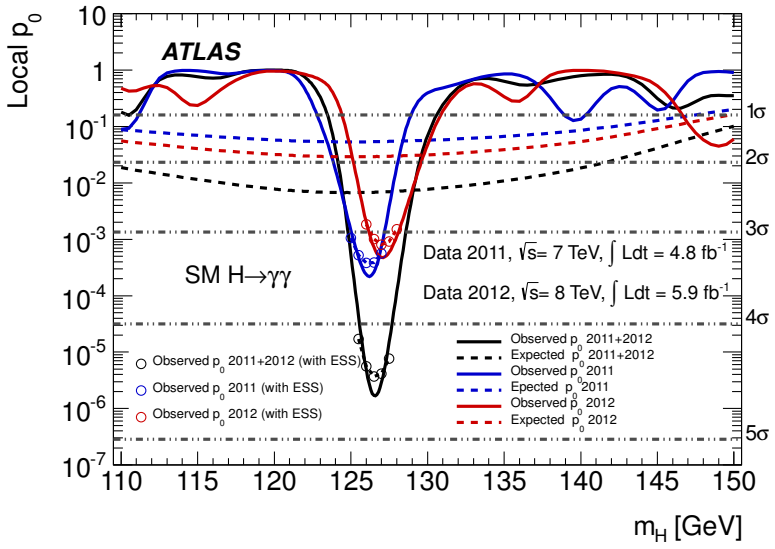

FIGURE 6.27: Expected and observed local p_0 values for a SM Higgs boson as a function of the hypothesised Higgs boson mass (mH) for the combined analysis and for the 7 TeV and 8 TeV data samples separately. The observed p0 including the effect of the photon energy scale uncertainty on the mass position is included via pseudo-experiments and shown as open circles [3].

In Figure 6.28 signal strength, as a function of the Higgs mass is shown. At $m_{\mathrm{H}} = 126.5$ GeV, the best fit value is $\hat{\mu} = 1.8 \pm 0.5$. The result of the best fit values of μ for each of the categories at $m_{\mathrm{H}} = 126.5$ GeV is shown in Figure 6.29.

Finally, the obtained likelihood contours in the (μ,m_{H}) plane are shown in Figure 6.30, corresponding to 68% and 95% CL contours.

6.9 Analysis update and properties of the new boson

The results presented in Section 6.8.5, led to the discovery of a Higgs-like particle, after combining with the results in the $H \to ZZ$ and $H \to WW$ searches [3]. After this publication, the status of"search" evolved in ATLAS to the"measurement of properties". Results with the complete 7 and 8 TeV datasets (4.8 + 20.7 fb^{-1}) are being released since winter 2013 [55]. In these analyses, the strategy is improved to be more sensitive to different signal production processes allowing a more precise measurement of their strengths.

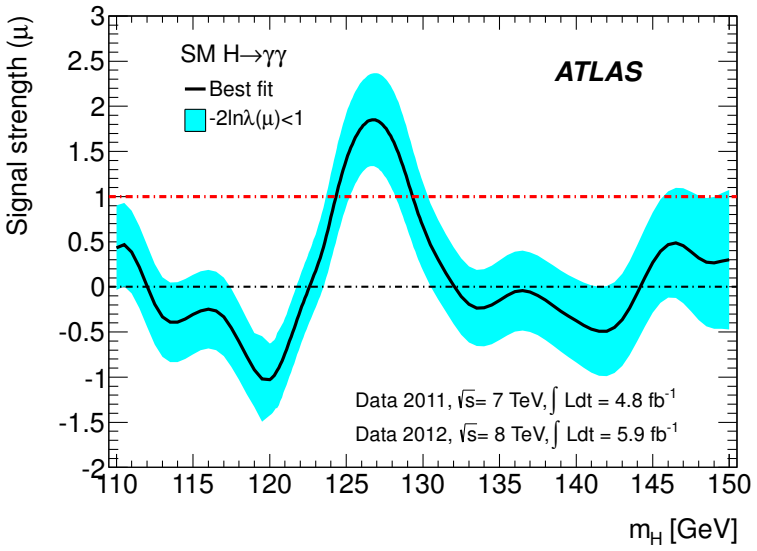

FIGURE 6.28: Best fit value for the signal strength as a function of the assumed Higgs boson mass for the combined analysis [3].

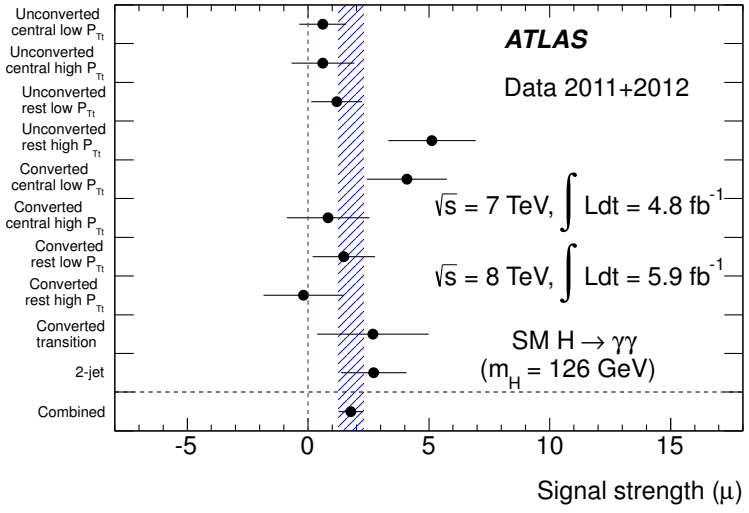

FIGURE 6.29: Best fit value for the signal strength for the different categories at a Higgs mass of 126 GeV for the for the combined $\sqrt{s} = 7$TeV and $\sqrt{s} = 8$TeV data samples. The band corresponds to the error of the combined result [3].

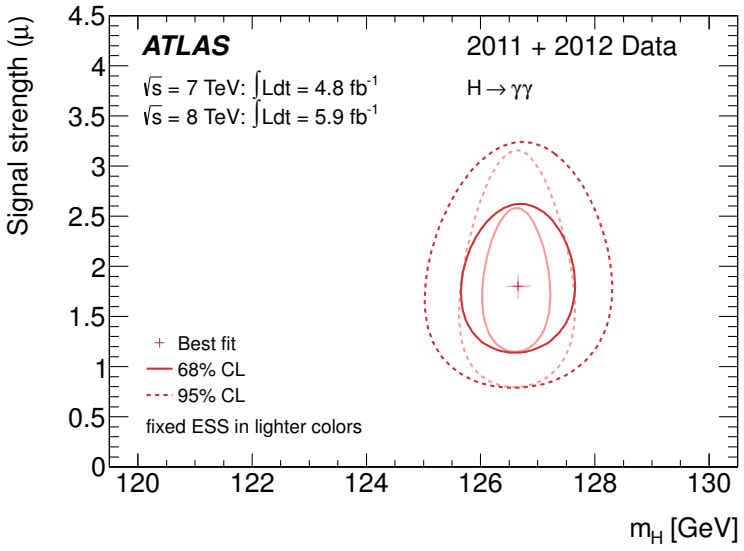

FIGURE 6.30: Confidence intervals contours for the H to gamma gamma channel in the (μ, m_{H}) plane. The 68% and 95% CL contours are for the combined 7 TeV and 8 TeV analysis. The light lines indicate the effect of holding constant at their best-fit values the nuisance parameters which describe the energy scale systematic (ESS) uncertainties in the likelihood [3].

In Figure 6.31, the inclusive invariant mass distribution of the diphoton candidates for the combined 7 and 8 TeV data sample is shown, overlaid with the signal-plus-background fit. The largest local signal significance in the combined data sample is found to be 7.4σ at $m_H = 126.5$ GeV, where the expected significance is 4.1σ, as shown in Figure 6.32.

The mass measurement is updated with the full 2012 dataset. In order to estimate the mass, a test statistic is used, where m_H is the parameter of interest, as explained in Appendix A, and the signal strength parameter μ is treated as a free parameter in the fit. The global resolution model, described in 6.7.1, is used (as well as in the rest of the $H \to \gamma\gamma$ analysis with the complete 8 TeV data sample), and allows to build the likelihood used in the test statistic. The best-fit m_H value is found to be:

$$m_H = 126.8 \pm 0.2(stat.) \pm 0.7(sys.) \text{ GeV}. \tag{6.12}$$

The result is shown in Figure 6.33, with the complete 8 TeV data sample, the value of the measured mass increases by 200 MeV from the result presented in Section 6.8.5. The dominant contribution to the systematic uncertainty comes from

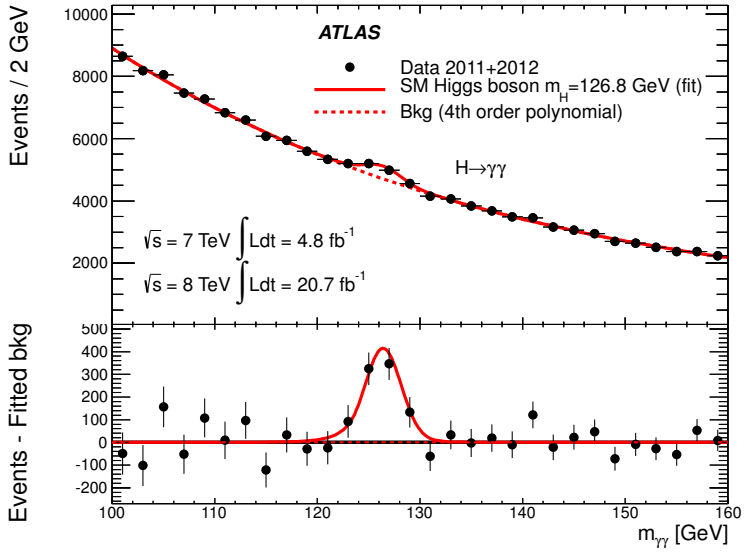

FIGURE 6.31: Invariant mass distribution of di-photon candidates for the combined 7 TeV and 8 TeV data samples. The result of a fit to the data of the sum of a signal component fixed to an hypothesised Higgs mass of 126.8 GeV and a background component described by a fourth-order Bernstein polynomial is superimposed. The bottom inset displays the residuals of the data with respect to the fitted background component [55].

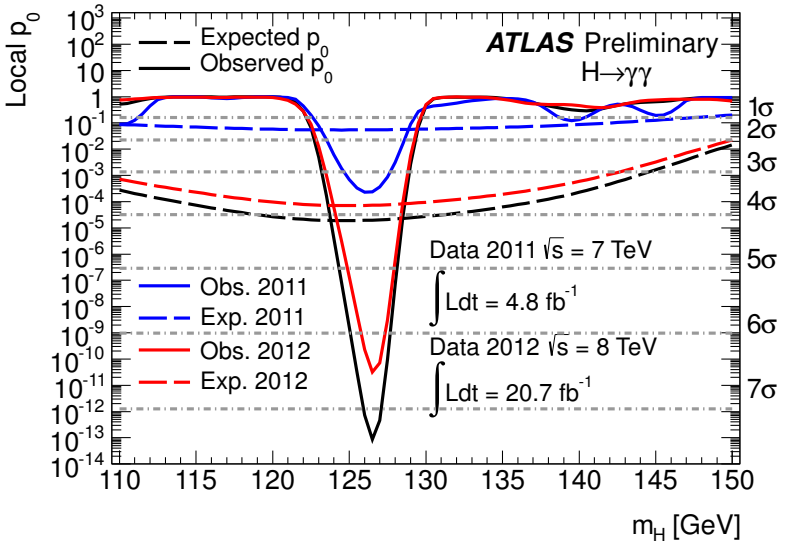

FIGURE 6.32: The observed local p_0 value as a function of m_H for the TeV data (blue), 8 TeV data (red), and their combination (black). The expected local p_0 under the SM Higgs boson signal plus background hypothesis is shown in dashed curves. The largest local significance in the combination of 7 TeV data and 8TeV data is found to be 7.4σ at m_H =126.5GeV, where the expected significance is 4.1σ [55].

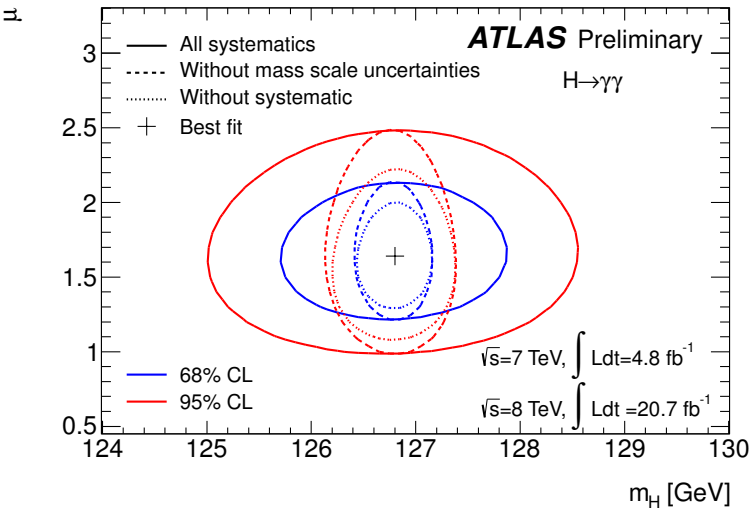

FIGURE 6.33: Confidence intervals contours for the H to gamma gamma channel in the (μ, m_{H}) plane. The 68% and 95% CL contours are for the combined root $\sqrt{s}$ = 7TeV and root $\sqrt{s}$ = 8TeV analysis. Results when photon energy scale systematic uncertainties are removed (dashed), and results when all systematic uncertainties are removed (dotted), are also shown [55].

the photon energy scale, that consists primarily of uncertainties from the standard in-situ calibration, and the electron to photon extrapolation which have been discussed in detail in Section 4.2.3.

The results in the $H \to ZZ$ and $H \to WW$ searches are also updated with the complete 8 TeV dataset, and a combined spin measurement is performed in [134]. The Standard Model spin parity hypothesis is compared with alternative hypotheses (corresponding to a graviton-inspired spin-2 tensor with minimal couplings to SM particles). The data are found to be compatible with the SM hypothesis of a spin-0 particle as shown in Figure 6.34.

Finally, the signal strength is also updated in the $\gamma\gamma$ channel, and compared to other channels as shown in Figure 6.35. The signal strength in the diphoton channel is:

$$\mu = 1.55 \pm 0.23(stat) \pm 0.15(syst) \pm 0.15(theory), \tag{6.13}$$

μ is found to be consistent across categories and is about 2 standard deviations larger than the SM Higgs hypothesis [135]. In addition, the categorisation in the $H \to \gamma\gamma$ analysis allows to measure the signal strength parameters for different Higgs boson production modes, to characterise their contributions to the observed excess.

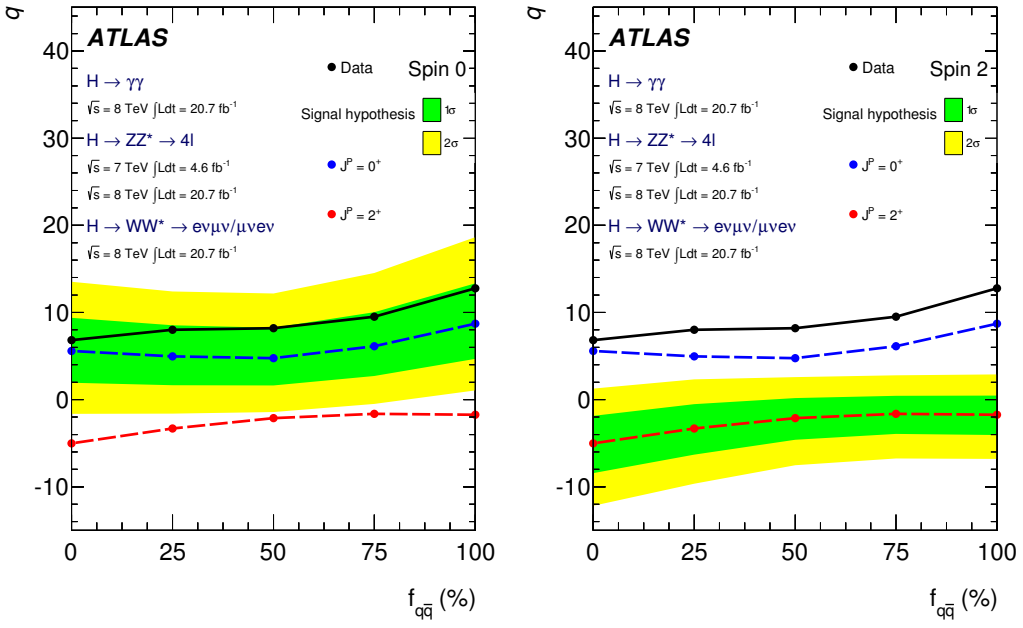

FIGURE 6.34: Expected distributions of likelihood ratio, for the combination of channels as a function of the fraction of the spin-2 production mechanism. The green and yellow bands represent, respectively, the one and two standard deviation bands for the 0+ (a) and for the 2+ (b) [134].

As described in Chapter 1, the decay of the Higgs boson into $\gamma\gamma$ and $Z\gamma$ are mediated via top and W loops. These two channels are therefore sensitive to new physics. Enhancement (or suppression) of these decays rates may occur via contributions from new heavy charged particles. The results shown in this chapter may suggest a hint of an enhanced decay ratio in the $\gamma\gamma$ decay channel. In this context the search for the Higgs boson in the $Z\gamma$ channel could provide additional correlated information. This analysis is presented in the next chapter.

The search for the Fermiophobic Higgs boson in the has been performed both in ATLAS and CMS experiment using the data collected at 7 TeV. This searches lead to the exclusion of the fermiophobic Higgs boson in the mass range 110-194 GeV is excluded at 95% confidence level [136].

6.10 Discussion

Several public results have been released by ATLAS [3, 55, 117, 122, 125, 137–141], in the search of the Higgs boson in the di-photon final state with intermediate

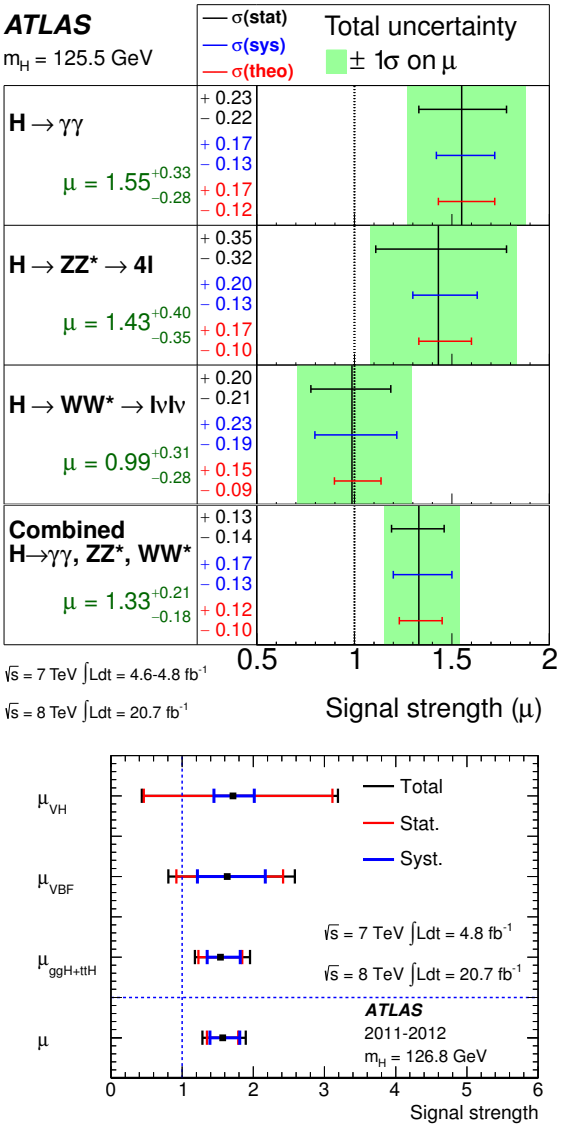

FIGURE 6.35: Top: The measured production strengths for a Higgs boson of mass m_H =125.5 GeV, normalised to the SM expectations, for diboson final states and their combination. The best-fit values are shown by the solid vertical lines. The total $\pm 1\sigma$ uncertainty is indicated by the shaded band, with the individual contributions from the statistical uncertainty (top), the total (experimental and theoretical) systematic (middle), and the theory uncertainty (bottom) on the signal cross section (from QCD scale, PDF, and branching ratios) shown as superimposed error bars. Bottom: Measured signal strengths, normalised to the SM expectation, for the three individual production mechanisms and for a Higgs boson mass of 126.8 GeV. The last line shows the result for a global strength parameter μ applied to all production modes. The error bars indicate the total uncertainty (black), the statistical uncertainty (red) and the systematic uncertainty (blue) [135].

datasets accumulated during the first run of the LHC. In these analyses, and as the $H \to \gamma\gamma$ search evolved in ATLAS, personal contributions in areas such as selection, categorisation, photon performance, improvement to the mass resolution and the global resolution model are recorded in public and private results. A significant part of these studies and contributions are presented in this thesis.

As shown along the chapter, the main contribution is the signal modelling. The signal model proposed in this thesis has been used in all public ATAS $H \to \gamma\gamma$ results from [139] onwards, and plays an important role in the mass measurement. Since the global resolution model is an analytical function of the Higgs mass, it is used to build a likelihood function used in the profile likelihood ratio for the mass measurement. Several ATLAS Higgs analyses now use signal models built following a similar logic as the one for the $H \to \gamma\gamma$ global resolution model presented in this Chapter.

Chapter 7

Search for the SM Higgs boson in the $H \to Z\gamma$ channel

Contents

7.1 Introduction

The analysis presented in Chapter 6 combined with the results of the Higgs searches in the ZZ and WW channels in ATLAS, provided a conclusive evidence for a new particle with a mass about 126 GeV [3]. Similar results were observed by CMS [142]. To determine if this new particle is the SM Higgs boson, it is critical to determine properties such as spin, mass and couplings. Furthermore, the search for additional final states of the SM Higgs boson, and/or other possible Higgs-like particles, should continue.

This chapter presents the search for the SM Higgs boson in the $Z\gamma$ decay channel, where the Z boson decays into electrons or muons. In this way, the three final state particles are completely reconstructed. In the low mass range, the Higgs decay rate to $Z\gamma$ is the same order of magnitude as the $\gamma\gamma$, but the low $Z \to ll$ branching fraction makes the total number of expected Higgs events to be about 20 times smaller than those for $H \to \gamma\gamma$ at 125 GeV[1]. This analysis is the first search performed in ATLAS on this channel and uses the whole 7 TeV and 8 TeV data samples (4.6 fb^{-1} and 20.7 fb^{-1} respectively). It is fully documented in [4].

The main background for this analysis is the SM Zγ ISR process (studied in [143]). Another source of background comes from production of a Z boson in association with jets, where the Z decays into leptons and one of the jets creates a fake photon. Smaller contributions arise from $t\bar{t}$ events, and WZ events.

In this Chapter the main features of this analysis are presented. The simulation samples are detailed first in Section 7.2, followed by the event selection in Section 7.3. Personal contributions to the signal and background modelling are present in 7.4 which led to the final models described in Sections 7.5.2 and 7.6. Finally, the results are discussed in Section 7.8[2]. The analysis strategy is very similar to the one in H$\to \gamma\gamma$, reason why some of the arguments in this chapter are general and referenced to sections of Chapter 6 where a more detailed discussion is presented.

[1] At 125 GeV the predicted cross section is $\sigma = 17.5$ (22.3) pb at 7 (8) TeV, the Higgs branching ratio into a Z boson and a photon is 1.54×10^{-3} and the branching ratio of the Z into electrons and muons is 6.7%

[2] Similarly to the Chapter 6, the final results are a product of several contributors. Studies presented in Sections 7.4 and 7.5.2 correspond to the personal contribution to the analysis.

7.2 Simulation Samples

To study the characteristics of signal and background events, MC samples are produced using various event generators. The simulated samples contain bunch-train pile-up, to give a realistic description of the experimental conditions under which data are taken. The interaction of particles with the detector materials is modelled with GEANT 4 [108] and the detector response is simulated. The MC events are reconstructed with the same software releases and the same algorithms used for collision data.

Signal samples for a Standard Model Higgs boson decaying to $Z\gamma$, followed by a decay of the Z to a charged lepton pair, are generated with POWHEG [144, 145], interfaced to PYTHIA8 [119] for showering and hadronization. Signal events are generated for seven different Higgs mass points, every 5 GeV at m_H = 120, 125, ... 150 GeV. Only the two dominant Higgs production processes are simulated, ggF and VBF. Together, these two processes constitute 95% of the total signal cross section. In each sample, the Z boson is forced to decay to charged lepton pairs ($\ell^+\ell^-$, $\ell = e, \mu$ but also $\tau^+\tau^-$), with equal fractions (1/3 for each channel, up to Poisson fluctuations) as expected.

Background samples as the SM ISR $Z\gamma$ events are generated with SHERPA 1.4.0 at 7 TeV and 1.4.1 at 8 TeV [110–112], using the CT10 family of PDFs calculated at next-to-leading order (NLO) [113]. Separate samples are produced for the $ee\gamma$ and $\mu\mu\gamma$ final states. Up to three additional partons are produced in the hard scattering processes, with matrix elements implemented at LO.

The background Z+jets events (with Z decaying into electron or muon pairs) are generated with SHERPA 1.4.0 and ALPGEN 2.13 [146] interfaced to HERWIG 6.510[147] for parton shower and fragmentation into particles and to JIMMY 4.31[148] to model the contributions of the underlying events, using the AUET2-CTEQ6L1 tune[149]. The ALPGEN samples are generated using the CTEQ6L1 parton distributions [150], while the SHERPA samples use the CT10 ones. For the ALPGEN samples, the final stated QED radiation is simulated with PHOTOS [151]. For both samples the LO matrix elements for the production of up to 5 partons are used for the event generation.

Background events from the $t\bar{t}$ process are generated with MC@NLO [152] interfaced to HERWIG 6.510 for parton shower and fragmentation and to JIMMY 4.31 for the underlying event. The CT10 family of PDFs are used.

Background events from the WZ (with leptonic decays) process at 7 TeV are generated with SHERPA 1.3.1 using the CTEQ6L1 PDFs. Up to three partons are produced in the hard scattering. For the 8 TeV samples, WZ events are generated with POWHEG interfaced to PYTHIA8.

7.3 Event Selection

The total integrated luminosity used in this analysis is 20.7 fb^{-1} at 8 TeV and 4.6 fb^{-1} at 7 TeV, which are the final values after the data are subjected to detector oriented quality requirements. A combination of single-lepton or di-lepton triggers is used to select the data (details are in Table 7.1). The primary vertex with the largest $\sum |\vec{p_T}|$ of tracks associated to it, is considered as the primary vertex of the hard interaction.

Selected muons can be classified in three reconstruction categories: Combined muons (CB), for which the track is reconstructed in both the ID and MS and the measurement is combined as explained in Chapter 5; standalone muons (StandA.) are reconstructed in the MS outside of the ID acceptance ($2.5 < |\eta| < 2.7$); and calo Muons (Calo), reconstructed in the ID in the centre of the barrel ($|\eta| < 0.1$), region without MS coverage, are identified by recognising the energy depositions in the calorimeters compatible with those of a minimum-ionising particle. The ID tracks associated with muons are required to have a minimal number of hits in the subdetectors, and to have a transverse and longitudinal impact parameter with respect to the PV. Details about the specific cuts used to select muons are found in Table 7.2. Similarly as done in Chapter 5, the momenta of the muons are corrected in MC to better reproduce the data. The ID, MS and CB momentum is smeared and a scale correction is applied. No correction is applied to data.

Electrons [3] and photons are reconstructed and calibrated as described in Chapter 4. Both photons and electrons are asked to pass quality and identification criteria. Electrons should have a well-reconstructed ID with one hit in the b-layer. The

[3] In the 8 TeV analysis the track associated to an electron candidate is fitted using a Gaussian-Sum Filter, which accounts for bremsstrahlung energy loss [153].

cuts to select electron candidates are in Table 7.3, and in Table 7.4 for photon candidates. The converted photon calibration described in Chaper 6 is applied on converted photons. On MC, corrections are applied to take into account known data-MC differences in photon and lepton efficiencies.

In case of overlap between electrons and muons which pass all selection criteria and share the same inner detector track ($\Delta R < 0.02$) the choice depends on the reconstruction of the leptons overlapping: if the muon is identified by the MS the electron is discharged, otherwise the muon candidate is rejected. To suppress FSR $Z\gamma$ background events, the photon is required to be outside of a cone of $\Delta R = 0.3$ around its closest lepton.

The Higgs candidate is selected (see Table 7.5) by the combination of a selected Z boson (the Z boson candidate is reconstructed by same flavour and opposite charge leptons, with a two-body invariant mass larger than the Z pole minus 10 GeV) and the hardest photon in the event which passes the selection criteria described above. Track and calorimeter isolation criteria and additional track impact significance selections are applied to the leptons forming the Higgs boson candidate. The total number of events selected in the 7 TeV and 8 TeV data is shown in Table 7.6.

Analysis Triggers		
Category	7 TeV analysis	8 TeV analysis
Muon	EF_mu18_MG || EF_mu18_MG_medium || EF_mu40_MSonly_barrel_medium	EF_mu24i_tight || EF_mu36_tight || EF_2mu13 || EF_mu18_tight_mu8_EFFS
Electron	EF_el20_medium || EF_el22_medium || EF_el22vh_medium1	EF_2e12Tvh_loose1 || EF_e24vhi_medium1 || EF_e60_medium1

TABLE 7.1: Trigger used to selected data, for the 2011 and 2012 analyses.

7.4 Preliminary studies in signal and background modelling

Early in the analysis, studies were performed to estimate the most sensitive photon cuts. In Figure 7.1, the photon p_T and η are shown for signal (ggF at $m_H = 125$ GeV) and background (SM $Z\gamma$) MC11 simulation samples. The photon p_T appears

Muons		
Category	7 TeV analysis	8 TeV analysis
General Cuts:	* Muons with a Z position $\lvert Z_{\rm PV}\rvert$ <10 mm to the PV (CB and Calo)	
	* $\lvert\eta\rvert$ <2.7 (CB) , 2.5 < $\lvert\eta\rvert$ <2.7 (StandA.) and $\lvert\eta\rvert$ <0.1 (Calo)	
Identification:	* Tight Identification criteria	
$p_{\rm T}$ min:	* $p_{\rm T}$ > 10 GeV (CB and StandA.) $p_{\rm T}$ > 14 GeV (Calo)	
Track Isolation:	* Ptcone30/P_t < 0.15	
Calo Isolation:	* Etcone20/E_t < 0.15 (StandA.) and Etcone20/E_t < 0.3 (Calo and CB)	
ID Cuts:	* Pixel b layer hit except the extrapolated muon track passes	
Cuts applied only	by an un-instrumented or dead area of the b-layer	
to CB and	* N^o pixel hits+N^o crossed	* N^o pixel hits+N^o crossed
Calo Muons	dead pixel sensors > 1	dead pixel sensors > 0
	* N^o SCT hits+N^o*crossed*	* N^o SCT hits+N^o crossed
	dead SCT sensors > 5	crossed dead SCT sensors > 4
	* N^o pixel holes+N^o SCT holes < 3	
Muons with	*N^o TRT hits(nTRTh)+N^o TRT outliers hits(nTRToh)>5(nTotal)	
0.1 < $\lvert\eta\rvert$ <1.9:	* nTRToh/nTotal > 0.9	
Rest of muons:	* If nTotal >5 then nTRToh/nTotal > 0.9	
Cosmic Cut:	* Impact parameter $\lvert d_0\rvert$ <10 mm to the PV (CB and Calo)	
	*$\lvert d_0\rvert/\sigma_{d0}$ < 3.5 where $\lvert d_0\rvert$ is the impact parameter	

TABLE 7.2: Selection criteria applied on muon candidates, for the 2011 and 2012 analyses. Combined muons are referred as "CB", Stand-alone muons as "StandA." and Calo muons as "Calo".

Electrons		
Category	7 TeV analysis	8 TeV analysis
General Cuts:	* Electrons with a Z position $\lvert Z_{\rm pv}\rvert$ <10 mm to the primary vertex	
	* Pseudo-rapidity region $\lvert\eta\rvert$ < 1.37 or 1.52 < $\lvert\eta\rvert$ < 2.47	
Identification:	* isEM loosePP++ and object quality (OQ) criteria	
Track Isolation:	$Ptcone20/p_T < 0.15$	
Isolation:	$Etcone20/E_T < 0.3$	$Etcone20/E_T < 0.2$
p_T min:	p_T > 10 GeV	
ID Cuts:	*At least 1 Pixel B layer hit	
	*$\lvert d_0\rvert/\sigma_{d0}$ < 6.5 where $\lvert d_0\rvert$ is the impact parameter	

TABLE 7.3: Selection criteria applied on electron candidates, for the 2011 and 2012 analyses.

to be a possible discriminant variable, considering that photons from the Higgs are significantly harder than the ones from background. If so, then cutting hard on the photon p_T (larger than 20 GeV) would improve the final signal to background ratio.

At this point in the analysis, following the $H \to \gamma\gamma$ experience, the three-body in invariant mass could be the discriminant variable to be used in the search.. The

Photons	
Category	7 TeV analysis and 8 TeV analysis
General Cuts:	Pseudo-rapidity region $\|\eta\| < 1.37$ or $1.52 < \|\eta\| < 2.47$
Identification:	Tight photons and OQ criteria
Isolation:	$E_{Tcone40} < 4GeV$ (topo based)
p_{T} min:	$p_T > 15$ GeV

TABLE 7.4: Selection criteria applied on photon candidates, for the 2011 and 2012 analyses.

Higgs events	
Category	7 and 8 TeV analysis
Muon channel	Two opposite-charge leptons and one photon
	At least one CB muon in the $m_{\mu\mu\gamma}$ reconstruction
m_{ll}	m_{ll} >81.18 GeV
Overlap	$\Delta R < 0.4$ from the photon to the closest lepton.

TABLE 7.5: Details about the selection of Higgs events, in the 2011 and 2012 analyses.

$H \to Z\gamma$ **data candidate events**		
$\sqrt{s}$	Electron channel	Muon Channel
7 TeV	1927	2621
8 TeV	13798	16678

TABLE 7.6: Selected Higgs candidate events in data for the 7 and 8 TeV analysis.

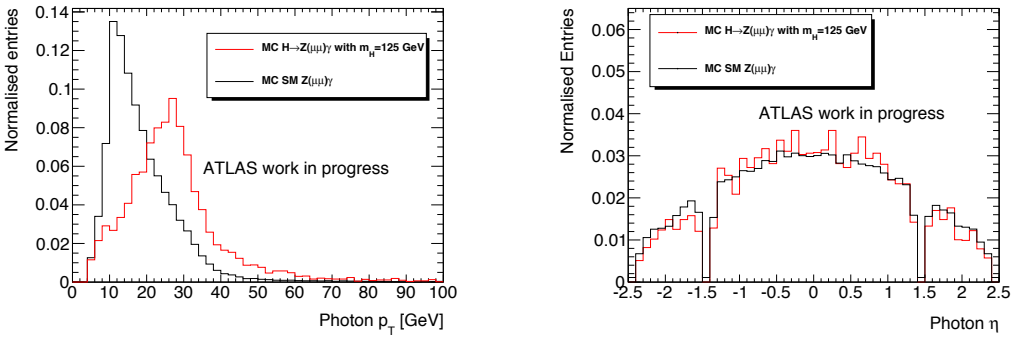

FIGURE 7.1: Photon p_T (left) and η (right) for signal (ggF with $m_H = 125$ GeV) and background (SM $Z\gamma$) events. MC11 samples are used.

effect of the photon p_T cut in the three-body invariant mass is investigated. In Figure 7.2, the reconstructed three-body invariant mass for different photon p_T cuts is shown for the SM $Z\gamma$ MC sample. The mass shape is fitted with a "bifurcated

gaussian"[4] in each case. The fitted mean value as a function of the p_T cut is shown in Figure 7.3. The cut clearly affects the mass shape, creating a turn-on effect in the interest region around of $m_{\ell\ell\gamma} = 125$ GeV at a high p_T cut,which would drastically affect the sensitivity of a signal+background likelihood fit. This feature shows that the idea of applying a hard cut on the photon p_T to eliminate background is inviable. In consequence, the cut on photon transverse momentum is fixed at $p_T > 15$ GeV.

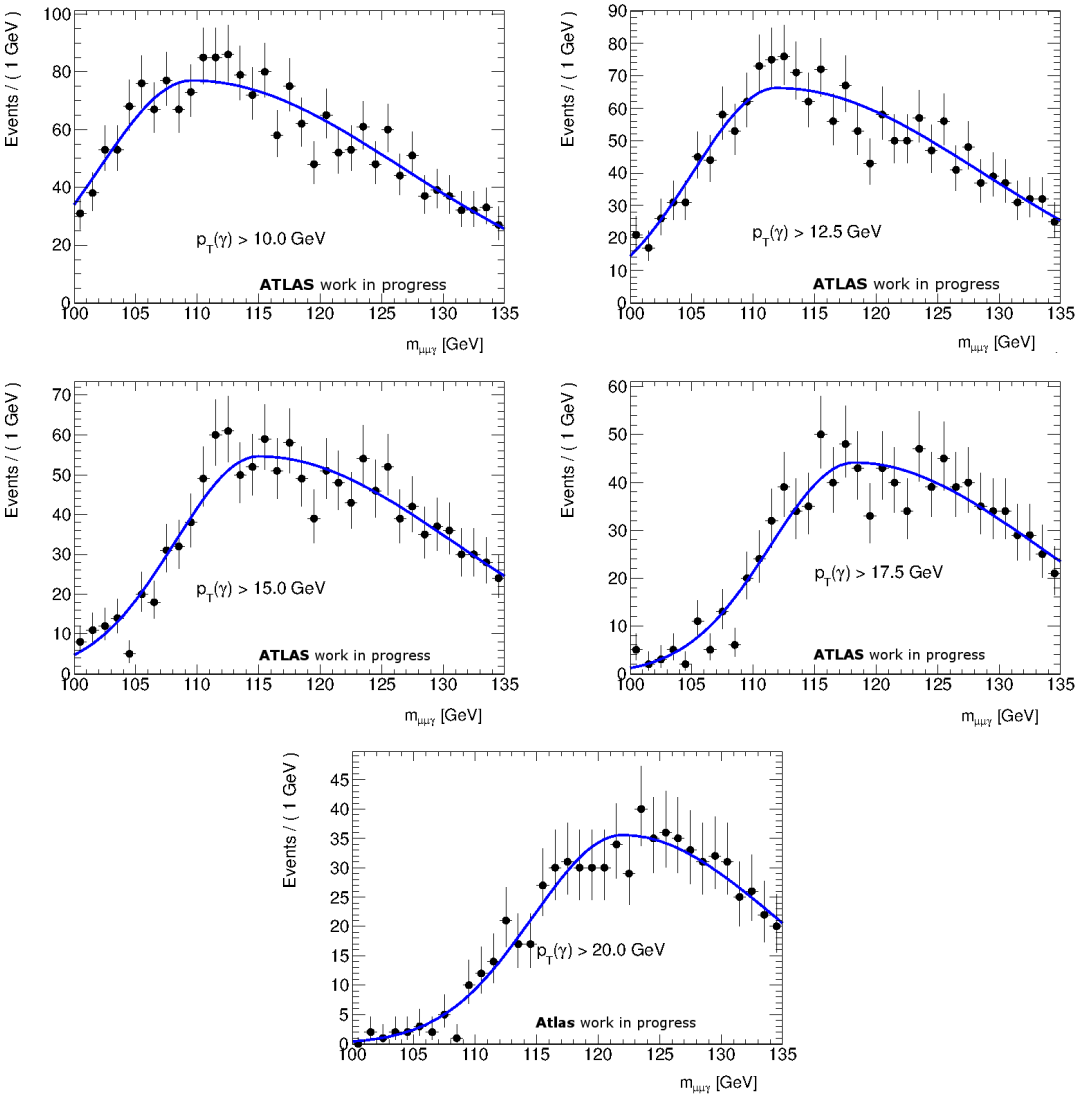

FIGURE 7.2: Three-body invariant mass distribution for SM $Z\gamma$ background for different cuts on the photon p_T. MC11 is used.

The optimal way of modelling the signal is also investigated. In Figure 7.4, the correlation pattern between the three and two-body invariant mass is shown in a wide range of the two-dimensional mass plane in the electron channel. Two patterns

[4]The "bifurcated Gaussian" is the concatenation of two half-gaussian functions, with different width and same mean

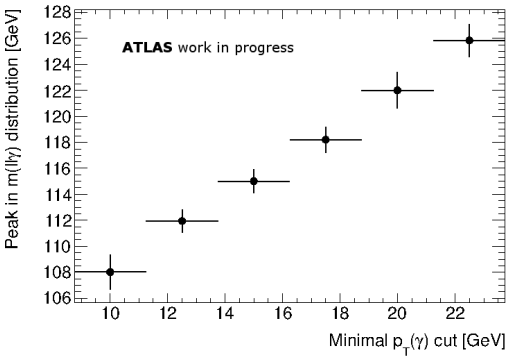

FIGURE 7.3: Fitted mean value of the background shape as a function of the photon p_T cut.

are observed, a linearly correlated component of the mean value of both distributions and an uncorrelated pattern towards the tails of the di-electron mass for the three-body invariant mass resolution. Figure 7.5 shows a zoomed mass plane for the muon channel, a 56% correlation factor is found in the muon ggF sample and the total correlation slope is about 0.5 GeV/GeV. Similar patterns are observed in the VBF samples as expected.

Some ideas of the signal modelling emerge of this result:

- A two-dimensional mass dependent model for signal and background.
- A one dimensional model of an optimal linear combination of $M_{\ell\ell\gamma}$ and $M_{\ell\ell\gamma}$ (i.e $M_{\ell\ell\gamma} - M_{\ell\ell}$).

While a two-dimensional model would exploit all available information, the complicated correlation pattern is difficult to implement.A one dimensional model is a simpler approach. Also, using the difference between the three-body and two-body invariant mass, $\Delta m = M_{\ell\ell\gamma} - M_{\ell\ell}$, has some additional advantages. First, this variable is almost un-affected by lepton energy scales uncertainties and second, it is insensitive to the FSR in $H \to \mu\mu$ signal contribution[5].

As a result, two observables are studied as possible discriminant variables: the conventional three-body invariant mass $M_{\ell\ell\gamma}$ and the mass difference $\Delta m = M_{\ell\ell\gamma} - M_{\ell\ell}$. As shown in Figures 7.6 and 7.7, both distributions are well described by the sum of a Crystal Ball line-shape plus a small wide gaussian component.

[5]The $H \to \mu\mu$ decay with final state radiation can contaminate the signal sample. Using the mass difference variable dilutes this effect. More information can be found [5]

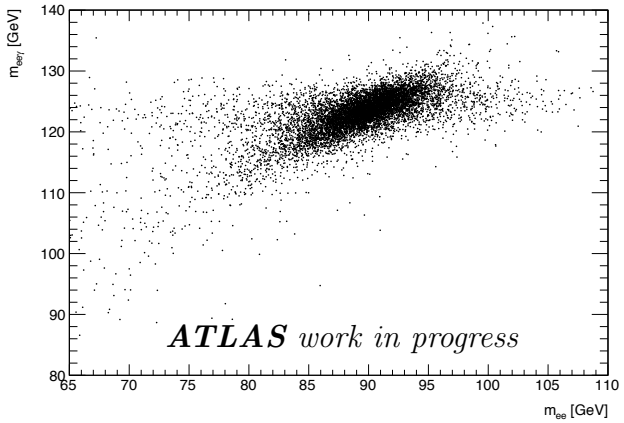

FIGURE 7.4: Scatter plot of the $m(\ell\ell)$ $m(\ell\ell\gamma)$ masses for a Higgs signal with $m_H = 125$ GeV, for the electron channel. MC12 samples are used.

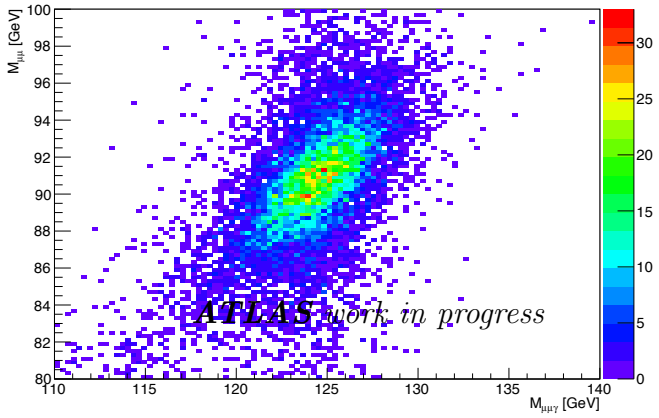

FIGURE 7.5: Scatter plot of the $m(\ell\ell)$ $m(\ell\ell\gamma)$ masses for a Higgs signal with $m_H = 125$ GeV, for the muon channel. MC12 samples are used.

7.4.0.1 Improvements on the Resolution

A narrower reconstructed mass resolution increases the analysis sensitivity, by diminishing the effective background. In order to improve the mass resolution two corrections are applied to the three-body invariant mass.

- The photon pseudo-rapidity is corrected after identifying the primary vertex and the photon impact point in the calorimeter (as in the $H \to \gamma\gamma$ analysis as explained in Chapter 6). By using a corrected photon transverse energy $E_t^\gamma = E^\gamma / \cosh \eta^\gamma$ the resolution improves by 2%.

- The four-momenta of the leptons is recomputed using a "Z mass constraint", based on a technique used in the $H \to ZZ$ analysis [154]:

  The momenta of the leptons are recomputed starting from the hypothesis of a true on-shell $Z \to ll$ decay and an unbiased gaussian function for the detector resolution. The "true" constraint di-lepton mass value is obtained by maximising the likelihood function:

$$\mathcal{L}(m_{\ell\ell}^{\text{true}}|m_{\ell\ell}^{\text{reco}}) = \mathcal{P}(m_{\ell\ell}^{\text{reco}}|m_{\ell\ell}^{\text{true}}) \times \mathcal{P}(m_{\ell\ell}^{\text{true}}) \tag{7.1}$$

  which implies finding the true $m_{\ell\ell}^{\text{true}}$ value that maximises the probability of measuring the observed reconstructed value $m_{\ell\ell}^{\text{reco}}$. The maximisation is performed on an event-by-event basis. The distribution function for $m_{\ell\ell}^{\text{true}}$ is given by the Breit-Wigner distribution:

$$\mathcal{P}(m_{\ell\ell}^{\text{true}}) = BW(m_{\ell\ell}^{\text{true}}; M_Z, \Gamma_Z) = \frac{N}{\left((m_{\ell\ell}^{\text{true}})^2 - M_Z^2\right)^2 + \Gamma_Z^2 M_Z^2}, \tag{7.2}$$

  where $M_Z = 91.1876$ GeV is the Z pole mass, $\Gamma_Z = 2.4952$ GeV is the natural width of the Z boson, and N is just a normalisation factor. The conditional probability $P(m_{\ell\ell}^{\text{reco}}|m_{\ell\ell}^{\text{true}})$ is the detector invariant mass response function and is modelled with a Gaussian:

$$P(m_{\ell\ell}^{\text{reco}}|m_{\ell\ell}^{\text{true}}) = G(m_{\ell\ell}^{\text{reco}}|m_{\ell\ell}^{\text{true}}, \sigma_m) = \frac{1}{\sqrt{2\pi}\sigma_m} e^{-\frac{(m_{\ell\ell}^{\text{reco}} - m_{\ell\ell}^{\text{true}})^2}{2\sigma_m^2}}. \tag{7.3}$$

  where the quantity σ_m is a per-event invariant mass resolution.

In Figures 7.6 and 7.7 the distribution of the invariant mass $M_{\ell\ell\gamma}$ and mass difference Δm are shown, both with and without PV correction, and using the Z vertex constraint. For both $M_{ll\gamma}$ and Δm the PV correction improves the resolution by about 2%. The Z mass constraint correction has an important improvement on the $M_{\ell\ell\gamma}$ resolution (8%), while in the Δm the improvement is negligible.

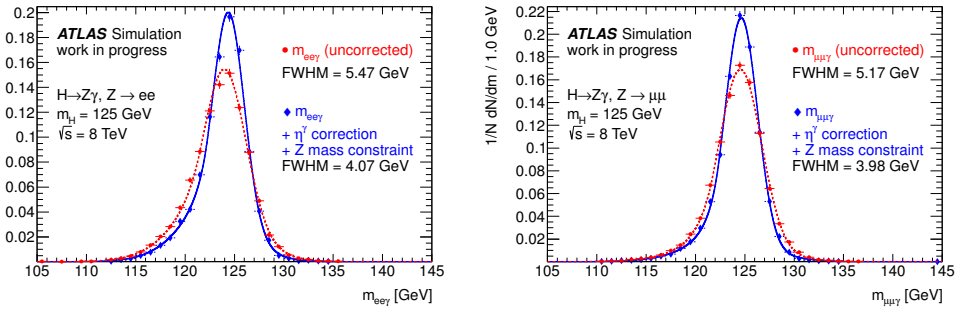

FIGURE 7.6: Reconstructed invariant mass distributions from the signal processes for each one of the resolution improvements. Red: Invariant mass distribution without improvements, Blue: Invariant mass distribution correcting the photon position by the primary vertex and the Z mass constraint. Left is the distribution for electrons, right for muons in MC samples at 8 TeV.

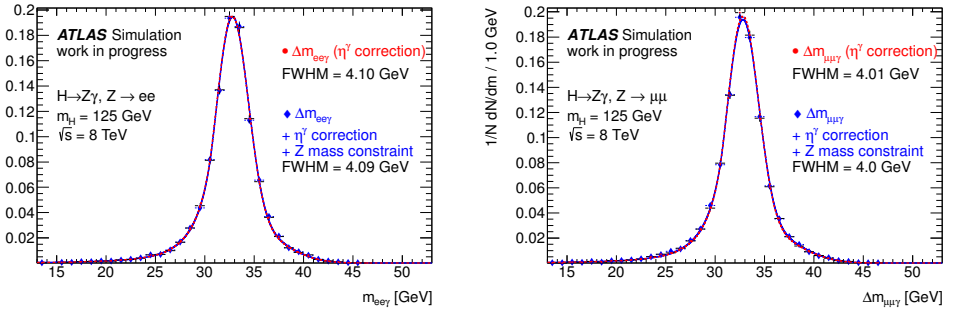

FIGURE 7.7: Reconstructed Δm distributions from the signal processes for each one of the resolution improvements. Red:Δm distribution only correcting the photon position by the primary vertex. Blue: Δm distribution correcting the photon position by the primary vertex and the Z mass constraint. Left is the distribution for electrons, right for muons in MC samples at 8 TeV.

7.5 Signal Model

7.5.1 Signal selection efficiency and expected yields

The Higgs boson cross sections, branching ratios [155, 156] and their uncertainties are compiled in [127, 128]. Details about the computation of these cross-sections are found in Section 7.2.

Higgs boson production and decay are simulated with several MC samples as described previously in Section 7.2. The full simulation allows the estimation of the signal selection efficiency and therefore of the expected signal yield, in a similar way as done in the $H \to \gamma\gamma$ channel, as presented in Equation 6.6.

For the signal efficiency, a quadratic dependence on the Higgs boson mass is assumed, as observed on the available mass points. Figures 7.8 and 7.9 show the signal efficiency obtained from the available 7 TeV and 8 TeV signal MC samples as a function of the generated nominal Higgs boson mass, and the results of the fits. The fitted function is the following:

$$\varepsilon = \varepsilon_{125GeV}\left(1 + \varepsilon_{lin}(M(ll\gamma) - 125GeV) + \varepsilon_{sqrt}(M(ll\gamma) - 125GeV)^2\right). \quad (7.4)$$

With the fitted mass dependencies of the signal efficiency, and the production cross section and branching fractions, the number of signal events for various Higgs boson mass hypotheses can be estimated. They are listed in Table 7.7 and Table 7.8 for the 7 TeV simulation and in Table 7.7 and Table 7.8 for 8 TeV.

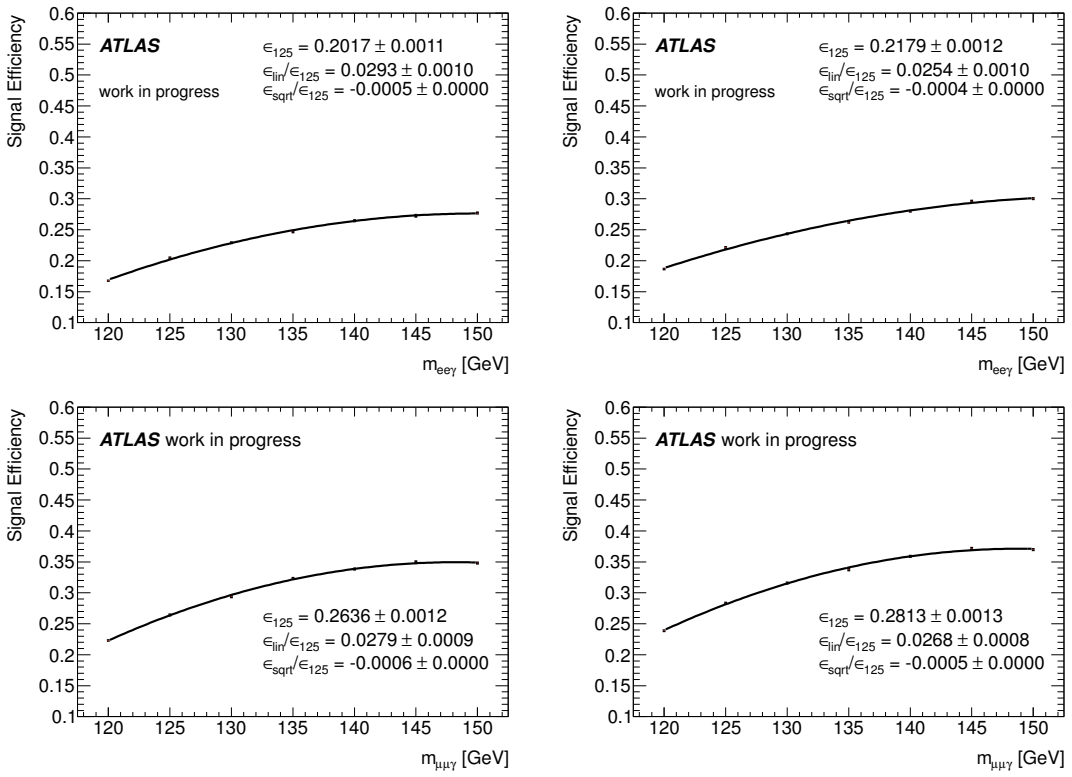

FIGURE 7.8: Signal efficiency for events produced in pp collisions at $\sqrt{s} = 7$ TeV. Top row: signal selection efficiency versus nominal Higgs mass for gluon fusion (left) and VBF (right) events, when the Z boson decays to e^+e^-. Bottom row: signal selection efficiency versus nominal Higgs mass for gluon fusion (left) and VBF (right) events, when the Z boson decays to $\mu^+\mu^-$.

TABLE 7.7: Number of expected signal events in the muon channel for each production process and Higgs boson masses in 5 GeV steps between 110 and 150 GeV, for 4.6 fb^{-1}, at $\sqrt{s} = 7\ TeV$.

m_H	$gg \to H$		VBF		WH		ZH		ttH		Total	
$[GeV]$	$\epsilon(\%)$	N_{evt}	$\epsilon(\%)$	N_{evt}	$\epsilon(\%)$	N_{evt}	$\epsilon(\%)$	N_{evt}	$\epsilon(\%)$	N_{evt}	$\epsilon(\%)$	N_{evt}
120	22.3	0.64	24.0	0.05	23.1	0.03	23.1	0.01	23.1	0.00	22.5	0.74
125	26.4	0.97	28.1	0.08	27.3	0.04	27.3	0.02	27.3	0.01	26.5	1.12
130	29.7	1.28	31.5	0.11	30.6	0.05	30.6	0.03	30.6	0.01	29.9	1.47
135	32.2	1.5	34.1	0.14	33.1	0.05	33.1	0.03	33.1	0.01	32.4	1.72
140	33.7	1.59	35.9	0.15	34.9	0.05	34.9	0.03	34.9	0.01	34.1	1.82
145	34.8	1.53	36.9	0.15	35.8	0.05	35.8	0.03	35.8	0.01	35.0	1.76
150	34.9	1.33	37.1	0.13	36.0	0.05	36.0	0.02	36.0	0.01	35.1	1.53

TABLE 7.8: Number of expected signal events in the electron channel for each production process and Higgs boson masses in 5 GeV steps between 110 and 150 GeV, for 4.6 fb^{-1}, at $\sqrt{s} = 7\ TeV$.

m_H	$gg \to H$		VBF		WH		ZH		ttH		Total	
$[GeV]$	$\epsilon(\%)$	N_{evt}	$\epsilon(\%)$	N_{evt}	$\epsilon(\%)$	N_{evt}	$\epsilon(\%)$	N_{evt}	$\epsilon(\%)$	N_{evt}	$\epsilon(\%)$	N_{evt}
120	16.9	0.49	18.8	0.04	17.9	0.02	17.7	0.01	17.7	0.00	17.1	0.57
125	20.2	0.75	21.8	0.06	21.0	0.03	21.0	0.02	21.0	0.00	20.4	0.86
130	22.9	0.99	24.4	0.09	23.6	0.04	23.6	0.02	23.6	0.01	23 .0	1.13
135	24.9	1.16	26.5	0.11	25.7	0.04	25.7	0.02	25.7	0.01	25.1	1.33
140	26.4	1.24	28.1	0.12	27.3	0.04	27.3	0.02	27.2	0.01	26.6	1.42
145	27.3	1.2	29.3	0.12	28.3	0.04	28.3	0.02	28.3	0.01	27.5	1.38
150	27.6	1.06	30.1	0.11	28.9	0.03	28.9	0.02	28.9	0.01	27.9	1.22

TABLE 7.9: Number of expected signal events in the muon channel for each production process and Higgs boson masses in 5 GeV steps between 110 and 150 GeV, for 20.7 fb^{-1}, at $\sqrt{s} = 8\ TeV$.

m_H	$gg \to H$		VBF		WH		ZH		ttH		Total	
$[GeV]$	$\epsilon(\%)$	N_{evt}	$\epsilon(\%)$	N_{evt}	$\epsilon(\%)$	N_{evt}	$\epsilon(\%)$	N_{evt}	$\epsilon(\%)$	N_{evt}	$\epsilon(\%)$	N_{evt}
120	25.6	4.23	27.4	0.35	26.5	0.17	26.5	0.09	26.5	0.03	25.8	4.87
125	29.5	6.24	31.2	0.53	30.4	0.23	30.4	0.13	30.4	0.04	29.7	7.18
130	32.6	8.08	34.3	0.71	33.4	0.28	33.4	0.16	33.4	0.05	32.8	9.29
135	34.9	9.36	36.6	0.85	35.7	0.31	35.7	0.18	35.7	0.06	35.1	10.7
140	36.4	9.85	38.0	0.91	37.2	0.30	37.2	0.18	37.2	0.06	36.6	11.3
145	37.1	9.45	38.7	0.90	37.9	0.28	37.9	0.16	37.9	0.05	37.3	10.8
150	37.0	8.21	38.5	0.80	37.7	0.23	37.7	0.13	37.7	0.05	37.2	9.41

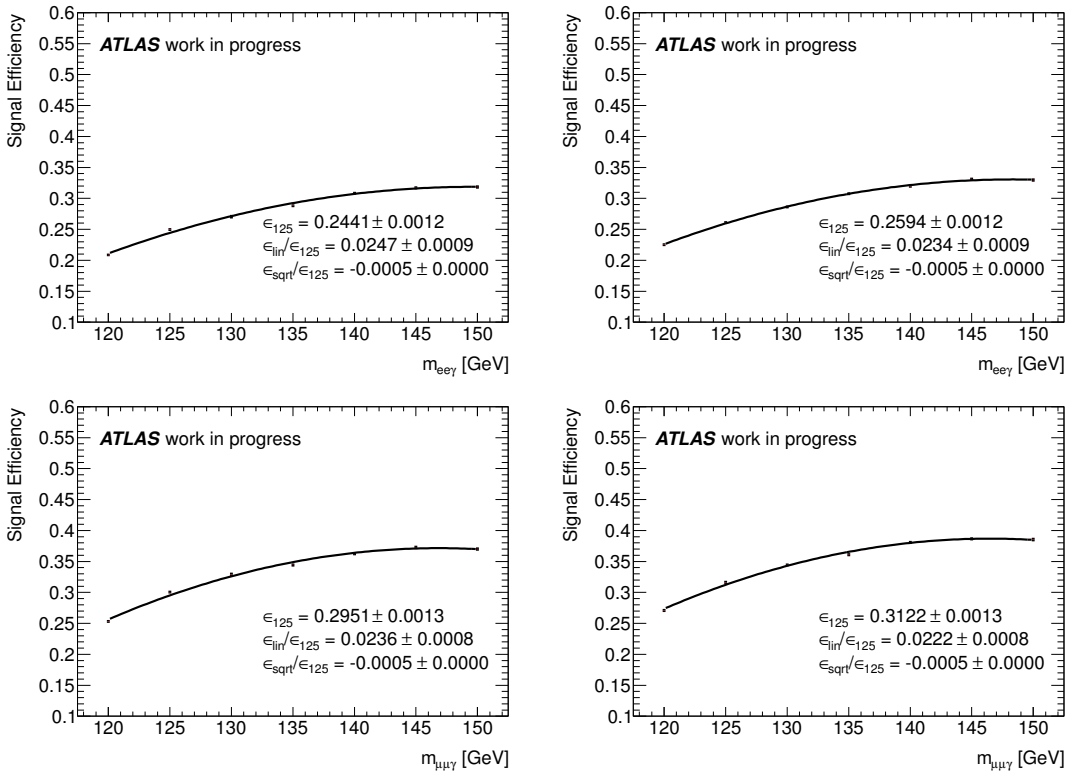

FIGURE 7.9: Signal efficiency for events produced in pp collisions at $\sqrt{s} = 8$ TeV. Top row: signal selection efficiency versus nominal Higgs mass for gluon fusion (left) and VBF (right) events, when the Z boson decays to e^+e^-. Bottom row: signal selection efficiency versus nominal Higgs mass for gluon fusion (left) and VBF (right) events, when the Z boson decays to $\mu^+\mu^-$.

TABLE 7.10: Number of expected signal events in the electron channel for each production process and Higgs boson masses in 5 GeV steps between 110 and 150 GeV, for 20.7 fb^{-1}, at $\sqrt{s} = 8\ TeV$.

m_H	$gg \to H$		VBF		WH		ZH		ttH		Total	
$[GeV]$	$\epsilon(\%)$	N_{evt}	$\epsilon(\%)$	N_{evt}	$\epsilon(\%)$	N_{evt}	$\epsilon(\%)$	N_{evt}	$\epsilon(\%)$	N_{evt}	$\epsilon(\%)$	N_{evt}
120	21.1	3.48	22.6	0.29	21.8	0.14	21.8	0.08	21.8	0.03	21.2	4.01
125	24.4	5.17	26.0	0.44	25.2	0.19	25.1	0.11	25.1	0.04	24.6	5.94
130	27.1	6.73	28.7	0.59	27.9	0.23	27.9	0.13	27.9	0.04	27.3	7.73
135	29.2	7.84	30.7	0.71	30.0	0.26	30.0	0.15	30.0	0.05	29.4	9.01
140	30.7	8.31	32.3	0.77	31.4	0.26	31.4	0.15	31.4	0.05	30.9	9.54
145	31.6	8.05	32.9	0.77	32.3	0.23	32.3	0.14	32.3	0.05	31.7	9.23
150	31.9	7.07	33.0	0.69	32.5	0.19	32.5	0.11	32.5	0.04	32.0	8.11

7.5.2 Global resolution model of Δm

Due to the advantages related to the Δm variable, it is chosen as discriminant variable, the $m_{\ell\ell\gamma}$ is only used as a comparison point. Thus, a signal resolution model of Δm is needed to perform the statistical analysis. The global resolution model developed to treat the signal in the $H \to \gamma\gamma$ channel can be easily extrapolated to this analysis. An analytical function of the mass which provides a full description of the signal in the whole mass range (details are found in Section 6.7) is used. From the available signal MC samples at different mass points both the global and dependent parameters of Δm are extracted from a simultaneous fit.

The Δm dependent parameters are the Crystal Ball mean value (μ_{CB}), resolution (σ_{CB}) and the mean value of the outlier (μ_{GA}). For all three parameters, a linear dependence is used :

$$d\mu_{\mathrm{CB}} = d\mu CB_{125\mathrm{GeV}} + \Delta\mu CB_{\mathrm{slope}} \times (\Delta m - \Delta m125), \tag{7.5}$$

$$\sigma_{\mathrm{CB}} = \sigma CB_{125\mathrm{GeV}} + \sigma CB_{\mathrm{slope}} \times (\Delta m - \Delta m125), \tag{7.6}$$

$$d\mu_{\mathrm{GA}} = d\mu GA_{125\mathrm{GeV}} + \Delta\mu GA_{\mathrm{slope}} \times (\Delta m - \Delta m125), \tag{7.7}$$

where $\Delta m125 = (125 - M_Z)$ GeV. The other parameters (α_{CB} and the fraction of the Crystal ball f_{CB}) are set a single global value and are extracted from the fit. Also, the relative width of the core and the outlier components ($\kappa_{\mathrm{GA}} = \sigma_{GA}/\sigma_{CB}$) are shown to remain unchanged with Δm and are set to a single value. The tail parameter n_{CB}, is set to 5 and fixed in the fit. Details about the signal model are summarised in [5].

The parameters from the precedent equations, extracted from the global fit can be found in Table 7.11. Figure 7.10 shows the distribution of Δm and the projection of the global fit for $m_H = 125$ in the 7 TeV and 8 TeV MC samples. The width of the Δm distribution is dominated by the Z-boson intrinsic width, with a sub-leading contribution of approximately 1 GeV from the photon energy resolution.

TABLE 7.11: The numerical results of the global fit. The linear dependence of the μ_{CB} shape parameter is given by $d\mu_{\mathrm{CB}}(\Delta m) = \Delta m + d\mu(\Delta m125) + \Delta_\mu \times (\Delta m - \Delta m125)$; and similarly for the σ_{CB} shape parameter with $\Delta m125 = (125 - M_Z)$ GeV. The width of the outlier component is set to $\sigma_{\mathrm{GA}} = \kappa_{\mathrm{GA}} \times \sigma_{\mathrm{CB}}$ with a single value for κ_{GA}.

Lepton Type	$d\mu_{CB}(\Delta m125)$ (MeV)	Δ_μ (MeV/GeV)	$\sigma_{CB}(\Delta m125)$ (GeV)	Δ_σ (MeV/GeV)	$\alpha_{CB}(\Delta m125)$	f_{CB} (%)	κGA	$d\mu_{GA}$ GeV
7 TeV								
μ	-232.7 ± 11.9	-0.228 ± 0.770	1.57 ± 0.01	0.51 ± 0.09	1.212 ± 0.060	77.3 ± 0.1	2.29 ± 0.07	1.84 ± 0.31
e	-249.9 ± 13.2	-0.312 ± 0.087	1.58 ± 0.01	0.57 ± 0.09	1.059 ± 0.013	81.9 ± 0.1	1.99 ± 0.04	2.34 ± 0.15
8 TeV								
μ	-238.9 ± 13.6	-0.299 ± 0.089	1.61 ± 0.02	0.80 ± 0.11	1.196 ± 0.049	79.4 ± 2.3	2.14 ± 0.08	2.16 ± 0.38
e	-244.1 ± 14.7	-0.406 ± 0.094	1.62 ± 0.02	0.86 ± 0.10	1.223 ± 0.032	78.9 ± 0.8	2.09 ± 0.03	1.83 ± 0.13

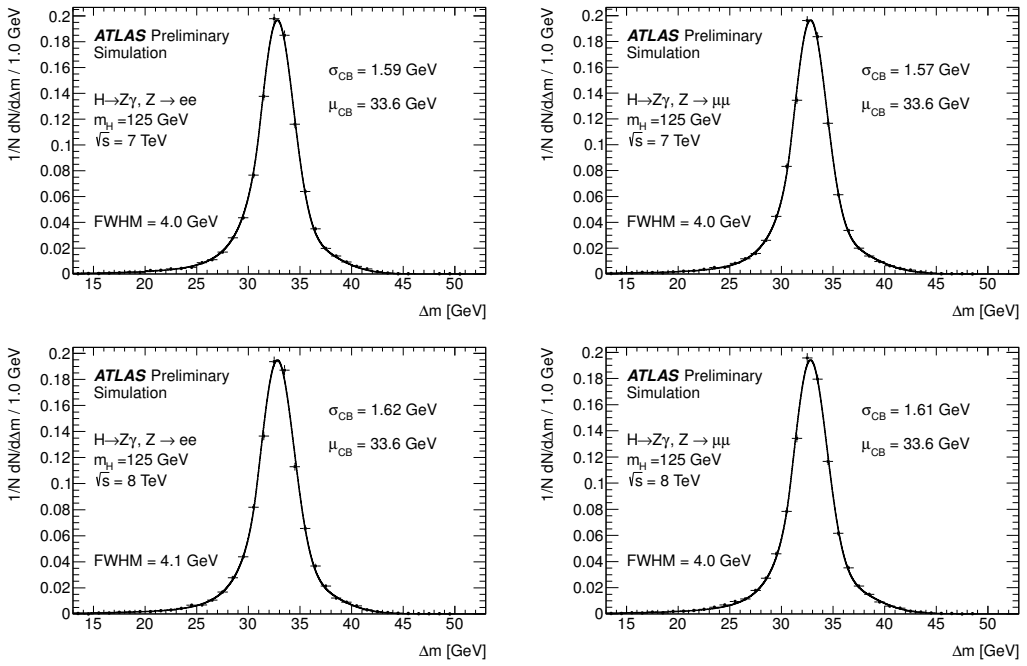

FIGURE 7.10: Distribution (normalised to unit area) of the difference Δm between the final state three-body invariant mass $m_{\ell\ell\gamma}$ and the di-lepton invariant mass $m_{\ell\ell}$ for signal events passing the full selection (dots), for $m_H = 125$ GeV and $\sqrt{s} = 7$ (top) or 8 (bottom) TeV. The line overlaid represents the projection of a global fit on the distribution with a model composed of the sum of a Crystal Ball (CB) and a Gaussian (GA) function. Left: electron channel, right: muon channel.

7.6 Background Model

A background model is needed to model the Δm spectrum in the search range. The model is carefully chosen so that is does not introduce significant biases.

Several functions are tested (i.e exponentials, polynomials, etc). The test consists of signal+background fits on the Δm distribution on generated background only toy MC in a similar way to the $H \to \gamma\gamma$ analysis (see discussion in Section 6.8.3).

The model found to provide the best sensitivity to the signal and the smaller bias is a third-order Chebychev polynomial in the fit range $24 < \Delta m < 64$ GeV. As described in Section 6.8.3 for $H \to \gamma\gamma$, the bias (so-called "spurious signal") induced by this model is treated as a systematic uncertainty on the fitted signal yield in the final statistical analysis. More information can be found in [157].

In Figure 7.11 background-only fits to the data are shown. The unbinned maximum likelihood fit is performed in the $24 < \Delta m < 64$ GeV range separately for the two lepton categories and on the 7 TeV and 8 TeV data.

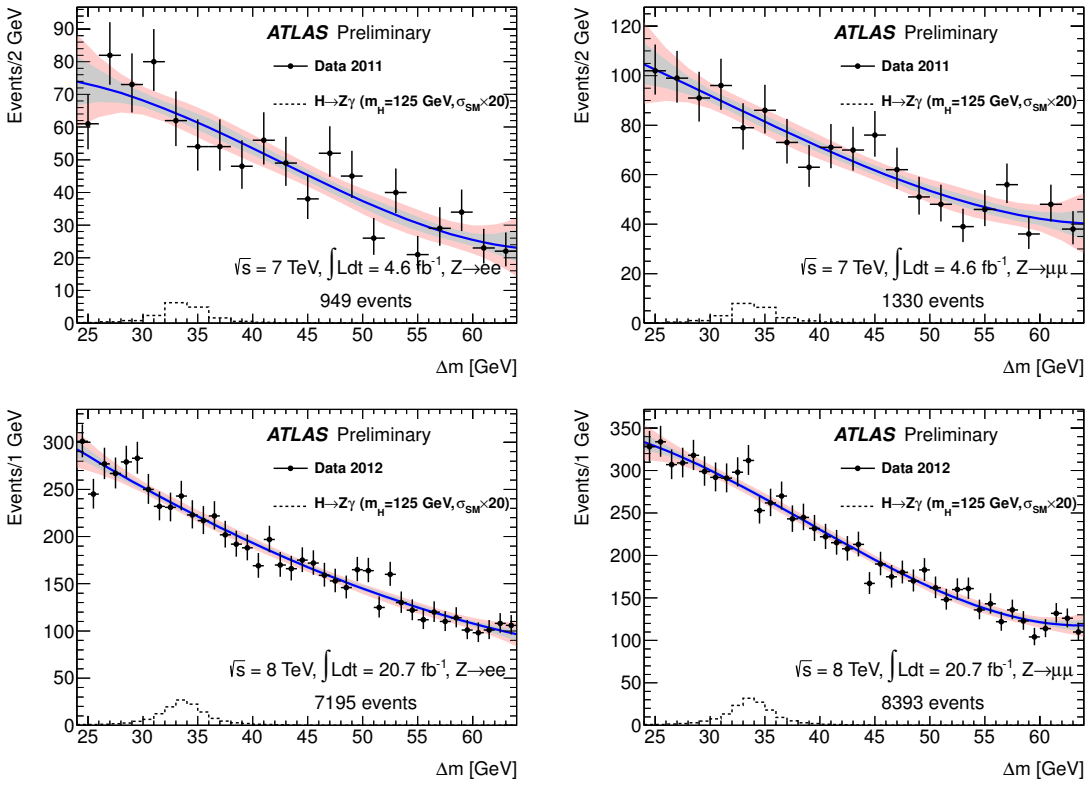

FIGURE 7.11: Background-only fits to the distribution of the mass difference Δm of selected events in data, for $Z \to ee$ (left) and $Z \to \mu\mu$ (right), at $\sqrt{s} = 7$ TeV (top) or 8 TeV (bottom). For both 7 and 8 TeV, a third order polynomial is used for the fit. Dots correspond to data, the blue line is the fit result and the gray and light red bands are the 1σ and 2σ uncertainty bands from the statistical uncertainties on the fitted background model parameters. The dashed histograms correspond to the SM signal expectation, for a Higgs boson mass of 125 GeV, scaled by a factor 20 for clarity [4].

7.7 Systematic uncertainties

There are three categories of systematic uncertainties for this analysis: theoretical uncertainties, experimental uncertainties in the expected signal yields, and systematics on the shape of the signal Δm distribution. Their evaluation is described next, the uncertainties related to the photon reconstruction are treated in the same way as the $H \to \gamma\gamma$ chapter detailed in Section 6.8.4. The final values are summarised in Table 7.13.

7.7.1 Theoretical uncertainties

The Higgs boson production cross sections and decay branching fractions as functions of the Higgs boson mass are compiled, together with their uncertainties, in [127]. These uncertainties are summarised in Table 7.12.

TABLE 7.12: Theoretical systematic uncertainties for the SM Higgs boson production cross section and branching fraction of the $H \to Z\gamma$ decay at $\sqrt{s} = 7$ and 8 TeV, for a Higgs boson mass of 125 GeV [4].

$\sqrt{s}$	Systematic uncertainty (%)										
	$\sigma(gg \to H)$		σ(VBF)		$\sigma(WH)$		$\sigma(ZH)$		$\sigma(t\bar{t}H)$		$B(H \to Z\gamma)$
	scale	PDF	scale	PDF	scale	PDF	scale	PDF	scale	PDF	
7 TeV	$^{+7.1}_{-7.8}$	$^{+7.6}_{-7.1}$	± 0.3	$^{+2.5}_{-2.1}$	$^{+0.2}_{-0.8}$	± 3.5	$^{+1.4}_{-1.6}$	± 3.5	$^{+3.3}_{-9.3}$	± 8.5	$^{+9.0}_{-8.8}$
8 TeV	$^{+7.3}_{-7.9}$	$^{+7.5}_{-6.9}$	± 0.2	$^{+2.6}_{-2.8}$	$^{+0.1}_{-0.6}$	± 3.4	$^{+1.5}_{-1.4}$	± 3.5	$^{+3.9}_{-9.3}$	± 7.8	$^{+9.0}_{-8.8}$

7.7.2 Uncertainties on the signal yields

Luminosity

Similarly to the $H \to \gamma\gamma$ analysis, the overall normalisation uncertainty on the integrated luminosity is 1.8% and 3.6% for 7 TeV data and 8 TeV data, respectively.

Acceptance of the kinematic requirements

The uncertainties related to the acceptance, or geometrical efficiency of the selection criteria are estimated by comparing the acceptance estimated with simulated signal events generated either using POWHEG or MCFM, both interfaced to PYTHIA. The uncertainty is 4% at 7 and 8 TeV.

Trigger efficiency

The uncertainty on the electron trigger efficiency is 0.4% (0.2%) at 8 (7) TeV. For the muon trigger it is 0.8 %(0.7 %) at 8 (7) TeV.

Electron reconstruction and identification

The uncertainties in the signal yields due to the electron energy scale (ES) and resolution are estimated by varying the electron momentum in MC by this uncertainties. Differences in the yields after these variations are assigned as the systematic uncertainties. The uncertainties due to the ES are 1.4% (0.3%) at 8 (7) TeV and 0.2% concerning resolution in both samples (8 and 7 TeV samples). The uncertainty on the yields due to the electron identification efficiency is 2.7 (3.0) at 8 (7) TeV.

Muon reconstruction

The uncertainty due to the momentum scale and resolution is estimated by varying the muon momentum in MC by its uncertainties. Again, differences in the expected yields after these variations are used as systematic uncertainties. The uncertainties are less than 0.1% at 7 and 8 TeV.

The uncertainty on the yields due to the muon identification efficiency is 0.6% (0.7%) at 8 (7) TeV.

Photon reconstruction

The uncertainty due to the photon identification efficiency is computed as in the $H \to \gamma\gamma$ analysis, described in Section 6.8.4. The final uncertainty on the signal yields is 2.9 % in both 7 and 8 TeV samples.

The uncertainty from the photon ES and resolution is estimated by varying the photon momentum by its uncertainties and observing the relative variation in the predicted signal yield. In the muon channel, the variation due to ES uncertainty is 0.3% (0.2%) at 8 (7) TeV, while in the electron channel the uncertainty is shared with the electron ES and resolution systematic uncertainty previously described.

Photon and electron calorimeter isolation requirements.

As discussed in Chaper 4, a difference is observed in the isolation distribution between data and Monte Carlo for photons and electrons, selected either in di-photon enriched events or in a control sample of electrons from $Z \to ee$. This difference is

on the order of 100 MeV (500 MeV) for the topological-cluster (standard cell) based isolation.

To estimate the systematic uncertainty due to the uncertainty on the efficiency of the isolation criteria, the photon and electron calorimeter isolation energies are shifted by the observed difference, and the signal yields are recomputed. This uncertainty is 0.4% (0.3%) in the electron channel, and 0.4 %(0.2%) in the muon channel for 8 (7) TeV.

7.7.3 Systematic Uncertainties on the signal peak and mass resolution

The systematic uncertainties on the signal peak value and mass resolution come from the uncertainties in the ES and the resolution of the leptons and the photon. The uncertainty is obtained by scaling or smearing the transverse momentum of each of the objects by its uncertainties and recomputing Δm.

The differences in shape from the recomputed Δm distribution with respect to the nominal are consider the systematic uncertainties due to the object ES and resolution.

A 5% uncertainty is found on the resolution of the $\Delta m_{ee\gamma}$ distribution due to the electron/photon uncertainties. In the $\Delta m_{\mu\mu\gamma}$ distribution this uncertainty is 2.4 % in both 7 and 8 TeV samples. The uncertainty on the $\Delta m_{\mu\mu\gamma}$ resolution due to the muon momentum resolution is negligible at 8 TeV and 1.5% at 7 TeV.

The uncertainty on the peak position is 200 MeV due to the electron/photon ES uncertainties in both samples. The impact of the muon momentum scale uncertainty on the peak position is negligible.

7.8 Results

An overview of the statistical analysis used in ATLAS for the Higgs searches is presented in Appendix A. The same approach is used in here. Upper limits on the signal strength set at 95% of Confidence Level using the CL_s method are shown in Figure 7.12. The expected limit varies between 7.3 and 22 times the SM expectation

TABLE 7.13: Summary of the systematic uncertainties on the signal yield and invariant mass distribution for $m_H = 125$ GeV, at $\sqrt{s} = 8(7)$ TeV [4].

Systematic Uncertainty	$H \to Z(ee)\gamma(\%)$	$H \to Z(\mu\mu)\gamma(\%)$
Signal Yield		
Luminosity	3.6 (1.8)	3.6 (1.8)
Trigger efficiency	0.4 (0.2)	0.8 (0.7)
Acceptance of kinematic selection	4.0 (4.0)	4.0 (4.0)
γ identification efficiency	2.9 (2.9)	2.9 (2.9)
electron reconstruction and identification efficiency	2.7 (3.0)	
μ reconstruction and identification efficiency		0.6 (0.7)
e/γ energy scale	1.4 (0.3)	0.3 (0.2)
e/γ isolation	0.4 (0.3)	0.4 (0.2)
e/γ energy resolution	0.2 (0.2)	0.0 (0.0)
μ momentum scale		0.1 (0.1)
μ momentum resolution		0.0 (0.1)
Signal Δm resolution		
e/γ energy resolution	5.0 (5.0)	2.4 (2.4)
μ momentum resolution		0.0 (1.5)
Signal Δm peak position		
e/γ energy scale	0.2 (0.2) GeV	0.2 (0.2) GeV
μ momentum scale		negligible

and the observed from 5.4 to 37, for Higgs masses from 120 to 150 GeV. At 125 GeV the observed (expected) limit is 18.2 (13.5) times the Standard Model. The results are dominated by statistical uncertainties: neglecting all systematics uncertainties the expected limit on the cross-section at 125 GeV decreases to 12.9 times the SM prediction [4].

7.9 Discussion

In this chapter, the first search of the Higgs boson in the $Z\gamma$ ($Z \to \ell\ell$ where $\ell = e$ or μ) decay channel is presented. The analysis is performed with the complete 7 and 8 TeV data samples from pp collisions performed in the Run I of the LHC and recorded by ATLAS. The analysis strategy is to search for a resonance over a large background spectrum, using the difference between the three-body and two-body invariant masses (Δm) as a discriminant variable. No significant deviations from the SM prediction are observed and upper limits on the cross-section of the SM Higgs boson are set. For a mass of 125 GeV, corresponding to the new found Higgs Boson-like particle the expected and observed limits are 13.5 and 18.2 times the Standard Model, respectively. The CMS experiment has released a result using the

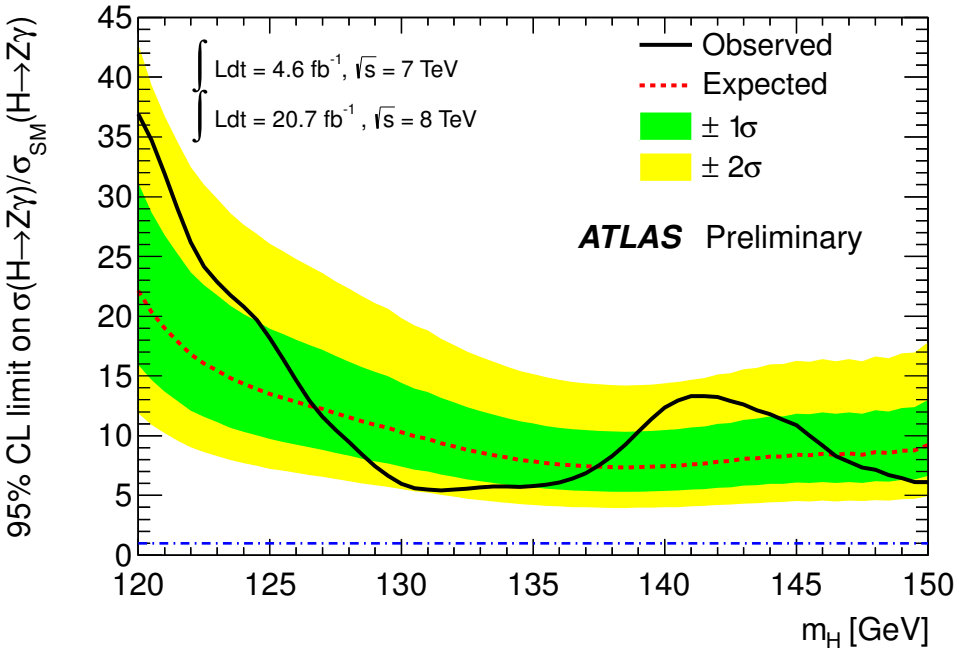

FIGURE 7.12: Observed 95% CL limits (solid black line) on the production cross section of a SM Higgs boson decaying to $Z\gamma$, as a function of the Higgs boson mass, using 4.6 fb^{-1} of pp collisions at $\sqrt{s} = 7$ TeV and 20.7 fb^{-1} of pp collisions at $\sqrt{s} = 8$ TeV. The median expected 95% CL exclusion limits (dashed red line) are also shown. The green and yellow bands correspond to the $\pm 1\sigma$ and $\pm 2\sigma$ intervals [4].

7 and 8 TeV datasets, where an upper limit on the $H \to Z\gamma$ cross-section times branching ratio is found to be about 9 times the SM for both expected and observed limits [158].

Following this first preliminary result, a better sensitivity could be achieved. Learning from the experience of $H \to \gamma\gamma$, some ideas can be easily extrapolated. A categorisation in the kinematics of the events (i.e the photon pseudo-rapidity) and the Higgs transverse momentum (using the p_{Tt} observable) would exploit the difference in resolutions. A VBF oriented selection would provide a category with a good signal-to-background ratio. Nevertheless, due to the low signal rate, the analysis is dominated by statistics, improvements would benefit the sensitivity but more data will still be needed to reach observation sensitivity. Higher luminosities and higher centre of mass collision energies after the LHC shutdown should allow to reach observation sensitivity of the SM Higgs in this channel.

Conclusions

The work presented in this document was developed in the ATLAS-LPNHE group in the period between 2010-2013. In the course of this thesis four main topics covering detector-oriented, performance and physics analyses concerning photons were performed. These include studies in the EMCAL HV system, the extraction of photon energy scales from a sample of radiative Z decays to validate the standard EMCAL calibration, and the search for the Higgs boson in the $\gamma\gamma$ and $Z\gamma$ decay channels.

The effect of the EMCAL electrode resistors and return currents in the HV system on the energy measurement was evaluated. The study was performed in a couple of long data-taking runs in 2011 and 2012 where the detector information such as return currents and operational high-voltage were mapped from high to low instantaneous luminosities. The effect was found to be small in the luminosities corresponding to Run I of the LHC, and this study demonstrated that it could become more important in the operation at higher luminosities expected for 2015 [1]. More studies based on detector information at a high luminosity environment are needed to determine the optimal procedure to eventually correct for this effect.

A data-driven validation to the standard EMCAL calibration (based on $Z \to ee$ decays and extrapolated to photons through MC simulation) was performed in this thesis using photons from a radiative Z decays sample. The analysis used the complete samples at $\sqrt{s} = 7$ and 8 TeV for a total integrated luminosity of 4.7 + 20.7 fb^{-1}. The photon energy scales were extracted for different regions of the calorimeter and as a function of the photon transverse momentum. The resulting scales are in good agreement with the nominal systematic uncertainties associated to the photon energy scales. The uncertainties on the scales extracted from radiative Z are dominated by the limited statistics, therefore can not compete with the standard in-situ calibration used on ATLAS. Nevertheless, the precision on the scales for photons

with low transverse energy, ($E_{\mathrm{T}} > 20$ GeV) is considerably better than the nominal systematic uncertainty associated to photons in this energy region. Therefore, it is recommended to use the measurement performed in this thesis as a nominal systematic uncertainty on the energy scales of low E_{T} photons in ATLAS.

One of the most important goals of the LHC and ATLAS was the search for the Higgs Boson, which was also the main topic of this thesis, where the search for the Higgs Boson in the $\gamma\gamma$ and $Z\gamma$ decay channels was presented. In the $H \to \gamma\gamma$ analyses, the $m_{\gamma\gamma}$ range is scanned from 110 to 150 GeV, looking for a narrow resonance over a large QCD combinatorial background. The analysis evolved significantly during the first run of the LHC, and contributions in event categorisation, photon performance, improvement to the mass resolution and signal modelling presented in this thesis were progressively included into the ATLAS analysis. The main contribution relies on the global signal resolution model, which was built to satisfy the need for an interpolation of the signal invariant mass PDF for the search. The global signal resolution model is an analytical function of the Higgs mass that provides a full description of the signal in the whole search mass range and was used in the discovery analysis based on 4.7 and 5.8 fb^{-1} of data at $\sqrt{s} = 7$ and 8 TeV, respectively. The analysis described in this document provided the observation of an excess of events around the invariant mass of the diphoton system of about 126.5 GeV. These results, combined with those obtained in the $H \to ZZ$ and $H \to WW$ channels in both ATLAS and CMS collaborations, confirmed the discovery of a new boson, consistent with the long searched-for Higgs boson [3].

The observation of this Higgs-like particle in the $\gamma\gamma$ channel increased the motivation for the search in the $Z\gamma$ (Z$\to ee, \mu\mu$) channel, given that both channels are sensitive to new physics. The result of the first search performed in ATLAS based on the total dataset recorded in the Run I of the LHC (4.7 + 20.7 fb^{-1}) are presented in this thesis. The analysis strategy is very similar to the one in $H \to \gamma\gamma$, with the main exception that the difference between the three-body and two-body invariant masses is used as a discriminating variable. The signal modelling developed for the $H \to \gamma\gamma$ analysis is easily extrapolated to this case. No significant deviations from the SM background expectations are observed and upper limits on the cross sections times branching ratio are set. For a mass of 125 GeV, the expected and observed limits are 13.5 and 18.2 times the SM, respectively [4]. Even if the analysis sensitivity can be improved by more sophisticated techniques, the analysis is dominated by

statistics. The observation sensitivity in this channel should be reached after the LHC shutdown.

The $H \to \gamma\gamma$ analysis was updated by ATLAS with the total data sample recorded in 2012. The analysis confirmed the result presented in this thesis [55], and performed measurement of properties such as the mass, spin and couplings of this new found particle, which was declared in March 2013 as a Higgs particle. Even if the Higgs mass determination is not the topic of this thesis, the contributions presented in this document were critical to this measurement. The global resolution model allowed to build a likelihood function for the profile likelihood ratio used in the mass evaluation. In addition, the study of the energy scale using radiative Z decays was considered as a cross-check of the calibration, reinforcing the precision of the mass measurement in the diphoton channel.

Measurements of the spin, couplings, decay rates and cross-sections are being performed in the $H \to \gamma\gamma$, $H \to ZZ$ and $H \to WW$ channels in ATLAS and CMS [134, 135, 159, 160]. All results hint that the new Higgs Boson is consistent with the SM prediction. Furthermore, after the first run of the LHC, some of the theories proposed to account for the limitations of the SM such as a fermiophobic Higgs, fourth generation, MSSM, were either excluded (under certain assumptions [56]) or their parameter space was constrained [161] and non-evidence for new particles was found. Nevertheless, more analyses and data are needed to confirm that the Higgs boson with mass of about 125 GeV is the SM Higgs boson (and the only one). Higher luminosities and higher centre of mass collision energies after the LHC shutdown will allow the search for new physics at higher energy regimes to continue.

Appendix A

Overview of the statistical analysis

In this appendix a short overview of the statistical methods used in the Higgs boson search is presented. A detailed description is found in [162].

Exclusion limits of the Higgs boson production cross-section are extracted using the $CL_{\rm s}$ method [163]. In this procedure, a signal plus background un-binned likelihood function $\mathcal{L}(\text{data}|\mu,\theta)$ is evaluated on data:

$$\mathcal{L}(\text{data}|\mu,\theta) = \text{Poisson}(\text{data}|\mu\cdot s(\theta)+b(\theta))\cdot p(\tilde{\theta}|\theta) \tag{A.1}$$

where the parameter μ is the signal strength and θ represent the nuisance parameters. Poisson(data$|\mu s+b$) stands for an unbinned likelihood of k events in the data sample:

$$k^{-1}\prod_{i}^{k}(\mu S f_s(x)+Bf_b(x))\cdot e^{-(\mu S+B)}, \tag{A.2}$$

where $f_s(x)$ and $f_b(x)$ are the pdf of the signal and background of the x observable [1], taken from the global resolution model explained in Section 6.7 and the background functions detailed in Section 6.8.3 for the $H\to\gamma\gamma$ channel and Section 7.6. S and B are the total expected signal and background events.

The compatibility of the data with hypothetical values of a strength parameter μ ($\mu=0$ is the background-only hypothesis and $\mu=1$ is the SM signal in addition

[1]The observable x in the $H\to\gamma\gamma$ analysis is the diphoton invariant mass ($m_{\gamma\gamma}$.) and in the $H\to Z\gamma$ case is the mass difference between the three and two-body invariant masses ($\Delta m = m_{\ell\ell\gamma}-m_{\ell\ell}$)

to the background), is evaluated through a test statistic ($\tilde{q}_{\mu)}$, based on the profile likelihood ratio [164] .

$$\tilde{q}_{\mu} = -2\ln\frac{\mathcal{L}(\text{data}|\mu,\hat{\theta}_{\mu})}{\mathcal{L}(\text{data}|\hat{\mu},\hat{\theta})}, \quad \text{for } -0 \leq \hat{\mu} \leq \mu,, \tag{A.3}$$

where $\hat{\theta}_{\mu}$ are the conditional maximum likelihood estimators of θ for the data and a signal strength parameter μ. The parameter estimators $\tilde{\mu}$ and $\hat{\theta}$ correspond to the global maximum of the likelihood. The constraint $0 \leq \tilde{\mu}$ demands for a positive signal rate, while the upper constraint is imposed by hand to guarantee that upward fluctuations of the data such as $\tilde{\mu} > \mu$ are not considered as evidence against the signal hypothesis with strength μ. In order to extract the $CL_{(s)}$, the next steps are followed:

- The $\hat{\theta}_{\mu}$ is evaluated for a given signal strength ($\tilde{\theta_{\mu}^{obs}}$) over the data and the nuisance parameters $\hat{\theta_0^{obs}}$ and $\hat{\theta_{\mu}^{obs}}$ that best describe the data for the signal+background and background-only hypothesis respectively are extracted by maximising the likelihood.

- The nuisance parameters are used to generate MC pseudo-data (toys) for the signal+background and background-only hypothesis. In each toy the value of $\tilde{q_{\mu}}$ is evaluated and PDFs of $f(\tilde{q_{\mu}}|\mu,\hat{\theta_{\mu}^{obs}})$ and $f(\tilde{q_{\mu}}|0,\hat{\theta_0^{obs}})$ are build for each hypothesis.

- Based on the built PDFs, two probabilities on the signal+background and background-only hypothesis are defined:

$$p_{\mu} = P(\tilde{q_{\mu}} \geq \tilde{q_{\mu}^{obs}}|signal + background) = \int_{\tilde{q_{\mu}^{obs}}}^{\infty} f(\tilde{q_{\mu}}|\mu,\hat{\theta_{\mu}^{obs}})d\tilde{q_{\mu}}, \tag{A.4}$$

$$1 - p_b = P(\tilde{q_{\mu}} \geq \tilde{q_{\mu}^{obs}}|background - only) = \int_{\tilde{q_{\mu}^{obs}}}^{\infty} f(\tilde{q_{\mu}}|\mu,\hat{\theta_{\mu}^{obs}})d\tilde{q_{\mu}}, \tag{A.5}$$

and the $CL_s(\mu)$ is defined as the ratio of these two probabilities

$$CL_s(\mu) = \frac{p_{\mu}}{1 - p_b} \tag{A.6}$$

the 95% Confidence Level (CL) upper limit on μ implies that the $CL_s = 0.05$

The previous steps are performed in the whole search mass range setting a limit over the 95 % of CL, over the data for the observed limits, and over pseudo-datasets generated by the background only models obtained by fitting the observed data. The systematic uncertainties are taken into account in the limit by incorporating nuisance parameters with a PDF that constrain the uncertainties in the likelihood function.

In the case of $H \to \gamma\gamma$ where due to an excess of events a certain m_{H} is unavailable to be excluded, the presence of the signal is quantified by the background-only p-value (p_0). This is the probability for the background to fluctuate and give an excess of events as large or larger than the observed one, and is based on a test statistic of the likelihood ratio of the background only hypothesis.

$$\tilde{q}_0 = -2\ln\frac{\mathcal{L}(data|0,\tilde{\theta}_0)}{\mathcal{L}(data|\hat{\mu},\hat{\theta})}, \quad \text{and} \quad -\hat{\mu} \geq 0,, \tag{A.7}$$

the $\hat{\mu} \geq 0$ constraint giving the same interpretation to a downward background fluctuation as an excess of events. Similarly to the CL_s method, a distribution of $f(\tilde{q_\mu}|0,\hat{\theta_0^{obs}})$ is built out of the for nuisance parameters obtained from data to a background only hypothesis ($\hat{\theta_0^{obs}}$). From such a distribution the p-value of a observed q_0^{obs} is evaluated as follows:

$$p_0 = P(q_0 \geq q_0^{obs}) = \int_{q_0^{obs}}^{\infty} f(q_0|0,\hat{\theta_0^{obs}})dq_0, \tag{A.8}$$

The p-value can be translated into an observed significance (Z), where a 5σ significance (Z = 5) would correspond in this case to $p_0 = 2.8 \times 10^{-7}$. The evaluation of such low probabilities is performed by relying on the asymptotic behaviour of the likelihood ratio test statistic used [164]. The p-value discussed above is evaluated at a fixed m_{H} and is referred to as a local p-value. Since the background-only hypothesis is tested many times in the mass range scan, the dilution effect associated with the multiple testing must be taken into account, the probability of having such a fluctuation in other mass points is included in the global significance, as a dilution effect associated with the multiple testing, also known as a trial factor or look-elsewhere effect.

In the $H \to \gamma\gamma$ analysis, both results of observed limits and p_0 obtained with 7 TeV and 8 TeV data are combined statistically. In addition, the analysis is also performed without the categorisation of event as a cross check.

The best fit value for the signal strength μ is extracted from a simultaneous fit to all categories. For every mass point (from 100 to 150 GeV in steps of 0.5 GeV), the signal shape parameters of the global resolution model at that point are fixed, and a common signal strength is fitted along with the nuisance parameter of the systematic uncertainties. The bias of quantifying the best fit value at the point where the larger deviation from the background-only hypothesis is evaluated with pseudo-experiments and found to be 8 % [117].

The signal strength and mass of the potential signal that are the most compatible with the data can be extracted of a profile likelihood ratio, where the Higgs boson mass m_{H} is included as the parameter of interest. The scan is performed in steps of 0.1 GeV. The global resolution model where the signal shape parameters such as the mean and width of the Crystal-Ball function and the theoretical uncertainties are a function of m_{H}. The impact of the photon energy scale on the mass measurement is evaluated using a procedure based on pseudo-experiments [165]. A 2-dimensional scan of the signal strength and the Higgs mass is performed obtaining likelihood contours corresponding to the 68% and 95% confidence level, these contour lines have been computed assuming that the test statistic follows the χ^2 distribution, for the case of two degrees of freedom.

Bibliography

[1] C. Rangel-Smith and J. Ocariz, "High voltage corrections due to electrode resistors in the electromagnetic calorimeter," Tech. Rep. ATL-LARG-INT-2013-003, CERN, Geneva, Jun 2013.

[2] A. Collaboration, "Supporting note for the 2011 em calibration analysis," Tech. Rep. ATL-COM-PHYS-2012-1473, CERN, Geneva, Oct 2012.

[3] The Collaboration, ATLAS, "Observation of a new particle in the search for the Standard Model Higgs boson with the ATLAS detector at the LHC," *ArXiv e-prints*, July 2012.

[4] A. Collaboration, "Search for the standard model higgs boson in the $h \to z\gamma$ decay mode with pp collisions at $\sqrt{s} = 7$ and 8 tev," Tech. Rep. ATLAS-CONF-2013-009, CERN, Geneva, Mar 2013.

[5] R.-S. et al., "Signal studies for $h \to z\gamma$," Tech. Rep. ATL-COM-PHYS-2013-081, CERN, Geneva, Jan 2013.

[6] A. proclaimed Website, "The standard model," 2013.

[7] S. L. Glashow, "Partial Symmetries of Weak Interactions," *Nucl. Phys.*, vol. 22, pp. 579–588, 1961.

[8] S. Weinberg, "A Model of Leptons," *Phys. Rev. Lett.*, vol. 19, pp. 1264–1266, 1967.

[9] A. Salam, *in Elementary Particle Theory, p. 367*. Stockholm: Almqvist and Wiksell, 1968.

[10] P. W. Higgs, "Broken symmetries, massless particles and gauge fields," *PL*, vol. 12, p. 132, 1964.

[11] P. W. Higgs, "Broken symmetries and the masses of gauge bosons," *PRL*, vol. 13, p. 508, 1964.

[12] P. W. Higgs, "Spontaneous symmetry breakdown without massless bosons," *PR*, vol. 145, p. 1156, 1966.

[13] F. Englert and R. Brout, "Broken symmetry and the mass of gauge vector mesons," *PRL*, vol. 13, p. 321, 1964.

[14] A. Djouadi, "The Anatomy of electro-weak symmetry breaking. I: The Higgs boson in the standard model," *Phys.Rept.*, vol. 457, pp. 1–216, 2008.

[15] T. Hambye and K. Riesselmann, "Matching conditions and higgs mass upper bounds revisited," *Physical Review D*, vol. 55, pp. 7255–7262, 1997.

[16] R. Barate *et al.*, "Search for the standard model Higgs boson at LEP," *Phys.Lett.*, vol. B565, pp. 61–75, 2003.

[17] T. T. N. Phenomina and D. C. Higgs Working Group), CDF Collaboration, "Combined CDF and D0 Upper Limits on Standard Model Higgs Boson Production with up to 8.6 fb^{-1} of Data," tech. rep., Fermilab, 2011.

[18] ALEPH, DELPHI, L3 and OPAL Collaborations, "The lep electroweak working group."

[19] M. Baak, M. Goebel, J. Haller, A. Hoecker, D. Kennedy, K. Mnig, M. Schott, and J. Stelzer, "Updated status of the global electroweak fit and constraints on new physics," *The European Physical Journal C*, vol. 72, no. 5, pp. 1–35, 2012.

[20] R. V. Harlander and W. B. Kilgore, "Next-to-next-to-leading order higgs production at hadron colliders," *Phys. Rev. Lett.*, vol. 88, p. 201801, May 2002.

[21] H. M. Georgi, S. L. Glashow, M. E. Machacek, and D. V. Nanopoulos, "Higgs bosons from two-gluon annihilation in proton-proton collisions," *Phys. Rev. Lett.*, vol. 40, pp. 692–694, Mar 1978.

[22] A. Djouadi, M. Spira, and P. Zerwas, "Production of higgs bosons in proton colliders. {QCD} corrections," *Physics Letters B*, vol. 264, no. 3–4, pp. 440 – 446, 1991.

[23] M. Spira, A. Djouadi, D. Graudenz, and R. Zerwas, "Higgs boson production at the {LHC}," *Nuclear Physics B*, vol. 453, no. 1–2, pp. 17 – 82, 1995.

[24] C. Anastasiou and K. Melnikov, "Higgs boson production at hadron colliders in {NNLO} {QCD}," *Nuclear Physics B*, vol. 646, no. 1–2, pp. 220 – 256, 2002.

[25] V. Ravindran, J. Smith, and W. van Neerven, "{NNLO} corrections to the total cross section for higgs boson production in hadron–hadron collisions," *Nuclear Physics B*, vol. 665, no. 0, pp. 325 – 366, 2003.

[26] U. Aglietti, R. Bonciani, G. Degrassi, and A. Vicini, "Two-loop light fermion contribution to higgs production and decays," *Physics Letters B*, vol. 595, no. 1–4, pp. 432 – 441, 2004.

[27] S. Actis, G. Passarino, C. Sturm, and S. Uccirati, "{NLO} electroweak corrections to higgs boson production at hadron colliders," *Physics Letters B*, vol. 670, no. 1, pp. 12 – 17, 2008.

[28] M. Ciccolini, A. Denner, and S. Dittmaier, "Strong and electroweak corrections to the production of a higgs boson + 2 jets via weak interactions at the large hadron collider," *Phys. Rev. Lett.*, vol. 99, p. 161803, Oct 2007.

[29] K. Arnold, M. Bähr, G. Bozzi, F. Campanario, C. Englert, T. Figy, N. Greiner, C. Hackstein, V. Hankele, B. Jäger, G. Klämke, M. Kubocz, C. Oleari, S. Plätzer, S. Prestel, M. Worek, and D. Zeppenfeld, "Vbfnlo: A parton level monte carlo for processes with electroweak bosons," *Computer Physics Communications*, vol. 180, no. 9, pp. 1661 – 1670, 2009.

[30] R. Cahn and S. Dawson, "Production of very massive higgs bosons," *Physics Letters B*, vol. 136, no. 3, pp. 196 – 200, 1984.

[31] P. Bolzoni, F. Maltoni, S.-O. Moch, and M. Zaro, "Higgs boson production via vector-boson fusion at next-to-next-to-leading order in qcd," *Phys. Rev. Lett.*, vol. 105, p. 011801, Jul 2010.

[32] M. L. Ciccolini, S. Dittmaier, and M. Krämer, "Electroweak radiative corrections to associated *WH* and *ZH* production at hadron colliders," *Phys. Rev. D*, vol. 68, p. 073003, Oct 2003.

[33] O. Brein, A. Djouadi, and R. Harlander, "{NNLO} {QCD} corrections to the higgs-strahlung processes at hadron colliders," *Physics Letters B*, vol. 579, no. 1–2, pp. 149 – 156, 2004.

[34] T. Han and S. Willenbrock, "{QCD} correction to the pp {WH} and {ZH} total cross sections," *Physics Letters B*, vol. 273, no. 1–2, pp. 167 – 172, 1991.

[35] W. Beenakker, S. Dittmaier, M. Krämer, B. Plümper, M. Spira, and P. Zerwas, "{NLO} {QCD} corrections to tth production in hadron collisions," *Nuclear Physics B*, vol. 653, no. 1–2, pp. 151 – 203, 2003.

[36] S. Dawson, L. H. Orr, L. Reina, and D. Wackeroth, "Next-to-leading order qcd corrections to pp to tth at the cern large hadron collider," *Phys. Rev. D*, vol. 67, p. 071503, Apr 2003.

[37] S. Dawson, C. Jackson, L. H. Orr, L. Reina, and D. Wackeroth, "Associated higgs boson production with top quarks at the cern large hadron collider: Nlo qcd corrections," *Phys. Rev. D*, vol. 68, p. 034022, Aug 2003.

[38] Z. Kunszt, "Associated production of heavy higgs boson with top quarks," *Nuclear Physics B*, vol. 247, no. 2, pp. 339 – 359, 1984.

[39] W. Beenakker, S. Dittmaier, M. Krämer, B. Plümper, M. Spira, and P. M. Zerwas, "Higgs radiation off top quarks at the tevatron and the lhc," *Phys. Rev. Lett.*, vol. 87, p. 201805, Oct 2001.

[40] L. H. C. S. W. Group, "Website of the lhc higgs cross section working group," 2012.

[41] A. Djouadi, J. Kalinowski, and M. Spira, "Hdecay: a program for higgs boson decays in the standard model and its supersymmetric extension," *Computer Physics Communications*, vol. 108, no. 1, pp. 56 – 74, 1998.

[42] X. Ruan and Z. Zhang, "Impact on the Higgs Production Cross Section and Decay Branching Fractions of Heavy Quarks and Leptons in a Fourth Generation Model," *ArXiv e-prints*, 2011.

[43] A. Denner, S. Dittmaier, A. Muck, G. Passarino, M. Spira, *et al.*, "Higgs Production and Decay with a Fourth Standard-Model-Like Fermion Generation," *Eur.Phys.J.*, vol. C72, p. 1992, 2012.

[44] I. Low, J. Lykken, and G. Shaughnessy, "Singlet scalars as Higgs imposters at the Large Hadron Collider," *Phys.Rev.*, vol. D84, p. 035027, 2011.

[45] G. D. Kribs, T. Plehn, M. Spannowsky, and T. M. Tait, "Four generations and Higgs physics," *Phys.Rev.*, vol. D76, p. 075016, 2007.

[46] G. Branco, P. Ferreira, L. Lavoura, M. Rebelo, M. Sher, *et al.*, "Theory and phenomenology of two-Higgs-doublet models," *Phys.Rept.*, vol. 516, pp. 1–102, 2012.

[47] F. Arbabifar, S. Bahrami, and M. Frank, "Neutral Higgs Bosons in the Higgs Triplet Model with nontrivial mixing," *Phys.Rev.*, vol. D87, p. 015020, 2013.

[48] A. Barroso, L. Brucher, and R. Santos, "Is there a light fermiophobic Higgs?," *Phys.Rev.*, vol. D60, p. 035005, 1999.

[49] J. F. Gunion, R. Vega, and J. Wudka, "Higgs triplets in the standard model," *Phys. Rev. D*, vol. 42, pp. 1673–1691, Sep 1990.

[50] A. Akeroyd, M. A. Diaz, M. A. Rivera, and D. Romero, "Fermiophobia in a Higgs Triplet Model," *Phys.Rev.*, vol. D83, p. 095003, 2011.

[51] A. Djouadi, "The anatomy of electroweak symmetry breaking tome ii: The higgs bosons in the minimal supersymmetric model," *Physics Reports*, vol. 459, no. 16, pp. 1 – 241, 2008.

[52] C.-W. Chiang and K. Yagyu, "Higgs boson decays to $\gamma\gamma$ and $Z\gamma$ in models with Higgs extensions," *Phys.Rev.*, vol. D87, no. 3, p. 033003, 2013.

[53] A. Collaboration, "Search for a fermiophobic higgs boson in the diphoton decay channel with 4.9/fb of atlas data at sqrt(s)= 7 tev," Tech. Rep. ATLAS-CONF-2012-013, CERN, Geneva, Mar 2012.

[54] E. Gabrielli, B. Mele, and M. Raidal, "Has a Fermiophobic Higgs Boson been Detected at the LHC ?," *Phys.Lett.*, vol. B716, pp. 322–325, 2012.

[55] A. Collaboration, "Measurements of the properties of the higgs-like boson in the two photon decay channel with the atlas detector using 25 fb^{-1} of proton-proton collision data," Tech. Rep. ATLAS-CONF-2013-012, CERN, Geneva, Mar 2013.

[56] C. Collaboration, "Searches for higgs bosons in pp collisions at sqrt(s) = 7 and 8 tev in the context of four-generation and fermiophobic models," *Phys.Lett.*, vol. B725, pp. 36–59, 2013.

[57] A. Collaboration, "Search for charged higgs bosons in the τ+jets final state with pp collision data recorded at $\sqrt{s} = 8$ tev with the atlas experiment," Tech. Rep. ATLAS-CONF-2013-090, CERN, Geneva, Aug 2013.

[58] A. Collaboration, "Search for neutral mssm higgs bosons in $sqrts = 7$ tev pp collisions at atlas," Tech. Rep. ATLAS-CONF-2012-094, CERN, Geneva, Jul 2012.

[59] L. Evans and P. Bryant, "LHC Machine," *JINST*, vol. 3, no. S08001, 2008.

[60] A. Collaboration, "The ATLAS Experiment at the CERN Large Hadron Collider," *JINST*, vol. 3, 2008.

[61] C. Collaboration, "The CMS experiment at the CERN LHC," *JINST*, vol. 3, no. S08004, 2008.

[62] L. Collaboration, "The LHCb Detector at the LHC," *JINST*, vol. 3, no. S08005, 2008.

[63] A. Collaboration, "The ALICE experiment at the CERN LHC," *JINST*, vol. 3, no. S08002, 2008.

[64] X. C. Vidal and R. Cid, "This is a test entry of type @misc: http://www.lhc-closer.es."

[65] "Atlas's website with luminosity related public results," 2013.

[66] "Lhc commissioning with beam," 2013.

[67] A. Chao, K. Mess, and M. Tigner, *Handbook of Accelerator Physics and Engineering: 2nd Edition*. World Scientific Publishing Company Incorporated, 2013.

[68] A. Collaboration, "Delivered luminosity versus time for 2010,2011,2012 (p-p data only)," 2012.

[69] A. Collaboration, "Peak luminosity versus time," 2011.

[70] A. Collaboration, "Number of interactions per crossing," 2011.

[71] A. Collaboration, "Vertex reconstruction plots: Collision performance plots for approval," Tech. Rep. ATL-COM-PHYS-2012-474, CERN, Geneva, Apr 2012.

[72] A. Salvucci, "Measurement of muon momentum resolution of the ATLAS detector," *EPJ Web Conf.*, vol. 28, p. 12039, 2012.

[73] Collaboration, ATLAS, "Expected Performance of the ATLAS Experiment — Detector, Trigger and Physics," 2009.

[74] A. Collaboration, "Electron performance measurements with the ATLAS detector using the 2010 LHC proton-proton collision data," 2011. ATLAS-COM-PHYS-2011-546.

[75] J. MAURER, "Operation and performance of the atlas liquid argon electromagnetic calorimeters," Jul 2013. Poster presented at The 2013 European Physical Society Conference on High Energy Physics. EPSHEP 2013 Stockholm, Sweden, 18-24 July, 2013.

[76] A. Collaboration, "Trigger operation public plots," 2012.

[77] C. W. Fabjan and F. Gianotti, "Calorimetry for particle physics," *Rev. Mod. Phys.*, vol. 75, pp. 1243–1286, Oct 2003.

[78] U. Amaldi, "Fluctuations in calorimetry measurements," *Physica Scripta*, vol. 23, no. 4A, p. 409, 1981.

[79] A. Collaboration, "Lar calibration description."

[80] A. Collaboration, "Calorimeter clustering algorithms: Description and performance," Tech. Rep. ATL-LARG-PUB-2008-002, CERN, Geneva, Apr 2008.

[81] A. Collaboration, "ATLAS liquid argon calorimeter: Technical design report," tech. rep., CERN, 1996.

[82] B. Aubert *et al.*, "Development and construction of large size signal electrodes for the atlas electromagnetic calorimeter," *Nucl. Instrum. Methods Phys. Res., A*, vol. 539, pp. 558–594. 43 p, May 2004.

[83] C. W and S. E, "Signal processing considerations for liquid ionization calorimeter in a high rate environment," *Nucl. Inst. Meth.*, vol. A 338, p. 467, 1994.

[84] C. Collard, "Electronic calibration of the atlas lar calorimeter," *Nucl. Instrum. Methods Phys. Res., A*, vol. 623, pp. 246–248. 3 p, Apr 2009. Conference proceedings deadline : 20/04/2009.

[85] L. Di Ciaccio *et al.*, "High Voltage corrections for the electromagnetic calorimeter," *ATLAS Internal Note*, vol. ATL-COM-LARG-2005-003, 2005.

[86] S. Arfaoui *et al.*, *The ATLAS liquid argon calorimeter high-voltage system: commissioning, optimisation, and LHC relative luminosity measurement.* PhD thesis, Marseille U., Luminy I U., Geneva, 2011. Presented 14 Oct 2011.

[87] D. Lacour, "Resistance model for barrel electrodes." private communication, 2012.

[88] F. Djama, "Resistance model for end cap electrodes." private communication, July 2012.

[89] A. Valassi *et al.*, "Lcg persistency framework (coral, cool, pool): Status and outlook," *Journal of Physics: Conference Series*, vol. 331, no. 4, p. 042043, 2011.

[90] A. Collaboration, "Expected photon performance in the atlas experiment," Tech. Rep. ATL-PHYS-PUB-2011-007, CERN, Geneva, Apr 2011.

[91] A. Collaboration, "Expected Performance of the ATLAS Experiment - Detector, Trigger and Physics," tech. rep., CERN, 2009.

[92] Collaboration, ATLAS, "Readiness of the ATLAS Liquid Argon Calorimeter for LHC Collisions," *Eur. Phys. J.*, vol. C 70, pp. 723–753, 2010.

[93] D. Banfi, L. Carminati, and L. Mandelli, "Calibration of the atlas electromagnetic calorimeter using calibration hits," Tech. Rep. ATL-LARG-PUB-2007-012. ATL-COM-LARG-2007-007, CERN, Geneva, Jul 2007.

[94] A. Collaboration, "Electron and photon reconstruction and identification in atlas: expected performance at high energy and results at 900 gev," Tech. Rep. ATLAS-CONF-2010-005, CERN, Geneva, Jun 2010.

[95] F. Djama, "Using $z^0 \rightarrow e^+e^-$ for electromagnetic calorimeter calibration," Tech. Rep. ATL-LARG-2004-008, Aix-Marseille 2. Cent. Phys. Part., Marseille, Jun 2004.

[96] A. Collaboration, "Electron performance measurements with the ATLAS detector using the 2010 LHC proton-proton collision data," *Eur.Phys.J.*, vol. C72, p. 1909, 2012.

[97] A. Collaboration, "Electron energy response stability with pile-up in 2012 data with 13 fb^{-1}," Tech. Rep. ATL-COM-PHYS-2012-1668, CERN, Geneva, Nov 2012.

[98] A. Collaboration, "Calibrated $z \to ee$ mass with 2011 data," Tech. Rep. ATL-COM-PHYS-2011-1637, CERN, Geneva, Dec 2011.

[99] A. Collaboration, "Higgs mass measurements and uncertainties in 2011 and 2012 data," Tech. Rep. ATL-COM-PHYS-2012-1774, CERN, Geneva, Dec 2012.

[100] A. Collaboration, "Event displays for photon analysis."

[101] A. Collaboration, "Photon shower shapes data/mc comparisons from $z + \gamma$ events," Tech. Rep. ATL-COM-PHYS-2013-600, CERN, Geneva, May 2012.

[102] A. Collaboration, "Measurements of the photon identification efficiency with the atlas detector using 4.9 fb1 of pp collision data collected in 2011," Tech. Rep. ATLAS-CONF-2012-123, CERN, Geneva, Aug 2012.

[103] A. Collaboration, "Photon identification efficiency measurements using $z \to \ell\ell\gamma$ events in 20.7 fb-1 of pp collisions collected by atlas at 8 tev in 2012," Tech. Rep. ATL-COM-PHYS-2013-244, CERN, Geneva, March 2012.

[104] A. Collaboration, "Egamma public plots," 2011.

[105] A. Collaboration, "Egamma public plots."

[106] K. Nakamura and P. D. Group, "Review of Particle Physics," *Journal of Physics G: Nuclear and Particle Physics*, vol. 37, no. 7A, p. 075021, 2010.

[107] Collaboration, ATLAS, "The ATLAS simulation infrastructure," *Eur. Phys. J. C*, vol. 70, pp. 823–874, 2010.

[108] S. Agostinelli *et al.*, "Geant4 - a simulation toolkit," *Nucl. Instrum. Methods A*, vol. 506, p. 250, 2003.

[109] T. Sjostrand, S. Mrenna, and P. Z. Skands, "PYTHIA 6.4 Physics and Manual," *JHEP*, vol. 0605, pp. 026, 2006.

[110] T. Gleisberg, S. Hoche, F. Krauss, A. Schalicke, S. Schumann, and J. Winter, "SHERPA 1. alpha: A Proof of concept version," *JHEP*, vol. 02, p. 056, 2004.

[111] T. Gleisberg *et al.*, "Event generation with SHERPA 1.1," *JHEP*, vol. 02, p. 007, 2009.

[112] S. Hoeche, S. Schumann, and F. Siegert, "Hard photon production and matrix-element parton-shower merging," *Phys. Rev. D*, vol. 81, p. 034026, 2010.

[113] H.-L. Lai, M. Guzzi, J. Huston, Z. Li, P. M. Nadolsky, *et al.*, "New parton distributions for collider physics," *Phys.Rev.*, vol. D82, p. 074024, 2010.

[114] S. Hassani, L. Chevalier, E. Lancon, J. Laporte, R. Nicolaidou, *et al.*, "A muon identification and combined reconstruction procedure for the ATLAS detector at the LHC using the (MUONBOY, STACO, MuTag) reconstruction packages," *Nucl.Instrum.Meth.*, vol. A572, pp. 77–79, 2007.

[115] A. Collaboration, "ATLAS Muon Momentum Resolution in the First Pass Reconstruction of the 2010 p-p Collision Data at $\sqrt(s) = 7Tev$," 2011. ATLAS-CONF-2011-046.

[116] O. Kortner, "Muon momentum scale uncertainties." private communication, January 2012.

[117] A. Collaboration, "Observation of an excess of events in the search for the standard model higgs boson in the gamma-gamma channel with the atlas detector," Tech. Rep. ATLAS-CONF-2012-091, CERN, Geneva, Jul 2012.

[118] F. Cerutti, C. Gatti, P. Kluit, O. Kortner, W. Liebig, J. Liu, G. Salamanna, A. Salvucci, E. van der Poel, and J. Zhu, "Muon momentum resolution in first pass reconstruction of pp collision data recorded by atlas in 2010," Tech. Rep. ATLAS-COM-CONF-2011-003, CERN, Geneva, Jan 2011. see CDS discussion for signoffs from edboard, pubcom delegate and physcoord delegate.

[119] T. Sjöstrand, S. Mrenna, P. Skands, "A brief introduction to PYTHIA 8.1," *Comput.Phys.Commun.*, vol. 178, pp. 852–867, 2008.

[120] D. Florian, G. Ferrera, M. Grazzini, and D. Tommasini, "Transverse-momentum resummation: Higgs boson production at the tevatron and the lhc," *Journal of High Energy Physics*, vol. 2011, no. 11, pp. 1–22, 2011.

[121] L. Dixon and M. S. Siu, "Resonance-continuum interference in the diphoton higgs signal at the lhc," *Phys. Rev. Lett.*, vol. 90, p. 252001, Jun 2003.

[122] A. Collaboration, "Search for the higgs boson in the diphoton final state with 38 pb^{-1} of data recorded by the atlas detector in proton-proton collisions at $sqrts$=7 tev," Tech. Rep. ATLAS-CONF-2011-025, CERN, Geneva, Mar 2011.

[123] R. Turra, C. Meroni, and M. Fanti, *Energy calibration and observation of the Higgs boson in the diphoton decay with the ATLAS experiment.* PhD thesis, Milano U., Jan 2013. Presented 18 Feb 2013.

[124] A. Collaboration, "Measurement of the backgrounds to the *hightarrowgammagamma* search and reappraisal of its sensitivity with 37 pb^{-1} of data recorded by the atlas detector," Tech. Rep. ATLAS-COM-CONF-2011-006, CERN, Geneva, Jan 2011.

[125] A. Collaboration, "Search for the higgs boson in the diphoton channel with the atlas detector using 209 pb-1 of 7 tev data taken in 2011," Tech. Rep. ATLAS-CONF-2011-085, CERN, Geneva, Jun 2011.

[126] A. Collaboration, "Search for the standard model higgs boson in the two photon decay channel with the {ATLAS} detector at the {LHC}," *Physics Letters B*, vol. 705, no. 5, pp. 452 – 470, 2011.

[127] LHC Higgs Cross Section Working Group, S. Dittmaier, C. Mariotti, G. Passarino, and R. Tanaka (Eds.), "Handbook of LHC Higgs Cross Sections: 1. Inclusive Observables," *CERN-2011-002*, CERN, Geneva, 2011.

[128] LHC Higgs Cross Section Working Group, S. Dittmaier, C. Mariotti, G. Passarino, and R. Tanaka (Eds.), "Handbook of LHC Higgs Cross Sections: 2. Differential Distributions," *CERN-2012-002*, CERN, Geneva, 2012.

[129] M. Cacciari, G. P. Salam, and G. Soyez, "The Anti-k(t) jet clustering algorithm," *JHEP*, vol. 0804, p. 063, 2008.

[130] H. HSG1 Working Group, "Background studies for the search of higgs boson decaying to two photons with 8tev data," Tech. Rep. ATL-COM-PHYS-2012-754, CERN, Geneva, Jun 2012.

[131] W. MathWordl, "Bernstein Polynomials."

[132] A. Denner, S. Heinemeyer, I. Puljak, D. Rebuzzi, and M. Spira, "Standard Model Higgs-boson branching ratios with uncertainties," *Eur. Phys. J.*, vol. C71, p. 1753, 2011.

[133] S. Dittmaier, S. Dittmaier, C. Mariotti, G. Passarino, R. Tanaka, *et al.*, "Handbook of LHC Higgs Cross Sections: 2. Differential Distributions," tech. rep., CERN, 2012.

[134] A. Collaboration, "Evidence for the spin-0 nature of the higgs boson using atlas data," tech. rep., CERN, 2013.

[135] A. Collaboration, "Measurements of higgs boson production and couplings in diboson final states with the atlas detector at the lhc," *Physics Letters B*, 2013.

[136] C. Collaboration, "Combination of SM, SM4, FP Higgs boson searches," Mar 2012.

[137] A. Collaboration, "Measurement of the backgrounds to the $h \to \gamma\gamma$ search and reappraisal of its sensitivity with 37 pb^{-1} of data recorded by the atlas detector," Tech. Rep. ATLAS-CONF-2011-004, CERN, Geneva, Feb 2011.

[138] A. Collaboration, "Update of the background studies in the search for the higgs boson in the two photons channel in pp collisions at s=7 tev," Tech. Rep. ATLAS-CONF-2011-071, CERN, Geneva, May 2011.

[139] Collaboration, ATLAS, "Search for the Standard Model Higgs boson in the two photon decay channel with the ATLAS detector at the LHC," *Phys. Lett.*, vol. B 705, pp. 452–470, 2011.

[140] Collaboration, ATLAS, "Search for a fermiophobic higgs boson in the diphoton channel with the atlas detector," Tech. Rep. ATLAS-CONF-2011-149, CERN, Geneva, Nov 2011.

[141] A. Collaboration, "Observation and study of the higgs boson candidate in the two photon decay channel with the atlas detector at the lhc," Tech. Rep. ATLAS-CONF-2012-168, CERN, Geneva, Dec 2012.

[142] The Collaboration, CMS, "Observation of a new boson at a mass of 125 GeV with the CMS experiment at the LHC," *ArXiv e-prints*, July 2012.

[143] A. Collaboration, "Measurement of Wgamma and Zgamma production in proton-proton collisions at $\sqrt{s} = 7$ TeV with the ATLAS Detector," *JHEP*, vol. 1109, p. 072, 2011.

[144] S. Alioli, P. Nason, C. Oleari and E. Re, "NLO Higgs boson production via gluon fusion matched with shower in POWHEG," *JHEP*, vol. 04, p. 002, 2009.

[145] P. Nason and C. Oleari, "NLO Higgs boson production via vector-boson fusion matched with shower in POWHEG," *JHEP*, vol. 02, p. 037, 2010.

[146] M. L. Mangano *et al.*, "ALPGEN, a generator for hard multiparton processes in hadronic collisions," *JHEP*, vol. 07, p. 001, 2003.

[147] G. Corcella, I. Knowles, G. Marchesini, S. Moretti, K. Odagiri, *et al.*, "HERWIG 6: An Event generator for hadron emission reactions with interfering gluons (including supersymmetric processes)," *JHEP*, vol. 0101, pp. 010, 2001.

[148] J. M. Butterworth, J. R. Forshaw, and M. H. Seymour, "Multiparton interactions in photoproduction at HERA," *Z. Phys.*, vol. C 72, pp. 637–646, 1996.

[149] A. Collaboration, "New ATLAS event generator tunes to 2010 data," tech. rep., CERN, 2011.

[150] P. M. Nadolsky, H.-L. Lai, Q.-H. Cao, J. Huston, J. Pumplin, *et al.*, "Implications of CTEQ global analysis for collider observables," *Phys.Rev.*, vol. D78, p. 013004, 2008.

[151] P. Golonka and Z. Was, "PHOTOS Monte Carlo: A Precision tool for QED corrections in Z and W decays," *Eur. Phys. J.*, vol. C 45, pp. 97–107, 2006.

[152] S. Frixione, P. Nason, and B. R. Webber, "Matching NLO QCD and parton showers in heavy flavour production," *JHEP*, vol. 08, p. 007, 2003.

[153] R. Frühwirth, "Track fitting with non-gaussian noise," *Comput. Phys. Commun.*, vol. 100, no. 1-2, pp. 1 – 16, 1997.

[154] Collaboration, ATLAS, "Search for the Standard Model Higgs boson in the decay channel $H \to ZZ^{(*)} \to 4\ell$ with the ATLAS detector," *Phys. Lett.*, vol. B 705, pp. 435–451, 2011.

[155] A. Djouadi, J. Kalinowski, and M. Spira, "HDECAY: A program for Higgs boson decays in the standard model and its supersymmetric extension," *Comput. Phys. Commun.*, vol. 108, pp. 56–74, 1998.

[156] A. Bredenstein, A. Denner, S. Dittmaier, and M. M. Weber, "Precise predictions for the Higgs-boson decay $H \to WW/ZZ \to$ 4leptons," *Phys. Rev.*, vol. D 74, p. 013004, 2006.

[157] Collaboration, ATLAS, "Background studies for $h \to z\gamma$," Tech. Rep. ATL-COM-PHYS-2013-082, CERN, Geneva, Jan 2013.

[158] C. Collaboration, "Search for a higgs boson decaying into a z and a photon in pp collisions at $\sqrt{s} = 7$ and 8 tev," 2013.

[159] C. Collaboration, "Properties of the observed higgs-like resonance using the diphoton channel," Tech. Rep. CMS-PAS-HIG-13-016, CERN, Geneva, 2013.

[160] C. Collaboration, "Observation of a new boson with mass near 125 gev in pp collisions at sqrt(s) = 7 and 8 tev," *JHEP*, vol. 06, p. 081, 2013.

[161] M. Baak, M. Goebel, J. Haller, A. Hoecker, D. Kennedy, K. Mnig, M. Schott, and J. Stelzer, "Updated status of the global electroweak fit and constraints on new physics," *The European Physical Journal C*, vol. 72, no. 5, pp. 1–35, 2012.

[162] A. Collaboration and CMS, "Procedure for the lhc higgs boson search combination in summer 2011," *ATLAS-PHYS-PUB-2011-011, CMS NOTE-2011/005*, 2011.

[163] A. L. Read, "Presentation of search results: The CL_s technique," *J. Phys.*, vol. G28, pp. 2693–2704, 2002.

[164] G. Cowan, K. Cranmer, E. Gross, O. Vitells, "Asymptotic formulae for likelihood-based tests of new physics," *Eur. Phys. J.*, vol. C71, p. 1554, 2011.

[165] A. Collaboration, "An update to the combined search for the Standard Model Higgs boson with the ATLAS detector at the LHC using up to 4.9fb^{-1} of pp collision data at $\sqrt{s} = 7$ TeV," *ATLAS-CONF-2012-019*, 2012.